ABSTRACT

Title of dissertation: MAGNETORHEOLOGICAL FLUID
DYNAMICS FOR HIGH SPEED
ENERGY ABSORBERS

Stephen G. Sherman
Doctor of Philosophy, 2016

Dissertation directed by: Professor Norman M. Wereley
Department of Aerospace Engineering

Fluids with a controllable yield stress allow rapid variations in viscous force in response to an externally applied field. These fluids are used in adaptive energy dissipating devices, which have a controllable force response, reducing shock and vibration loads on occupants and structures. This thesis investigates the physics of these fluids at high speeds and shear rates, through particle modeling and fluid dynamics. The focus is on the experimentally observed reduction in controllable force at high speeds seen in magnetorheological (MR) fluid, a suspension of magnetizable particles that develop a yield stress when a magnetic field is applied.

After ruling out particle dynamic effects, this dissertation takes the first rigorous look at the fluid dynamics of a controllable yield stress fluid entering an active region. A simplified model of the flow is developed and, using computational fluid dynamics to inform a control volume analysis, we show that the reduction in high speed controllable force is caused by fluid dynamics. The control volume analysis provides a rigorous criteria for the onset of high speed force effects, based purely on nondimensional fluid quantities. Fits for pressure loss in the simplified flow are constructed, allowing yield force prediction in arbitrary flow mode geometries. The fits are experimentally validated by accurately predicting yield force in all of the known high speed devices. These results should enable the design of a next generation of high performance adaptive energy absorbers.

MAGNETORHEOLOGICAL FLUID DYNAMICS WITH APPLICATION TO HIGH SPEED ENERGY ABSORBERS

by

Stephen G. Sherman

Dissertation submitted to the Faculty of the Graduate School of the
University of Maryland, College Park in partial fulfillment
of the requirements for the degree of
Doctor of Philosophy
2016

Advisory Committee:
Professor Norman M. Wereley, Chair/Advisor
Professor James Baeder
Professor Howard Elman
Professor Alison Flatau
Professor Derek Paley

Acknowledgments

This thesis would not have been possible without an advisor who encouraged and enabled me to do the best work I could. For this, and so much more, I thank my advisor Prof. Norman Wereley. For putting me on this path, all the credit, or perhaps blame, belongs to Prof. Derek Paley, my undergraduate advisor. If I had not been assigned a new professor who needed bodies for his new lab, I doubt I ever would have gone down this path.

I must also thank my other committee members, Prof. James Baeder, Prof. Alison Flatau and Prof. Howard Elman, for their advice and support in writing this thesis. And of course, none of this would have been possible without Prof. Wereley, Paley and Baeder writing the letters of recommendation that won the fellowship that supported this work.

I also would have been unable to complete this without my labmates and friends. I must thank Andrew Becnel, Ami Powell and Harinder Singh, who passed on their knowledge of MR fluids. The final section of this thesis is impossible to imagine without Dr. Young-Tai Choi, whose counsel was invaluable. To my group mates, Tom Pillsbury, John Chambers, Caitlin King, Mingfu Wen, Robert Vocke, Ryan Robinson, Brian Powers, John Chambers, John Kunkel, Lei Xie, Erica Hocking and Xian-Xu Bai, whose patience I will never be able to repay. To Shane, Will, Joe and Elizabeth, for always being willing to get lunch.

Finally, to my parents and sister, for supporting me in all my adventures and for encouraging me to pursue this crazy goal.

This material is based upon work supported by the National Science Foundation Graduate Research Fellowship Program under Grant No. DGE1322106. Any opinions, findings, and conclusions or recommendations expressed in this material are those of the author(s) and do not necessarily reflect the views of the National Science Foundation.

Table of Contents

List of Tables

List of Figures

List of Symbols and Abbreviations

Fluid quantities

τ	Shear stress
τ_{y}	Yield stress
τ_{w}	Wall shear stress
γ	Shear strain
$\dot{\gamma}$	Shear rate
p	Local pressure
P	Average cross section pressure
u	Local velocity
v_0	Reference velocity
v_{gap}	Active gap mean velocity, typical choice for v_0
v_p	Piston velocity
$\frac{dp}{dx}$	Pressure gradient in the flow direction
N	Number of grid elements in the crosss flow direction
η	Viscosity
η_∞	Plastic viscosity or viscosity at high shear rate
η_0	Low shear rate viscosity
η_c	Carrier fluid viscosity
ρ	Density
K	Hydraulic loss coefficient

Geometric quantities

h	Active gap height
D_h	Active gap hydraulic diameter
L	Length
L_A	Active region length
L_N	Passive region length
A	Area
A_{p}	Piston cross section area
A_{res}	Fluid reservoir cross section area
A_{gap}	Active gap cross section area

Force model

β	Profile momentum factor
n_p	Pressure active length correction
n_v	Viscous loss active length correction
ΔP	Duct pressure loss
x'	$(x/D_h)/\mathrm{Re}$
x_{e,τ_w}	Wall shear stress entrance length
$x_{\mathrm{e},u}$	Velocity entrance length

Particle quantities

a	Radius
σ	Characteristic diameter
$\mathbf{x}$	Position
k	Collision stiffness parameter
F	Force
N	Number of particles
m	Dipole moment
$\mathcal{M}$	Particle mass

Magnetics

H	H field
B	B field
M	Magnetization
μ_0	Vacuum permeability
μ_r	Relative permeability
χ	Susceptibility

Nondimensional numbers

Re	Reynolds number	Inertial to viscous	$\frac{\rho v_\mathrm{gap} D_h}{\eta_\infty}$
He	Hedstrom number	Dimensionless yield stress	$\frac{\rho \tau_\mathrm{y} D_h^2}{\eta_\infty^2}$
Bi	Bingham number	Yield to viscous	$\frac{\tau_\mathrm{y}\, h}{\eta_\infty v_\mathrm{gap}}$
C_{τ_y}	Yield stress coefficient	Yield to inertial	$\frac{\tau_\mathrm{y}}{\frac{1}{2} v_\mathrm{gap}^2}$
Mn	Mason number	Particle viscous to magnetic	$144 \frac{\eta_c \dot{\gamma}}{\mu_0 M^2}$
δ	Dimensionless plug thickness	Yield stress to wall stress	τ_y/τ_w
η^*	Regularization parameter	Post-yield to pre-yield viscosity	η_∞/η_0

Superscripts and subscripts

B	Bingham
b	biviscous
N	Newtonian
0	Reference
y	Yield
c	Transition to turbulence or carrier fluid
p	Parabolic
w	Wall
e	Entrance
gap	Active gap
res	Reservoir
rep	Repulsion
fit	Curve fit
act	Activation flow
∞	high shear rate

Abbreviations

MR	Magnetorheological
ER	Electrorheological
MREA	MR energy absorber
SAOS	Small amplitude oscillatory shear
GPU	Graphics processing unit
CFD	Computational fluid dynamics

Chapter 1: Introduction

Mitigating vibration and impact loads is an essential task for designing safe and reliable systems. Devices designed to prevent these unwanted loads fall into three categories: passive, semi-active and active, defined by the level of control each device gives [1]–[4]. Passive devices resist motion with a fixed force, and are fixed systems. Classic examples are elastomeric isolators, viscous energy absorbers, frictional dampers and deformable structures. Active devices can apply a variable force that resists or encourages motion, but are necessarily more complicated, with typical devices being actuated by hydraulic, pneumatic or piezoelectric mechanisms. Semi-active devices can apply a variable force, but only one that resists, and offer a balance of complexity and controllable force.

The benefit of a controllable energy absorption device is that closed-loop control can be used to reduce loads more effectively across a wider range of disturbances than with a fixed device. Semi-active dampers have become popular because the balance between controllability and complexity allows improved performance in small volumes at affordable prices. Some variants of semi-active dampers include variable orifice dampers and viscous dampers with controllable yield stress fluids. This dissertation focuses on controllable yield stress fluid devices, the most popular type of semi-active damper [5].

Controllable yield stress fluids are fluids that upon the application of an external electric/magnetic field, develop a controllable yield stress, and can thus be used to create a controllable force. There are two main types of controllable yield stress fluids, electrorheological (ER) and magnetorheological (MR) fluids, named for their change in viscosity (rheological response) upon application of an electrical or magnetic field respectively. Both fluids consist of micron scale particles in a carrier oil, and upon application of an electric/magnetic field, develop chain-like microstructures and a yield stress whose strength is dependent on the strength of the applied field. Electrorheological fluids are suspensions of dielectric particles, typically silica, in a non-conducting oil, invented by Winslow [6], have yield stresses of about 5 kPa, and operate at electric fields of roughly 1 kV/mm. Magnetorheological fluids, invented by Rabinow [7] are suspensions of magnetically permeable particles, typically iron, in oil and have yield stresses of around 50 kPa. Magnetorheological fluids are more popular than ER fluids, as they offer larger yield stresses, operate at lower voltages, and are insensitive to the presence of impurities. However, the physics of ER and MR fluids are very similar, and insights from one fluid can be applied to the other. While the focus of this dissertation is on MR fluids, all of the models and results in this dissertation should be equally applicable to ER fluids.

Devices using ER/MR fluids work in some combination of three modes: shear, flow and squeeze. This dissertation focuses on flow mode devices, and in flow mode, the Bingham plastic model is the classic rheological model for the fluid:

$$\tau = \tau_{\mathrm{y}} + \eta_\infty \dot{\gamma} \tag{1.1}$$

where stress τ is composed of a field-dependent yield stress τ_y and a field independent plastic viscosity η_∞. Flow mode devices work by pushing lots of fluid through a small gap, generating viscous pressure losses. For controllable yield stress fluids, part of the gap, the *active gap*, has an electric/magnetic field running through it, generating a controllable yield stress, altering the pressure loss in the gap, and thus providing a controllable viscous force. The the controllable component of the force output is known as the *yield force*, and is the difference in force between when the applied field is on and when the field is off , $F_{\mathrm{y}} = F_{\mathrm{on}} - F_{\mathrm{off}}$.

Magnetorheological devices have found wide application in the automotive industry, particularly as adaptive suspensions [5], [8]. Recently, interest has grown into using MR devices to absorb high-speed impacts for improved automotive and helicopter crash safety [9], [10]. However tests at impact speeds have shown a disappearing yield force, potentially preventing these devices from being used in impact absorbers.

In particular two sets of experiments come to mind. Goncalves [11] and Goncalves *et al.* [12] tested a capillary rheometer capable of reaching 37 m/s in the active gap, and sees a drop in controllable force when the fluid spends less than one millisecond in the active region. In my group, Mao [13] and Mao *et al.* [14] tested the impact performance of dampers at peak piston velocities up to 5 m/s, corresponding to fluid speeds over 40 m/s in the active gap and saw a smaller reduction in yield force. Perhaps surprisingly, in the course of this research we realized that some seismic energy absorbers also operate at high speeds, despite piston velocities below 0.5 m/s, as large piston to gap area rations mean gap velocities can be in excess of 25 m/s [15]. In these devices, yield force decreases as fluid velocity increases, and we call this reduction *high speed yield force falloff*. Our problem is that there are no models for yield force that produce the experimentally observed high speed yield force falloff.

But for devices operating at conventional speeds, if we know the yield stress, the Bingham plastic model accurately predicts the yield force. But since existing Bingham plastic yield force models cannot predict high speed yield force falloff, nor can they predict phenomenon like squeeze-shear strengthening of MR fluids [16], it is clear that we need an improved understanding of the physics. Since the field induced microstructure causes the yield stress, it seems reasonable to investigate the microstructure. To do this, we turn to particle modeling.

1.1 Particles

Particle modeling is popular because a basic model will easily reproduce the basic features of experimentally observed microstructure. With the aid of a microscope, the microstructure is revealed to be thick columnar structures spanning the active gap, breaking and reforming under shear. These columnar structures are often idealized as particle chains, and chains form the classic explanation for why the yield force exists. However, nearly all good images of ER/MR fluids under shear are of suspensions with a particle volume fraction, ϕ, less than 2% [17], [18], whereas a typical engineering scenario uses fluids that are totally opaque, as the suspension has a high solids loading, $\phi > 20\%$.

For dense fluids, the preferred method for understanding the chain structures is to numerically simulate them. There has been masses of work in this area, but the general goal is nearly always the same: to understand the chains in order to understand the yield stress. But in all these simulations, yield stress is underpredicted by a factor of three or greater for conventional MR fluids at large magnetic fields [18]–[30]. However, the changes in simulated yield stress and particle structure correlate reasonably well to experimental results, making them useful in designing novel fluids [29], [30].

Since my group was designing devices that were experiencing counter-intuitive experimental results, investigating the chain structures in real devices seemed like it might provide useful insight into the problem. However, devices are large, and most papers in the literature look at small, often 2D, control volumes, typically using $\approx 10^3$ particles. At the start of my graduate career, there existed a potential solution to this problem: the ability to run highly parallel code up to 100× faster by using the computers graphics processing unit (GPUs) instead of its CPU [31]. So I wrote a custom code capable of simulating the behavior of 10^6 particles in an MR fluid on a single GPU [19], an increase of roughly 100× over the literature. With typical 8 µm particles, this number is sufficient to simulate a cubic fluid element with height $h = 0.5\,\mathrm{mm}$ (typical parallel-plate rheometer measurements have a gap height of

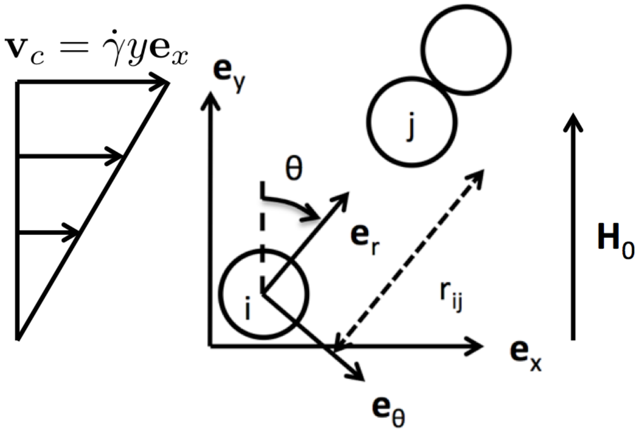

Figure 1.1: Diagram of two particles in a shearing fluid.

0.5 mm), thereby meeting the goal of simulating at experimental length scales.

But increasing simulation scale had no effect (when properly scaled) on the particle chain structure or the yield stress [19]. The lack of change in chain structure showed directly that the experimental phenomena were not length scale related, and the lack of change in yield stress that simulating at device scales would not resolve the yield force inaccuracy. However, we had developed a good tool, and the set of physics used in the particle dynamics has obvious limitations, so I hoped to improve the accuracy by improving the physics. In order to understand my attempts at improving the physics, the next section goes through the construction of the typical model, as well as serving as a literature review of how others have approached this same problem.

1.2 The equations of motion

The particles in ER/MR fluids are electrically/magnetically polarizable particles, typically spherical in shape, and placed in between the poles of a large electric/magnetic circuit. In this, case the classic treatment is to model the particles as uniform spheres interacting in a uniform external magnetic field. Since linearly polarizable spheres in a uniform field develop a pure dipole moment, the standard approximation is to treat the particles as point dipoles. Similarly, so will particles in a magnetic field large enough to fully saturate the particle. Specializing for MR fluids here on out, for particle i with position $\mathbf{x}_i$, shown in Fig. 1.1, with radius a_i, vector magnetization $\mathbf{M}$, and mean magnetization M, the dipole moment is $\mathbf{m}_i = 4\pi a_i^3 \mathbf{M}/3$. We also adopt the chemical engineering notation, where the reference diameter is σ. The magnetic field from dipole j at $\mathbf{x}_i$ is

$$\mathbf{B}_{ij} = \frac{\mu_0}{4\pi} \frac{3\hat{\mathbf{r}}_{ij}(\mathbf{m}_j \cdot \hat{\mathbf{r}}_{ij}) - \mathbf{m}_j}{r_{ij}^3}, \tag{1.2}$$

where $\mathbf{r}_{ij} = \mathbf{x}_i - \mathbf{x}_j$. The force on dipole i in an arbitrary $\mathbf{B}$ field is $\mathbf{F}_i = \nabla(\mathbf{m}_i \cdot \mathbf{B})$. Then the force on dipole i from the magnetic field of dipole j is [32]

$$\mathbf{F}_{ij}^{\mathrm{m}} = \frac{3\mu_0 m_i m_j}{4\pi r^4} \left(\hat{\mathbf{r}}_{ij}(\hat{\mathbf{m}}_i \cdot \hat{\mathbf{m}}_j + \hat{\mathbf{m}}_i(\hat{\mathbf{r}}_{ij} \cdot \hat{\mathbf{m}}_j) + \hat{\mathbf{m}}_j(\hat{\mathbf{r}}_{ij} \cdot \hat{\mathbf{m}}_i) - 5\hat{\mathbf{r}}_{ij}(\hat{\mathbf{r}}_{ij} \cdot \hat{\mathbf{m}}_i)(\hat{\mathbf{r}}_{ij} \cdot \hat{\mathbf{m}}_j) \right),$$

where superscript m denotes magnetic forces.

Next we specialize for the case where the external applied field is large and the the dipole moments are aligned. Using θ_{ij} as defined in Fig. 1.1, the magnetic force is

$$\mathbf{F}_{ij}^{\mathrm{m}} = F_{ij}^{\mathrm{m}} \frac{(3\cos^2\theta_{ij} - 1)\mathbf{e}_r + \sin 2\theta_{ij} \mathbf{e}_\theta}{(r_{ij}/(a_i + a_j))^4} \tag{1.3}$$

with the dipole force magnitude,

$$F_{ij}^{\mathrm{m}} = \frac{3\mu_0 m_i m_j}{4\pi(a_i + a_j)^4}$$

and reference force magnitude

$$F_0 = \frac{\pi}{48}\mu_0 M^2 \sigma^2.$$

Multipole moments or mutual dipole models can be used to increase the fidelity of the magnetic models at intermediate field strengths [27], [33], reducing off-axis repulsion forces. However, as discussed below these models have a minimal effect on predicted yield stresses when compared at an equivalent magnetization.

For particle contact repulsion forces, we choose the standard Klingenberg style model [34],

$$\mathbf{F}_{ij}^{\mathrm{rep}} = -2F_{ij}^{\mathrm{m}} \exp\left[-k\left(\frac{r_{ij}}{\sigma} - 1\right)\right]\mathbf{e}_r \tag{1.4}$$

Alternate repulsion force models exist [20], [26], including ones more physically realistic, but these generally have minimal impact, as $k > 50$ is sufficiently stiff for most problems of interest [20].

The other major force on the particle is the viscous drag force. Since the particles are very small spheres, the Reynolds number is nearly zero, viscous drag forces can be represented by Stokes drag for an isolated sphere,

$$\mathbf{F}_d = -6\pi\eta_c a_i(\dot{\mathbf{x}}_i - \mathbf{v}_c) = -D_i(\dot{\mathbf{x}}_i - \mathbf{v}_c),$$

with with particle i drag factor $D_i = 6\pi\eta_c a_i$, reference drag factor $D_0 = 3\pi\eta_c\sigma$, and carrier fluid velocity $\mathbf{v}_c$. To capture the effects of shearing, the carrier fluid velocity is assumed to be the shear flow velocity profile, $\mathbf{v}_c = \dot{\gamma} y \mathbf{e}_x$. While assuming an isolated sphere is problematic at large volume fractions, simulations employing smoothed particle hydrodynamics and Lattice Boltzmann methods showed no major changes to the observed yield stress [21], [22], [26].

The next observation is that, in the dynamics, the accelerations of the particles are negligible [25], [34]. Starting with the equations of motion for a single particle,

$$\frac{4\pi\rho a_i^3}{3}\ddot{\mathbf{x}}_i = -D_i(\dot{\mathbf{x}}_i - \dot{\gamma} y\, \mathbf{e}_x) + \sum_{\substack{j=1 \\ j\neq i}}^{N} \left(\mathbf{F}_{ij}^{\mathrm{m}} + \mathbf{F}_{ij}^{\mathrm{rep}}\right). \tag{1.5}$$

Note that for computational ease, force interactions are cut off when $r_{ij} \geq 4\sigma$, or at 0.5% of the particles-in-contact maximum.

Nondimensionalizing through force F_0, time scale $D_0\sigma/F_0 = 144\eta_c/\mu_0 M^2$, and length scale σ, using $\mathcal{M}_i$ for mass, and dividing by F_0 yields:

$$\frac{\mathcal{M}_i F_0}{D_0^2\sigma}\ddot{\mathbf{x}}_i^* = -\frac{D_i}{D_0}(\dot{\mathbf{x}}_i^* - \frac{D_0\sigma\dot{\gamma}}{F_0} y^*\, \mathbf{e}_x) + \sum_{\substack{j=1 \\ j\neq i}}^{N} \left(\frac{\mathbf{F}_{ij}^{\mathrm{m}}}{F_0} + \frac{\mathbf{F}_{ij}^{\mathrm{rep}}}{F_0}\right) \tag{1.6}$$

where $\ddot{\mathbf{x}}_i^*$, $\dot{\mathbf{x}}_i^*$ and y^* are dimensionless acceleration, velocity and y coordinate respectively. The leading term is here fairly small, $\approx 10^{-2}$ but perhaps not truly negligible. However, results show that models including acceleration produce yield stresses equivalent to those that do not [21]. This finding is unsurprising, as the yield stress is essentially a static phenomenon. Dropping acceleration, we obtain the simplified model

$$\frac{D_i}{D_0}\dot{\mathbf{x}}_i^* = \frac{D_i}{D_0}\mathrm{Mn}\,y^*\,\mathbf{e}_x + \sum_{\substack{j=1\\ j\neq i}}^{N}\left(\frac{\mathbf{F}_{ij}^{\mathrm{m}}}{F_0} + \frac{\mathbf{F}_{ij}^{c}}{F_0}\right). \tag{1.7}$$

This expression introduces Mason number,

$$\mathrm{Mn} = \frac{D_0\sigma\dot{\gamma}}{F_0} = 144\frac{\eta_c\dot{\gamma}}{\mu_0 M^2}, \tag{1.8}$$

the ratio of particle shear forces to particle magnetic forces. This definition has the benefit of using a consistent length scale used in the derivation, unlike in [35], which mixes length scales, producing a factor of 9/2 in the front. The Mason number is the most useful concept that comes out of particle dynamics, because if viscosity is plotted against Mason number, measurements at different magnetic fields collapse onto the same master curve. This works best with Mason number in terms of M, not H, as τ_{y}/M^2 is approximately constant for any applied field, due to the measured magnetic properties accounting for material nonlinearities and self interaction [35], [36]. Becnel *et al.* [37], [38] used this to demonstrate that high shear-rate shear-mode devices exhibit the same Mason number scaling as low speed devices, demonstrating that the physics at low and high shear rates are unchanged.

The advantages of using M^2 extends to modeling the particle interactions. For magnetic force models using nonlinear material properties and magnetically interacting particles, the particles will mutually magnetize, increasing M, and causing stronger interactions when compared to magnetization by the reference H field alone.

However, finite element calculations and mutual dipoles models show that these interactions are stronger only when compared at an equivalent H [35], [36], as at an equivalent M forces are nearly unchanged. Therefore, developing more refined models of interacting spheres will have minimal benefit, as we know at saturation the particles are definitely dipoles, and from experiments using Mason number analysis, that the fluid behavior at saturation magnetization is similar to the behavior at lower field strengths.

There are other concerns, such as thermal effects from Brownian motion, but these are expected from theory to be negligible for typical high solids-loading MR fluids at large magnetic fields [39]. To demonstrate this, I performed a rheological study on a series of typical MR fluids combined with a nondimensional analysis of remnant magnetization effects and demonstrated that the observed changes in suspension viscosity due to temperature were equivalent the temperature changes in viscosity of the carrier fluid [40], which is contained in Appendix C.

1.3 Improving particle model accuracy

But as stated before, this typical model of MR fluid has a substantial limitation: it does not predict yield stress accurately. More problematically, it also seems that refining the existing force terms produces little benefit, something that I learned after investigating various improvements.

First, in Sherman *et al.* [19], Appendix D, we explored the effects of volume size on the chain structures in the fluid, leveraging our high performance code. We also made the observation that our simulation code was reproducing the lamellar sheet phenomenon seen experimentally. However, during later work it became clear that the sheet formations are strongly influenced by the force cut off, and in fact are likely a numerical artifact. Similar large scale work [20], saw similar sheet structures, but doesn't draw the conclusion that we have, that they are a numerical artifact. However, the force cut is placed far enough away that these sheets have no effect on yield force.

Later, in Sherman and Wereley [41], Appendix E we improved particle model accuracy by including a realistic particle size distribution. We observed significant changes in the particle structure during chain and sheet formation, as well as some changes to stress during $\gamma = 4$–8. However, this averaging period was based on uniform sized results, but with a size distribution some transients can still be seen. Later, a much more thorough paper [42], which included both thermal and inertial effects, investigated the same concerns. They found that the size distribution affected the structure, smoothing the yielding process, but that steady state stress was essentially unaffected. While the conclusions between the two vary slightly, I think both papers agree that adding a size distribution changes the particle structure and the transients of the stress response.

The most direct approach is to refine the existing force terms, as discussed in the previous section. In particular, Hanna Lagger used a model which refined all the existing force terms simultaneously [20]–[22], improving magnetic, contact and hydrodynamic force model accuracy, but still produced yield stresses roughly one third of those seen experimentally. Since the equations of motion used by all authors underestimate the yield stress by such a large factor, and improving accuracy of individual elements produces no major change in yield force, I believe that a fundamental force is missing.

Since the error in yield force scales with magnetic field, it follows that we need to add a force that also scales with magnetic field but is not a magnetic force, as magnetic forces have already been investigated. The only force that I can think of that satisfies this criteria is friction, where the magnetic attraction forces will cause large normal forces, and thus large amounts of friction that depend on magnetic field strength. I believe the lack of friction to be the most viable explanation as to why most simulations fail to produce accurate yield stresses.

Including friction also explains a series of experimental results. Vereda *et al.* [43] looked at spherical particles with different amounts of surface roughness, and concluded that friction is needed to accurately model the particle dynamics. They show that particle surface roughness has a significant impact on experimental measurements of yield stress, but demonstrate via FEM that surface roughness does not effect the magnetic particle forces at equivalent M^2. From this, the authors conclude that friction must be responsible for the enhancement in yield stress caused by increasing the surface roughness. Similarly, for slender rod particles, several authors have concluded that friction is needed to accurately model the interactions between rods [44]–[46]. Many authors also report that precise yield stress values are dependent on the testing instrument surface roughness and material [47], [48], with magnetic wall materials increasing yield stress, a result consistent with particles interacting with boundary-image particles and resulting normal and friction forces.

Friction is also the most viable explanation for squeeze-shear strengthening, where an applied normal force increases shear mode shear stresses [49].

However, properly implementing static friction is complicated, as it can easily drive the timestep to zero, and advanced techniques are not available for the acceleration free models used here. Simulations using friction have been performed particle chains under small amplitude oscillatory strain and found including friction improved accuracy [50]. However, to my knowledge, there is also no way to estimate friction ahead of time in a way that will produce sufficiently accurate (5–10% error) forces. Estimating friction, as demonstrated in the previous papers, is strongly dependent on the particle shape, surface roughness, and any fluid additives, and thus requires tribological models for each of those parameters. These are details we normally neglect, but when attempting to construct an accurate friction model, cannot. It is not coincidental that the design of MR fluids focuses heavily on particle shape, size, and surface coating, as these are properties with significant impact on yield stress, as well as other important concerns like settling time, offstate viscosity and lifetime absorbed energy [46], [51], [52].

Then to develop an accurate simulation model that includes friction, we need to know the fine details of the particle morphology and surface coating thickness and chemistry, develop correction factors, and then use them as inputs to a high fidelity code for predicting yield stress. While developing and experimentally validating such a model is feasible, the challenge is substantial, as it will require a tremendous number of measurements and an expert of knowledge of tribology. Such a test campaign would have benefits beyond obtaining an accurate yield stress, as it would also resolve questions about those other secondary properties such as settling time, offstate viscosity and lifetime absorbed energy.

While particle models are the only way forward for predicting fluid properties, the focus of this dissertation is different: predicting device yield force. Our most basic assumption about yield force is that it comes from the yield stress via some established relationship. Since this assumption holds for most devices, predicting yield force boils down to knowing the yield stress. There are two ways to accurately know the yield stress: 1) measure the yield stress, or 2) create and validate a model of friction at the particle level. Since measuring yield stress of a fluid takes about two hours, and developing a friction model will take years, measuring yield stress sounds preferable when possible. However, this is not a valid approach for devices that lack an accurate yield force model, such as in high speed and squeeze-strengthened devices.

In these situations, we need to develop new yield force models. We can do this in two ways: by developing a highly accurate friction model or by correcting the Bingham plastic model. Since the Bingham plastic model is so simple, I claim it is preferable to investigate and fix the failures of existing Bingham plastic yield force models, rather than attempt to understand the true nature of interparticle friction.

1.4 Particle model analysis

However, the inability to predict yield stress accurately does not prevent us from using particle models to understand the physics of these fluids, as the relative trends are widely agreed to be accurate.

First, we realized that we wanted to link insight developed at the particle scale to the bulk scale. Sherman *et al.* [53], Appendix F, does this by exploring the relationship between the Bingham and Mason numbers, the nondimensional numbers governing the macroscopic (fluid) and microscopic (particle) scales respectively. The core observation is that $\mathrm{Bi} \propto \mathrm{Mn}^{-1}$. This simple result allows us to translate trends that occur at different scales. As an example it allows us to neglect high Mason number ($\mathrm{Mn} > 0.1$) theoretical results, as we know that they are experimentally irrelevant, as Bingham number is small, and thus controllable force is low. This same thinking also helped us when analyzing a series high shear experiments, as we were able to show that the high shear rate experiments fall onto the same Mason number master curve as the low shear rate data, experimentally demonstrating that the yield stress persists at large shear rates [37], [38]. When thinking about high speed yield force falloff, the focus of this thesis, Mason number analysis gives us confidence that the yield stress can exist at the high shear rates associated with high speeds.

Sherman and Wereley [54], Appendix G, explores a result from [55], where it was shown that there is an upper Mason number limit on the existence of stable chains. This could indicate a point at which the yield stress should disappear, and could serve as an explanation for high speed yield force falloff. Our simulation work demonstrated that this only happens at extremely low volume fractions, $\phi < 0.02$, where the particles actually form single width chains instead of the typical thick column and sheet structures. We can also apply the Bi-Mn relationship to determine that this effect would only occur when controllable force is low, and is not a viable explanation for high speed force falloff.

Finally, Appendix H examines the particle dynamics and showed the existence of two primary time scales, the particle dynamics time scale and the shear rate time scale. We then used our simulation code to show that the response time scales with the shear rate, giving a response time of a constant shear. We show that this fixed response shear is consistent with experimental measurements of response time, and is small enough that assuming a zero yield stress response time is reasonable. A fixed shear response time implies that response time is speed independent, and would manifest as a fixed apparent shortening of the active region.

1.5 Fluid Dynamics

So if we want to develop a model for high speed yield force falloff by fixing existing models, we need to identify what needs improvement. I believe the best way to improve current yield force models is to look at the problem through the lens of fluid dynamics, and supporting my view are the following observations:

1. The fluid is moving at large velocities $v_{\text{gap}} > 10\,\text{m/s}$ and the Reynolds number is relatively large, $\text{Re} > 1000$;
2. 'High speed' in the context of controllable yield stress fluids is not defined;
3. Existing yield force models assume $\text{Re} = 0$ or $\text{Re} = \infty$;
4. Fluid dynamics does interesting things when the Reynolds number is not zero, and nobody has performed a rigorous exploration of 2D flows of controllable

yield stress fluids with a large Reynolds number.

This dissertation is an examination of the fluid dynamics of controllable yield stress fluids and shows that high speed yield force falloff can be described with Bingham plastic rheology and a yield force model that accounts for Re > 0. Chapter 2 is an analysis of a simplified version of Goncalves' experiment, defines 'high speed' and produces a set of fits that describe the simplified flow. Chapter 3 shows that these fits accurately predict high speed yield force falloff in a series of practical devices, with conclusions contained in Chapter 4. These results will enable device designers to accurately predict yield force at high speeds.

1.6 Contributions

The main contributions of this dissertation are:

1. A rigorous nondimensional analysis of MR fluids. We demonstrated that the Reynolds and Hedstrom numbers are the most convenient descriptors of MR fluid dynamics, while Reynolds and Bingham are the most fundamental. We also found that yield stress coefficient, $C_{\tau_y} = \tau_y/0.5\rho v_0^2$, can be used to estimate the onset of high speed effects.

2. A simplified model of controllable yield stress fluids entering an active region in flow mode, which we call 'activation flow'. This model is the first rigorous generalizable model of the fluid dynamics of active region flow.

3. A simplified control volume analysis which lets us determine when speed effects

will become apparent, contained in Eq. 2.34 and 2.35. These limits can be turned into a simple criteria for when quasi-static models can be used safely: $C_{\bar{\tau}_y} > 0.4$ and $\mathrm{Re} < 120$ for a typical device with $L_A/D_h = 5$ wishing to stay within 5% of the fully developed solution.

4. A set of rigorous control volume based fits to activation flow that are accurate from $0 < \mathrm{Re} < 5000$, $10^3 < \mathrm{He} < 10^6$, $2 < L_A/D_h < 14$. These fits are contained in Eq. 3.1 to 3.8, and should accurately predict yield force in flow mode devices.

5. An experimental validation of the claim that activation flow describes the fluid dynamics of high speed devices by accurately predicting yield forces for all of the known high speed MR fluid devices.

6. A demonstration that fluid dynamics is a useful way to think about MR fluids. This includes both classic control volume analysis and computational fluid dynamics.

Chapter 2: Flow of a controllable yield stress fluid into an active region

2.1 Introduction

High speed yield force falloff is a phenomenon seen in flow mode magnetorheological energy absorbers operating at large fluid velocities, where the yield force $F_{\mathrm{y}} = F_{\mathrm{on}} - F_{\mathrm{off}}$, decreases at high speeds. This would place an upper limit on device operating speeds, limiting the design space. In particular, Goncalves [11] and Goncalves *et al.* [12] tested a capillary rheometer with a 37 m/s maximum flow rate, and observed a 90% reduction in apparent yield stress at high speeds in short active regions. Later, Mao [13] and Mao *et al.* [14] tested a double-rod damper with a maximum active region fluid velocity of 40 m/s and saw an up to 50% reduction in yield force at maximum speed. Perhaps surprisingly, some seismic dampers operate at large gap velocities and can see high speed force falloff [15], [56]. A second intriguing category of evidence is that as device engineers, we change yield force models at high speeds. At low speeds, a fully developed Bingham plastic flow model is typically used [8], and at high speeds, switching to a parabolic profile with superposed yield stress at high speeds [14], an approach which can reduce yield force by up to 33%.

This paper investigates high speed yield force falloff, and concludes it is the result of fluid dynamics, and develops a model capable of predicting yield force in all of the previously mentioned experiments.

In explaining the high speed yield force falloff effect, the simplest explanation is shear thinning at high shear rates. In high speed flow mode devices, the shear rates may be extremely large, $\dot{\gamma} \gg 100\,000\,\mathrm{s}^{-1}$ and there is a paucity rheological test data in this region. The most direct form of rheological measurement is conducted in shear mode, but typical shear mode parallel plate or cone and plate rheomters are limited to $1000\,\mathrm{s}^{-1}$ or even less. However there are other shear mode geometries that allow for higher shear rates. Laun *et al.* [57] develop an enclosed parallel plate test cell, creating a double gap test cell with a maximum shear rate $\dot{\gamma} = 10\,000\,\mathrm{s}^{-1}$, and report stresses in agreement with traditional low speed geometries. Becnel *et al.* [38] tested a concentric cylinder and a rotary vane device [37], both reaching up to $25\,000\,\mathrm{s}^{-1}$, and found that both devices produced measurements that agreed with conventional test results. Güth and Maas [58] and Güth *et al.* [59] tested a Taylor-Couette cell up to $34\,000\,\mathrm{s}^{-1}$, and observed a 10% reduction in force at high speeds. These experiment also showed a strong sensitivity to inertial effects, with Taylor number instabilities causing a large increase in device force output. In reviewing these results, the yield stress apparently persists at high shear rates, and shear thinning is on the order of that observed at low shear rates, so that shear thinning is unlikely to explain high speed force falloff.

Flow mode rheometers allow higher shear rates, with wall shear rates in a typical slit type capillary rheometer easily exceeding $20\,000\,\mathrm{s}^{-1}$. Wang and Gordaninejad

[60] tested a flow mode rheometer with 1 mm gap at 1 m/s mean velocity, and observed an apparent increase in shear thinning compared to parallel plate rheometer measurements. Gabriel and Laun [61] tested a slit rheometer with 0.34 mm gap and 1.2 m/s mean velocity and reported reduced viscosity at high speed when compared compared to parallel plate measurements. Both studies quote maximum shear rates on the order of $50\,000\,\mathrm{s}^{-1}$, and have results similar to other high shear rate shear mode studies [38], [57]–[59].

However, capillary rheometer experiments at high speeds introduces two new concerns: viscous heat production effects and inertial effects. Viscous heat production causes the fluid temperature to increase, which in turn decreases viscosity, and will appear as an apparent shear thinning. We believe thermal–viscous effects are a major contributor to the shear thinning seen in the previous papers. Capillary rheometer analysis assumes there are no inertial effects, but there is no known criteria for inertial effects, nor any description of what those effects would be. This study investigates inertial effects in a rheometer type flow, and provides both a prediction for the onset and effects of inertia. Our results show that no inertial effects occurred in the previous papers.

However, there have been very high speed capillary rheometer tests where inertia does have an effect. The best and only example of this is in Goncalves [11] and Goncalves *et al.* [12], where a slit device with variable length active region and a gap height of 1 mm is tested at mean flow speeds up to 37 m/s. Goncalves treats the device as a rheology experiment, and observes that when the fluid residence time in the active region drops below 1 ms, the device yield force falls by up to 90%.

In Goncalves [11], the authors attribute this effect to a yield stress response time, which would pose a major challenge to designing high speed MR fluid devices, as it would place an upper bound on device speed for compact geometries. However, the authors report a significant 12 °C temperature rise, and critically, their analysis uses a quasi-static model to determine yield stresses, which, we will show causes erroneous conclusions. While Goncalves' analysis is limited by the quasi-static perspective, it remains the only proper high-speed flow-mode experiment, and is the primary focus of this work.

The idea of the yield stress taking time to develop is not unprecedented. There have been extensive tests determining the time it takes for yield stress to develop after the magnetic field switched on. Koo *et al.* [62] investigate the response time of a commercial MR damper at low speeds , finding a 10 ms field rise time, and a 20 ms force rise time, but emphasize the impact that system compliance can have on such measurements. Sahin *et al.* [63] measured the pressure rise in flow mode devices after a step current is commanded , and find a flow mode response time of 10 to 20 ms. Laun and Gabriel [64] measure shear mode response times at shear rates of $100\,\mathrm{s}^{-1}$ under a sinusoidal magnetic field, and find response times of 2 to 3 ms. For device engineering, these fluid response times are short enough that they are dwarfed by magnetic circuit response times, and thus not of major concern. While these time domain results could be extended to the analysis of steady flow of fluid entering an active region, time dependent fluid rheology is a substantial complication we would like to avoid. If we can show that high speed yield force falloff is a fluid dynamic effects, it is a preferable explanation over time dependent fluid properties, as it introduces no new physics.

Another explanation is that at very high shear rates, the yield stress disappears completely. Martin and Anderson [55] develop an analytical chain model that suggests there are no stable particle chains above a critical Mason number, and particle chains are the standard explanation for the cause of the MR effect. We developed and ran a particle simulation of this regime [54], and our results indicated that there is no yield stress falloff for typical fluid volume fractions, even beyond the no-chain limit, as the particles are sufficiently close to be interacting magnetically even when the chains break down. Checking the critical Mason number against these high speed flow results of interest, the Mason number is close to, but below the critical Mason number, casting doubt on this shear rate dependent explanation. In our recent work, we observed that force rise time corresponded to a fixed shear angle, as expected from theory [65]. Thus, we expect that increasing shear rates would reduce response time, and since high speed flow experiments operate at extremely large shear rates, this would push the response time towards zero.

We hypothesize that the loss of yield force at high speed, or high speed yield force falloff is in a fact a fluid dynamic effect, and we investigate this idea through computational fluid dynamics (CFD) and control volume analysis. While our goal is to investigate high speed yield force falloff, 2D flow in a duct also a problem of basic interest, as there have been few examinations of 2D inertial flows of variable yield stress fluids. We approach the problem by developing a simplified model of magnetorheological fluid entering an active region, designed to replicate the experiment of Goncalves [11] while assuming a zero response time fluid. We demonstrate that this model captures the fundamental behaviors and successfully describes high speed yield force falloff.

Most computational fluid dynamics work on fluids with yield stress has focused on creeping flow, but here we look at the effects of non-zero Reynolds number. Abdali *et al.* [66] looks at creeping entry and exit flows of Bingham plastics, and tabulates the Bagley correction as a function of Bingham number, an approach we mimic. Mitsoulis *et al.* [67] look at pressure-driven creeping Bingham flow over a cavity, and uses a continuation scheme to reduce computational effort. Taylor [68] computed the fully-developed cross-sectional velocity profiles of Bingham plastics in rectangular ducts, and concludes that ducts of 10:1 cross section aspect ratio can be effectively treated as parallel plates. For inertial Bingham plastic flows, the primary focus has been on entrance region flows for thermal transport. Min *et al.* [69] and Vradis *et al.* [70] both look at entrance flows, and conclude that the flow is strongly two dimensional, and that increasing Bingham number reduces entrance length, but do not collect any force correction factors.

Previous work on using CFD for active magnetorheological fluid is fairly limited, especially for pressure driven flows. Park *et al.* [71] used the fluid dynamics and magnetism solver from ANSYS to get the varying magnetic field, and thus yield stress, in a shear mode brake. Bompos and Nikolakopoulos [72] successfully simulated an eccentric shear mode magnetorheological journal bearing using ANSYS. Gedik *et al.* [73] looked at a problem similar to ours, but the MR fluid is modeled using a magnetohydrodynamics code, which gives plug-like velocity profiles, but returns pressure losses several orders of magnitude below experimentally expected values.

Parlak and Engin [74] used ANSYS CFX to simulate the performance of a low speed MR damper, and their results compare reasonably well to experiment, but has a coarse grid and a possible lack of convergence. Bullough *et al.* [75] uses ANSYS Fluent to look at pressure driven and shear flow in a Couette cell, and finds good agreement with analytical models. In these papers, velocities are low and yield stresses large, so inertia and momentum effects are small, which ensures that no interesting fluid dynamics are observed.

However, we are not the first to identify a high speed regime. Goldasz and Sapinski [76] identify the existence of a high speed regime when performing a nondimensional analysis of the pre-yield fluid dynamics of MR fluids. In the high speed regime, Gołdasz and Sapiński [77] used CFD to develop qualitative insight into MR fluid flow, and take an approach extremely similar to the one used in this study. They examine several model problems of fluid entering a region of yield stress, and observe large regions of not fully developed flow, and a decreasing yield force at high speeds. We see the same things, but we rigorously quantify our results using control volume analysis.

In this study, we perform an analysis that provides force correction factors applicable to essentially all flow mode devices, and show through control volume and numerical analysis that high speed force falloff is a fluid dynamic effect. We develop a simplified model of Goncalves' experiment, 'activation flow', where fully developed Newtonian flow instantly develops a yield stress in a 2D duct. This model matches the analysis used in Goncalves, but with the addition of 2D flow and inertial effects. First, we show that including the momentum flux terms in a 1D

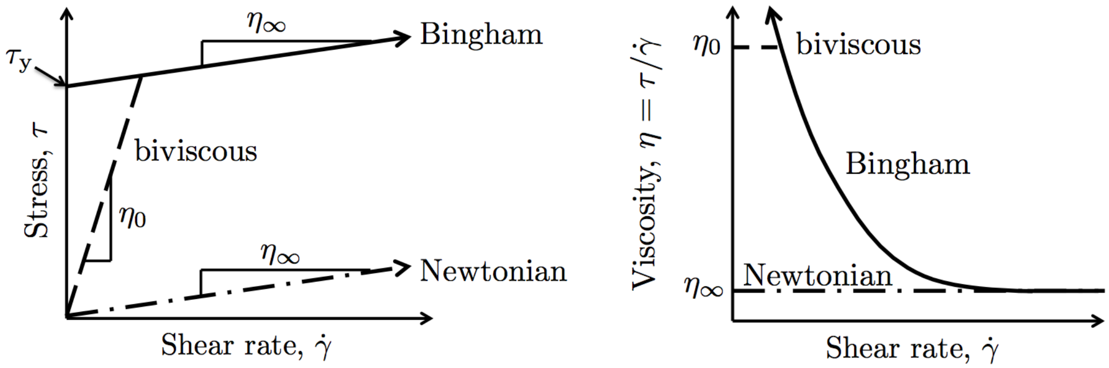

(a) Shear stress (b) Viscosity

Figure 2.1: Rheological models. Solid is Bingham plastic, dashed is biviscous, dash-dot is Newtonian.

pressure loss model will produce high speed yield force falloff. We then examine 2D flow, modifying an OpenFOAM CFD solver to handle a fluid with spatially varying viscosity (one that has no response time), and validate it to carefully define the region of solver accuracy. We then run our CFD model over a wide span of non-dimensional operating conditions, and observe, as expected, reduced pressure losses compared to classic fully developed models. From this, we conclude that the apparent loss of yield stress seen in Goncalves is not a response time effect, but, instead, an inertia and momentum dependent fluid dynamic effect. We then develop fits for pressure loss that should be applicable to a large class of devices.

2.2 Background

2.2.1 Rheology

The standard rheological model for MR fluids is as a Bingham plastic

$$\tau = \tau_y + \eta_\infty \dot{\gamma}, \tag{2.1}$$

where τ_y is the yield stress, η_∞ is the plastic viscosity and $\dot{\gamma}$ is the shear rate. This is shown in Fig. 2.1. Another alternative to the Bingham plastic model is to look at shear thinning models. Two popular choices are the Herschel-Bulkley model, $\tau = \tau_y + k\dot{\gamma}^n$ and the Casson plastic model, $\sqrt{\tau} = \sqrt{\tau_y} + \sqrt{\eta\dot{\gamma}}$ both of which can offer accuracy improvements. We do not use these shear thinning models, as we would like to see if the high speed force falloff can be explained using only the Bingham plastic model. However, we do make the standard simplifying assumption that the plastic viscosity is equal to the field-off viscosity. From the perspective of shear thinning, this assumption reduces shear stress, as field-on measurements typically have a slightly larger plastic viscosity.

However, when numerically modeling fluids with yield stress, viscosity, $\eta = \tau/\dot{\gamma}$, is infinite at zero shear rate, an unacceptable feature. The standard fix is to regularize the pre-yield behavior through a finite viscosity, covered thoroughly in a review by Mitsoulis [78]. The classic solution is to put a limiter on viscosity, creating a piecewise continuous stress curve called the biviscous model,

$$\tau = \begin{cases} \tau_y + \eta_\infty \dot{\gamma}, & \text{if } \tau_y + \eta_\infty \dot{\gamma} < \eta_0 \dot{\gamma} \\ \eta_0 \dot{\gamma}, & \text{otherwise} \end{cases} \tag{2.2}$$

where η_0 is the low shear viscosity, and is also shown in Fig. 2.1. To quantify the error of the Bingham plastic approximation, the viscosity ratio can be defined, $\eta^* = \eta_\infty/\eta_0$, the ratio of high shear rate to low shear rate viscosity, with $\eta^* = 10^{-3}$ as the standard choice. An alternative model is to use a smooth approximation [79],

$$\tau = \eta_\infty \dot{\gamma} + \tau_y \left(1 - \exp\left[-m\dot{\gamma}\right]\right) \tag{2.3}$$

with stiffness parameter m. This exponential model can improve solver performance, but for equivalent values of η^*, the smooth model is a much poorer approximation of the Bingham plastic solution. Mitsoulis makes a compelling case the that exponential model, with sufficient stiffness, offers the best mix of performance and accuracy. Here, we choose the biviscous model, as it is more familiar to device engineering and offers straightforward analytical solutions, which we wanted for verification.

Nondimensional description of Bingham plastic behavior is typically done through the Bingham number and the Hedstrom number. The Bingham number, is defined as the ratio of yield stress forces to viscous stress forces,

$$\text{Bi} = \frac{\tau_y h}{\eta_\infty v_0}, \tag{2.4}$$

where v_0 is the mean velocity, and h is the gap height. The Bingham number is the most fundamental description of Bingham plastics, as it solely determines velocity profile shape [80]. However, the Bingham number is dependent on both yield stress and velocity simultaneously, so it is awkward to work with.

Hedstrom number comes from the chemical engineering literature [81], [82],

$$\mathrm{He} = \frac{\rho \tau_y D_h^2}{\eta_\infty^2} \tag{2.5}$$

where ρ is fluid density, and D_h is the hydraulic diameter. Hedstrom number is an essential description of Bingham plastics, as it can be used to nondimensionalize yield stress. Hedstrom number has appeared in the ER fluids literature [75], [83], as a way of reporting yield stresses, but has not caught on in the MR fluids world. For comparing MR fluid experiments (variable τ_y) to traditional Bingham plastics (fixed τ_y), Hedstrom number is invaluable, as the chemical engineering literature reports flow data in terms of He and Re [82]. Critically, this allows us to use extensive chemical engineering literature for the Bingham plastic transition to turbulence, a concern for high speed flow experiments.

Reynolds number, the essential Newtonian nondimensional number, is the ratio of inertial to viscous forces, where for a Bingham plastic,

$$\mathrm{Re} = \frac{\rho v_0 D_h}{\eta_\infty}. \tag{2.6}$$

For traditional Newtonian fluids, Reynolds number is the governing parameter. Here

Re is used to nondimensionalize velocity.

We also make extensive use of yield stress over dynamic pressure, which we call yield stress coefficient,

$$C_{\tau_\mathrm{y}} = \frac{\tau_\mathrm{y}}{\frac{1}{2}\rho v_0^2} \tag{2.7}$$

the ratio of yield stress to inertial forces. Uses of this ratio in the literature are minimal. Hedström [81] examined the inverse, and found no particular application. Alexandrou *et al.* [84] uses it great effect when characterizing the flow structure of Bingham plastics filling a cavity. Bresch *et al.* [85] uses this term when modeling rapidly moving avalanches as Bingham plastics. We show that this ratio is fundamental in estimating the onset of dynamic behavior in a magnetorheological fluid. Note that only two nondimensional numbers are needed to describe the flow,

$$C_{\tau_\mathrm{y}} = 2\mathrm{He}/\mathrm{Re}^2 = 4\mathrm{Bi}/\mathrm{Re} \tag{2.8}$$

allowing C_{τ_y} to be determined from any other pair.

We use these different nondimensionalizations of yield stress for different purposes. When solving the fluid equations, we will operate in Bingham-Reynolds space, as these are the two independent variables for the flow velocity profile, with Bi controlling steady state flow profile and Re controlling the length of the transition zone. When comparing our results to experimental results, we will work with Hedstrom number instead of Bingham number, as a constant He number is equivalent to an experiment occurring at fixed magnetic field. Finally, when discussing entrance

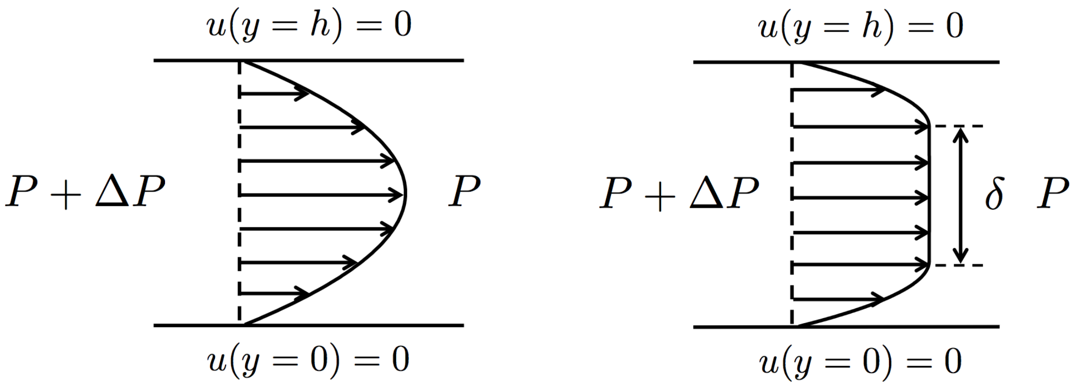

(a) Parabola (b) Plug

Figure 2.2: The basic steady-state 1-D flow profiles, parabolic flow and plug flow.

lengths and other inertial effects, we use C_{τ_y} and Re, as it clarifies limiting trends.

2.2.2 1D Flow

Since we are modeling the activation of MR fluid in a rectangular duct, the fully developed velocity profile and wall shear stress for both Newtonian and biviscous fluids provide means to analyze and verify the CFD output. We will denote Newtonian solutions with subscript N, fully developed Bingham plastic plug flow with B, fully developed biviscous solutions with subscript b, and biviscous fluids with parabolic profile with subscript p. Steady ($\partial u/\partial t = 0$), fully developed ($\partial u/\partial x = 0$) flow through a straight duct is the solution to the equation:

$$\frac{d\tau}{dy} = \frac{dp}{dx} \tag{2.9}$$

By substituting in a rheological model for τ, an equation in u is obtained. Through control volume analysis, this can be rewritten as $dp/dx = -2\tau_w/h$, where τ_w is wall shear stress, and h is gap height. For a Newtonian fluid, $\tau = \eta_\infty \partial u/\partial y$, with mean flow v_0 and no-slip boundary conditions, the steady-state velocity profile is a parabola

$$u_N = 6v_0 \left(\frac{y}{h} - \frac{y^2}{h^2} \right) \tag{2.10}$$

with corresponding pressure gradient

$$\left(\frac{dp}{dx} \right)_N = -12 \frac{\eta_\infty v_0}{h^2} \tag{2.11}$$

and associated wall shear stress $\tau_{wN} = 6\eta_\infty v_0/h$. An image is shown in Fig. 2.2a.

There are multiple approaches for determining pressure losses in a fully developed Bingham plastic, where the central core of the fluid moves of as solid. This is often referred to as 'plug' flow, and is shown in Fig. 2.2b. Goncalves uses the steady-state Bingham plastic pressure loss equations from Phillips [86],

$$\mathcal{P}^3 - (1 + 3\mathcal{T})\mathcal{P}^2 + 4\mathcal{T}^3 = 0 \tag{2.12}$$

where $\mathcal{P}$ is the ratio of Bingham plug flow pressure gradient to Newtonian flow pressure gradient,

$$\mathcal{P} = -\frac{dp}{dx} \frac{h^2}{12 v_0 \eta_\infty} \tag{2.13}$$

and $\mathcal{T}$ is a nondimensionalized yield stress,

$$\mathcal{T} = \frac{\tau_y h}{12 v_0 \eta_\infty}. \tag{2.14}$$

Note $\mathcal{T} = \mathrm{Bi}/12$. Goncalves uses this method in reverse, taking observed pressure losses and uses the polynomial to obtain an apparent yield stress. However, this assumes the fully developed velocity profile, an assumption which does not hold at large velocities.

For biviscous fluids, Wereley *et al.* [87] provides a polynomial for δ, the fraction of unyielded ($\eta = \eta_0$) fluid in the gap, which can in turn be used to obtain pressure loss. Here, we modify the equation to use a Bingham number based on dynamic yield stress, not static yield stress, obtaining

$$\left[\frac{1}{2}\delta^3 - \left(\frac{3}{2} + \frac{6}{\mathrm{Bi}}\right)\delta\right](1 - \eta^*) + 1 = 0 \tag{2.15}$$

where δ is found from the physically sensible root, $0 \leq \delta \leq 1$. When a sensible solution does not exist, the fluid is completely preyield, corresponding to $\mathrm{Bi} > 6(1 - \eta^*)/\eta^*$, and acts as a Newtonian fluid with viscosity η_0. Pressure loss in biviscous plug flow is

$$\left(\frac{dp}{dx}\right)_b = -\frac{2\tau_y}{(1 - \eta^*)\delta h} \tag{2.16}$$

When $\eta^* = 0$, (2.15) will reduce to the Bingham plastic solution and can be arranged such that it is equivalent to (2.12). Plug thickness can also be used to obtain the velocity profile,

$$
\begin{aligned}
u_b^a &= \frac{v_0\ \mathrm{Bi}}{\delta(1-\eta^*)} && \\
u_b &= u_b^a \left\{[1-(1-\eta^*)\delta]\bar{y} - \bar{y}^2\right\} && 0 < \bar{y} < \frac{1}{2}(1-\delta) \\
u_b &= u_b^a \left[\eta^*(\bar{y}-\bar{y}^2) + 0.25(1-\eta^*)(1-\delta)^2\right] && \frac{1}{2}(1-\delta) < \bar{y} < \frac{1}{2}(1+\delta) \\
u_b &= u_b^a \left\{[1-(1-\eta^*)\delta](1-\bar{y}) - (1-\bar{y})^2\right\} && \frac{1}{2}(1+\delta) < \bar{y} < 1
\end{aligned}
\tag{2.17}
$$

where $\bar{y} = y/h$ is the normalized gap coordinate. Note that u/v_0 is solely a function of Bingham number. For $\eta^* = 10^{-3}$, midline velocity for a biviscous fluid differs by only 0.5% at $\mathrm{Bi} = 10^3$.

We can also consider the case of Bingham plastic with a parabolic profile, which is equivalent to superimposing a yield stress on the Newtonian solution (2.10). For a Bingham plastic, the parabolic flow pressure loss is

$$
\left(\frac{dp}{dx}\right)_p = -\left(\frac{12 v_0 \eta_\infty}{h^2} + \frac{2\tau_y}{h}\right), \tag{2.18}
$$

and corresponding wall shear stress is $\tau_{wp} = \tau_{wN} + \tau_y$. In a parabolic profile, the biviscous model perfectly approximates the Bingham plastic model when $\mathrm{Bi} < 6(1-\eta^*)/\eta^*$. In this work, this condition is always true.

In a controllable fluid, the controllable force range is a key quantity. This can be captured by the wall shear stress ratio, τ_w/τ_{wN}, the relative change in viscous stress caused by the magnetic field at a given point. These shear stress ratios are especially useful when describing the development of viscous losses in 2D flow, as in

2D flow, $\partial p/\partial x \neq 2\tau_w/h$ and $\partial p/\partial x$ is no longer constant in the y direction. A fully developed biviscous fluid has wall shear stress ratio,

$$\frac{\tau_{wb}}{\tau_{wN}} = \frac{\text{Bi}}{6\delta}\frac{1}{1-\eta^*} \tag{2.19}$$

When the flow is fully developed and $\eta^* = 0$, by construction, $\tau_{wb}/\tau_{wN} = \mathcal{P}$. For a biviscous fluid with parabolic profile and $\text{Bi} < 6(1-\eta^*)/\eta^*$,

$$\frac{\tau_{wp}}{\tau_{wN}} = 1 + \frac{\text{Bi}}{6}. \tag{2.20}$$

In a flow transitioning from parabolic flow to plug flow, we can use these values as bounds for the local flow behavior.

2.2.3 Quasi 1D flow

Before attempting full solutions of the Navier Stokes equations, it is tempting to try and reduce the problem to a quasi 1D duct. In these models, an axial velocity profile form is assumed, and using conservation of mass, momentum, and an additional cross-flow pressure gradient relationship, a one dimensional differential equation for flow development can be created. This nonlinear differential equation is marched down the duct, providing entrance length and pressure losses.

For Bingham plastics, these methods have been primarily used to analyze entrance region flows, where uniform flow at the inlet develops into plug flow, typically at low Reynolds and Bingham numbers. Chen *et al.* [88] looks at this problem through various analytical boundary layer methods, with a spatially dependent plug flow thickness, and finds that a $\frac{1}{2}\rho v^2$ type correction factor is dependent only on steady-state plug thickness. Shah and Soto [89] look at a similar scheme, where the flow profile is discretized, and finds near perfect agreement with Chen's second method.

However, when compared to full 2D solutions of the entrance flow problem, these solutions fall short. Vradis *et al.* [70] finds that the quasi 1D solutions are 'fundamentally different', missing a key adverse pressure gradient at the entrance. Min *et al.* [69] conclude that the assumptions involved in the quasi 1D methods are 'not accurate' and also emphasize the importance of capturing the adverse pressure gradients, as well as the need to capture viscosity gradient terms. With these results in mind, it seems appropriate to focus on full 2D flow.

2.2.4 2D flow

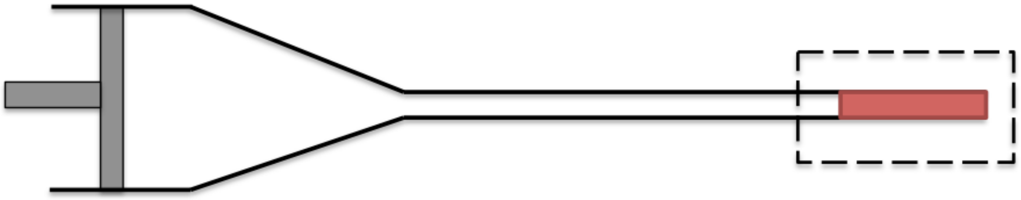

Figure 2.3: A simplified model of Goncalves' experiment. The active region is shaded.

The 'activation flow' that we investigate here is is the study of fluid entering a region of uniform yield stress, designed as a simplification of Goncalves' high speed capillary slit experiment, which is shown Figure 2.3. In Goncalves, a large piston pushes fluid into a rectangular duct through a smooth entrance, producing a mean duct flow velocity v_0 greater than $30\,\mathrm{m/s}$. The high aspect ratio $10\,\mathrm{mm} \times 1\,\mathrm{mm}$ rectangular duct has a total length of $101\,\mathrm{mm}$, with either an active region of $L_A = 6.35\,\mathrm{mm}$ or $25.4\,\mathrm{mm}$ placed at the end of the duct, with the fluid leaving the active region through a sharp exit into the air. These active lengths correspond to $L_A/D_h = 3.49$ and 13.97 respectively, and in these active regions, the field is assumed to be uniform, a reasonable assumption as the active region is a small gap between two large magnetic flux guides.

In order to examine the fluid dynamic effects on the yield force, we focus on the active region, using the simplified representation shown in Figure 2.4. The active region of length L_A is treated as a spatial region where the fluid has a yield stress, so here the fluid has zero response time. The passive region of the duct is designed to be long enough that the flow is fully developed at the start of the active region, which allows us to truncate the upstream portion. This allows us to simplify down to a short passive region with $L_N = 2.5D_h$ and inlet boundary conditions as fully developed parabolic Newtonian flow, (2.10). The short passive region is needed as the yield stress causes fluid dynamics effects upstream of the active region. The exit boundary condition is a uniform pressure, representing the exit into free air. The specific L_A we look at are those of Goncalves' experiment, $L_A/D_h = 3.4925$ and 13.97, as well as $L_A/D_h = 2$ and 7 to investigate finite length effects and to increase coverage of the device design space. This simplified representation has three degrees of freedom, v_0, τ_y and η_∞, and forms the simplest possible model that we believe than can capture the physics of high speed yield force falloff.

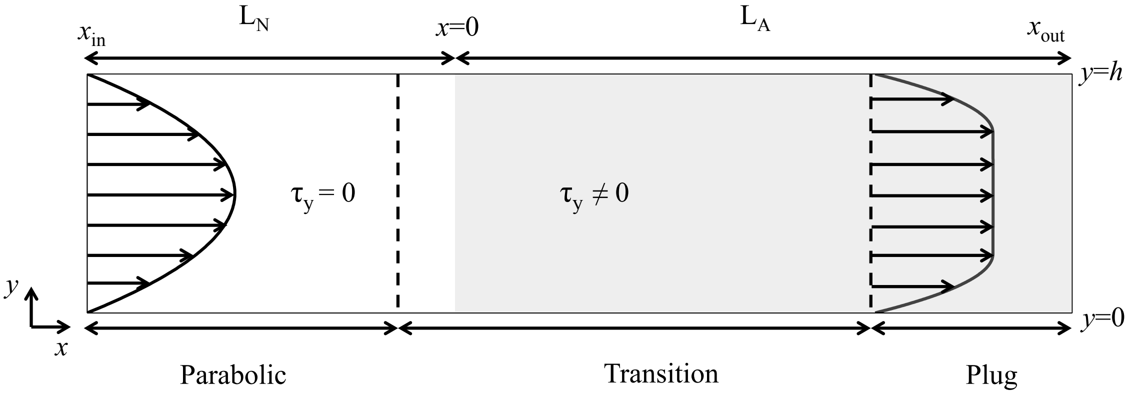

Figure 2.4: Simulation model of the end of Goncalves duct.

By solving for the full 2D flow, we aim to determine how the flow transitions from Newtonian parabolic flow to fully developed Bingham plastic flow, and what losses are encountered in the transition. Typically, pressure losses of MR devices are typically modeled by assuming fully developed flow everywhere,

$$\Delta P_{\text{slow}} = \left(\frac{dp}{dx}\right)_b L_A + \left(\frac{dp}{dx}\right)_N L_N \tag{2.21}$$

neglecting any effects from the transition from Newtonian parabolic flow to biviscous plug flow. This fully developed everywhere assumption is popular at low speeds, and is largely successful. However, at high speeds, there is no consideration of ρv_0^2 effects on yield force.

An alternative model is to assume that the velocity profile is parabolic everywhere, yielding

$$\Delta P_{\text{fast}} = \left(\frac{dp}{dx}\right)_p L_A + \left(\frac{dp}{dx}\right)_N L_N. \tag{2.22}$$

By construction, there are no transition losses or active region inertial effects. The form is popular in high speed pressure loss models [14]. This will be valid at $\text{Re} = \infty$, as inertia will keep the flow in a parabolic shape in the active region. Equation 2.22 predicts lower pressure losses than the low speed model, and is typically used when designing high speed devices.

Goncalves chooses the low speed model, but in his experiments, $\text{Re} = 1400$, so we expect transition effects and inertial terms to be present, causing the low speed analysis to incorrectly indicate that the yield stress disappears at high speeds.

In our activation flow model, we expect flow profile changes upstream of the active region to be present but minimal, causing the velocity profile at the start of the active region to be be nearly parabolic, and for the flow to rapidly transition to fully developed plug flow. We expect that the length of the transition zone will be affected by inertia and captured by Re and C_{τ_y}, but as we show below, transition effects on wall shear stress are fairly small, and insufficient to explain high speed force falloff. But if we do a proper control volume analysis and include momentum flux effects, we show that basic fluid mechanics gives us a negative loss term, and a viable explanation for the high speed force falloff effect.

2.2.4.1 Transition zone effects

We can estimate the effect of the transition from plug to parabolic by comparing the 1D pressure loss models. If the flow changes from parabola to plug in a reasonably gradual manner, we expect pressure losses to be bounded by the plug and parabolic solutions. From Equation 2.16 and 2.18 fully parabolic flow has 2/3 the yield induced

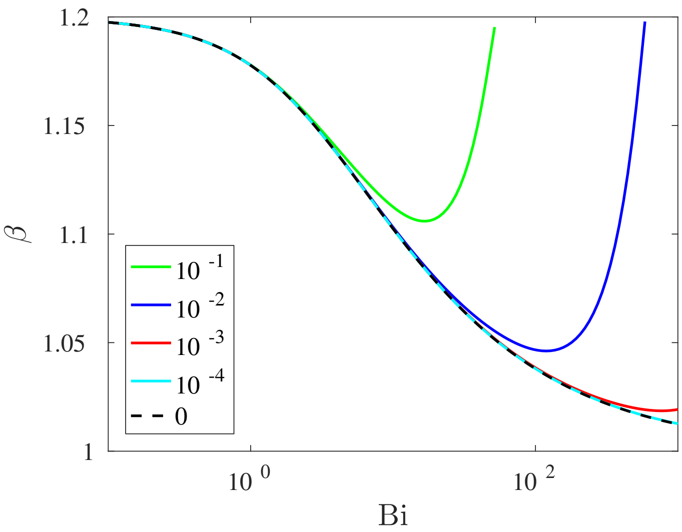

Figure 2.5: Profile momentum, β vs. Bingham number for various values of η^*.

pressure gradient of fully developed flow, or Bi → 0, or

$$\lim_{\mathrm{Bi}\to 0} \frac{\tau_{wp} - \tau_{wN}}{\tau_{wb} - \tau_{wN}} = 2/3.$$

This means that transition effects, in the case of fully parabolic flow everywhere, could cause a 33% reduction in yield force. However, since transition length should be fairly short for most cases, the actual impact of this term will be much smaller ($\approx 10\%$), and thus insufficient to describe the up to 90% force falloff seen in Goncalves.

2.2.4.2 Momentum flux effects

To explain the remainder of the high speed force falloff effect, we need to look at the effect of momentum flux. For a rectangular control volume, pressure loss is

$$\int_0^h p(x_{in}, y) - p(x_{out}, y) dy = \rho \int_0^h u(x_{out}, y)^2 - u(x_{in}, y)^2 \, dy + 2 \int_{x_{in}}^{x_{out}} \tau_{\mathrm{w}}(x) \, dx \quad (2.23)$$

If we assume a constant pressure at the inlet and outlet, and define profile momentum factor,

$$\beta(x) = \frac{\int_0^h u(x,y)^2 dy}{v_0^2 h}, \tag{2.24}$$

pressure loss can be rearranged, using skin friction factor, $C_f = \tau_w / \frac{1}{2}\rho v_0^2$ and hydraulic diameter, D_h to account for 3-D effects, to obtain

$$\frac{p(x_{in}) - p(x_{out})}{\frac{1}{2}\rho v_0^2} = 2\left[\beta(x_{out}) - \beta(x_{in})\right] + \frac{4}{D_h}\int_{x_{in}}^{x_{out}} C_f(x)\, dx. \tag{2.25}$$

For a fully developed Bingham plastic flow, β can be found in terms of Bi and δ by substituting in (2.17) into (2.24) with $\eta^* = 0$,

$$\beta_B(\mathrm{Bi}) = \frac{\mathrm{Bi}^2\,(\delta-1)^4}{16\,\delta} - \frac{\mathrm{Bi}^2\,(\delta-1)^5}{30\,\delta^2}, \tag{2.26}$$

Figure 2.5 plots β for a Bingham plastic, as well as a selection of biviscous fluids. The biviscous solution for profile momentum factor is substantially more complicated:

$$\begin{aligned}
\beta_b(\mathrm{Bi},\eta^*) &= \frac{\mathrm{Bi}^2\,\left(15(\delta-1)^4 + A\right)}{240\,\delta\,(1-\eta^*)^2} - \frac{\mathrm{Bi}^2\,(\delta-1)^3\,\left(8(\delta-1)^2 + B\right)}{240\,\delta^2\,(1-\eta^*)^2} && (2.27)\\
A &= 4\delta^2(\delta(7\delta-20)+15)\eta^{*2} - 20\delta(2\delta-3)(\delta-1)^2\eta^* && (2.28)\\
B &= 20\delta^2\,\eta^{*2} - 25\,\delta^2\,\eta^* + 25\delta\eta^* && (2.29)
\end{aligned}$$

For a Bingham plastic, increasing Bi reduces β, with $\beta_B(\mathrm{Bi}=0) = 6/5$ and $\beta_B(\mathrm{Bi}=\infty) = 1$. Figure 2.5 also places the strictest limits yet on the biviscous model, as it shows how reducing η^* improves reproduction of Bingham plastic behavior.

From this, we find that the standard value of $\eta^* = 10^{-3}$ will accurately reconstruct the velocity profile up to Bi ≈ 200, so that $\beta_B \approx \beta_b$.

In the experimental context, the decrease in β with increase in Bi explains the high speed fall off in force. Looking at pressure loss, Equation (2.25), when Bi > 0, $\beta(x_{out}) - \beta(x_{in}) < 0$, since $\beta(x_{in})$ occurs at Bi $= 0$, the maximum value of β. Since this term is negative, we now have a steady state yield stress induced negative velocity squared term that will reduce overall pressure loss. We believe this momentum flux effect is the main cause of high speed yield force falloff.

2.2.4.3 Flow features of interest

To capture both the transition zone and momentum flux effects, we use CFD to solve for the full 2D velocity profile. Since the CFD model includes inertia, the transition zone is no longer neglected, and will extend both upstream and downstream of $x = 0$, the start of the active region, with a velocity dependent length. We decided to use fixed active lengths, instead of a velocity scaled duct, as we wanted to investigate the effects of finite duct length.

Our activation flow model has the advantage of being simple: a 2D rectangle with with three parameters – velocity, yield stress and active length, or in nondimensional form, Re, Bi, and L_A/D_h. The approximation of treating the active region as a region of uniform yield stress is the largest assumption made here, but it is the most useful. By assuming a uniform yield stress, we do not need to know how yield stress varies with field, we do not need to account for body forces, and we do not need to choose a basis for comparing field strength in different geometries. This dramatically simplifies the analysis, and is also consistent with the majority of existing 1D yield force models, which also treat the active regions as zones of uniform yield stress. We do not need to account for the three dimensional behavior, as [68] showed that Bingham plastics in a 10:1 aspect ratio rectangular duct can be treated effectively as a 2D flow, and our reference experiment occurs in a 10:1 aspect ratio rectangular duct. The assumption of fully developed flow in the inlet, combined with sufficient passive length ($L_N/D_h > 1$) to include effects passed upstream, make our results independent of L_N, which eliminates a model degree of freedom. We are unaffected by the biviscous approximation, as we have shown earlier that $\eta^* = 10^{-3}$ is small enough that the difference between the biviscous model and the Bingham plastic model will be negligible. While these simplifying assumptions limit our ability to accurately model Goncalves' results, the simplicity gained allows us to draw clear and precise conclusions about the nature of the flow.

In this simplified 2D model, we use our CFD solution to determine:

1. *That our results are sensible.* We have assumed a region of uniform yield stress, which simplifies the problem, but the tradeoff is a potentially problematic discontinuous change in the rheological properties. We would also like to show that the viscosity regularization is having no effect, so we must demonstrate η^* independence. Finally, we need to demonstrate grid independence, to show that our results are unaffected by the CFD setup.

2. *An effective nondimensional scaling of the geometry.* We are using fixed length

active regions that include the exact active lengths of Gonvalves, but this approach does not work for arbitrary devices. If we develop an effective nondimensional scaling for duct length and the force correction, our numerical results can be used with any device.

3. *The change in force caused by inertial effects.* For device engineering, this is the primary concern. We would like to develop fits or tabulate this in a way that is easily applicable to a large class of devices, and to present it in a physically intuitive manner.

In order to validate our numerical results, we must compare to the experimental data we have. The challenge is that in an experiment, the rheology (the yield stress in particular) is essentially unknown. However, a CFD model requires that the rheology of the material be specified up front, so exact matching of operating conditions is not feasible. To get around this, we take our simplified 2D CFD model and simply sweep all numerically feasible nondimensional operating conditions. With enough test points, we can reasonably interpolate between them, freeing us from having to run a new set of CFD calculations every time we modify a rheological parameter.

2.2.5 Correction Factor

Since we are investigating a force effect, characterizing the change in force in a clear and intuitive manner is essential. Typical low speed viscoplastic entry and exit flow analyses employ the Bagley correction [90], which effectively adds additional contraction length to account for the viscous losses caused by the entrance/exit.

For controllable fluid entering an active region, we modify the Bagley correction factor, modeling extra viscous losses as the active region getting longer, while the passive region grows shorter by an equivalent length. This pressure correction model can be expressed as

$$\Delta p = \left(\frac{dp}{dx}\right)_b (L_A + n_p D_h) + \left(\frac{dp}{dx}\right)_N (L_N - n_p D_h). \tag{2.30}$$

where n_p, the pressure active length correction, is the change in active length measured in hydraulic diameters. For an activation flow, where observed pressure loss at high speeds is less than expected fully developed pressure loss, $n_p < 0$, a lost active length. From an observed pressure loss, Δp, we can rearrange to solve for n_p,

$$n_p = \frac{\Delta P - \left(\left(\frac{dp}{dx}\right)_N L_N + \left(\frac{dp}{dx}\right)_b L_A\right)}{\left(\left(\frac{dp}{dx}\right)_b - \left(\frac{dp}{dx}\right)_N\right) D_h}. \tag{2.31}$$

We considered other forms for our correction factor. A relative change in active region length can also be used, but for ducts of different length that are both fully developed by the exit, the relative change would be quote different values. By reporting a change in length in units of length, for two flows that are both fully developed, both will have the same n_p, simplifying analysis. Another option is a hydraulic ρv_0^2 type loss coefficient. Since the β effects are scaled by a ρv_0^2 term, it is tempting, as we would expect the loss coefficient to be dependent only on Bi, since β_B is a function of Bi only. While this is almost the case, our CFD results show a non-negligible Reynolds number dependence, and when Re is low, hydraulic loss coefficient is very sensitive to error, while n_p stays near zero, as the flow effect we are characterizing is not a ρv_0^2 effect. However, we can use β_B to generate a good analytical approximation for force loss.

We may also want to isolate the wall shear stress terms. By using Equation 2.25 to use solved quantities $p + u^2$ instead of τ_w, we can get the viscous active length correction

$$n_v = \frac{\Delta(p + u^2) - \left(\left(\frac{dp}{dx}\right)_N L_N + \left(\frac{dp}{dx}\right)_b L_A\right)}{\left(\left(\frac{dp}{dx}\right)_b - \left(\frac{dp}{dx}\right)_N\right) D_h} \tag{2.32}$$

where $\Delta(p+u^2)$ is the difference of the up and downstream values of $p+u^2$ integrated over the duct cross section. This lost viscous length corresponds to the reduction in viscous force on the damper walls, or the pressure loss when the effect of inlet/outlet momentum (β) can be ignored. This term may be of use for devices where active regions are followed by exits that can turn the momentum at the exit back into pressure. However, in Goncalves' experiment and typical MR energy absorbers, the exits do not recover any pressure, and n_v is not applicable.

2.2.5.1 An analytical estimate for change in active length

Since the profile momentum terms are the expected cause of the majority of the high speed force falloff effect, we can transform those losses into n_p and use that to develop some analytical insight into the problem. If we assume $\eta^* = 0$ and that the flow is fully developed everywhere, but include β effects,

$$\Delta P = (\frac{dp}{dx})_N L_N + (\frac{dp}{dx})_b L_A + (\beta - 6/5)\rho v_0^2$$

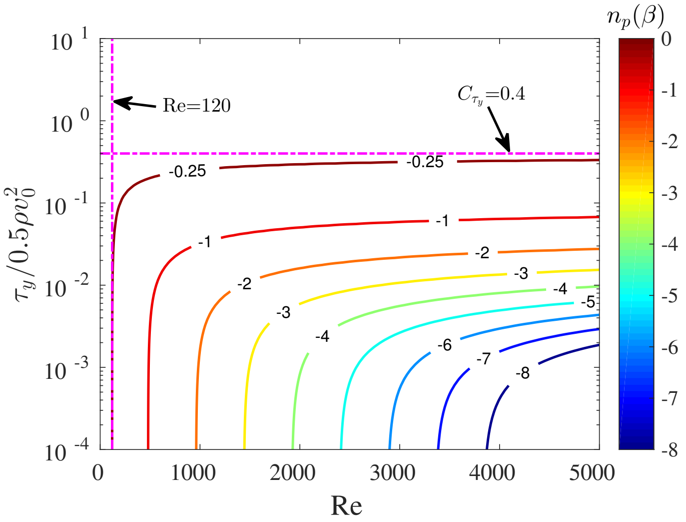

Figure 2.6: Pressure active length correction from momentum flux effects, $n_p(\beta)$, Eq. (2.33). The straight pink lines are the limiting values for $n_p = -0.25$ from Equation 2.34 and Equation 2.35.

we can then find the associated entrance correction, n_p,

$$n_p(\beta) = \frac{\beta_B - 1.2}{2(C_{\tau_y}/\delta - 24/\mathrm{Re})} \quad \text{or} \quad \frac{n_p(\beta_B)}{\mathrm{Re}} = \frac{\beta_B - 1.2}{24\,(\mathrm{Bi}/6\delta - 1)} \tag{2.33}$$

where we have rearranged to be dimension free, and is plotted in Figure 2.6. Note that the assumption of fully developed flow in $n_p(\beta)$ causes n_p to significantly overestimate the missing force if the flow is not fully developed.

Since the expanded form of Equation 2.33 is quite complicated, instead we look to determine bounds on the magnitude of $n_p(\beta)$ as a simple way of generating insight into the problem. Our approach is take to perform a limiting analysis on yield forces, viscous forces and inertial forces in Equation 2.33. In the limit of no viscous effects, $\mathrm{Re} \to \infty, \mathrm{Bi} \to \infty$, sets $\delta \to 1$ and $\beta_B \to 1$, yielding,

$$\lim_{\eta \to 0} n_p(\beta_B) = -\frac{1}{10C_{\tau_y}}, \tag{2.34}$$

corresponding to the horizontal part of the contours in Figure 2.6. This limit produces a conservative bound on $n_p(\beta)$, with solutions approaching the bound when $\mathrm{Re} > 10^4$. In the limit of no yield stress, $C_{\tau_y} \to 0, \mathrm{Bi} \to 0$, and with the help of Matlab's symbolics toolbox,

$$\lim_{\tau_y \to 0} n_p(\beta_B) = -\frac{\mathrm{Re}}{480} \tag{2.35}$$

the vertical part of the contours in Figure 2.6. Since this is in the limit of zero yield stress, this rule of thumb will only be accurate when $\mathrm{Bi} < 1$, so experimentally observing the predicted change in force in this region will be challenging. In the limit of no inertial effects, by construction, $n_p(\beta_B) = 0$.

The main use of these limits is to generate simple, convenient rules of thumb for when a certain value of n_p will be reached, as each limit is dependent solely on a single non-dimensional parameter. If we want to know when the momentum flux terms will cause a 5% difference in yield force from the fully developed value, we look for a 5% reduction in active length, or $n_p(\beta) = -.05 \times L_a$, and then solve for Re and C_{τ_y}. When n_p is below the 5% threshold, inertial effects are negligible and the flow is quasi-static, and will be accurately modeled by the plug flow solutions. Substituting in, our quasi-static criteria are:

$$C_{\tau_y} > \frac{2}{L_A/D_h} \quad \text{and} \quad \mathrm{Re} < 24\, L_A/D_h$$

For a typical value of $L_A/D_h = 5$, this tells us inertial effects will be noticeable when

Re > 120 and $C_{\tau_y} < 2/5$. However, since most devices have multiple active regions each with different L_A/D_h, a looser criteria is more useful. Observing that many devices have designs with $L_A/D_h \approx 5$, we use the specialized criteria, Re < 120 and $C_{\tau_y} > 2/5$ as our quasi-static criteria no matter the length.

2.2.6 Computational Fluid Dynamics

To improve our analysis beyond 2D control volumes, we use computational fluid dynamics to obtain the full velocity profiles in our model. We chose OpenFOAM's finite volume simpleFoam solver, [91], as the baseline for our solver, as it is proven, open source, cluster capable and easily modifiable CFD code. We picked this modification of the SIMPLE method [92], as it is the classic method for solving incompressible flow, and critically, comes with OpenFOAM by default. For this paper, we implemented a spatially dependent rheological model, which required only minor modifications to the viscosity calculation (replace a scalar lookup with a field lookup), and left the solver itself unaltered.

The SIMPLE method solves the steady, incompressible Navier–Stokes equations,

$$\rho u_j \frac{\partial u_i}{x_j} - \frac{\partial \tau_{ij}}{\partial x_j} = -\frac{\partial p}{\partial x_i} \tag{2.36}$$

where for generalizable Newtonian fluids, the viscous stress tensor

$$\tau_{ij} = 2\eta(\dot{\gamma}) e_{ij} \tag{2.37}$$

and viscosity $\eta = \tau(\dot{\gamma})/\dot{\gamma}$ and τ is the 1D rheological model, and $\dot{\gamma}$ is the shear rate. The rate of strain tensor is

$$D_{ij} = \frac{1}{2}\left(\frac{\partial u_i}{\partial x_j} + \frac{\partial u_j}{\partial x_i}\right), \tag{2.38}$$

and shear rate is defined as

$$\dot{\gamma} = \sqrt{2D_{ij}D_{ji}}. \tag{2.39}$$

These non-Newtonian parts add highly nonlinear couplings to the velocity equations, and required many solver iterations to relax.

Note that by assuming a generalizable Newtonian fluid, we have assumed that the fluid is isotropic. Experiments by Kuzhir *et al.* [93] have shown that yield stress is reduced when the magnetic field is parallel to the fluid velocity. However, in the duct flows investigated here, magnetic field and velocity are essentially perpendicular, so anisotropic effects should be minimal.

2.3 Results

2.3.1 Numerical validation

In order to evaluate the accuracy of the solver, we consider the case of a 2D periodic duct, and compare against the exact solution to test the accuracy of the solver. We ended up using the default OpenFOAM schemes with a very fine grid spacing. Here, grid spacing is characterized by N, the number of equally spaced elements from the wall to the center line of symmetry, with the number of horizontal

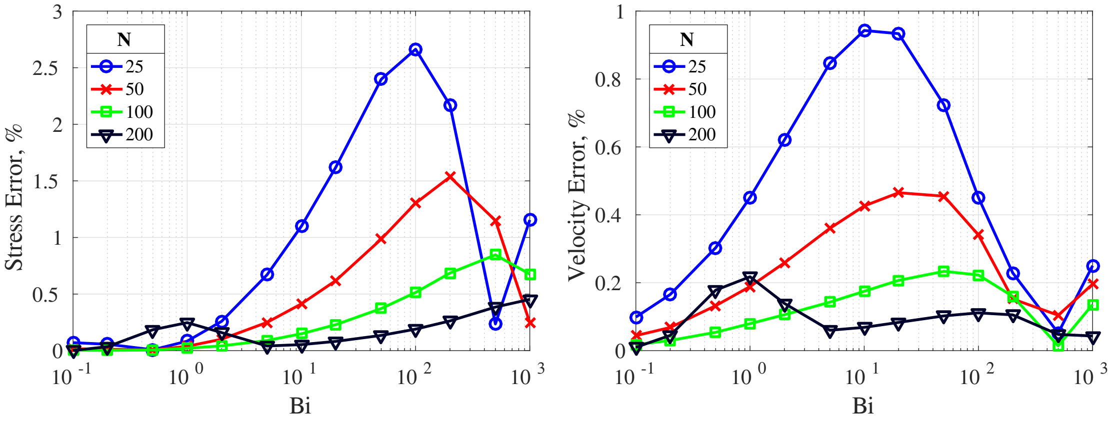

(a) Wall Shear Stress (b) Midline Velocity

Figure 2.7: Two dimensional periodic pipe error as a function of N, the number of elements to the midline.

elements changing equivalently. We also tried the higher order QUICK scheme, a popular choice for finite volume viscoplastic flows [94], but this introduced small, but problematic, oscillations in the solution, so we reverted to the default second order schemes on a fine grid. Solver convergence was set to be quite strict, with all residuals below 10^{-8}, which we found was required to obtain a close match to the steady state solution.

Figure 2.7 plots steady solution error, $|u/u_b - 1|$ and $|\tau_w/\tau_{wb} - 1|$, for both midline velocity and wall shear stress, for three grids with 25, 50, and 100 uniform elements to the center line of symmetry. Looking for sub 1% accuracy, we find that only N=100 and N=200 achieve this criteria. However, the N=200 solutions have a rise in error at low Bi, from running out of time due to slow convergence, with N=200 taking twice the number of iterations than N=100. We also note that when using over 100 elements to the center line of symmetry, the grid size can be smaller than the particles in the fluid, as a typical particle diameter is 2–8 µm and typical

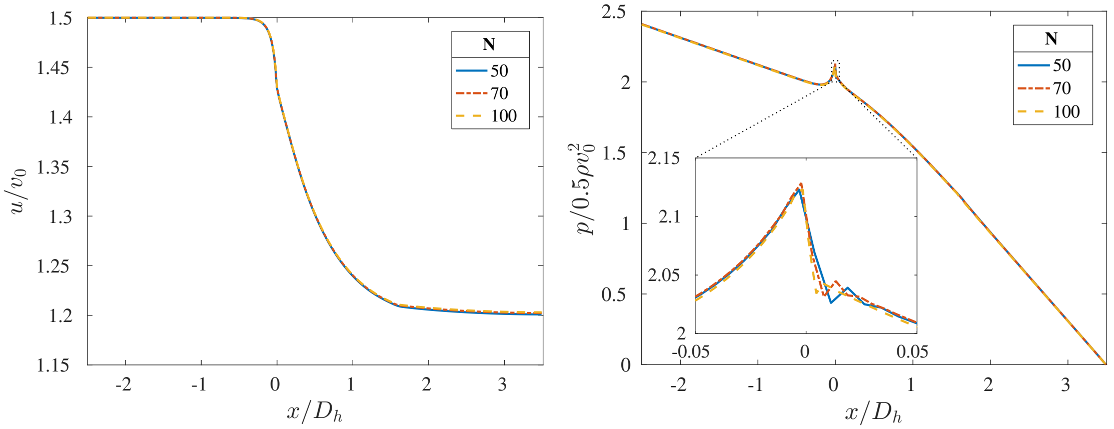

(a) Midline velocity (b) Midline pressure

Figure 2.8: Activation flow solution as a function of mesh size at Re = 500 and Bi = 10.

device gap height is 0.5 mm. For the periodic duct, we also tested for solver error as a function of Reynolds number and found no effect, as expected, affirming the choice to operate in Reynolds-Bingham space. From this, we chose $N = 100$, as it achieves accuracy goals while improving convergence rates compared to N=200.

Next, we looked at the effect of grid size on the activation flow geometry, considering scaled meshes with $N = 50, 700$ and 100 elements to the midline at a representative test condition of Re = 500, Bi = 10. Visually, the results are nearly identical, shown in Fig 2.8. Maximum difference in pressure loss, exit velocity, and active length correction was 0.25%, 0.17%, and 1.2% respectively. The difference in n_p from N=50 to N=100 was 0.007, a negligible amount. Since the observed changes are small, we conclude that our results are grid independent, and that a coarser mesh could have been used with minimal consequences.

We also checked to see if the effects of the yield stress step increase at $x = 0$ caused any issues. All velocities, (u, v), were continuous and oscillation free. However,

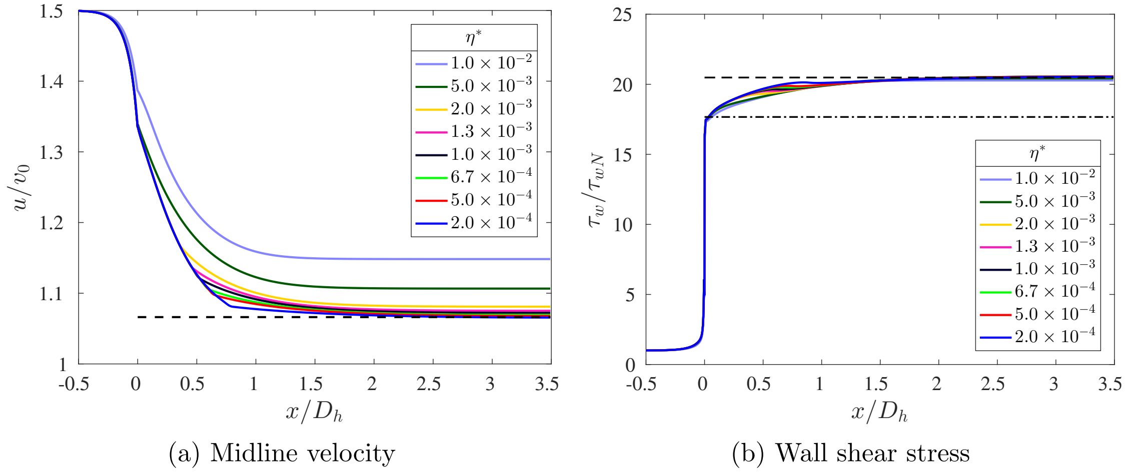

(a) Midline velocity

(b) Wall shear stress

Figure 2.9: Solution as a function of η^* at Re $= 2000$, Bi $= 100$.

leading up to $x = 0$, there is, as expected, a large adverse pressure gradient, but unexpectedly, a small pressure discontinuity at $x = 0$. However, this discontinuity is independent of mesh size, so all results are consistent. There are also some very small, highly damped oscillations on both sides of the discontinuity. Downstream of $x = 0$, all solutions returned to the same trend regardless of grid. From these investigations, we conclude that the simplifying benefits of a step increase in yield stress are worth the small numerical artifacts introduced into the solution.

We also tested the effect of η^* on the actual activation flow problem, looking at Re $= 1, 200, 1000, 2000$ and at each Re, Bi $= 1, 10, 100$. Figure 2.9 plots midline velocity and wall shear stress at Re $= 2000$, Bi $= 100$, the case where the largest η^* effects were observed. The midline velocity is strongly dependent on η^*, as predicted, but wall shear stress is essentially unaffected. The largest velocity effects are seen as the fluid approaches steady state, with the start of the slow convergence portion happening earlier for a system with higher η^*. Thus, when defining *entrance length*, the point at which the flow has reached steady state and the transition zone ends, we choose a fairly loose 90% relative convergence criteria to ensure that entrance length results are unaffected by η^*, while still being close enough to steady state that any further convergence can largely be neglected. With this criteria, for $\eta^* < 10^{-3}$, transition length is independent of η^*.

More importantly, total change in force is nearly independent of η^*, with a maximum difference in n_p of 0.038 between $\eta^* = 10^{-3}$ and $\eta^* = 2 \times 10^{-4}$ at $\mathrm{Re} = 1, \mathrm{Bi} = 1$. This error decreased with Re, where at Re = 2000, Bi = 100, the maximum n_p change was 0.009. This apparent change in active length is small enough that effect of η^* can be neglected. From these results, we conclude that the biviscous model with $\eta^* = 10^{-3}$ is a sufficiently accurate numerical approximation of Bingham plastic behavior for our problem.

2.3.2 Activation flow

2.3.2.1 Basic Flow visualization

In our activation flow model, we consider the two active lengths tested in Goncalves, $L_A/D_h = 3.4925$ and $L_A/D_h = 13.97$, as well as $L_A/D_h = 2$ and 7. For all cases there is an upstream Newtonian region of length $L_N/D_h = 2.5$. The grid had 75,000, 100,000, 125,000 and 140,000 cells for $L_A/D_h = 2$, 3.5, 7 and 14 respectively. On these four grids, we tested from $\mathrm{Re} = 0.1 - 5000$ and $\mathrm{Bi} = 0.1 = 200$, for a little over 1100 test points. For simplicity, we focus on Bi = 10, as it is a representative test condition that shows the tested effects clearly.

We start by looking at images of velocity at a fairly short duct length. For

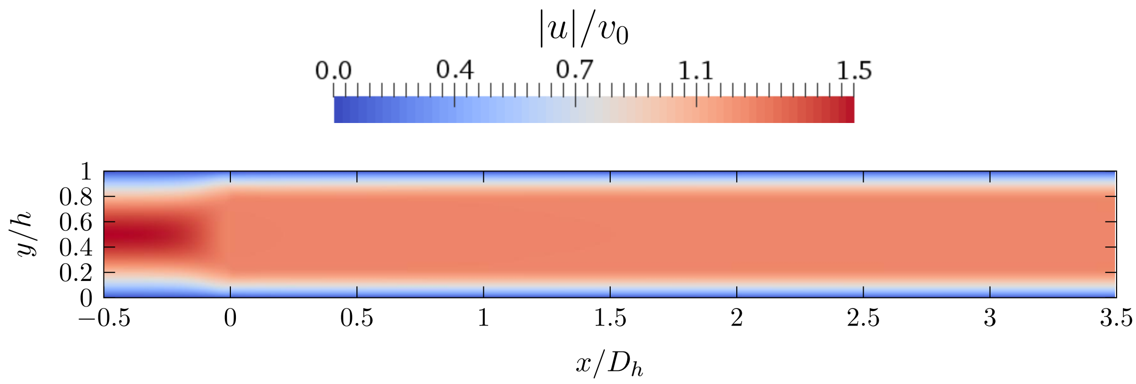

(a) $\mathrm{Re} = 0.1,\ C_{\tau_y} = 400,\ \mathrm{He} = 2$

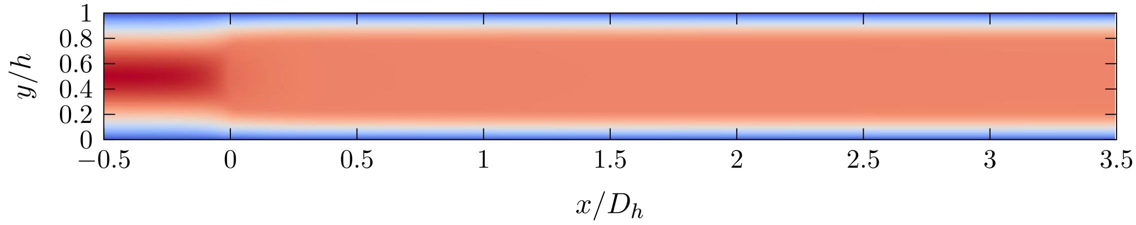

(b) $\mathrm{Re} = 100,\ C_{\tau_y} = 0.4,\ \mathrm{He} = 2 \times 10^3$

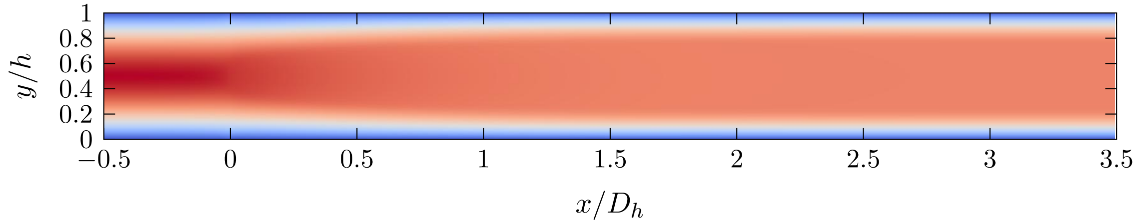

(c) $\mathrm{Re} = 500,\ C_{\tau_y} = 0.08,\ \mathrm{He} = 10^4$

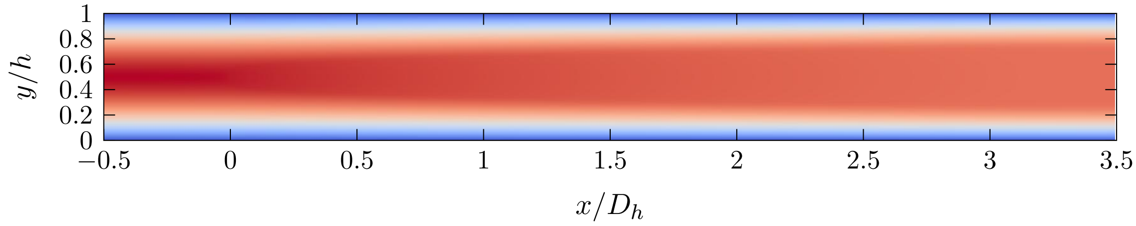

(d) $\mathrm{Re} = 2000,\ C_{\tau_y} = 0.02,\ \mathrm{He} = 4 \times 10^4$

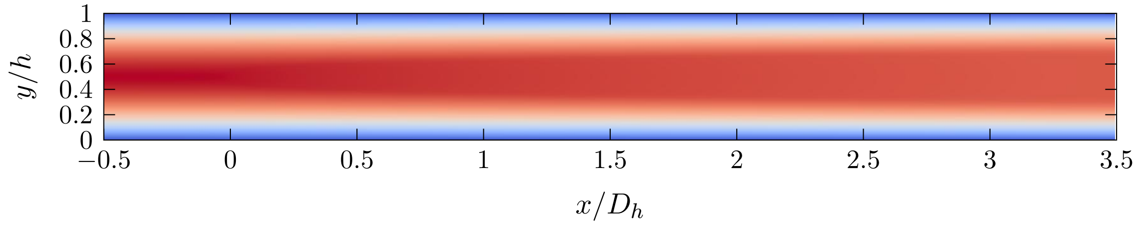

(e) $\mathrm{Re} = 4000,\ C_{\tau_y} = 0.01,\ \mathrm{He} = 8 \times 10^4$

Figure 2.10: Normalized velocity at $\mathrm{Bi} = 10$. The active region starts at $x = 0$.

$L_A/D_h = 3.5$ and Bi=10, normalized velocity, $|u|/v_0$ is shown in Figure 2.10, where we compare results at fixed Bingham number, so that only inertia affects the velocity profile. In these velocity profiles, the key features to observe are the length and starting position of the transition zone, and the region of uniform velocity, the plug. At low Re, the transition zone starts before the active region, and reaches the fully developed shape almost immediately after $x = 0$. Then, as Re increases, we observe that the transition zone gets longer and effects upstream of $x = 0$ also get smaller. Finally, at Re $\geq$ 2000, a close look shows that the flow does not quite enter fully developed form. Essentially, nothing unexpected is observed: there are no recirculation zones, no discontinuities and no oscillations. This means that there is only one real flow feature of interest, the transition zone.

To understand the transition zone, it helps to visualize plug growth. Figure 2.11 shows images of normalized apparent viscosity, η/η_∞, allowing clear observation of the plug, or the region where $\eta = \eta_0$. At low Re, the region of $\eta/\eta_\infty = 1000$, an effective proxy for the unyielded plug region, exists for the entire active region, with a small bump at the entrance, from the flow adjusting to the presence of yield stress. At Re=500, the low viscosity transition region can be seen, with the plug eventually reaching steady state size. At Re=2000, the transition region extends the length of the active region, and never reaches steady state plug form, as shown by the region of $\eta/\eta_\infty = 1000$ being slightly narrower at Re=2000 than at Re=500, something difficult to see in Figure 2.10.

More rigorously, Figure 2.12 looks at normalized midline velocity, $u(x, 0.5h)/v_0$ and wall shear stress. Looking at velocity, we confirm our previous observations,

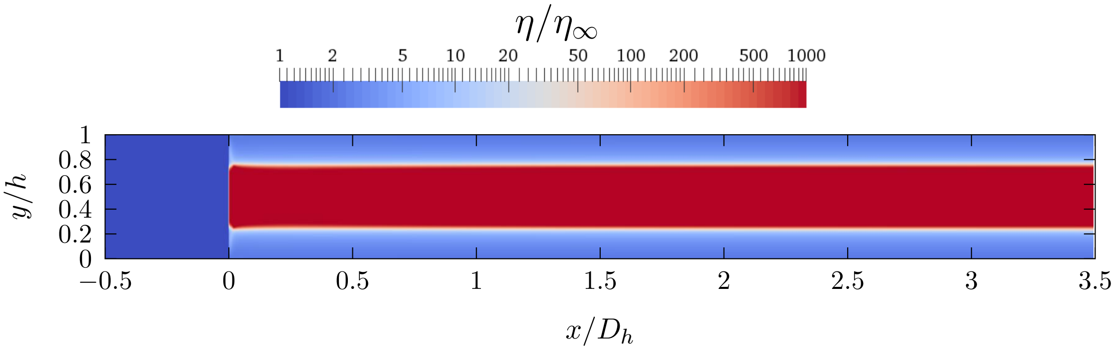

(a) $\mathrm{Re} = 0.1,\ C_{\tau_y} = 400$

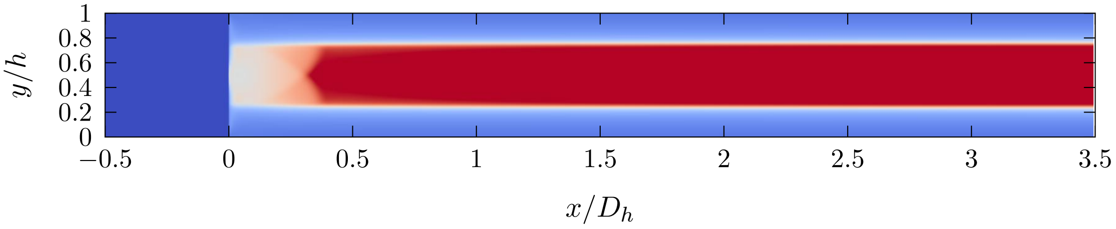

(b) $\mathrm{Re} = 100,\ C_{\tau_y} = 0.4$

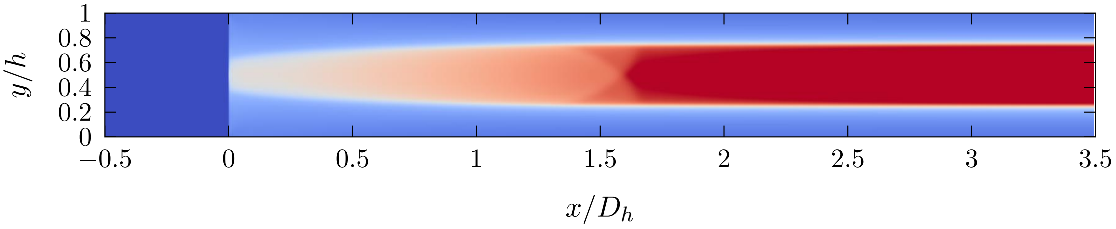

(c) $\mathrm{Re} = 500,\ C_{\tau_y} = 0.08$

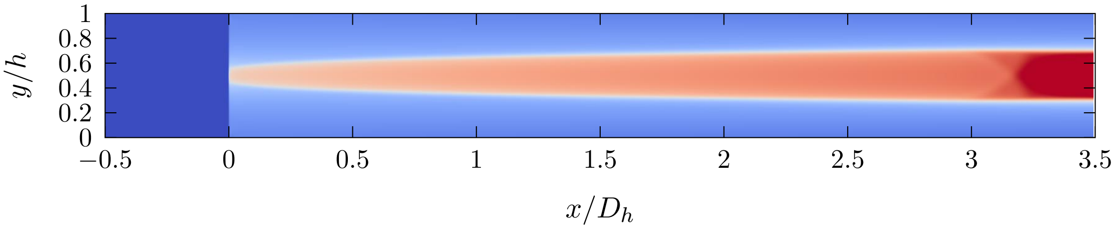

(d) $\mathrm{Re} = 2000,\ C_{\tau_y} = 0.02$

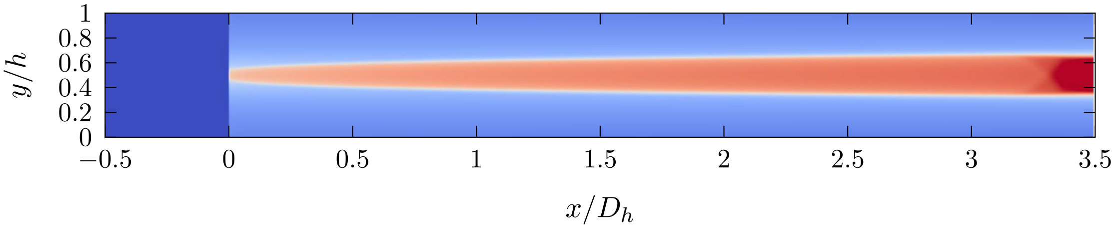

(e) $\mathrm{Re} = 4000,\ C_{\tau_y} = 0.01$

Figure 2.11: Plug visualization through viscosity at $\mathrm{Bi} = 10$. The active region starts at $x = 0$.

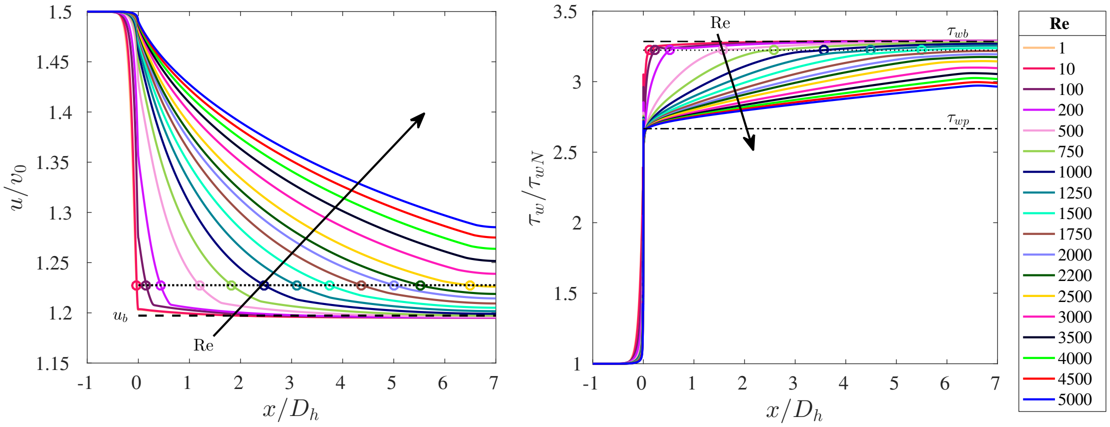

(a) Velocity

(b) Wall shear stress

Figure 2.12: Normalized velocity and wall shear stress as a function of Re for Bi = 10 and $L_A/D_h = 7$. Dashed lines, $--$, is the fully developed solution, Equation 2.17 or 2.19, and $-\cdot$ is parabolic wall shear stress, Equation 2.20 and $\cdots$ is the 90% entrance length convergence criteria.

namely, significant upstream velocity changes at low Re, a lengthening transition zone with increasing Re, and no convergence to the steady state solution at high Re. Figure 2.12 shows the effect of finite duct length, which is the velocity ceasing to converge to the steady state solution for the final $0.5D_h$. This is caused by wall-midline pressure difference being smoothed by the constant pressure boundary conditions, and is a fairly small effect.

Wall shear stress tells a similar story. At low Re, shear stress rises ahead of the active region, corresponding to the early transition. In the active region, after a short transition length, low Re wall shear stress almost immediately approaches τ_{wb}, while at high Re, the transition zone is longer, with shear stress reaching the fully developed value further down the duct. Finite duct length are again visible, where near the exit, wall shear stress stops rising, and possibly decreases slightly. Again, no unexpected phenomenon are observed, and aside from a small oscillation

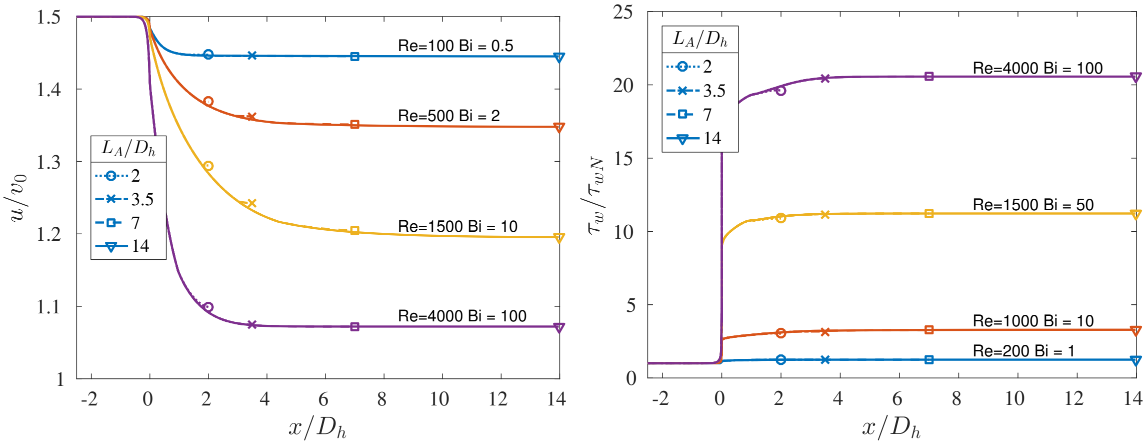

(a) Midline velocity (b) Wall shear stress

Figure 2.13: Comparison of velocity and wall shear stress across various active lengths.

around the onset of yield stress, wall shear rises from the parabolic value to the fully developed value in a smooth exponential like manner.

The most critical feature of the transition zone is the distance down the duct that the transition zone spans, which is contained in the entrance length. Previously, we defined a 90% relative entrance length criteria, which for midline velocity, is a 90% convergence to u_b from u_N, and for shear stress, a 90% convergence to plug shear stress, τ_{wb}, from parabolic shear stress, τ_{wp}. In Figure 2.12, midline velocity and wall shear stress are plotted as a function of x and Re at Bi $= 10$, and shows how the solutions grow. The key features to observe are the near linear increase in x_e with Re, and that at low Re, the entrance length can be negative, due to the flow profile changing before $x = 0$.

To examine exit effects directly, Figure 2.13 compares u and τ_w at a representative set of low C_{τ_y} flow conditions, and demonstrates that at any x, all solutions are extremely similar, with a small difference observed for $L_A/D_h = 2$. The fact

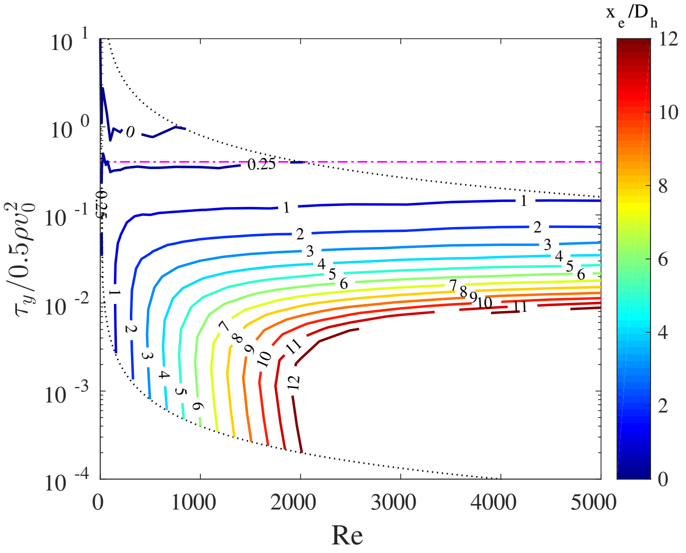

Figure 2.14: Velocity entrance length $x_{e,u}$ for $L_a/D_h = 14$. Dotted black lines are the bounds of sampled space. The pink dashed line is $C_{\tau_y} = 0.4$.

that all active lengths produce nearly the same result at a given x, means that if we correct for the small exit effects, we should be able to develop a model valid for any arbitrary entrance length.

Entrance length characterizes the size of the transition zone, and is shown in Figure 2.14 plotted as a function of Re and C_{τ_y}. Note that velocity based entrance length can be negative, as the flow can transition upstream of the active region.As x_e increases, the transition zone is growing. When $x_e < 0$ the flow transitions to fully developed Bingham plastic flow before the fluid is a Bingham plastic, and Figure 2.14 places x_e at $C_{\tau_y} = 1$. To identify when the transition zone really starts growing, we can relax the criteria slightly, choosing $x_e = 0.25D_h$ as a short entrance. This occurs roughly at $C_{\tau_y} = 0.4$ for $x_{e,u}$, roughly where we expect β to start affecting force output. We also note the strong resemblance in shape to the contours of n_p and $x_{e,u}$.

Figure 2.15 displays integrated friction losses, pressure losses and both high

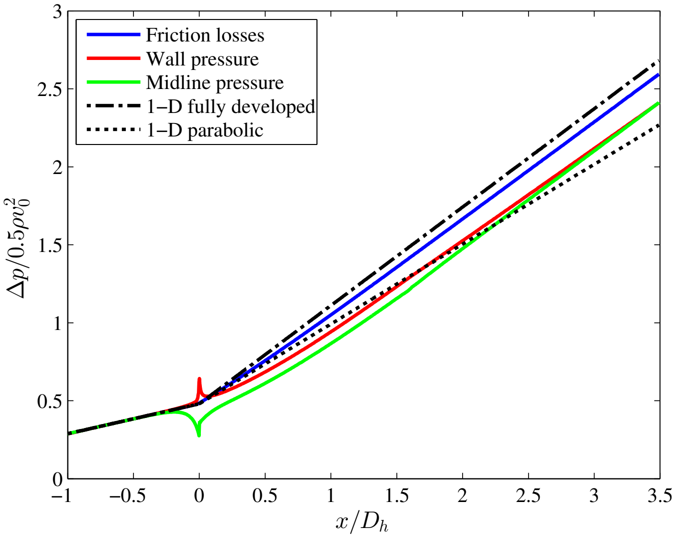

Figure 2.15: Pressure loss as a function of position at Re=2000.0, Bi=10.0. Fully developed losses are from Equation 2.21, and parabolic losses from Equation 2.22.

and low speed models, and clearly shows the impact of β. The effect of the transition zone is small, as demonstrated by the small difference between friction losses and the fully developed model. Pressure losses, which include β effects, show a much larger difference, dropping below the parabolic model at $x/D_h = 1$. Also, note that pressure at the wall and midline diverge at the start of the active region, and do not return to the same value until the end of the duct, where they meet due to the exit boundary condition of a fixed, uniform pressure. The difference in pressure at center and wall can be explained by applying Bernoulli's equation, $p + \frac{1}{2}\rho v^2 = C$, as from the inviscid perspective, the fluid decelerates at the center of the flow, so there should be a rise in pressure. In all our simulations, $p_{\mathrm{mid}} - p_{\mathrm{wall}} \leq \tau_{\mathrm{y}}$, which is sensible, as we are modeling a fluid with a yield stress, so it can support a pressure up to τ_y. For most test points, this sustained pressure difference exists for a significant duct length beyond the velocity and wall shear stress entrance length. This pressure difference also explains the the acceleration of the midline velocity towards the end of the duct seen in Figure 2.12, as the exit boundary condition specifies a uniform pressure, so the pressure difference is resolved by accelerating the central core of the fluid. This also means for the majority of the flow conditions, $|dp/dy| > 0$. Aside from the exit effects, this is pressure difference is largely negligible.

2.3.2.2 Graetz coordinate and fits

To further simplify these flow profiles, we note that for many situations, we can largely eliminate Reynolds number dependence through use of a Graetz-type coordinate [95, p. 292]. The Graetz coordinate scales length by Reynolds number, is denoted here by a $'$, where $x' = x/D_h/\mathrm{Re}$. In Figure 2.16, using the results from $L_A/D_h = 14$, we show midline velocity and wall shear stress in the Graetz coordinate, and we observe that the overwhelming majority of the curves collapse into a single curve. The curves that do not line up correspond to $C_{\tau_y} > 1$, with movement away from the high Re fit starting when $C_{\tau_y} > 0.4$. In Figure 2.16 this corresponds to $\mathrm{Re} < 100$ at $\mathrm{Bi} = 10$ and $\mathrm{Re} < 1000$ at $\mathrm{Bi} = 100$. This failure to coalesce when $C_{\tau_y} > 0.4$ demonstrates the effectiveness of our C_{τ_y} criteria for the onset of inertial effects. We also note the small absolute change wall shear stress exhibited at $\mathrm{Bi} = 100$, as the difference between plug and parabolic flow is small. Finally, for all conditions, when $\mathrm{Re} \leq 10$, scaling fails due to a lack of resolution from the x/D_h scaled grid.

Since Graetz scaled wall shear stress and velocity curves collapse at a constant

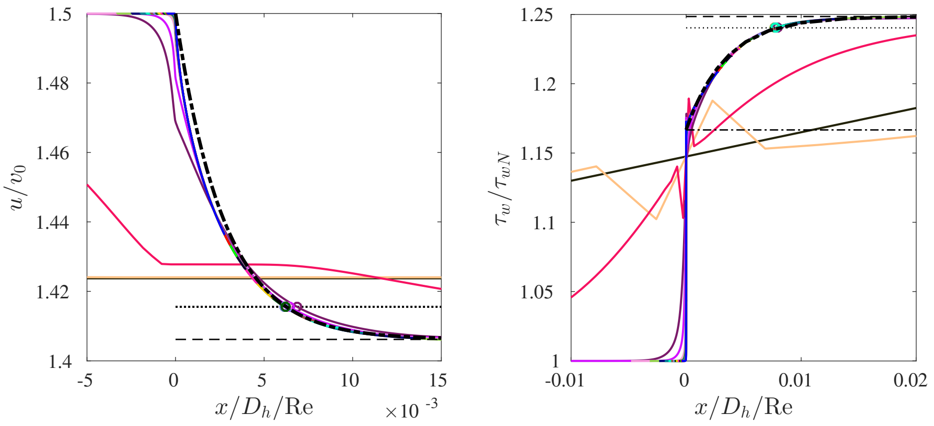

(a) $\mathrm{Bi} = 1, u/v_0$ (b) $\mathrm{Bi} = 1, \tau_w/\tau_{wN}$

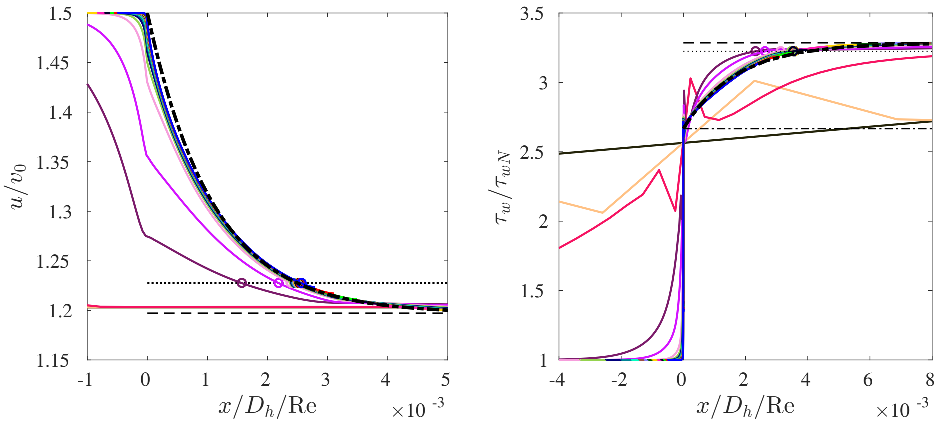

(c) $\mathrm{Bi} = 10, u/v_0$ (d) $\mathrm{Bi} = 10, \tau_w/\tau_{wN}$

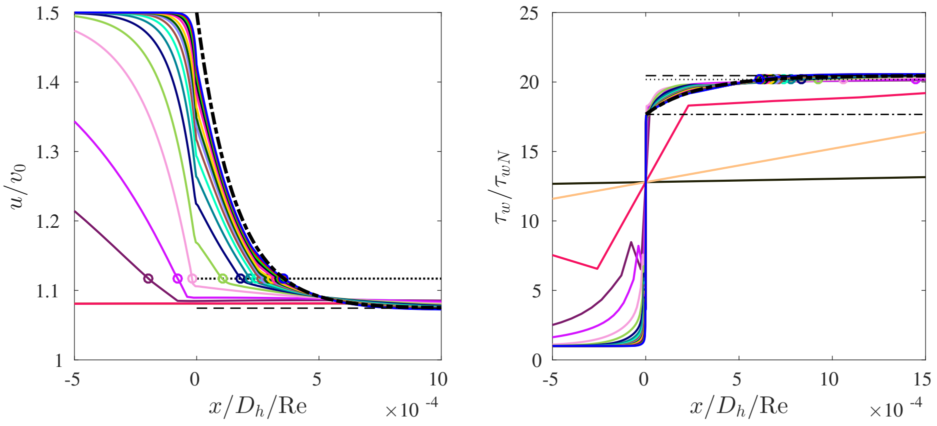

(e) $\mathrm{Bi} = 100, u/v_0$ (f) $\mathrm{Bi} = 100, \tau_w/\tau_{wN}$

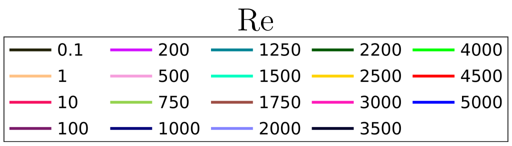

Figure 2.16: Velocity and wall shear stress in terms of Graetz coordinate. The thick dashed black lines are entrance length based fits. Dashed lines a fully developed value, dotted line is the entrance length criteria, and dash-dot is the parabolic wall shear stress value.

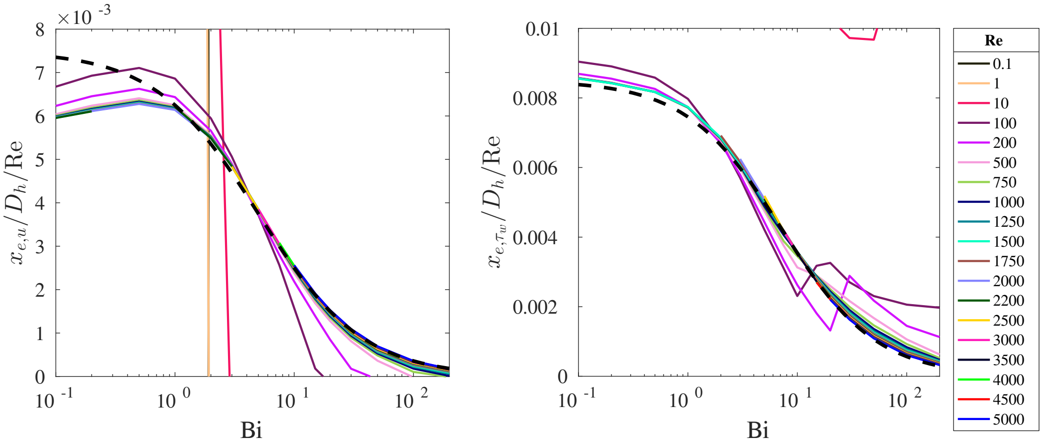

(a) Midline velocity criteria (b) Wall shear stress criteria

Figure 2.17: Graetz scaled entrance length. Dashed lines are fits of $x_{e,u}$ and x_{e,τ_w}.

Bingham number, we should be able to construct fits dependent only on Bingham number. To do this, first we fit entrance length as a function of Bi, and then use entrance length to define $u_{\mathrm{fit}}(x)$ and $\tau_{\mathrm{w,fit}}(x)$. Graetz scaled entrance length is shown in Figure 2.17. Velocity based entrance length is fit as

$$x'_{\mathrm{e},u} = \frac{7.5 \times 10^{-3}}{1 + 0.2\,\mathrm{Bi}} \tag{2.40}$$

which is effective for Bi > 1, and wall shear stress based entrance length is fit as,

$$x'_{\mathrm{e},\tau_w} = \frac{8.7 \times 10^{-3}}{1 + 0.14\,\mathrm{Bi}} \tag{2.41}$$

which holds up well across all Bi. We can then use the 90% convergence based entrance length criteria in an exponential fit. This yields, for $x > 0$, fits for midline velocity and wall shear stress

$$
\begin{aligned}
u_{\text{fit}}(x) &= u_N - (u_N - u_b)\left(1 - \exp\left(\log(.1)\frac{x}{x_{e,u}}\right)\right) && (2.42)\\
\tau_{\text{w,fit}}(x) &= \tau_{wp} + (\tau_{wb} - \tau_{wp})\left(1 - \exp\left(\log(.1)\frac{x}{x_{e,\tau_w}}\right)\right). && (2.43)
\end{aligned}
$$

These fits are shown in Figure 2.16 as the dashed black lines. While not perfect, these very simple fits are effective enough, especially at low C_{τ_y}. We also note that $\beta(x)$ has a shape similar to $u(x)$, so we can use $x_{e,u}$ to construct a fit for $\beta(x')$, Previously, we noted that towards the exit, both u and β stop converging in final $0.5D_h$. Inserting this exit correction and fitting to minimize n_p error produces

$$\beta_{\text{fit}}(x) = 6/5 + (\beta_B - 6/5)\left(1 - \exp\left(\log(.1)\frac{x - 0.56D_h}{x_{e,u}}\right)\right). \tag{2.44}$$

To obtain pressure loss at any point in the duct, these fits can be placed into our control volume analysis, Equation (2.25), giving

$$\Delta P_{\text{fit}} = \frac{4}{D_h}\left(\tau_{wN}L_N + \int_0^{L_A} \tau_{\text{w,fit}}(x)dx\right) + (\beta_{\text{fit}}(L_A) - 6/5)\rho v_0^2. \tag{2.45}$$

With these fits, we have a description of the fluid behavior in ‘activation’ flow that is dependent only on the fundamental dimensionless quantities that govern the flow.

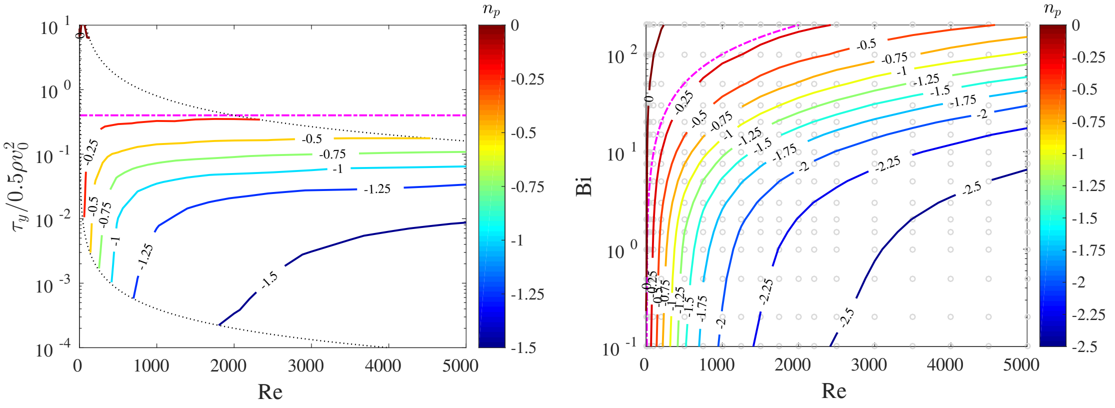

(a) $n_p,\ L_A/D_h = 2,\ C_{\tau_y}$ (b) $n_p,\ L_A/D_h = 3.5,$ Bi

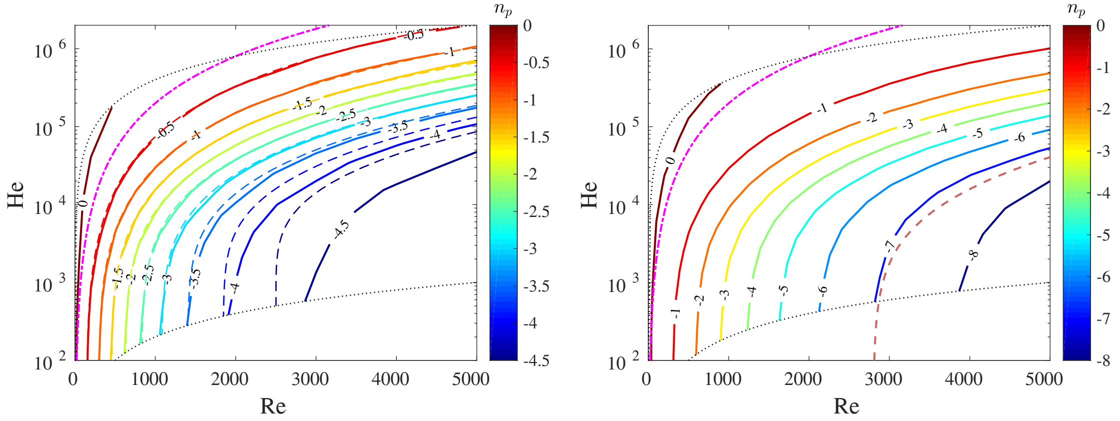

(c) $n_p,\ L_A/D_h = 7,$ He (d) $n_p,\ L_A/D_h = 14,$ He

Figure 2.18: Inertia correction in various forms. The dotted lines are the upper and lower bounds on sampled space and the pink dashed line is $C_{\tau_y} = 0.4$. The slid contours are obtained directly from CFD. The light grey circles in Fig. 2.18b are the CFD test points. Dashed contours in Fig. 2.18c are Eq. 2.45, and the brown dashed line in Fig. 2.18d is the transition to turbulence.

2.3.2.3 Force correction factor

The next step is to use both the CFD and fit pressure loss data to examine the change in force. Figure 2.18 presents contour plots of n_p for various active lengths, as they reveal trends in n_p not otherwise visible. Figure 2.18a demonstrates that n_p has limiting values in Re and C_{τ_y} as expected. We can also see that the $C_{\tau_y} = 0.4$ rule of thumb, the dashed pink line, very closely approaches the contour of $n_p = 0.25$ when $\mathrm{Re} > 120$ in Figure 2.18a-c. Since $x_{e,u}$, $n_p(\beta) = 0.25$, and n_p coincide at $C_{\tau_y} = 0.4$, from here on out, we use this as our one size fits all criteria for the onset of speed effects.

The fitted pressure model, ΔP_{fit} can be placed into n_p to obtain $n_{p,\mathrm{fit}}$, which we can then compare against CFD data. Figure 2.18c compares the solid CFD contours with dashed line contours from the fit at $L_A/D_h = 7$ (the case with worst fit performance), and shows that fit is very accurate when $n_p > -0.5 L_A/D_h$. For the region $\mathrm{He} = 10^3 - 10^6$ and $\mathrm{Re} = 1 - 5000$, across all active lengths, error $(n_{p,\mathrm{fit}} - n_{p,\mathrm{cfd}})/L_A$ is at worst 8.2% and on average, 3.5%, giving us confidence in their accuracy.

As desired, when the flow is fully developed by the exit, n_p is unaffected by L_A, which can be seen in contours of $n_p = 1$ and 2 in Figure 2.18c and d. We also note that the position of the $n_p = 0$ line is not reliable, as the precise location is very sensitive to solution error.

Since we are considering a pipe-like flow with $\mathrm{Re} > 2000$, we should consider the role of turbulence. For a Bingham plastic in parallel plate, Hanks and Pratt developed and experimentally validated a laminar-turbulent transition Reynolds number for parallel plates [96],

$$\frac{\mathrm{He}}{33600} = \frac{\delta_c}{1-\delta_c^3}$$

$$\mathrm{Re}_c = \frac{\mathrm{He}}{12\delta_c}\left(1 - \frac{3}{2}\delta_c + \frac{1}{2}\delta_c^3\right)$$

where you solve for $\delta_c = \tau_y/\tau_{wc}$, a critical plug thickness to obtain the transition Reynolds number, Re_c. In Figure 2.18d, we place a dashed brown line on Re_c. While the area to the right of the transition line occupies a large region in Re–He space, at $\mathrm{Re} \leq 5000$, $\mathrm{Bi}_c \leq 2$. Since Bi is so low, this region will be rarely encountered in controllable devices.

A more readily applicable way of looking at this data is shown in Figure 2.19, which plots n_p as a function of Re for various He, comparing interpolated CFD data and our curve fits. All the same sensible trends are observed - increasing Re increases the force falloff, and raising He decreases it. In this form, we can also see mostly clearly that the fits are accurate when $n_p > -0.5L_A/D_h$. Figure 2.20 plots n_v and shows the excellent performance of $\tau_{\mathrm{w,fit}}$, which is accurate within 1.2%. We can also see the very small positive n_v bias at low $C_{\overline{\tau}_{\mathrm{y}}}$, with typical values of $n_v = 0.05$, roughly the size of discretization bias error.

Finally, Figure 2.21 plots yield stress induced pressure loss, $\Delta P_{\mathrm{y}} = \left(\frac{dp}{dx}\right)_b (L_A + n_p) - \left(\frac{dp}{dx}\right)_N (L_A + n_p)$, both with and without n_p. This ΔP_{y} is normalized by the parabolic model, and is also a normalized yield force. Here, we see a rise in ΔP_{y}

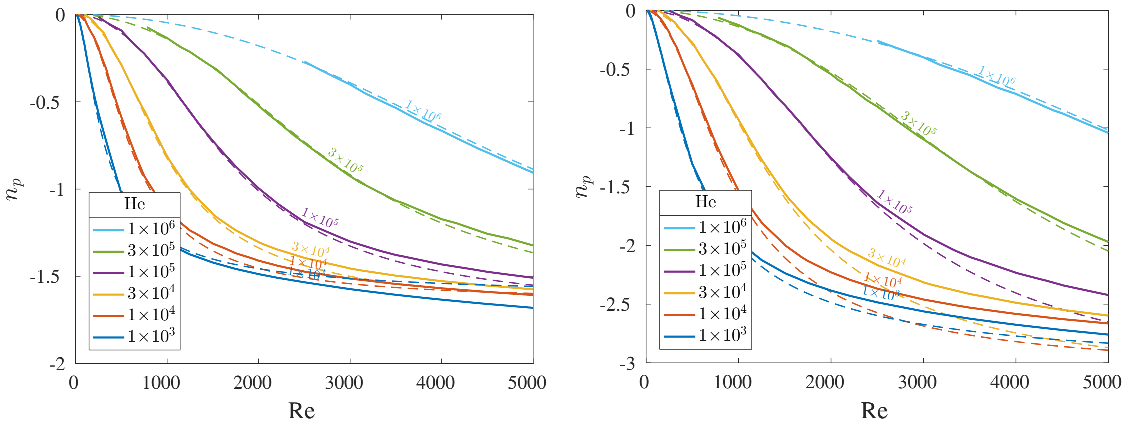

(a) $n_p,\ L_A/D_h = 2$ (b) $n_p,\ L_A/D_h = 3.5$

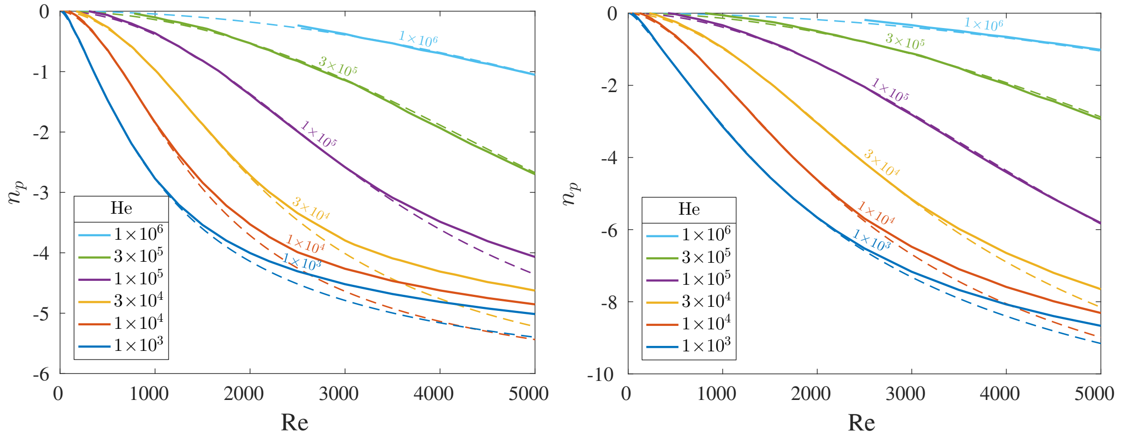

(c) $n_p,\ L_A/D_h = 7$ (d) $n_p,\ L_A/D_h = 14$

Figure 2.19: Active length correction, n_p from $\mathrm{He} = 10^3 - 10^6$. Dashed lines are fits of n_p.

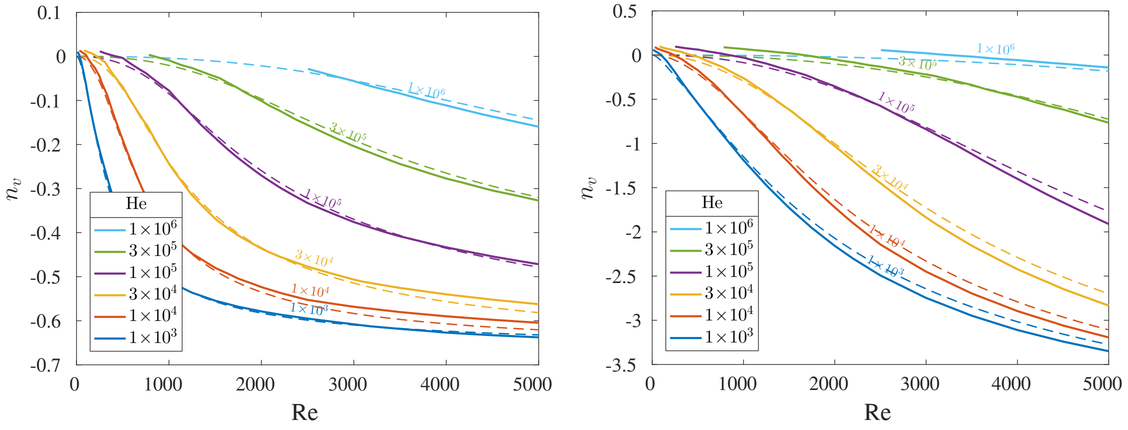

(a) $n_v,\ L_A/D_h = 2$ (b) $n_v,\ L_A/D_h = 14$

Figure 2.20: Active length viscous correction, n_v. Dashed lines are fits.

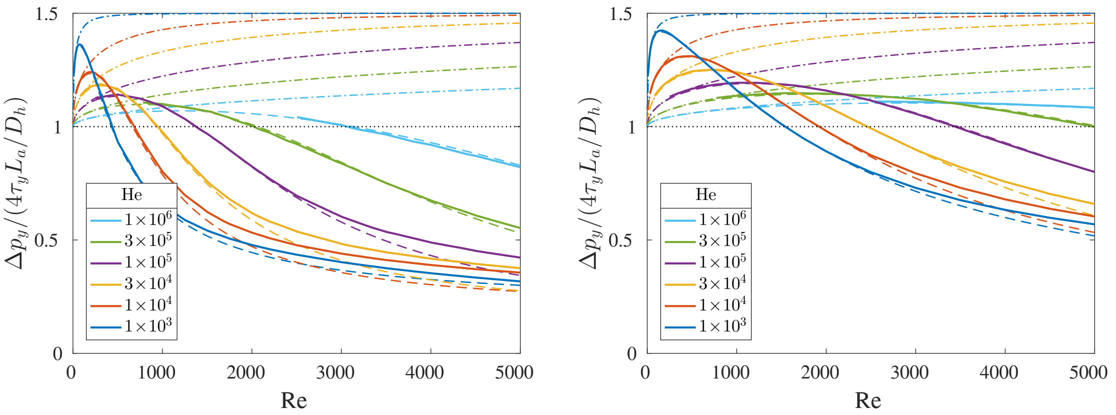

(a) $\Delta P_{\mathrm{y}},\ L_A/D_h = 3.5$ (b) $\Delta P_{\mathrm{y}},\ L_A/D_h = 14$

Figure 2.21: Apparent yield force, normalized by parabolic yield force using n_p. Solid lines are CFD, dashed lines are fits, dash dot is the fully developed model, and dotted is the parabolic model.

from the formation of the plug, followed by a large decrease in yield force caused by inertia and momentum effects, one which can go below $\Delta P_{\mathrm{y,p}}$. This crossing point serves as our definition of high speed flow: high speed flows are those where $\Delta P_{\mathrm{y}} < \Delta P_{\mathrm{y,p}}$.

From this we can make a basic estimate of the yield force falloff in Goncalves. In those experiments, He = 10^4 to 3×10^4, and max Re = 1400. Here, can see that yield force is dropping 50–60% for $L_A/D_h = 3.5$, and 10–20% for $L_A/D_h = 14$. While this isn't definitive, nor enough to claim a full description of the yield force falloff seen in Goncalves, we clearly have captured a significant portion of the trend. In the next chapter, we examine Goncalves' device and all of the high speed MR devices known us. Then, by accurately predicting yield force at high speeds, we demonstrate that we can describe high speed yield force falloff using only classic fluid dynamics, and without a response time.

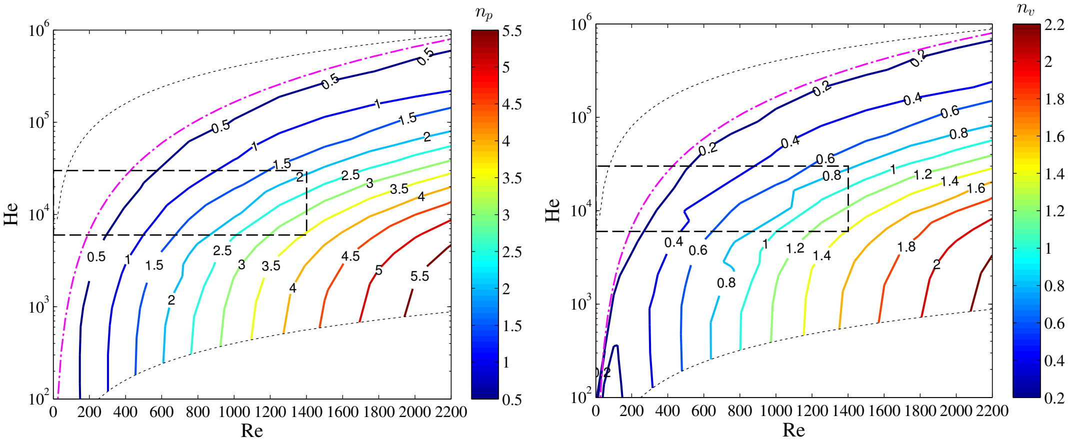

(a) n_p

(b) n_v

Figure 2.22: Deactivation correction factors for $L_A/D_h = 4$ and $L_N/D_h = 13.97$. The box is the test window of Goncalves.

2.3.3 Deactivation Flow

The follow-on to looking at fluids entering the active region is to investigate the reverse situation, a 'deactivation' flow where fully developed Bingham plastic suddenly loses its yield stress and returns to Newtonian flow, or alternatively, Figure 2.4 with the flow direction flipped left to right. The boundary conditions are the same as before, except the inlet velocity is specified as the exact fully developed biviscous solution, Equation (2.17).

Figure 2.22 plots correction factors for deactivation flow with a long Newtonian region, $L_N/D_h = 13.97$, and inlet active region $L_A/D_h = 4$. The active region was was lengthened, because as before, there is a wall/midline pressure difference that needs to be resolved smoothly. The primary result is that the deactivation flow correction factor is almost identical to the negative of the activation flow correction factor for $L_A/D_h = 13.97$. This indicates that in a long active region with long entrances and exits, using the fully developed quasi-static pressure loss model will not cause problems, as despite there being significant inertia effects, the activation and deactivation corrections will cancel each other out. Then in a flow mode rheometer where L_A is long enough for the flow to be fully developed, and an exit region long enough for the flow to return to Newtonian flow, such as the capillary rheometer in [60], [97], we expect the activation and deactivation flow effects to cancel each other out, and to see minimal inertia and momentum effects.

However, typical damper designs have the active region in a contraction, so there is no exit passive region, and there will be no momentum recovery at the exit, n_p will apply. But if the passive region between two active regions is smooth, we speculate that the activation and deactivation factors will mostly cancel each each other out, and speed effects will only be observed at the first entrance. But in general, accurate analysis of real devices with multiple gaps will require more detailed analysis, and we may pursue such work in the future.

2.4 Conclusions

In this study, we performed a rigorous analysis of the 2D fluid dynamics of a controllable fluid entering or exiting an active region. To allow us to draw generalizable conclusions, we worked with a simplified model, capable of replicating the work of Goncalves. Using our flow model with zero yield stress response time, we are able to produce a reduction in yield force at high speed. We conclude the following:

1. The high speed yield force falloff effect in Goncalves is caused by the fluid dynamics. The yield stress causes the velocity to develop a plug like profile, reducing fluid momentum, causing a pressure rise.

2. This high speed force falloff effect can be viewed as a change in active length. Fits accurately matching CFD results from $\mathrm{He} = 10^3 - 10^6$ and $\mathrm{Re} = 1 - 5000$ are reported in Equations 2.43, 2.44 and 2.45, and plotted in Figure 2.18.

3. Momentum effects in near quasi-static flow can be estimated from Eq. 2.34 and 2.35. These can be turned into a simple criteria for when quasi-static models can be used safely: $C_{\tau_y} > 0.4$ and $\mathrm{Re} < 120$ for a typical device with $L_A/D_h = 5$ wishing to stay within 5% of the fully developed solution. We also define high speed flows as when $\Delta P_{\mathrm{y}} < \Delta P_{\mathrm{y,p}}$, or when high speed yield force falloff becomes readily apparent.

4. Deactivation flow correction factors are almost the exact opposite of the activation flow factors, indicating that the rare device with a long exit region will not experience these effects.

In the next chapter, we experimentally validate these fits on a range of devices operating from $\mathrm{He} = 10^4 - 10^6$ and up to Re=4500. Going forward, we would like to improve the efficiency of the solver, as solution convergence was slow, and there no doubt exist more efficient methods. We would also like to examine more realistic geometries, to capture the fluid dynamic effects present in real devices, and see how they affect active region flow and force output. Overall, we believe that proper 2D fluid dynamics will prove essential in accurate design of high speed energy absorbers.

Chapter 3: Experimental validation

3.1 Introduction

High speed yield force falloff is a phenomenon seen magnetorheological (MR) fluid flow mode devices, where the yield force, defined as $F_{\mathrm{y}} \triangleq F_{\mathrm{on}} - F_{\mathrm{off}}$, drops as active gap velocity increases. This can be clearly seen in Goncalves' high speed capillary rheometer tests [11], [12], the impact absorber tests of Mao [13] and Mao *et al.* [14], and the seismic dampers built by the Sanwa Tekki corporation [15], [56]. This is phenomenon is not predicted by existing yield force models, where existing models predict either an increasing or constant yield force with increasing speed.

Goncalves hypothesized that the yield force falloff is caused by a fundamental response time, where below a certain fluid active region residence time, there is no yield stress. Mao [13] and Mao *et al.* [14] used an alternate active region force model, where the amplification of the viscous force by the yield stress induced plug does not occur. The Sanwa Tekki group tried to resolve the missing yield force by removing upstream Newtonian valve losses [98], but we believe the yield stress altering the fluid dynamics far upstream is unlikely.

We believe that the reduction in yield force is caused by active region fluid dynamics, but note that existing methods for predicting F_{y} and F_{on} are not grounded in rigorous fluid dynamics. These methods obtain F_{y} by assuming a 1-D velocity profile, and subtracting off the fully developed Newtonian losses. To obtain F_{on}, first a model of the offstate is constructed, and then F_{y} is added to the off-state forces to obtain on-state forces, or $F_{\mathrm{on,model}} = F_{\mathrm{off,model}} + F_{\mathrm{y,model}}$. Aside from the fact that it works at low speeds, this procedure is questionable, as it involves adding the difference between the solutions to two different nonlinear fluid dynamics problems.

At high speed, where on-state force predictions are inaccurate, we need to question the three components of predicting on state forces: off-state forces, adding and yield forces. At high speeds, Min Mao's dissertation [13] demonstrated that off-state force modeling can be quite accurate, so this is unlikely to be the source of error. There are then two candidates for the source of inaccuracy: the assumption that yield force can be superimposed and the accuracy of the yield force model. The ability to add yield force to off-state losses is a powerful assumption for the device designer, as predicting off-state forces is fairly straightforward, and existing yield force models are simple analytical expressions. If we can't add a yield force, it means that we need to perform full active Bingham plastic CFD of the entire device, which in our experience is cumbersome and impractically slow. Then from a perspective where we seek simplicity and productivity, it is much preferable to assume that we can superimpose a yield force, and then seek to create a more accurate yield force model.

The obvious flaw in existing yield force models is that they are based on simple 1D solutions. Our approach is to develop a correction based on Goncalves' experiment and apply it to practical devices, using the last chapter's exploration of the fluid dynamics in Goncalves' device. To analyze Goncalves' experiment, we created 'activation flow', a simplified 2D CFD model where fully developed Newtonian flow enters a region of uniform yield stress with a constant pressure exit. This simplified model is the first rigorous examination of high speed variable yield stress fluid flow, and we claim it captures the fluid dynamics common to flow-mode devices. In our analysis of activation flow, the main cause of high speed force falloff is a change in control volume momentum flux from the velocity profile developing a 'plug'. We then used the CFD results to develop a fit for yield force based on control volume analysis of activation flow, as analytical criteria for the onset of fluid dynamic effects. In this paper, we show that the yield force obtained from the analysis of activation flow accurately predicts yield force at high speeds in practical devices.

To validate this model we need to identify devices which operate in the high speed regime where the fluid dynamics affect yield forces. Table 3.1 collects piston velocity v_p and yield force F_y for a series of devices that caught our eye. But since our explanation for this behavior is a fluid dynamic one, we include the scaled active length, L_A/D_h, and the two governing nondimensional numbers: Reynolds and Hedstrom number, Re and He. These fluid dynamic quantities are defined using the properties of the active gap, with $\mathrm{Re} = \rho v_\mathrm{gap} D_h/\eta_\infty$, the dimensionless velocity and $\mathrm{He} = \rho \tau_\mathrm{y} D_h^2/\eta_\infty^2$, the dimensionless yield stress. Excluded from this list are papers that do not list enough geometric and fluid dynamic properties to compute the required properties. The advantage of nondimensional analysis is that it allows comparison of physically dissimilar devices, expanding the range of devices we can validate against. For example, it may not be readily apparent that a high-force

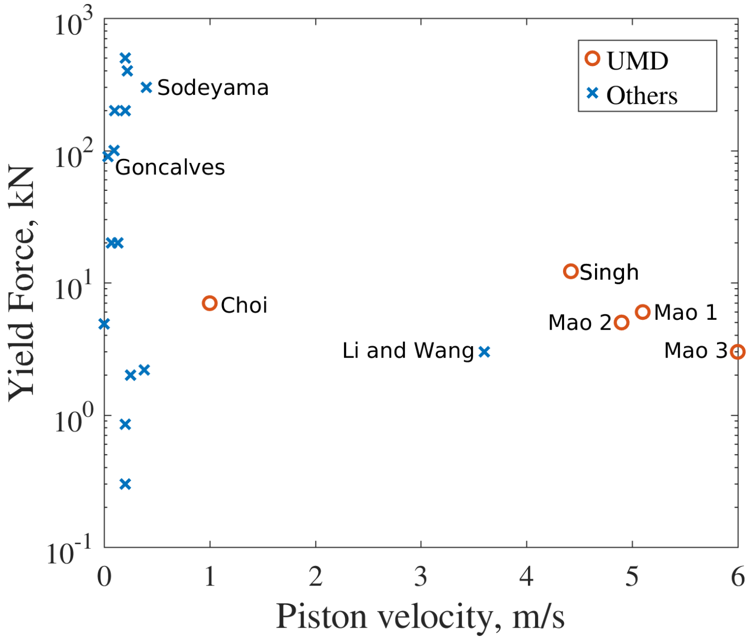

(a) Physical units

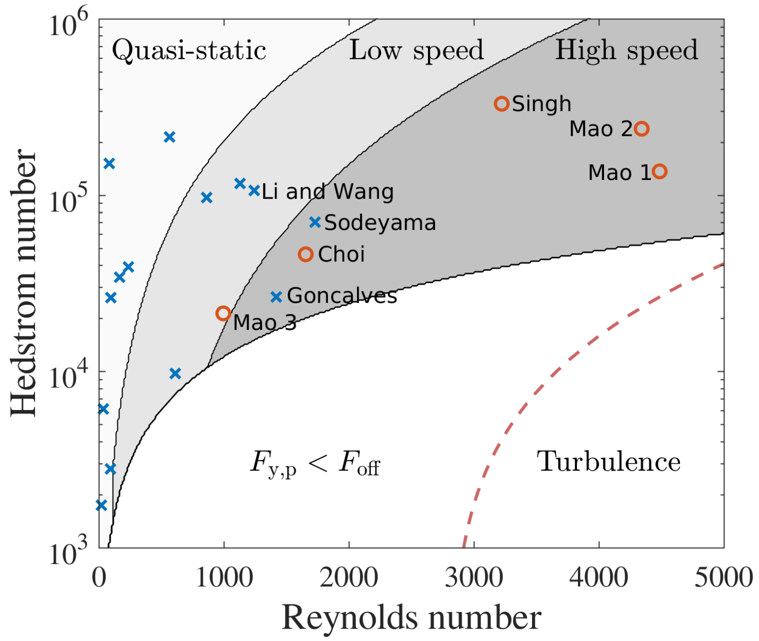

(b) Dimensionless

Figure 3.1: Fluid dynamic properties of MR dampers in both raw units and nondimensional form. See Table 3.1 for details.

Author	F_{y}, kN	v_p, m/s	Re	He	L_A/D_h
S.B. Choi *et al.* [99]	0.3	0.2	240	4×10^4	9.2
S.B. Choi *et al.* [100]	2	0.4	170	3.4×10^4	5
Fujitani *et al.* [98]	300	0.25	570	2.1×10^5	2.7
Goncalves *et al.* [12]*	35	0.036	1400	2.7×10^4	3.9 - 15.7
Gordaninejad *et al.* [101]	100	0.1	83	1.5×10^5	3.6
Li and Wang [102]	3	3.6	1200	1.1×10^5	7.5
Li and Xu [103]	20	0.13	36	6.3×10^3	13
Parlak and Engin [74]	0.8	0.2	96	2.6×10^4	5
Rodriguez *et al.* [104]	16	0.07	860	9.7×10^4	5.5
Sodeyama *et al.* [56]	100	0.2	1100	1.2×10^5	2.5
Sodeyama *et al.* [15]*	160	0.4	1700	7×10^4	6
Tu *et al.* [105]	400	0.2	93	2.8×10^3	10
Yang [106]	170	0.08	20	1.7×10^3	5.5
UMD					
Y.T. Choi *et al.* [107]*	7	1	1600	4.6×10^4	6.25
Mao *et al.* [14], 1*	6	5.1	4500	1.4×10^5	6.2
Mao *et al.* [14], 2*	5	4.9	4300	2.4×10^5	5.1
Mao *et al.* [108], 3	2	6	1000	2.1×10^4	2.5
Singh *et al.* [109]*	12	4.4	3223	3.3×10^5	4.7

Table 3.1: Fluid dynamic properties of potential high speed magnetorheological dampers. We compare our model to the devices marked with an asterisk.

low-speed seismic damper [15] and a high speed impact absorber [107] have similar fluid dynamics, but Table 3.1 shows that they do, and later we demonstrate that both devices see similar amounts of high speed force falloff.

Figure 3.1 displays Table 1 visually, comparing the traditional presentation of device size and speed, F_{y} vs v_p, and our dimensionless form, Re vs He. In the dimensionless presentation, we leverage our analysis to separate the space into five regions. Using a typical geometry of $L_A/D_h = 5$, we split space into the three areas: the quasi-static regime where $C_{\tau_{\mathrm{y}}} > 0.4$ and $\mathrm{Re} < 120$, and $F_{\mathrm{y}} \approx F_{\mathrm{y,\,B}}$; the low speed regime where yield force will larger than parabolic model prediction $F_{\mathrm{y,\,act}} > F_{\mathrm{y,p}}$; and the high speed regime $F_{\mathrm{y,\,act}} < F_{\mathrm{y,\,p}}$ where yield force falls below the high parabolic model, and thus where high speed yield force falloff should be large. We also indicate the region where controllable force is low, $F_{\mathrm{y,\,p}} < F_{\mathrm{off}}$, or $\mathrm{Bi} < 6$, as well as the region of turbulent flow. This also motivates the extensive nondimensional analysis in the previous chapter, as all four nondimensional numbers—Re, He, Bi and $C_{\tau_{\mathrm{y}}}$—are needed to describe various elements of the fluid dynamics.

This paper compares our activation flow yield force model to all the devices in the high speed region. We do not look at devices in the low speed and quasi-static regions as in this region, as existing models perform well for those devices, and by construction, our model is largely indistinguishable. First, we look at Goncalves' capillary slit rheometer with a single active region [12], the inspiration for the activation flow model, and show reasonably accurate predictions. We follow this with the two double rod dampers of Mao *et al.* [14], which operate at the largest Reynolds numbers ever, and demonstrate that activation flow yield force predictions are highly accurate. We then examine Singh's 12 kN damper [109], which has the largest Hedstrom number of any known device, and show excellent model performance. Next, we look at the 2 kN the landing gear damper in Choi with gas reservoir and two active regions, and show reasonably effective yield force predictions. We exclude Li and Wang [102], who do not present any force–velocity data, and Mao's bi-fold damper [108], which has a large bend in the active region and a significant spring term. We conclude by looking at a damper from the Sanwa Tekki Corporation [15], and discuss several of their other seismic devices and what they tell us about high speed force falloff.

3.2 Background

We claim that activation flow is a more accurate yield force model, and allows use of yield force superimposition at high speeds. To do so, we need to account for off-state forces, yield forces, how we apply this to a typical contraction device, turbulence effects, and concerns about time domain effects.

3.2.1 Off-state forces

To obtain experimental yield forces, we need to obtain the off-state force at arbitrary values, as many experiments do not have on-state and off-state measurements at the exact same piston velocities. Off-state forces are composed of viscous ($\sim v$) and dynamic terms ($\sim v^2$), with dynamic losses becoming substantial at high speed. At even larger speeds, turbulent losses also become significant. Since we are working with models that treat yield force as totally independent of the off-state forces, we don't need to know any details of the off-state fluid dynamics. For most of the devices here, this allows us to 'predict' off-state forces by curve fitting experimental off-state forces. However, when looking at Goncalves' slit rheometer, we perform a full model of the offstate forces.

In general, we fit the force–velocity data to a quadratic or higher polynomial. The quadratic term force term $F = ... + A_{\mathrm{p}} K \frac{1}{2} \rho v_{\mathrm{gap}}^2 + ...$ is of importance, as conservation of momentum requires that $K > 1$ for a typical device with a lossy exit. This is of critical importance when examining Goncalves' device. For several devices higher order polynomials are needed to capture the increase in force caused by the transition to turbulence.

3.2.2 Yield Force

In our previous paper, we developed a set of fits designed to describe activation flow, where fully developed Newtonian flow enters an active region, instantly develops a yield stress and then converges to fully developed Bingham plastic flow. Our model for pressure loss in activation flow is below:

$$
\begin{aligned}
\mathrm{Re} = {} & \frac{\rho v_0 D_h}{\eta_\infty} \qquad \mathrm{Bi} = \frac{\tau_\mathrm{y} h}{\eta_\infty v_0} \qquad \mathrm{He} = \frac{\rho \tau_\mathrm{y} D_h^2}{\eta_\infty^2} \qquad C_{\tau_\mathrm{y}} = \frac{\tau_\mathrm{y}}{\frac{1}{2}\rho v_0^2} && (3.1)\\
\tau_\mathrm{wN} = {} & 12 v_\mathrm{gap} \eta_\infty / D_h \qquad \tau_\mathrm{wB} = \tau_\mathrm{y}/\delta \qquad \tau_\mathrm{wp} = \tau_\mathrm{y} + \tau_\mathrm{wN} && (3.2)\\
\delta = {} & 2a\cos(1/3\cos^{-1}(a^{-3}) - 2\pi/3) \qquad a = \sqrt{1 + 4/\mathrm{Bi}} && (3.3)\\
\beta = {} & \frac{\int_0^h u(x,y)^2 dy}{v_0^2 h} \qquad \beta_B = \frac{\mathrm{Bi}^2\,(\delta-1)^4}{16\,\delta} - \frac{\mathrm{Bi}^2\,(\delta-1)^5}{30\,\delta^2} && (3.4)\\
x_{\mathrm{e},u} = {} & \frac{7.5\times 10^{-3}}{1+0.2\,\mathrm{Bi}} \mathrm{Re}\, D_h \qquad x_{\mathrm{e},\tau_w} = \frac{8.7\times 10^{-3}}{1+0.14\,\mathrm{Bi}} \mathrm{Re}\, D_h && (3.5)\\
\tau_{\mathrm{w,\,act}}(x) = {} & \tau_\mathrm{wp} + (\tau_\mathrm{wB} - \tau_\mathrm{wp}) \left(1 - \exp\left(\log(.1)\frac{x}{x_{\mathrm{e},\tau_w}}\right)\right) && (3.6)\\
\beta_\mathrm{act}(x) = {} & 6/5 + (\beta_B - 6/5)\left(1 - \exp\left(\log(.1)\frac{x - 0.56 D_h}{x_{\mathrm{e},u}}\right)\right) && (3.7)\\
\Delta P_{\mathrm{y,\,act}} = {} & \frac{4}{D_h}\int_0^{L_A} (\tau_\mathrm{w,act}(x) - \tau_\mathrm{wN})\, dx + (\beta_\mathrm{act}(L_A) - 6/5)\rho v_\mathrm{gap}^2 && (3.8)
\end{aligned}
$$

This fit should be an effective description of the CFD data from $10^3 < \mathrm{He} < 10^6$, $0 < \mathrm{Re} < 5000$, and $2 < L_A/D_h < 14$, a range that covers nearly every ER and MR flow mode device built. We also have the existing yield force models,

$$
\begin{aligned}
\Delta P_{\mathrm{y,\,B}} = {} & \frac{4(\tau_\mathrm{wB} - \tau_\mathrm{wN})L_A}{D_h} && (3.9)\\
\Delta P_{\mathrm{y,\,p}} = {} & \frac{4(\tau_\mathrm{wp} - \tau_\mathrm{wN})L_A}{D_h} = \frac{4\tau_\mathrm{y} L_A}{D_h} && (3.10)
\end{aligned}
$$

the fully developed and parabolic flow yield force models respectively. Yield force in a flow mode device is typically obtained from pressure loss, when neglecting wall shear stresses, from $F = A_\mathrm{p}\Delta P$, where A_p is the area of the damper piston head.

For improved accuracy, we include the piston wall shear stress forces, so

$$F = A_{\mathrm{p}} \Delta P + \int_{x_{in}}^{x_{out}} \tau_w \, 2\pi r dx,$$

where ΔP contains dynamic losses, and the second term contains the shear stresses on the piston. This can be rewritten, separating wall shear stress losses and dynamic loss terms K,

$$F = A_{\mathrm{p}} \left[\frac{4 \int_{x_{in}}^{x_{out}} \tau_w \, dx}{D_h} \left(1 + \frac{\pi r_{\mathrm{p}} D_h}{2\mathrm{A}_{\mathrm{p}}} \right) + K \frac{1}{2} \rho v_{\mathrm{gap}}^2 \right] \tag{3.11}$$

with β effects as part of K. This also demonstrates the utility of constructing a fit based on control volume analysis, as it allows it to be easily modified to suit alternate geometries. In all the devices here, the extra wall shear stress contribution $\pi r_p D_h / 2A_p$ is small, increasing wall shear stresses by less than 5%, but provides an improvement.

Our goal to is demonstrate that the activation flow pressure losses contained in $\Delta P_{\mathrm{y,\,act}}$ can accurately predict yield force at high speeds. We do so by comparing yield force prediction from it and from the two existing flow models: fully developed flow and parabolic flow. Fully developed flow, 'plug flow', is characterized by a growing yield force with increasing speed, eventually limiting out at 1.5× the yield force at zero speed, but assumes that there are no inertial effects, or $\mathrm{Re} = 0$. Parabolic flow assumes that the velocity profile is unchanged from the fully developed Newtonian case ($\mathrm{Re} = \infty$), and is just the addition of the yield stress to the Newtonian wall

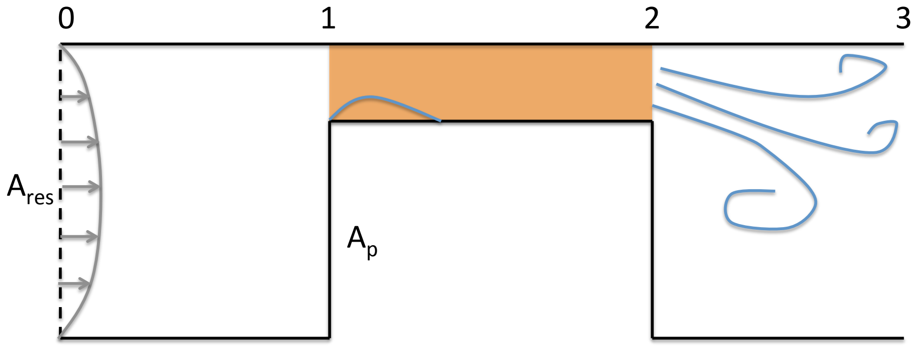

Figure 3.2: Schematic of a step contraction.

shear stress. Parabolic flow is accurate at large Bi, where plug amplification is small, as well as at moderate velocities where yield force falloff is present, but a small effect. The activation flow model exhibits an increase in F_y at low velocities, like plug flow, followed by its unique feature, a decrease in F_y as velocity increases, where it eventually predicts forces that are less than the parabolic model, which simply adds a yield stress. We define the onset of high speed flow as when the activation flow model predicts a yield force below the parabolic model, $\Delta P_{\mathrm{y,\,act}}/\Delta P_{\mathrm{y,\,p}} < 1$. In Fig. 3.1 this is used to identify the set of high speed devices which we will validate the activation flow yield force model against.

3.2.3 Contraction flow

Activation flow is an idealized and simplified representation of Goncalves' device, but here we claim that you can apply this model to a typical MR damper. These devices are very different in construction, where Goncalves' device is an active region following a long passive region, while most ER and MR dampers place the active region in a short step-like contraction. An example of this is shown in Fig. 3.2, where the contraction is the region between points 1 and 2.

In order to justify applying activation flow to yield force predictions in step contractions, it first makes sense to examine Newtonian flow in a step contraction. For a typical Newtonian contraction with length L_A, after a careful reading of White [95, p. 290-293] and Merritt [110, p. 39-48], we identify these useful observations:

1. There are minimal viscous losses between 0 and 1 in Fig. 3.2, so from conservation of momentum, $P_0 - P_1 = \frac{1}{2}\rho v_{\text{gap}}^2$.
2. Losses inside the contraction are modeled using fully developed viscous losses and a velocity squared correction term, or $P_1 - P_2 = 4\tau_{\text{wN}} L_A / D_h + \frac{1}{2} K \rho v_{\text{gap}}^2$, with K capturing the extra losses encountered in the contraction.
3. At the exit, $P_2 = P_3$, as there is no pressure recovery due to turbulent losses.
4. Combining, total pressure loss is $P_0 - P_3 = 4\tau_{\text{wN}} L_A / D_h + \frac{1}{2}(1 + K)\rho v_{\text{gap}}^2$
5. Fully developed viscous losses imply that we have assumed a fully developed velocity profile between 1 and 2.
6. The correction factor, K, includes the change in momentum from changing velocity profile. For a Newtonian fluid in a rectangle, $K \approx 0.5 - 0.67$ of which 0.4 is from momentum (β) effects, with the rest coming from an increased τ_w in the entrance of the flow.
7. The classic simplified model of a contraction flow, entrance flow, is a straight pipe/duct with a uniform velocity inlet.

These assumptions tell us that all the interesting fluid dynamics occur in the contraction between 1 and 2 in Fig. 3.2. Then to obtain the yield force, we should solve a contraction/entrance flow type problem and subtract off Newtonian losses. For Bingham plastic entrance flow, we should get a decreasing yield force as speed increases, as Chen *et al.* [88] shows that in quasi-1D models, K decreases with increasing Bi, due to the reduced change in momentum and shorter entrance length reducing extra viscous losses. However, 1D methods, while capturing broad trends, are known to be inaccurate for Bingham plastic entrance flow problems [69], [70]. Second, the inlet boundary condition of uniform flow causes a large non-physical wall shear stress spike, as in a controllable yield stress fluid, large changes happen upstream of the region of yield stress. Fixing this requires abandoning entrance flow and using the more complex contraction flow geometry. However, fully solving for flow past a contraction has various subtle challenges [111], and accurately adding a variable yield stress will only add more complications.

The state of the art in active region MR fluid modeling at high speeds [13], [109] uses an unchanged K factor and the parabolic model for τ_{w}. If yield stress is independent of velocity, then the unchanged K and assumed wall shear stresses must be the source of error. Using the insights gained from activation flow and our knowledge of Newtonian contraction flow, we can construct an estimate for the true losses in a contraction with yield stress with the following three requirements. First, we expect a reduced K compared to the Newtonian case, as we know that β contribution to K will be smaller. Also, the β effects should be reduced if the flow is not fully developed, $x < x_{\mathrm{e},u}$. Second, we expect a reduction in the τ_{w} contribution to K, as both the extra wall shear stresses are less (the steady state profile is flatter), and the entrance length is shorter. Third, to be grounded in solid physics, the yield force model should reduce to plug flow at low speeds. Activation flow satisfies all three criteria, allowing us to use our model of activation flow to predict yield force in contraction flow. While the entrance lengths and wall shear stresses from activation flow are unlikely to be a close match to the real contraction flow values, we show that the activation flow entrance lengths provide an accurate prediction of yield force.

An alternate reasoning for this choice comes from invoking linear superposition. In a Newtonian flow, viscous losses in the contraction are found from fully developed parabolic flow, with an additional K term to capture any losses. Then to estimate yield force from the current solution of parabolic flow everywhere, we superimpose the transition from parabolic to plug (activation flow) to obtain the yield forces. While this is a conceptually simple explanation, superposition of solutions to different equations is unlikely to be strictly valid.

3.2.4 Turbulence

In a paper on experimentally verifying a laminar flow duct model when Re > 2000, turbulence is a major concern. Fortunately, the yield stress adds viscosity, delaying the onset of turbulence. Hanks [96] develops a theory for the critical Reynolds number as a function of Hedstrom number for traditional Bingham plastics in a duct:

$$\frac{\mathrm{He}}{33600} = \frac{\delta_c}{1-\delta_c^3} \tag{3.12}$$
$$\mathrm{Re}_c = \frac{\mathrm{He}}{12\delta_c}\left(1-\frac{3}{2}\delta_c+\frac{1}{2}\delta_c^3\right) \tag{3.13}$$

and finds excellent agreement with experiments conducted on 0.8 µm to 4.8 µm sized aluminum silicate pigment particles, which is roughly equivalent to an MR fluid with no field. Figure 3.1 plots Re_c and show that none of the devices we validate against operate in the turbulent regime, with only a few of Mao's test points approaching the turbulent transition.

While it appears easy to rule out turbulence in active flow, turbulence is actually a potential explanation for high speed yield force falloff. In particular, Govier and Aziz [82, p. 229-233] note the consistent observation that in a turbulent pipe flow, at equivalent Reynolds numbers, Bingham plastic friction factors are expected be less than or equal to the Newtonian friction factor when $\mathrm{He} < 10^6$. However, this is only true for fully turbulent flow. According to Hanks' turbulence criteria, the experiments discussed in this paper should never be fully turbulent.

Even then, the presence of turbulence is challenging to rule out, as we do encounter scenarios where $\mathrm{Re} > \mathrm{Re}_c$ in the passive region but $\mathrm{Re} < \mathrm{Re}_c$ in the active region. Then if the flow is turbulent in the passive region, but in the active region, $\mathrm{Re} < \mathrm{Re}_c$, but only slightly, it seems plausible that the active region would still be turbulent due to the upstream turbulence. Second, if the passive region is turbulent and the active region flow instantly becomes laminar, then the assumed parabolic inlet profile is no longer valid, as turbulent flows have a much flatter inlet profile. This would cause us to overestimate β effects and thus high speed yield force falloff. For devices with a straight slot/pipe type design, the effect of upstream turbulence cannot be ruled out. This is a potential issue in testing Singh's large damper, but one that doesn't seem to arise. In contraction type devices, upstream turbulence should be less critical, as the flow profile will dominated by the effects of contraction.

Experimentally, evidence of turbulence in traditional Bingham plastic flows is expected to be sharp and clear [112]. However, a brief examination of the MR literature shows no sharp transitions or onstate measurements dropping below the off-state values. Mao *et al.* [14] comes close to turbulence and sees a small reduction in yield stress, but we show below this can be explained by the laminar activation flow model. Browne *et al.* [9] conducts a series of impacts tests, which are likely in the turbulent regime, but show a near constant yield force at high speeds. The lack of evidence for turbulence is perhaps unsurprising, as the Bingham plastic literature is based on suspensions with $\tau_{\mathrm{y}} < 100\,\mathrm{Pa}$. For MR fluids, yield stresses are orders of magnitude larger and caused by an external applied field, so the assumption of Bingham plastic behavior may not hold. However, Güth and Maas [58] show that in a shear cell with large gap, Taylor-Couette instabilities are suppressed with increasing magnetic field, a result consistent with the fluid behaving as a Bingham plastic.

Govier and Aziz [82] review turbulent Bingham plastic and Herschel-Bulkley friction factor equations, and show substantial variation in form and value of the estimates. They conclude that the turbulent Bingham plastic friction factors should be estimated using the Newtonian friction factor. However, we never conclusively

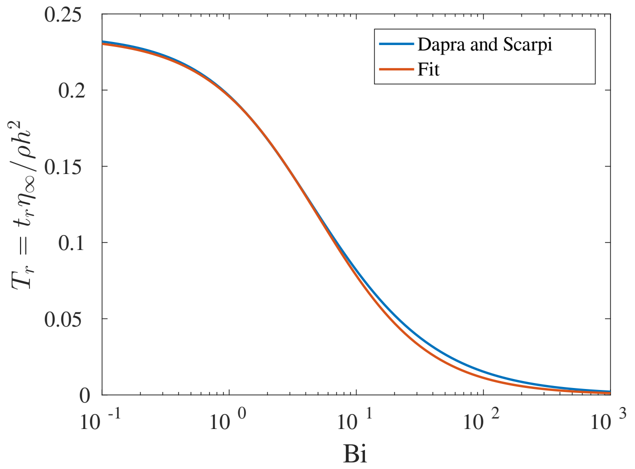

Figure 3.3: Response time for Bingham plastic channel start up flow.

reach the turbulent regime, so choosing a model is not necessary. For CFD, Malin [113] argue that existing turbulence models, $k-\epsilon$ and $k-\omega$, are sufficient to describe the flow of Bingham plastics, but such claims are based on comparison to measurements with $\tau_\mathrm{y} < 10\,\mathrm{Pa}$. Overall, we conclude that it is unlikely that any of the devices here are turbulent in the active region, but that any strong conclusions about the nature of turbulence in MR fluids will require careful experimental measurement.

3.2.5 Time domain effects

We also need to rule out time domain effects, since many of the high speed tests we look at are impact tests taking 20 ms or less. The experiments here are not looking at force rise time to an applied current, but rather the force rise time to an applied velocity. This flow response time, t_r, can be approximated by classic startup flow, where a constant pressure gradient is suddenly applied to a stationary fluid in a duct. For Newtonian fluids, Schlichting [114, p. 85] shows that fluid response time is independent of velocity, with a dimensionless response time, $T_r = t_r\eta/\rho h^2$.

The same scaling holds for Bingham plastics, with an analytical solution for startup flow of a Bingham plastic between infinite parallel plates available in Daprà and Scarpi [115]. The solutions are presented here in our notation, in terms of applied pressure gradient ∇P, the time dependent plug thickness δ_t, and steady state plug thickness, δ. By solving for plug thickness,

$$\delta_T(T) = \delta \left\{ 1 - \frac{4}{\pi} \sum_{k=0}^{\infty} \frac{(-1)^k}{2k+1} \exp\left[-\frac{\pi^2}{4} \left(\frac{2k+1}{1-\delta} \right)^2 4T \right] \right\}^{-1} \tag{3.14}$$

and velocity, $v^* = 4u\mu/h\nabla P$,

$$v^*(T) = \frac{1}{2}(1-\delta_T)^2 - \frac{16(1-\delta_T)^2}{\pi^3} \sum_{k=0}^{\infty} \frac{(-1)^k}{(2k+1)^3} \exp\left[-\frac{\pi^2}{4} \left(\frac{2k+1}{1-\delta_T} \right)^2 4T \right] \tag{3.15}$$

for the time at which velocity reaches 90% of the steady state value, we can obtain a response time.

The response time is shown in Figure 3.3. Since solving these equations is cumbersome, we construct fit $T_r = 0.235/1 + 0.2\mathrm{Bi}$, which is also shown. For a typical experiment here, $h = 1\,\mathrm{mm}$, $\rho = 3\,\mathrm{g/cm^3}$, and $\eta_\infty = 0.1\,\mathrm{Pa\,s}$ and $\mathrm{Bi} > 10$, $T_r < 0.1$, so $t_r < 3\,\mathrm{ms}$, which is close to, but below, the time scales seen in the experiments investigated here. We then expect no difficulties in using our steady state activation flow model on any of the drop stand experiments.

We also note that the response time to an applied field has been analyzed elsewhere, but we believe incorrectly. Choi and Wereley [116] solves the transient 1D flow profile using Newtonian fluid basis functions, which can introduce an unwanted stress discontinuity. Phillips [86] attempts a simple estimate for response time, but flips a negative sign in the pressure gradient, yielding an incorrect result.

Parameter	Mao 1 [14]	Mao 2 [14]	Singh [109]	Goncalves [12]	Sodeyama [15]	Choi [107]
D_h, mm	1.83	2.42	5.18	1.62	3.0	1.67
L_A, mm	15.2	16.3	30.5	6.35 or 25.4	10	14
r_p, mm	19.7	19.43	28.1	-	-	15.9
A_p, mm^2	963	927	1968	8107	2.9×10^4	2553
$A_{\text{res}}/A_{\text{gap}}$	9.8	7.5	5.1	1026	67	30.4
η_∞, Pa s	0.072	0.072	0.112	0.13 – 0.17	0.13	0.092
ρ, g/cm^3	3.52	3.52	3.08	3.06	3.06	3.08

Table 3.2: Key parameters for the high speed devices in Table 3.1.

3.3 Devices

With these observations in mind, the most direct course of action is to simply see if the model contained in Eq. 3.8 works. We will compare it against experimental measurements from all of the high speed devices in Fig. 3.1, with details in Table 3.2. Experimental forces and velocities are taken from the authors' filtered results, with no additional post-processing.

We will show both total modeled force and yield force for each device using the three yield force models, $F_{\mathrm{y,p}}$, $F_{\mathrm{y,B}}$ and $F_{\mathrm{y,act}}$. For the yield force diagrams, the right axis maps yield force into the parabolic apparent yield stress,

$$\tau_{\mathrm{y,app}} = \frac{F_{\mathrm{y}} D_h}{4 A_{\mathrm{p}} L_A (1 + \frac{\pi r_p D_h}{2 A_{\mathrm{p}}})} \tag{3.16}$$

This allows us to see what the apparent yield stress falloff is.

3.3.1 Goncalves' slit rheometer

Goncalves tests a capillary slit rheometer at large gap speeds. In this device, a large piston pushes Lord MR132LD into a slit with an active region placed at the end of the duct. The fundamental observation is that as speed rises, there is a reduction in yield force at high speeds. There is also an increase in yield force at low speeds over the zero speed value, as expected from fully developed Bingham plastic flow. This experiment is the only steady-state high speed test of MR fluid, and forms an essential test case for our activation flow analysis.

In general, the constitutive properties of Lord MR132LD are not clear, and it appears to have some level of plasticity in the off-state. Goncalves' dissertation contains off-state rheometer measurements from the fluid datasheet, which are performed on a very low speed cup and bob rheometer ($0 < \dot{\gamma} < 160\,\mathrm{s}^{-1}$), and indicate that at 40 °C the fluid is a Bingham plastic with $\tau_y = 12\,\mathrm{Pa}$ and $\eta_\infty = 0.17\,\mathrm{Pa\,s}$. As we discuss later, Sodeyama *et al.* [15] also shows datasheet measurements of viscosity of Lord MR132LD, here at larger shear rates, ($0 < \dot{\gamma} < 1000\,\mathrm{s}^{-1}$), and also observes substantial shear thinning. These off-state measurements also indicate Bingham plastic behavior in the off-state, with $\tau_y = 13\,\mathrm{Pa}$ and $\eta_\infty = 0.11\,\mathrm{Pa\,s}$. This indicates that there is substantial uncertainty about the actual viscosity of the fluid, but in both cases the yield stress is small enough to be negligible. For consistency we assume the fluid is Newtonian and fit η_∞ and K, a hydraulic loss coefficient, to the off-state measurements.

To validate our analysis, we extract the pressure loss data from Goncalves' thesis using a visual data extraction tool, and compare our activation flow model to the experimental results. We also make the following three observations about the experiment: there is a large uncorrected temperature rise in the slit, there are no v^2 effects from the contraction and there is uncertainty in the geometric properties.

3.3.1.1 Temperature effects

In the experiment, the measured temperature rise across the slit is 11 °C, sufficient to cause substantial changes to the viscosity of the fluid. There is also a gradual 2 °C temperature rise during testing. A back of the envelope calculation indicates this should change viscosity by 20-30%, which would produce a change in force as large as the observed yield stress falloff. This means that to make precise conclusions, we need to carefully develop a temperature correction.

However, we do not have comprehensive Lord MR132LD temperature viscosity data, so we need to estimate the viscosity temperature effects. We construct an estimate using the principle that suspension viscosity over carrier viscosity is independent of viscosity [117], an assumption that we verified on other Lord fluids [40]. This allows us to use measurements of the carrier viscosity temperature dependence to correct the suspension data. For Lord MR132LD, the carrier fluid is a Chevron Phillips Synfluid 4 cSt polyalphaolephin oil [11], and the data sheet tells us that kinematic viscosity $\nu = 3.9\,\mathrm{mm}^2/\mathrm{s}$ at 100 °C, $16.8\,\mathrm{mm}^2/\mathrm{s}$ at 40 °C and $2498\,\mathrm{mm}^2/\mathrm{s}$ at -40 °C. From this, we fit to the ASTM D341 temperature correction standard for hydrocarbon oils [118], which gives kinematic viscosity, ν, as a function of T:

$$Z = \exp[\exp(A - B\log T)]$$

$$\nu = (Z-0.7) - \exp[-0.7847 - 3.295(Z-0.7) + 0.6119(Z-0.7)^2 - 0.3193(Z-0.7)^3]$$

where here, exp and log are in base 10, and $A = 8.7452$ and $B = 3.4684$ are fluid properties fit using the listed data.

We estimate the temperature rise in the duct due to viscous heating:

$$\Delta T = \Delta T_{\text{visc}} \frac{v^2}{v_{\text{ref}}^2} \left(\frac{L_N}{L_{\text{tot}}} + \left(1 + \frac{\text{Bi}}{6}\right) \frac{L_A}{L_{\text{tot}}} \right) + \frac{\Delta T_{\text{res}}}{v_{\text{ref}}}.$$

This is based off the measured off-state temperature rise from entrance to to exit of $\Delta T_{\text{visc}} = 11\,^{\circ}\text{C}$, at the maximum velocity, v_{ref}. The additional and unmeasured heating from yield stress forces is estimated through the parabolic model in the active region, appearing as the $1 + \text{Bi}/6$ terms. The term on the end comes from the measured reservoir temperature rise $\Delta T = \Delta T_{\text{res}}/v_{\text{ref}}$, where $\Delta T_{\text{res}} = 2\,^{\circ}\text{C}$. This equation is split up to estimate temperature at the entrance, start of active region, and exit. Then, viscosity in the active and passive region is calculated using the mean temperature of each region. This predicts a max temperature rise of $20\,^{\circ}\text{C}$ and an up to 40% change in viscosity from the entrance to the exit for $L_A = 25.4\,\text{mm}$ at $H = 200\,\text{kA/m}$. We do not include any change in yield stress due to temperature due to a lack of data.

3.3.1.2 Velocity squared effects

Second, control volume analysis tells us that there's a missing ρv_{gap}^2 term. Goncalves' device works by pushing a large piston which forces the fluid through a nozzle into a small slit, and roughly matches the step contraction type device in Fig. 3.2.

If we assume that there are no viscous losses in the nozzle, and that $A_{\text{res}}/A_{\text{gap}} \gg 1$, then via Bernoulli: $P_0 + 0.5\rho v_{\text{res}}^2 \approx P_0 = P_1 + 0.5\rho v_{\text{gap}}^2$. If the viscous pressure loss is $P_1 - P_2 = \Delta P_N$, then the measured pressure difference between the reservoir and exit is $P_0 - P_2 = \Delta P_N + 0.5\rho v_{\text{gap}}^2$. For $v_{\text{gap}} = 30\,\text{m/s}$, $0.5\rho v_{\text{gap}}^2 = 1\,\text{MPa}$, and should introduce a clearly visible v^2 pressure loss in the measurements, but this is not observed, a rather surprising result. However, we will show that by including our previously developed temperature correction model, we can obtain realistic values of K.

3.3.1.3 Geometry

Third, in a personal communication with Fernando Goncalves, he noted that the slit cross section used in the analysis was $8.889\,\text{mm} \times 0.889\,\text{mm}$, not the $1\,\text{mm} \times 10\,\text{mm}$ listed. This resolves a discrepancy in the area ratio calculation, as with the listed properties the area ratio is 811:1, not the 1000:1 listed. For all results, we use $h = 0.889\,\text{mm}$. This makes $L_A/D_h = 15.7$ and 3.925 instead of $L_A/D_h = 13.97$ and 3.4925. While the CFD results that underlie the fit in Eq. 3.8 have a maximum $L_A/D_h = 13.97$, we still use the activation flow fits, as we are confidant that Graetz coordinate scaling will allow accurate extrapolation.

As an aside, when Goncalves is determining the fluid properties, off-state measurements are conducted on both active lengths, and report a 15% difference in viscosity with a 1.8 °C temperature difference. A 15% change is excessive, and indicates that there may be other uncertainties in the device geometry.

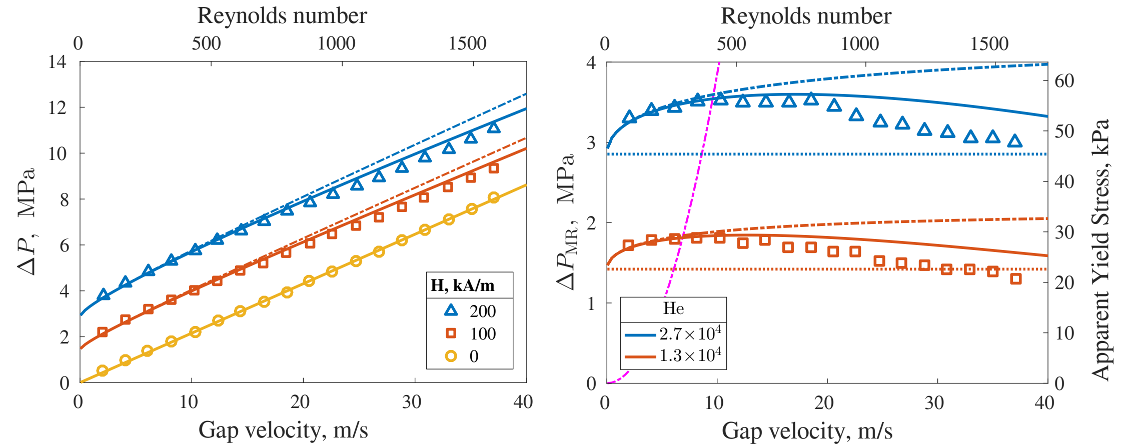

(a) $L_A = 25.4\,\mathrm{mm}$

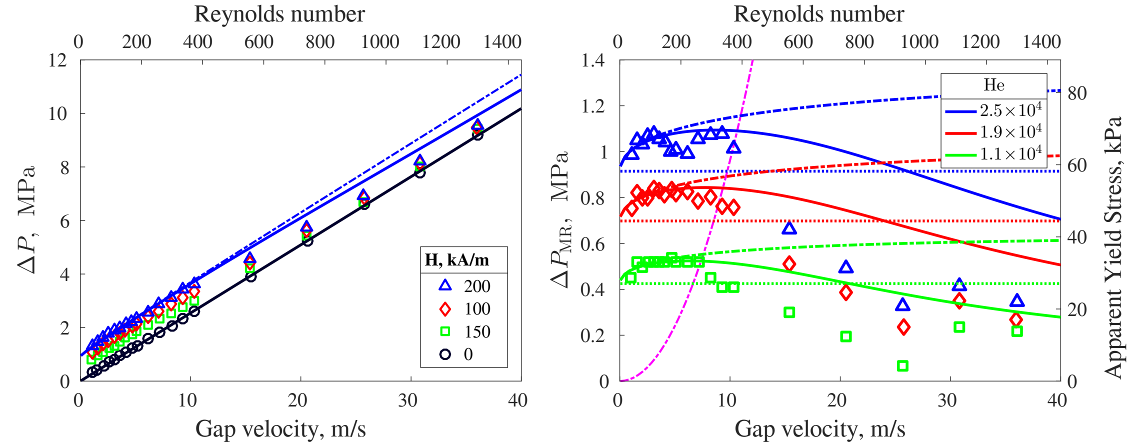

(b) $L_A = 6.35\,\mathrm{mm}$

Figure 3.4: As reported. For $L_A = 25.4\,\mathrm{mm}$, $\eta_\infty = 0.116\,\mathrm{Pa\,s}$, $K = 0.01$, and for $L_A = 6.35\,\mathrm{mm}$, $\eta_\infty = 0.137\,\mathrm{Pa\,s}$, $K = 0.02$. Solid lines are activation flow based fits, dotted lines the parabolic model, dash-dot plug flow. Pink dashed line is $C_{\tau_y} = 0.4$.

3.3.1.4 Results

In Fig. 3.4, we compare the fully developed Bingham plastic model, the parabolic model and the activation flow model with no temperature correction to the experimental pressure loss measurements. We can also identify the three flow regimes, a quasi-static, low speed and high speed regimes. The quasi-static regime should have yield forces that are accurately predicted by the plug flow model, and is estimated to occur when $C_{\tau_y} > 0.4$. Fig. 3.4 shows that when $C_{\tau_y} > 0.4$ experimental forces are quite close to plug flow, and very accurately predicted by activation flow, confirming our basic claims about the applicability of activation flow. However, the criteria fairs poorly for the long $L_A/D_h = 15.7$ duct, as it is based on a $L_A/D_h = 5$ duct. In the low speed regime, where $C_{\tau_y} < 0.4$ and $F_{\mathrm{y,act}} > F_{\mathrm{y,p}}$, activation flow is reasonably accurate in the long duct, but underestimates the yield force decrease in the short duct. High speed is defined as $F_{\mathrm{y,act}} < F_{\mathrm{y,p}}$, and in this region, activation flow, while predicting a reduced yield stress, fails to correctly estimate the magnitude of yield force falloff. Overall, activation flow clearly improves accuracy, but struggles at high speeds.

We can also assess accuracy by comparing our values to those obtained in Goncalves. There, yield stress is calculated using the Phillips polynomial, which fits τ_{y} assuming fully developed flow, and η_∞ coming from the off-state measurement at the equivalent speed. Here, we assume that η_∞ is a constant, and that there is a velocity independent K term, and determine these quantities by first fitting to F_{off}. We then using the off-state fit values of η_∞ and K for a fit of τ_{y} on low speed F_{on}

data. The main differences between our approach and Goncalves' is our inclusion of a K term and assumption of constant η_∞ and τ_y.

As expected, both methods produce highly similar results. Here, $K \approx 0$ as expected, and $\eta_\infty = 0.11\,\mathrm{Pa\,s}$ and $0.14\,\mathrm{Pa\,s}$, close to the reported $\eta_\infty = 0.14\,\mathrm{Pa\,s}$ in Goncalves. For the two methods, yield stresses at low speeds are similar, where at $H = 200\,\mathrm{kA/m}$, for $L_A = 25.4\,\mathrm{mm}$, we fit $\tau_\mathrm{y} = 45\,\mathrm{kPa}$ vs. $48\,\mathrm{kPa}$ in Goncalves, and for $L_A = 6.35\,\mathrm{mm}$ we fit $58\,\mathrm{kPa}$ vs. $55\,\mathrm{kPa}$ in Goncalves. Part of the difference is caused by the activation flow model assuming constant viscosity (no shear thinning), which increases apparent yield stress at low speed by 5-10%. However, when compared to the datasheet value of $\tau_y = 42\,\mathrm{kPa}$ at $H = 200\,\mathrm{kA/m}$, both models predict yield stresses that are too large. Overall, for the long duct, our simplified model captures 60% of the apparent yield force reduction, but captures only 30% in the short duct. While this constitutes an improvement, it remains plausible that the yield force falloff is caused by some other effect.

We attempt to resolve these uncertainties in Fig. 3.5 by applying the temperature corrected viscosity model, and otherwise using the same procedure. Including the temperature changes reduces the reference viscosity by about 5%, and enables a realistic $K > 1$ factor for both ducts. Temperature induced shear thinning affects all three models, as the yield stress induced temperature rise causes a reduction in viscosity, reducing $F_\mathrm{y,p}$ and $F_\mathrm{y,B}$ slightly due to the lower η_∞ in the active region. In the activation flow model, temperature has a much larger effect, as the reduction in η_∞ raises Re and Bi at a given velocity, increasing yield force falloff. Figure 3.5 shows that including temperature effects makes the activation flow prediction highly

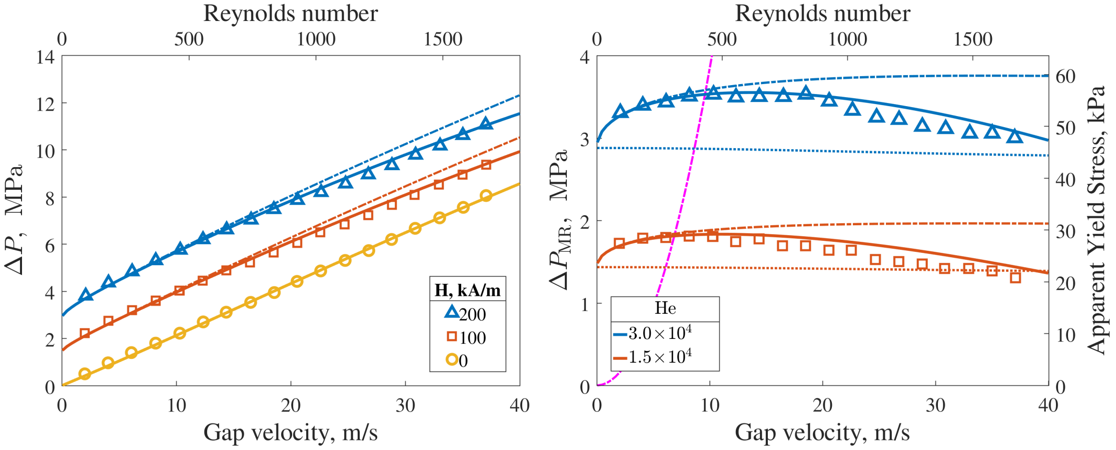

(a) $L_A = 25.4\,\mathrm{mm}$

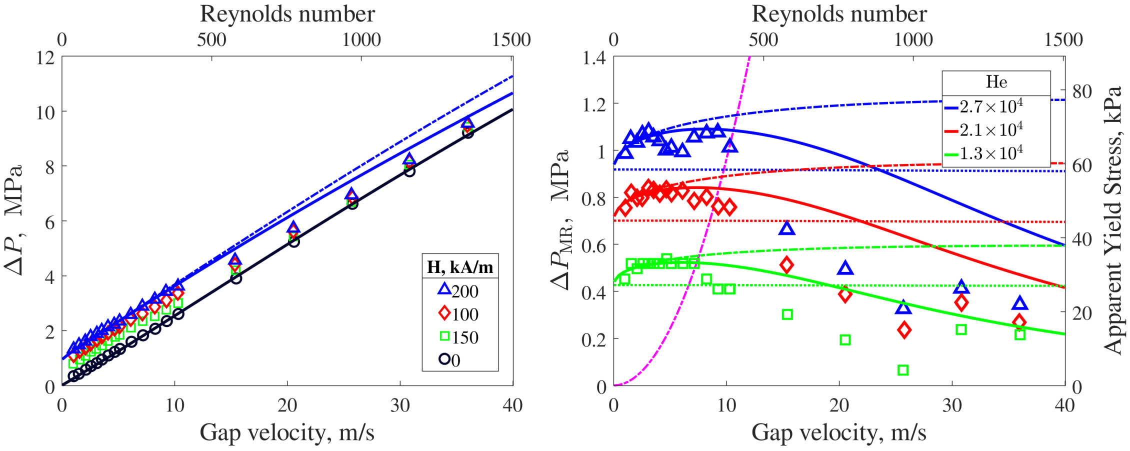

(b) $L_A = 6.35\,\mathrm{mm}$

Figure 3.5: Temperature increase modeled by $\Delta T \propto v\,\Delta P$, and the ASTM D341 viscosity-temperature correction for the carrier fluid. For $L_A = 25.4\,\mathrm{mm}$, $\eta_\infty = 0.110\,\mathrm{Pa\,s}$, $K = 1.07$, and for $L_A = 6.35\,\mathrm{mm}$, $\eta_\infty = 0.131\,\mathrm{Pa\,s}$, $K = 1.22$. Pink dashed line is $C_{\tau_y} = 0.4$.

accurate for the long duct, and in the short duct captures 65% of the force falloff for the short duct. Note that τ_{y} is unaffected by the temperature changes, as we fit τ_{y} at low speeds. Our main conclusion is that the inclusion of temperature effects allows for a realistic $K > 1$ and improves the the accuracy of force predictions to the point where activation flow seems to be accurate.

In this experiment, the activation flow model is accurate in quasi-static and low speed flows, but at high speeds in short ducts, yield force falloff is underestimated. This prevents us claiming confirmation that yield stress falloff is caused by fluid dynamic effects, but the activation flow force model does capture the essential trends of a reduced yield force at high speeds, and allows estimation of when these effects will occur. In particular, the one-size-fits-all quasi-static criteria, $\tau_{\mathrm{y}}/0.5\rho v_{\mathrm{gap}}^2 > 0.4$, successfully identifies the onset of fluid dynamic effects for both the short and long duct. However, we noted many uncertainties in the experiment, and while including a temperature–viscosity correction improves accuracy, the poor performance in the short duct means questions still remain.

3.3.2 Min Mao's double ended rod damper

Next we look at the two practical high speed impact absorbers designed by Mao *et al.* [14]. These dampers operate at $\mathrm{Re} > 4000$ in the active region, the highest active region Reynolds numbers that we are aware of. These devices are of a double piston rod damper design and have minimal spring terms as there is no accumulator. Both devices have 4 contraction type active regions, two with the listed L_A in Table 3.2 and two active regions with $0.5L_A$. The dampers were tested with the same custom fluid, with properties listed in Table 3.2, and we assume all active regions have the same yield stress. These devices also serve as the first test of our claim that the activation flow analysis can be applied to practical devices with contraction-type active regions.

The focus of this paper is on the yield force, so we avoid the substantial challenges of accurate off-state modeling, the focus of Mao's thesis [13], by curve fitting the off-state experimental data to a cubic polynomial, and then adding $F_{\mathrm{y,model}}$ to $F_{\mathrm{off,fit}}$ obtain $F_{\mathrm{on,model}}$. Similarly, to obtain an experimental F_{y} for fitting purposes, we use $F_{\mathrm{y}} = F_{\mathrm{on}} - F_{\mathrm{off,fit}}$, since on and off state measurements don't occur at the same speeds. We note that since predictions of yield force model are set by fluid properties and the geometry of the gap, yield force predictions are completely unaffected by the specific details of the off-state model.

The devices here of a typical damper design, where the active region is an annulus and one of the walls is moving. This poses a challenge as the activation flow model is based on a parallel plate solution with stationary walls. However, the gap width to piston diameter ratio is quite low, so we are firmly within the rectangular limit, as a concentric annulus with $b < r < a$ can be treated as a rectangle for $b/a > 0.7$, White [95, p. 120-124], a criteria achieved for all the devices in this paper. We neglect the moving walls, as it has previously been shown to have a negligible effect for devices with $A_{\mathrm{p}}/A_{\mathrm{gap}} > 3$ [119]. We also operate in the piston frame, where the flow rate through gap is $Q = A_{\mathrm{res}}v_{\mathrm{p}}$, so $v_{\mathrm{gap}} = A_{\mathrm{res}}/A_{\mathrm{gap}}v_{\mathrm{p}}$. This is a slightly different choice than the typical wall frame $Q = A_{\mathrm{p}}v_{\mathrm{p}}$, but we choose piston frame

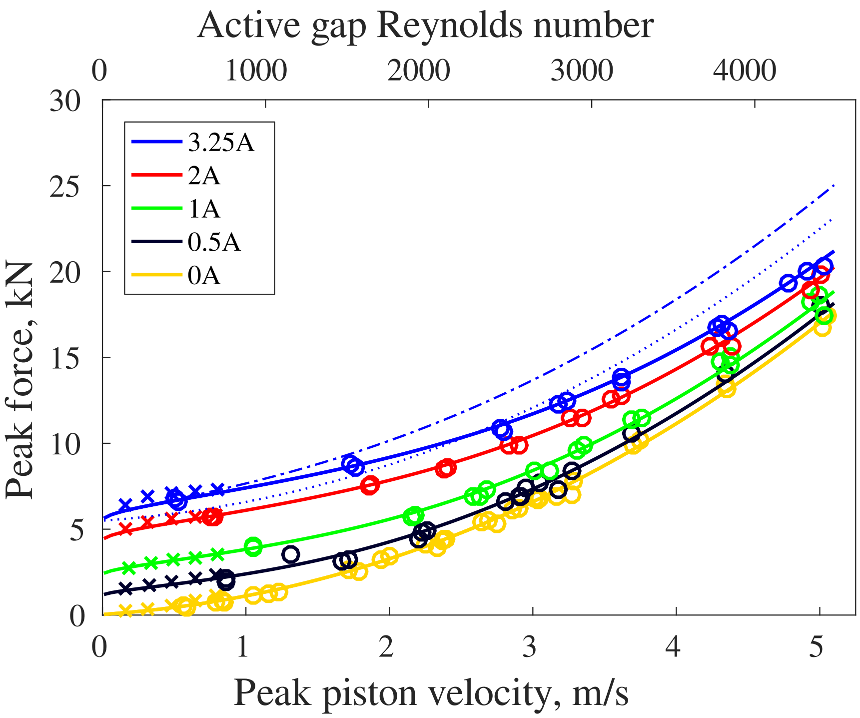

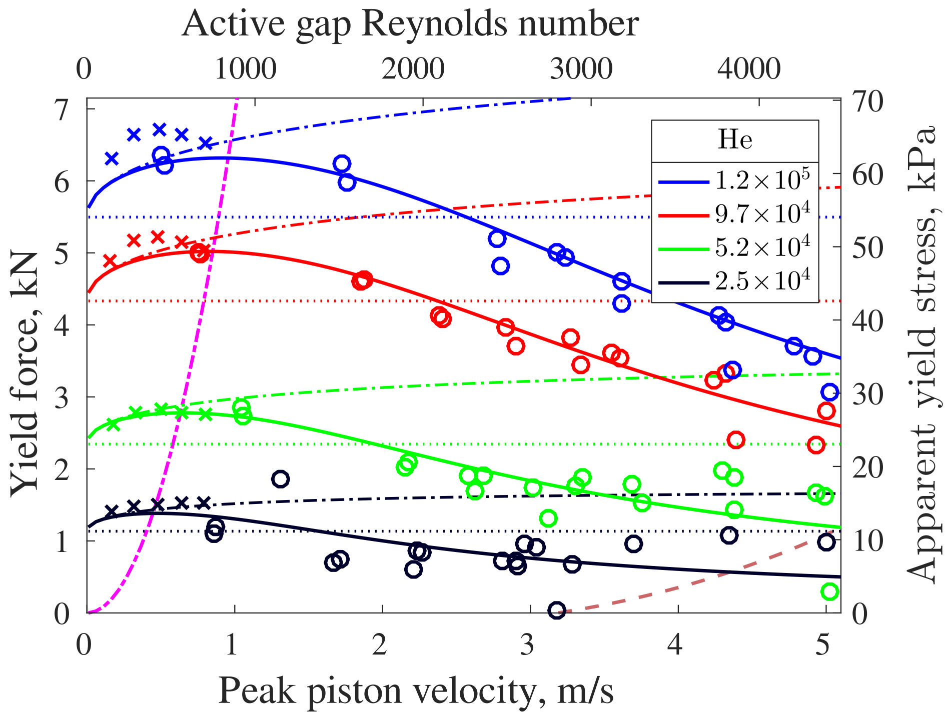

Figure 3.6: Min Mao's SSMREA1 [14]. Solid lines are activation flow based fits, dotted lines the parabolic model, dash-dot plug flow. The x symbols correspond to sinusoidal testing data, circles are drop stand data. In the yield force diagrams, pink dash dot is $\tau_{\mathrm{y,app}}/0.5\rho v_{\mathrm{gap}}^2 = 0.4$, and dashed brown is the onset of turbulence for a Bingham plastic.

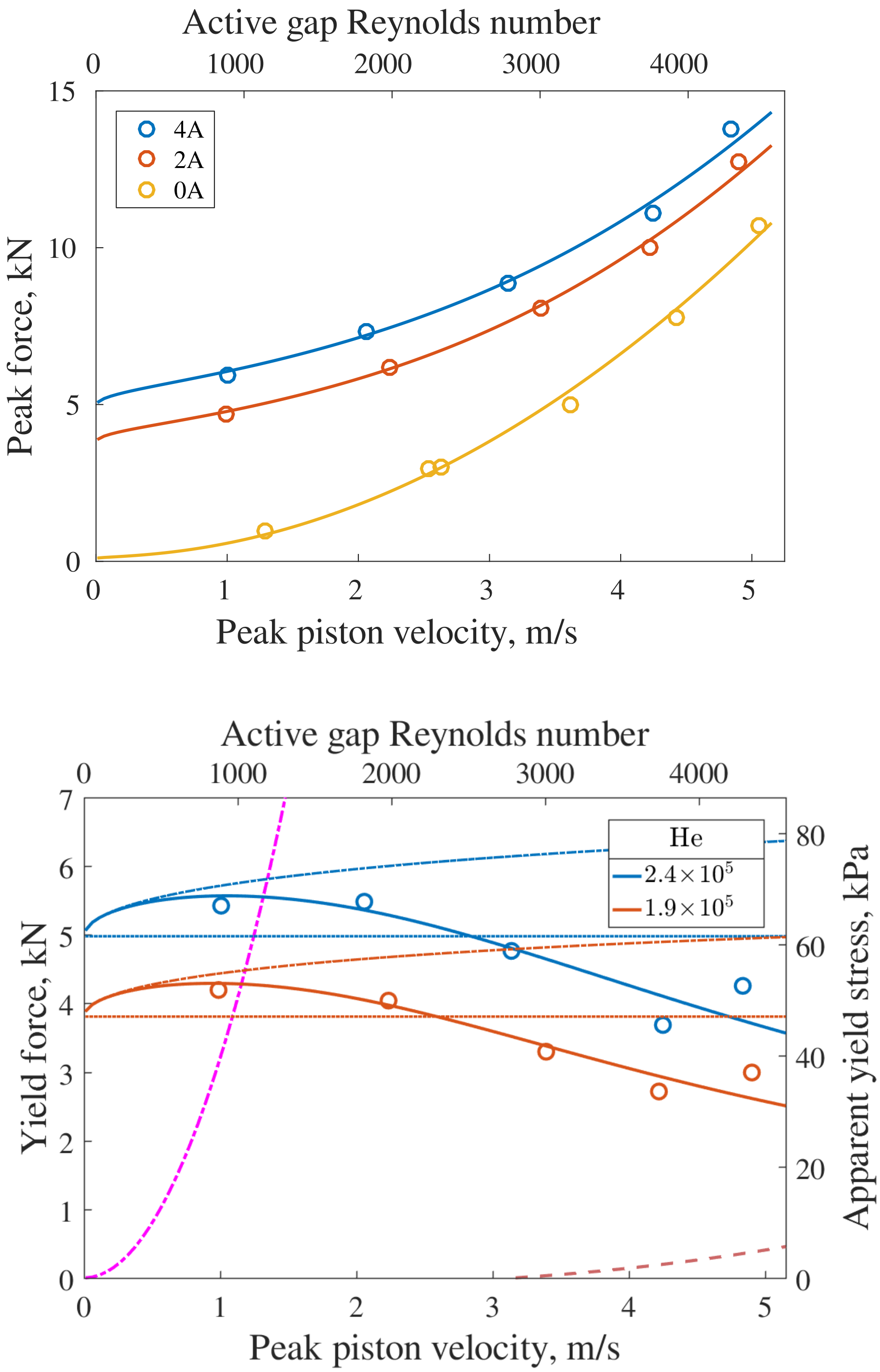

Figure 3.7: Mao's SSMREA2 [14]. Solid lines are activation flow based fits, dotted lines the parabolic model, dash-dot plug flow. The x symbols correspond to sinusoidal testing data, circles are drop stand data. In the yield force diagrams, pink dash dot is $\tau_{\mathrm{y,app}}/0.5\rho v_{\mathrm{gap}}^2 = 0.4$, and dashed brown is the onset of turbulence for a Bingham plastic.

as it is easier to model in CFD and should be equally accurate. The choice of the piston frame flow rate for defining gap velocity also increases flow rate, reducing some of the error from assuming stationary walls.

For the practical devices, our procedure for experimental validation is simpler than in Goncalves - we just use the given geometric and fluid properties, which fixes Re and L_A/D_h, and then fit $\tau_{\mathrm{y}}(\mathrm{He})$ to minimize error in F_{y}. We note that since $\Delta n_p \propto \log(\Delta \mathrm{He})$, the force curve shape is fairly insensitive to the precise value of τ_{y}. We also include both sinusoidal and drop stand testing data on the same plot, a rarity, as they are often separated since don't show the same trends, but include it here, as it demonstrates the flexibility of our model, which is accurate for both low and high speed cases.

Figure 3.6 and 3.7 shows that the activation flow model accurately describes yield force at any speed, while the parabolic and plug flow models capture none of the observed trends at low and high speeds. The off-state force fit has an RMS force error of 220 N and 320 N in device 1 and 2 respectively, which serve as a reasonable estimates of experimental uncertainty. Activation flow yield force has RMS error of 220 and 340 N, indicating our fits are within the experimental uncertainty. The fit τ_{y} are also physically realistic, where at maximum applied current $\tau_{\mathrm{y}} = 55\,\mathrm{kPa}$ for SSMREA1 and $\tau_{\mathrm{y}} = 62\,\mathrm{kPa}$ for SSMREA2, close to the design goal of $\tau_{\mathrm{y}} = 60\,\mathrm{kPa}$ for both devices.

For SSMREA1's low current cases, $I = 0.5\,\mathrm{A}$ and $1\,\mathrm{A}$, model performance is worse once $\mathrm{Re} > 2800$ and turbulence starts to be a concern. We also see that the quasi-static $C_{\tau_{\mathrm{y}}} > 0.4$, and high speed criteria are effective, as expected from the excellent performance of the fit. The excellent model performance observed here give us a high level of confidence that the activation flow force model can be applied to this and other contraction type devices.

3.3.3 Harinder Singh's large damper

Singh *et al.* [109] designs a 12 kN MR damper for impact mitigation. This damper is single rod design with pressurized diaphragm, but here we've made no attempt to correct for spring terms, as for the data available they are expected to be relatively small. The device has six active regions, four with the L_A in Table 3.2, two with $0.5L_A$, and we assume all regions have the same τ_y. The device is nominally of the contraction-type design, but the passive regions were later smoothed into a flat shape so as to reduce turbulent exit losses. This means that our modeled boundary conditions may not hold up, as at high speeds, the flow exiting one active region may not return to parabolic shape by the time it reaches the next active region. Similarly, if the flow goes turbulent, our active region model will break down. However, for this device, these issues seem to be a concern for only one point.

Offstate forces were fit to a cubic, in order to capture the rising forces near the exit. The device was tested with Lord MR132DG, with maximum $\tau_\mathrm{y} \approx 50\,\mathrm{kPa}$ and we use the manufacturer specified properties in our model, shown in Table 3.2. Due to drop stand height limitations and load cell ringing, there is limited high-speed high-force drop stand data, with sinusoidal MTS data used for $I = 5.5\,\mathrm{A}$ and $I = 4\,\mathrm{A}$.

Figure 3.8 compares the three active flow models to all available experimental

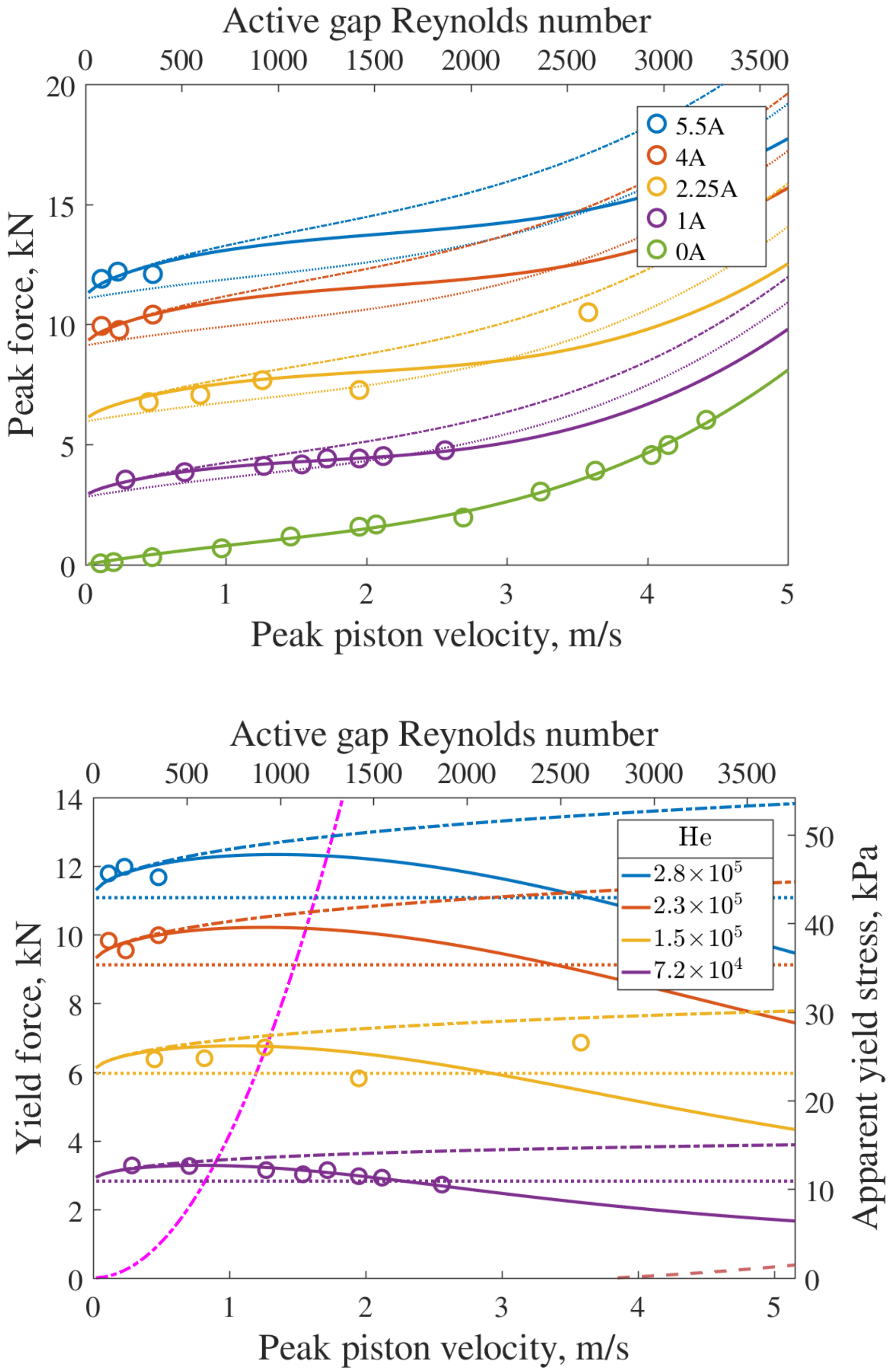

Figure 3.8: Singh's large damper [109]. Solid lines are activation flow based fits, dotted lines the parabolic model, dash-dot plug flow. In the yield force diagram, pink dash dot is $\tau_{\mathrm{y,app}}/0.5\rho v_{\mathrm{gap}}^2 = 0.4$, and dashed brown is the onset of turbulence for a Bingham plastic.

measurements. Again, the activation flow model matches the experimental data extremely well, accurately capturing the $I = 1\,\mathrm{A}$ force-velocity data, and performing well for the low speed $I = 2.25\,\mathrm{A}$ tests. At the higher currents, where the flow is quasi-static, the activation flow model captures the yield stress amplification from the plug. For the test point at $v_p = 3.5\,\mathrm{m/s}$ and $I = 2.25\,\mathrm{A}$, model performance is poor, possibly due to either the turbulence or exit profile concerns outlined above. The fit yield stress estimates are accurate where at $I = 5.5\,\mathrm{A}$, we fit $\tau_\mathrm{y} = 43\,\mathrm{kPa}$, in excellent agreement with the FEA estimate of 45 kPa. We also clearly see the effectiveness of the quasi-static criteria, $C_{\tau_\mathrm{y}} > 0.4$, with all tests points in that region conforming to the plug flow model.

3.3.4 Choi and Robinson

Choi *et al.* [107] build an 8 kN MR oleo-pneumatic damper for helicopter landing gear. Oleo-pneumatic dampers have gas and fluid mixed in a single chamber, with device expansion and contraction causing the fluid to flow through the annular active region. Spring effects are substantial in this design, making analysis challenging. Specific properties are listed in Table 3.2, and note both the small gap and very large area ratio.

In Figure 3.9, we compare our model to a series of MTS ramp experiments where the damper was pressurized at 50 PSI, and we have attempted to remove spring forces. Yield stress is fit to the high speed F_y measurements using our previous procedure. The fit at high speed means that high speed yield force predictions

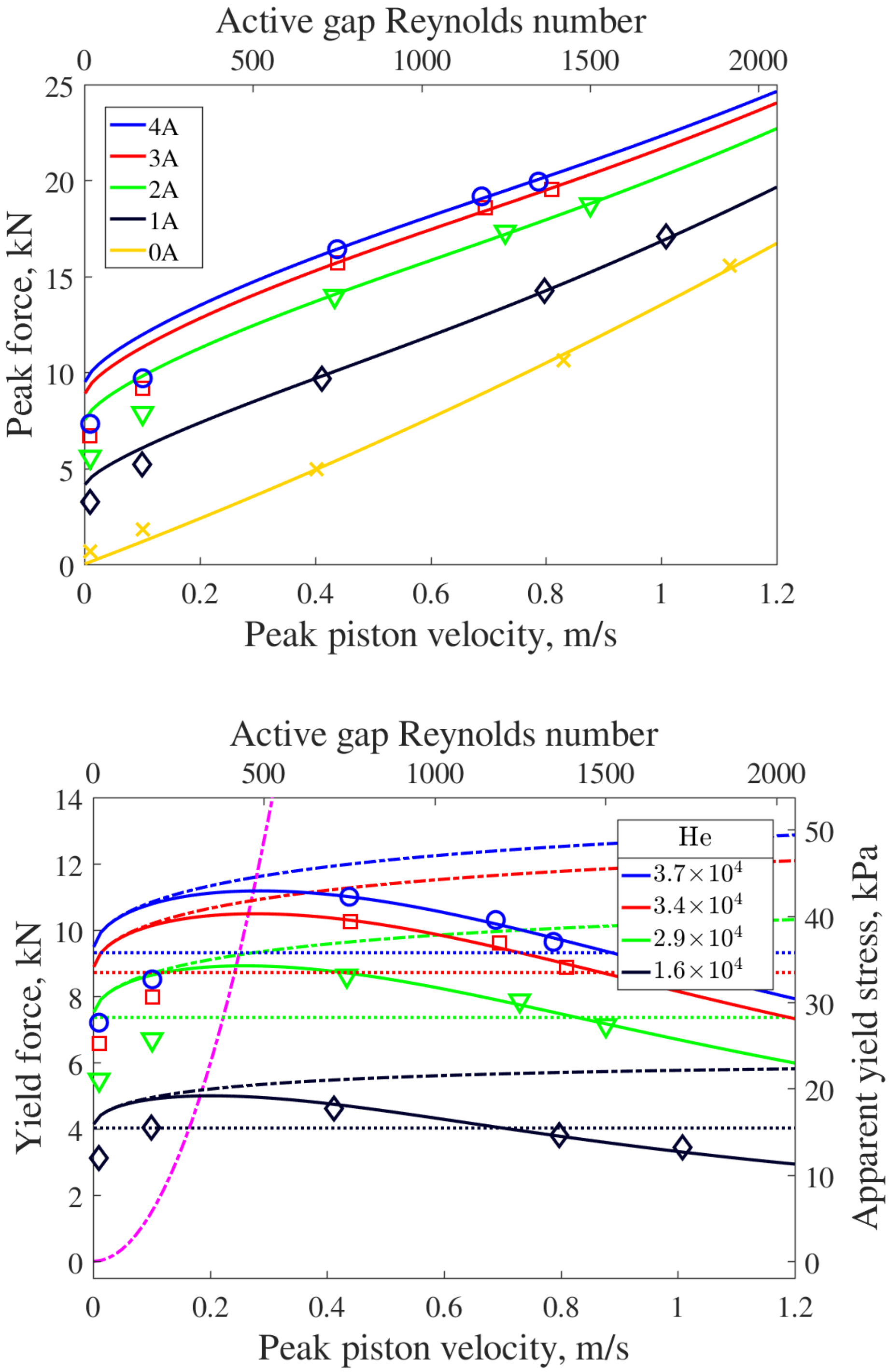

Figure 3.9: Choi's landing gear damper [107]. Solid lines are activation flow based fits, dotted lines the parabolic model, dash-dot plug flow. In the yield force diagram, pink dash dot is $\tau_{\mathrm{y,app}}/0.5\rho v_{\mathrm{gap}}^2 = 0.4$, and dashed brown is the onset of turbulence for a Bingham plastic.

are accurate, but low speed model performance is as poor as existing models. Fit yield stress at 4A is 36 kPa, which is below the design value of 45 kPa. Overall, the activation flow model is an improvement over existing models, capturing the high speed decrease in yield force. However, at low speeds performance is poor, possibly due to the high compliance inherent to the oleopneumatic design.

3.3.5 Sanwa Tekki seismic dampers

Surprisingly, the same fluid dynamics seen in the previous high speed impact devices can also be seen in building scale seismic dampers. Due to the high forces required for a building scale device, $A_{\mathrm{res}}/A_{\mathrm{gap}}$ can be very large, sending v_{gap} into the high speed region. While a variety of seismic dampers have been built [106], only the Sanwa Tekki designs enter into the high speed regime [15], [56], [98], as other groups building seismic MR dampers choose fluids with very high viscosity, so as to prevent settling [105], [106], [120]. The Sanwa-Tekki group typically use a double rod piston design with an external bypass for the active region, indicating that the device should to conform to the activation flow model.

While the authors do not specifically call out a high speed force falloff, we note in [56], that the 200 kN device they built has has $L_A/D_h = 2.5$ and sees a reduced yield force when $v_{\mathrm{p}} = 20\,\mathrm{cm/s}$ or $\mathrm{Re} \approx 1100$, $\mathrm{He} \approx 1.2 \times 10^5$. However, there is no point validating our model against this data, as the force-velocity plots in [56] are unclear, and a conference proceeding version [121] has a 50 kN spread in force data. However, a basic activation flow analysis indicates that there should be a small but noticeable reduction in yield force. It is worth noting that these tests were conducted with Lord MR132LD in a short gap ($L_A/D_h < 4$), the same scenario our model struggled with when examining Goncalves duct.

Even more interestingly, in the same paper, the authors also test the same device with a custom, highly viscous MR fluid, and no disappearing yield force is observed. This is consistent with our fluid dynamic hypothesis, but contradicts the trends expected from a chain/rheological response time. Previously we demonstrated that the particle dynamics response time $t_r \propto \eta_c/\mu_0 M^2$. So when the fluid is made more viscous, the rheological response time should increase, which should make the yield stress falloff more visible, not less. We also note that earlier in [56], they test a 2 kN and 20 kN devices and observe no force falloff. In these devices, Re and He are such that no falloff is expected, as seen in Fig. 3.1.

Later, when designing a 400 kN device [98], they take a new approach to predicting device force, and remove upstream orifice losses when the current is on. This approach reduces the apparent yield force, but it seems unlikely that yield stress would affect behavior so far upstream. However, this effort appears unneeded, as no force falloff is seen in their experimental data, consistent with $\mathrm{Re} = 560$ and $\mathrm{He} = 2 \times 10^5$.

Finally, in [15], they publish a close look at a 300 kN seismic damper, a double rod design with annular contraction style active region with $L_A/D_h = 6$ and ten active regions, using Lord MR132LD, like Goncalves, with other details in Table 3.1. They present clear F vs v_p results from a sinusoidal excitation test, which we extract for use with our model. Note that $v_{\mathrm{gap}} = 27\,\mathrm{m/s}$ at $v_p = 0.4\,\mathrm{m/s}$, which means that this

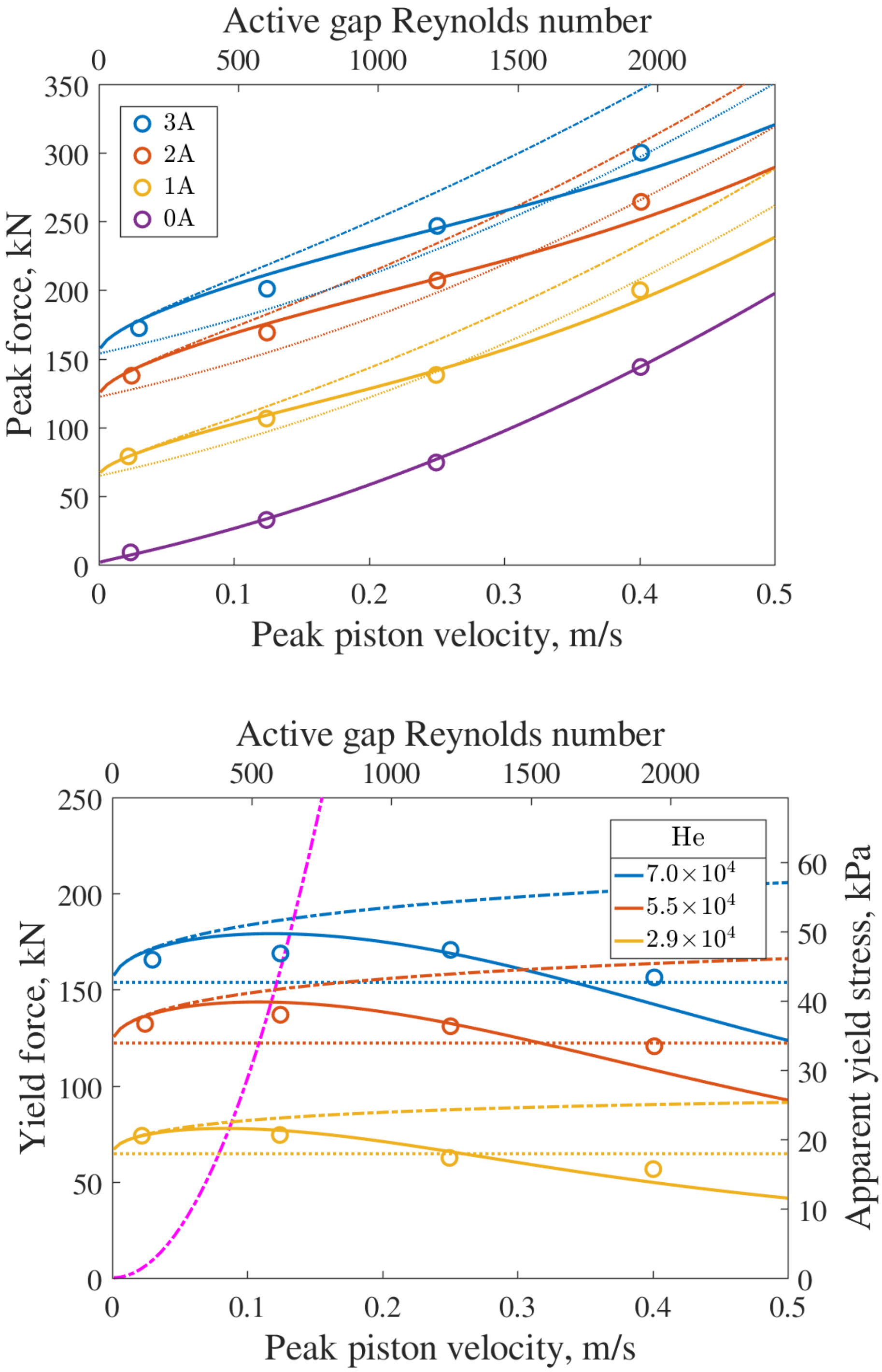

Figure 3.10: Sodeyama's 300 kN seismic damper [15]. Solid lines are activation flow based fits, dotted lines the parabolic model, dash-dot plug flow. In the yield force diagram, pink dash dot is $\tau_{\mathrm{y,app}}/0.5\rho v_{\mathrm{gap}}^2 = 0.4$

device is firmly in the high speed regime. They also show a rheometer measurement of η at zero field, which exhibits strong shear thinning, and $\eta_\infty = 0.11\,\mathrm{Pa\,s}$ at $1000\,\mathrm{s}^{-1}$. We compare our activation flow model to their experimental data in Fig. 3.10, where $\tau_\mathrm{y} = 43\,\mathrm{kPa}$ at 3 A, a reasonable value. While no major force falloff is observed, our model produces a small rise in yield force followed by a small reduction, a trend seen in the data. With just four measurements at each input current, the amount of measurement uncertainty is difficult to estimate. However, the model developed here clearly captures the observed decrease in yield force at high speeds that the other models cannot. Overall, this is a successful validation of the activation flow analysis, as it is clearly more accurate than existing models.

3.4 Conclusions

In this paper, we validated our claim that the activation flow force model will predict device yield force against all of the known high speed MR fluid devices. We designed our activation flow model to capture the fluid dynamics seen in the high speed capillary rheometer of Goncalves, and despite some experimental uncertainties, showed we could reproduce a significant portion of the measured high speed force falloff effect seen in his experiment. We then looked at four impact absorbers designed by our group, and showed outstanding agreement between the activation flow model and experimental yield force data. Finally, we looked at one of the very large dampers built by the Sanwa-Tekki corporation and showed that they were also experiencing high speed force falloff, and that our model could accurately predict the observed yield forces. While we didn't look at low speed or quasi-static experiments, we emphasize that our model should be as or more accurate as existing models in those regimes. From this we conclude that high speed force falloff is a consequence of fluid dynamics, not a response time.

However, in constructing our model we omitted many details so we could get a clear understanding. For future work, we would like start adding in the details we omitted to see how they refine the solution. In particular, experimental data seems to indicate worse model performance in short active regions, $L_A/D_h < 4$, possibly due to the assumption of uniform yield stress no longer being valid in a low aspect-ratio duct. Future work in this area should look at higher fidelity models, ones that include the effect of the moving wall, non-uniform yield stresses and better models of the upstream flow.

Validation of these high fidelity models will require high-quality experimental data, which necessitates an improved version of Goncalves rheometer. In particular, highly accurate viscosity data is needed, and that requires a device that is temperature controlled, or at least one that measures wall temperature, so fluid film temperature can be estimated. The device would also need to correct for entrance effects, ideally by obtaining pressure loss through pressure taps in the passive region. To verify that this succeeded, significant effort would need to be spent calibrating the rheometer against fluids with known properties across the operating temperatures and pressures. After a similar set of measurements on the carrier fluid, only then could active field measurements begin with enough accuracy to make definitive claims on the effectiveness of high fidelity CFD models and secondary concerns like turbulence.

In conclusion, we believe that the fluid dynamic model outlined in the previous two chapters provides an accurate and effective description of the fluid dynamics in flow mode ER/MR devices. We demonstrated this by accurately modeling yield force for a comprehensive series of devices. This should enable accurate design of ER and MR devices in an expanded design space, enabling a next generation of controllable seismic and shock absorbers.

Chapter 4: Conclusions

This dissertation is an investigation into the fundamentals of controllable yield stress fluids, focusing on the disappearance of yield force at high speeds in magnetorheological fluids devices. First, we briefly discuss the dynamics of the particles in MR fluids, and show that current models are limited by their lack of friction. Then, we showed that high-speed yield force falloff has all the symptoms of a fluid dynamics problem, turning this dissertation into an exploration of the fluid dynamics of controllable yield stress fluids.

Chapter 2 rigorously investigates the fluid dynamics of controllable yield stress fluids entering an active region. The key observation that is at high speeds, the formation of the plug reduces the momentum of the fluid, causing a pressure rise. This pressure rise explains much of the observed high speed yield force falloff. To obtain generalizable results, we created a simplified model of a controllable yield stress fluid entering an active region, the 'activation flow', designed to capture the fluid dynamics of any ER/MR flow mode device. We then modified and and validated an OpenFOAM CFD solver, and used it to solve for the full 2-D profile over a nondimensional space large enough to include nearly every MR ever built. Using the CFD data, we developed a set of fits for wall shear stress and profile momentum, which allows the prediction of high speed force falloff in arbitrary flow mode ducts.

We also showed that Reynolds and Hedstrom of the active gap are the most convenient nondimensional numbers for describing the fluid dynamics of the system, as they act as the dimensionless velocity and yield stress respectively. By reporting these two quantities and the device geometry, a complete description of the flow mode fluid dynamics can be obtained. However, the Reynolds and Bingham number are the most fundamental description of the fluid dynamics, and should be used in rigorous analyses. Here, Reynolds and Bingham number are then used in a control volume analysis to estimate the magnitude and onset of high speed effects, resulting in Equation 2.34 and 2.35. These simple equations allow prediction of the onset and magnitude of inertial effects in an extremely compact form. Notably, Equation 2.34 depends solely yield stress coefficient, $C_{\tau_\mathrm{y}} = \tau_\mathrm{y}/0.5\rho v_0^2$, allowing speed effects to be predicted with a single nondimensional number. We also argued that changes in force are best viewed as changes in apparent active length, as it is easy to analyze and gives geometry independent results that are intuitive at low speeds.

Chapter 3 uses the nondimensional analysis tools in the previous chapter to identify which experimental devices will exhibit high speed yield force falloff, and then compares the yield force predictions of Chapter 2 to experimental force measurements from those devices. After addressing concerns about time-domain fluid dynamics and turbulence, we demonstrate that activation flow accurately describes high-speed yield force falloff in devices that operate at high speeds, and is identical to existing yield force models at low speeds.

These results also expand our understanding of the behavior of magnetorheological fluids outside of the realm of high-speed devices. By showing that fluid dynamics explains a complex experimental phenomenon, we demonstrate that CFD and classic control volume analysis should be used to investigate other phenomenon and other geometries. There are many devices that do not conform to the flow mode step-contraction geometry we discuss here, and applying the methods used here should enable both accurate force prediction and even more creative designs.

4.1 Future work

There are many possible directions for future work. One basic step would be to validate the model against a set of ER devices, as all of the physical models used here are valid for ER fluids. Another option is to refine the particle model through an investigation of the tribological interactions of the particles. This will require extensive characterization of the fluid, additives and particles, and then taking that data and using it to develop particle force models. With a comprehensive set of experiments, such a test campaign should enable accurate magnetorheological fluid design.

Improving the bulk modeling is likely to be the most productive choice. More efficient numerical methods and schemes are the most important next step to take, as our approach while accurate, was highly inefficient. The biviscous regularization model is not ideal, and solver performance can be improved substantially by choosing a smooth regularization [78], [79], as there is no real need to validate against exact 1-D solutions. Grids could also be much coarser, as the sub 1% error threshold used here was unnecessarily strict. Second, the solver we chose, the SIMPLE method, is not particularly sophisticated, and performance was poor. Performance could be increased by resolving the non-Newtonian elements through an explicit inclusion in the solver equations [122]. When combined with a smooth viscosity model, major performance improvements should be possible.

With a better numerical method, the next step would be to increase the fidelity of the physical model. There are lots of basic improvements to make, like making the duct an annular channel and including the moving damper wall. A more challenging improvement would be to include a spatially varying magnetic field and thus spatially varying rheology. To handle the spatially varying rheology, a Mason number master viscosity curve would provide a smooth and consistent viscosity model, providing accuracy while maintaining nondimensionality. Adding the varying field would improve model fidelity as well as removing discontinuities, but specializes results to the fluid with the given master curve, and most significantly, makes the analysis much harder. Alternate rheological models may provide additional accuracy, but should give results substantially similar to those using the Bingham plastic model.

Beyond refinements to activation flow type models, different flow geometries can be investigated, such as bifold and radial flow designs [101], [123]. Another option is to investigate how deactivation flow type behavior impacts solutions, so as to enable the analysis of flow mode devices that do not conform to the step contraction model. Similarly, actual contraction geometries could be examined, though this risks needing to model and verify the turbulent behaviors of MR fluid.

The other direction is to build an improved version of Goncalves' experiment.

It should be capable of reaching even larger gap velocities $v_{\text{gap}} > 50\,\text{m/s}$, but more importantly, would include more rigorous controls for fluid and thermal properties. In particular the device should be extensively calibrated using the known properties of an existing fluid, so as to ensure device analysis accuracy. Similarly, the tested fluid should be extensively measured on different rheometers, to provide a strong baseline of comparison. It's worth noting that that the operating pressure of any new device would be large, $\Delta P > 10\,\text{MPa}$, and that while compressibility is not a concern, oils do change viscosity at large applied pressures. Second, to rigorously avoid entrance effect terms, pressure taps need to be used to obtain pressure loss. Third, the device needs to be actively cooled, or at least have entrance, wall and exit temperature measured to enable accurate correction for thermal effects. Such a device would provide definitive measurements of high speed force yield force falloff, and could begin to address active region turbulence effects.

But the best option is to take the experimentally validated force models from this thesis and use them to build efficient high speed devices. With analytical expressions for force, the activation flow model is amenable to use in any design and analysis code, and should dramatically expand the design space of flow mode magnetorheological devices. This expanded design space will allow a next generation of impact and seismic energy absorbers capable of saving lives in ever more dangerous situations.

Appendix A: Flow Images

This appendix contains images of normalized velocity and viscosity from Bi = 1 to Bi = 300 from Re = 0.1 to Re = 4000 at $L_A/D_h = 3.4925$. They are presented at constant Bi, which helps reveal the C_{τ_y} related trends in the data. The active length, $L_A/D_h = 3.4925$ was chosen solely for clarity of presentation, and all of the trends seen here are independent of L_A/D_h.

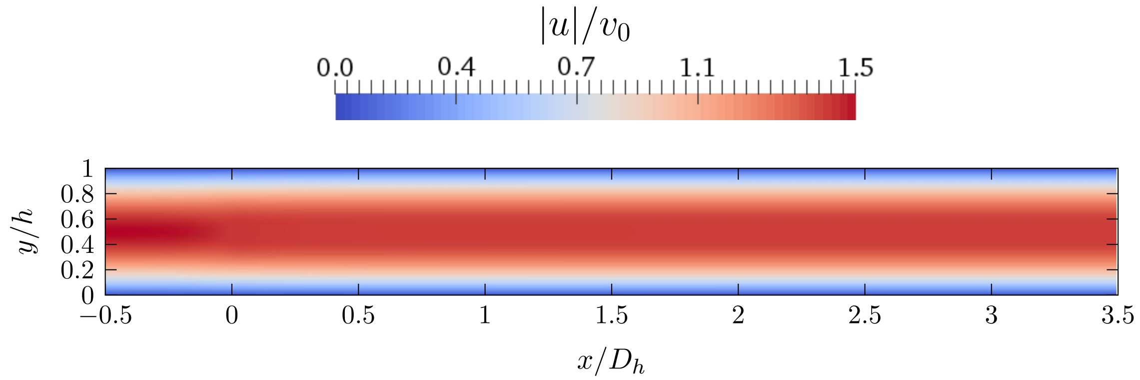

(a) $\mathrm{Re} = 0.1,\ C_{\tau_y} = 40,\ \mathrm{He} = 0.2$

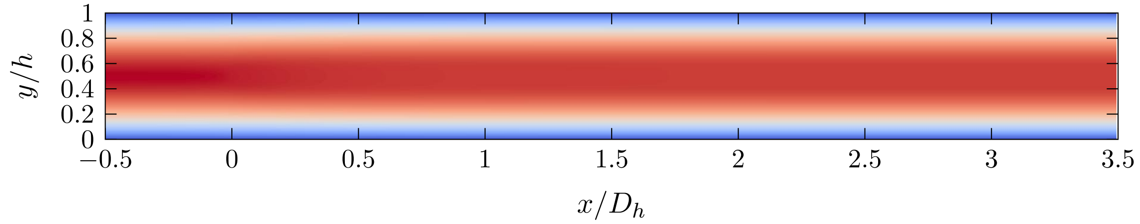

(b) $\mathrm{Re} = 100,\ C_{\tau_y} = 0.04,\ \mathrm{He} = 2 \times 10^2$

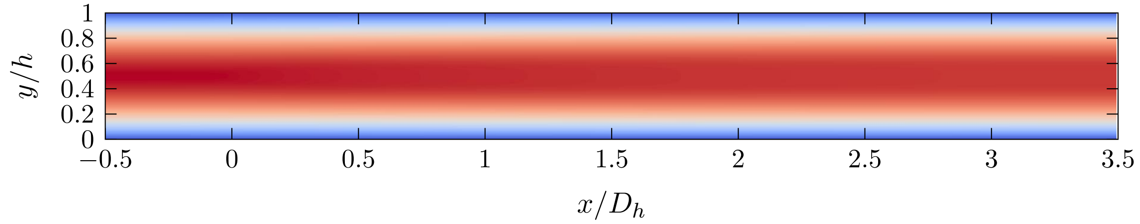

(c) $\mathrm{Re} = 500,\ C_{\tau_y} = 0.008,\ \mathrm{He} = 10^3$

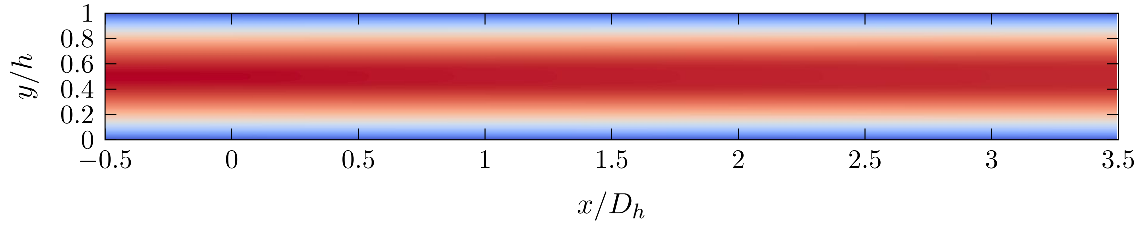

(d) $\mathrm{Re} = 2000,\ C_{\tau_y} = 0.002,\ \mathrm{He} = 4 \times 10^3$

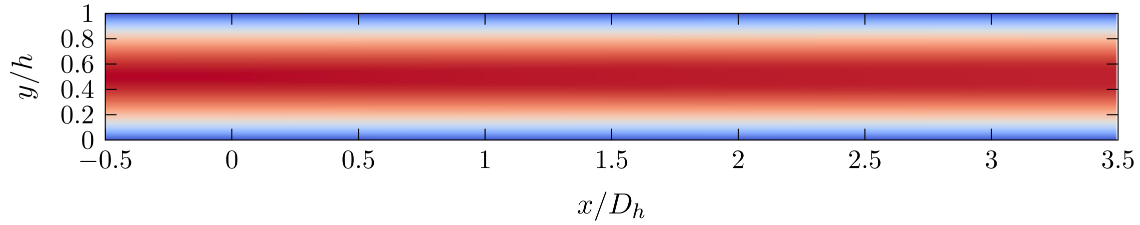

(e) $\mathrm{Re} = 4000,\ C_{\tau_y} = 0.001,\ \mathrm{He} = 8 \times 10^3$

Figure A.1: Normalized velocity at $\mathrm{Bi} = 1$. The active region starts at $x = 0$.

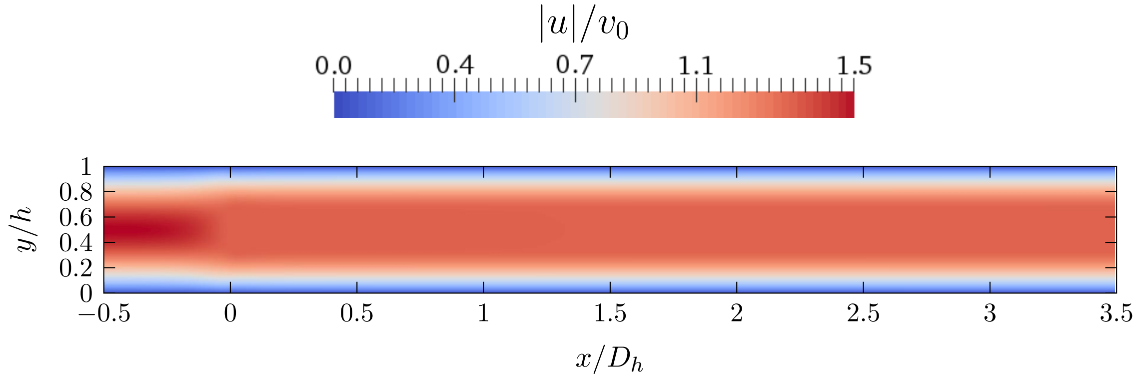

(a) $\mathrm{Re} = 0.1,\ C_{\tau_y} = 120,\ \mathrm{He} = 0.6$

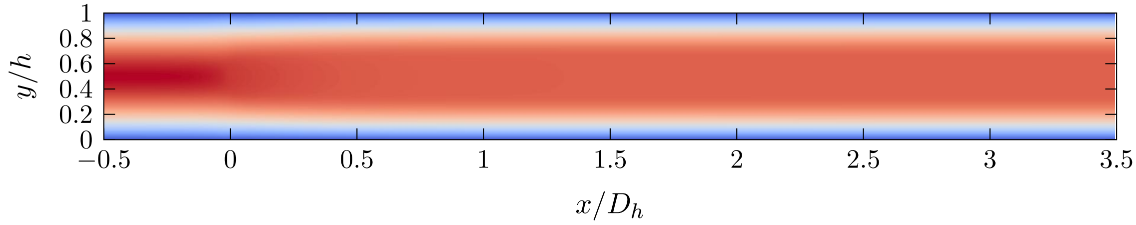

(b) $\mathrm{Re} = 100,\ C_{\tau_y} = 0.12,\ \mathrm{He} = 6 \times 10^2$

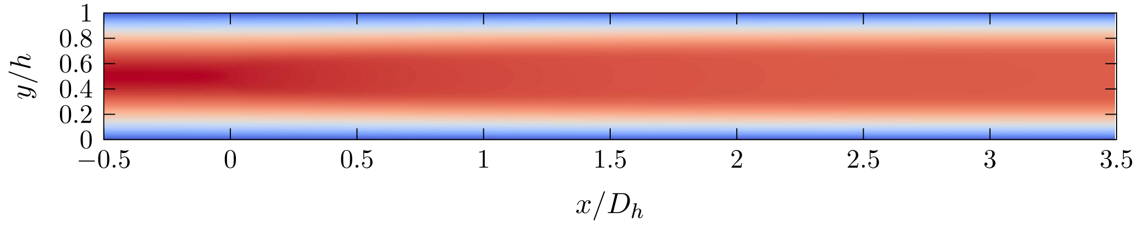

(c) $\mathrm{Re} = 500,\ C_{\tau_y} = 0.024,\ \mathrm{He} = 3 \times 10^3$

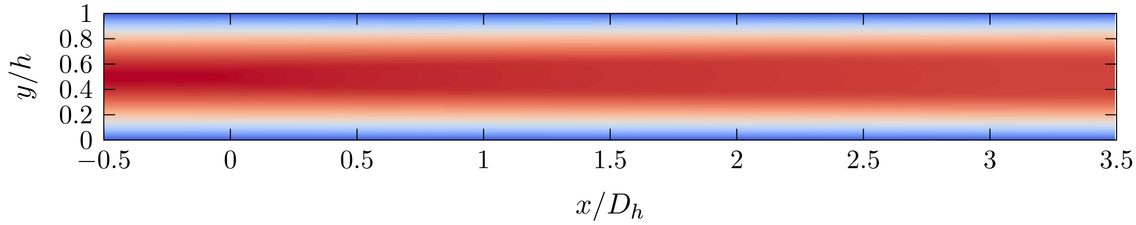

(d) $\mathrm{Re} = 2000,\ C_{\tau_y} = 0.006,\ \mathrm{He} = 1.2 \times 10^4$

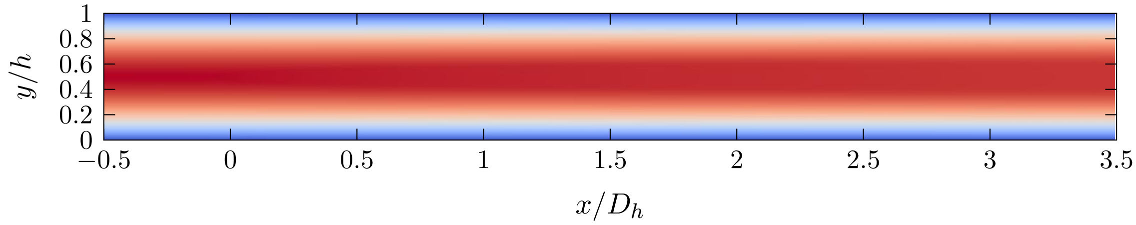

(e) $\mathrm{Re} = 4000,\ C_{\tau_y} = 0.003,\ \mathrm{He} = 2.4 \times 10^4$

Figure A.2: Normalized velocity at $\mathrm{Bi} = 3$. The active region starts at $x = 0$.

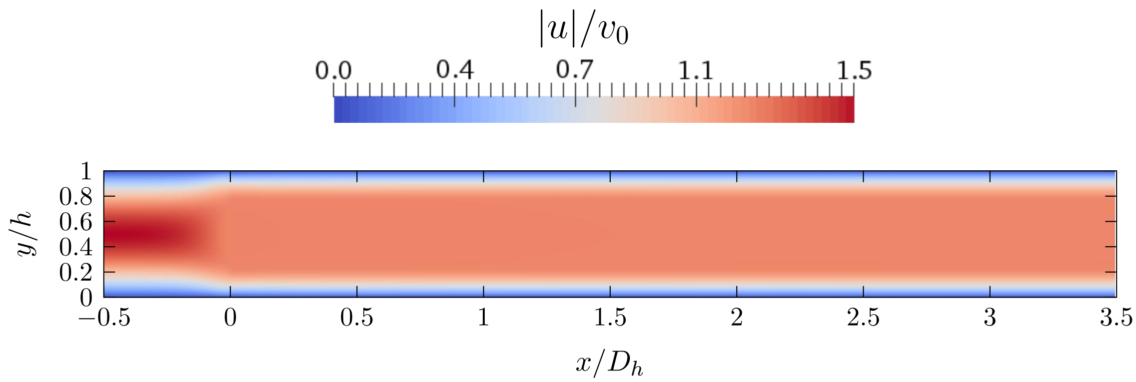

(a) $\mathrm{Re} = 0.1,\ C_{\tau_y} = 400,\ \mathrm{He} = 2$

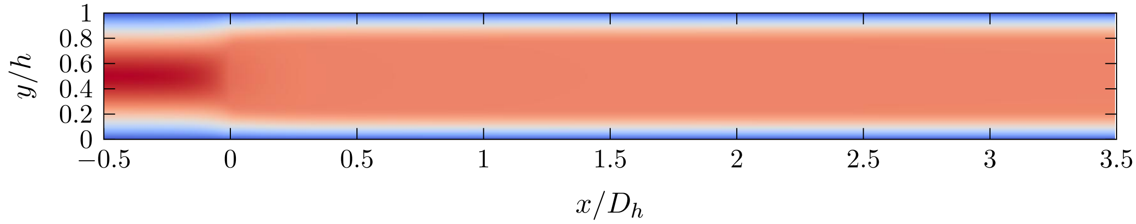

(b) $\mathrm{Re} = 100,\ C_{\tau_y} = 0.4,\ \mathrm{He} = 2 \times 10^3$

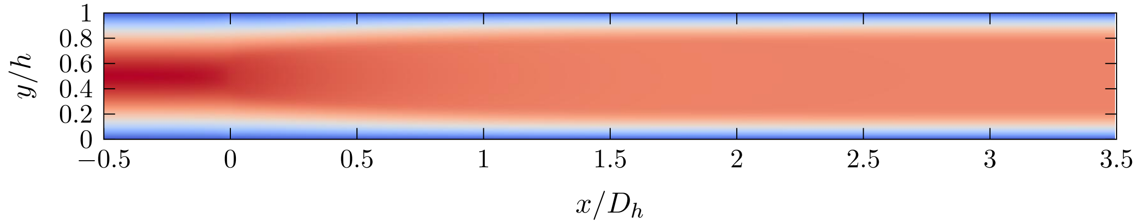

(c) $\mathrm{Re} = 500,\ C_{\tau_y} = 0.08,\ \mathrm{He} = 10^4$

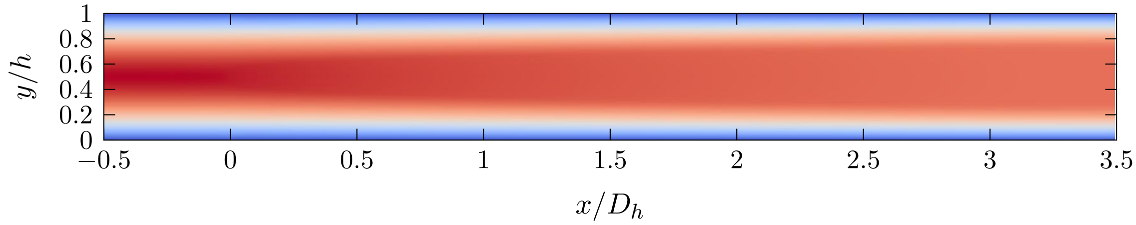

(d) $\mathrm{Re} = 2000,\ C_{\tau_y} = 0.02,\ \mathrm{He} = 4 \times 10^4$

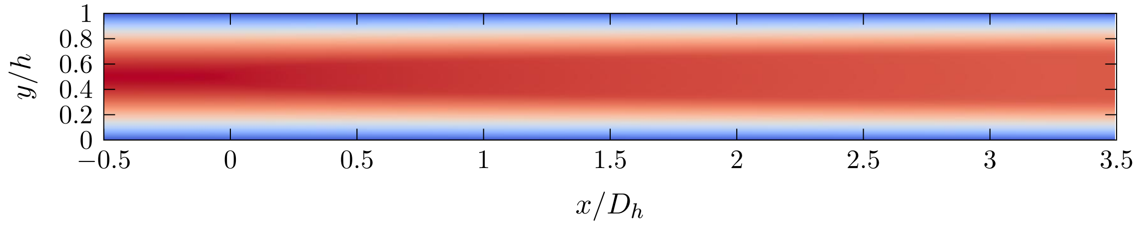

(e) $\mathrm{Re} = 4000,\ C_{\tau_y} = 0.01,\ \mathrm{He} = 8 \times 10^4$

Figure A.3: Normalized velocity at $\mathrm{Bi} = 10$. The active region starts at $x = 0$.

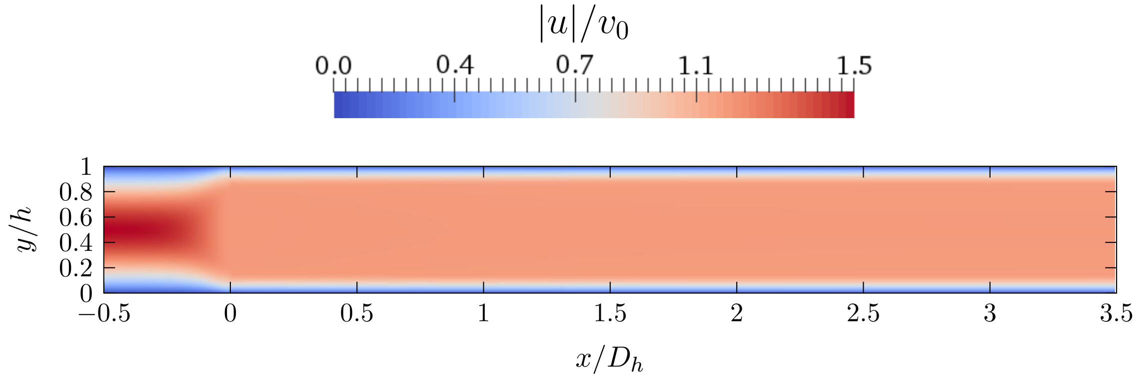

(a) $\mathrm{Re} = 0.1,\ C_{\tau_y} = 1200,\ \mathrm{He} = 6$

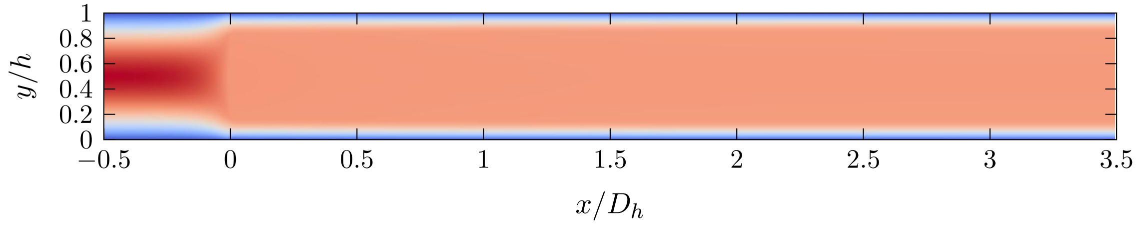

(b) $\mathrm{Re} = 100,\ C_{\tau_y} = 1.2,\ \mathrm{He} = 6 \times 10^3$

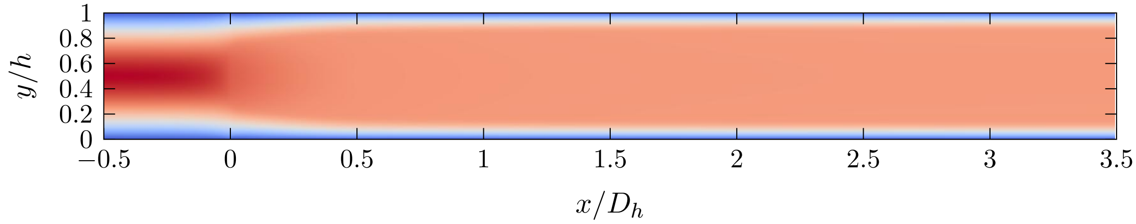

(c) $\mathrm{Re} = 500,\ C_{\tau_y} = 0.24,\ \mathrm{He} = 3 \times 10^4$

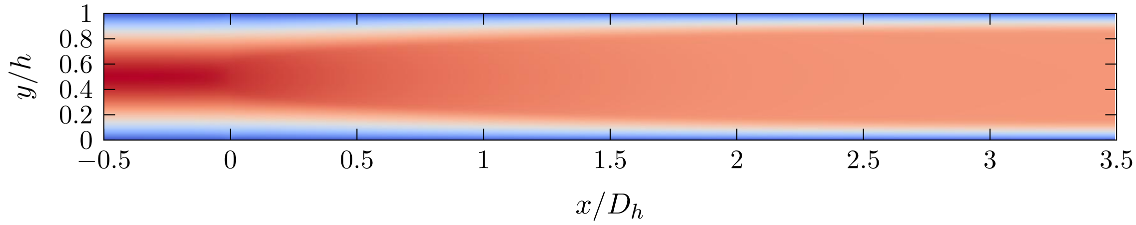

(d) $\mathrm{Re} = 2000,\ C_{\tau_y} = 0.06,\ \mathrm{He} = 1.2 \times 10^5$

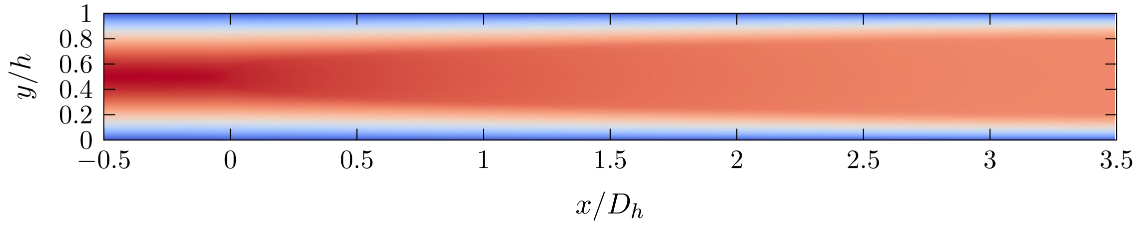

(e) $\mathrm{Re} = 4000,\ C_{\tau_y} = 0.03,\ \mathrm{He} = 2.4 \times 10^5$

Figure A.4: Normalized velocity at $\mathrm{Bi} = 30$. The active region starts at $x = 0$.

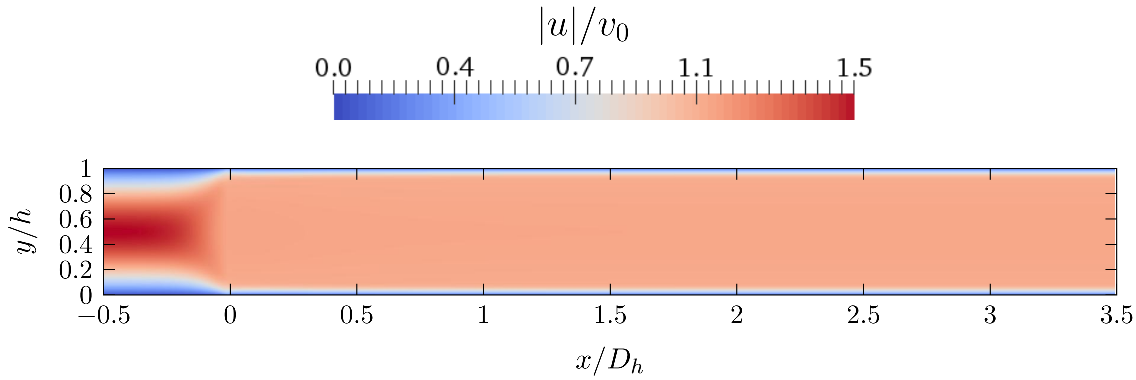

(a) $\mathrm{Re} = 0.1,\ C_{\tau_y} = 4000,\ \mathrm{He} = 20$

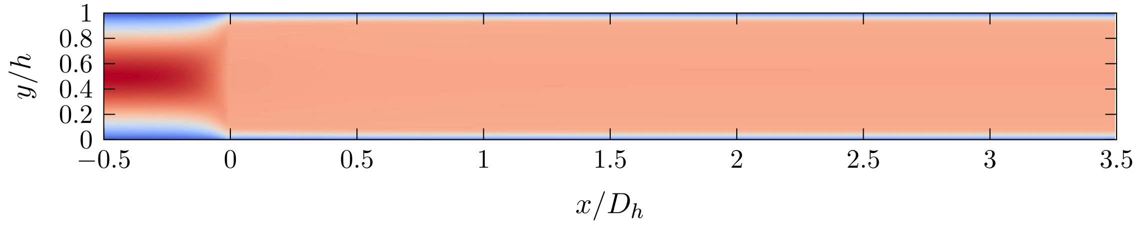

(b) $\mathrm{Re} = 100,\ C_{\tau_y} = 4,\ \mathrm{He} = 2 \times 10^4$

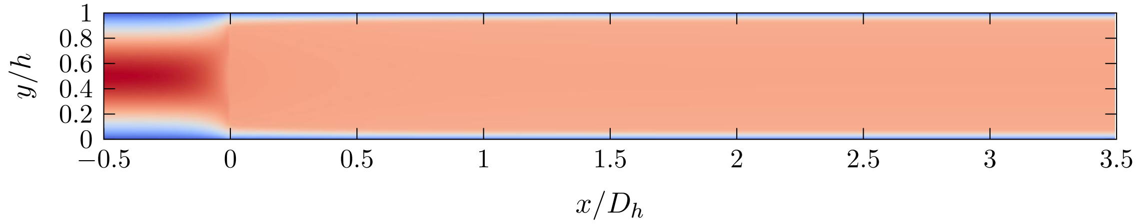

(c) $\mathrm{Re} = 500,\ C_{\tau_y} = 0.8,\ \mathrm{He} = 10^5$

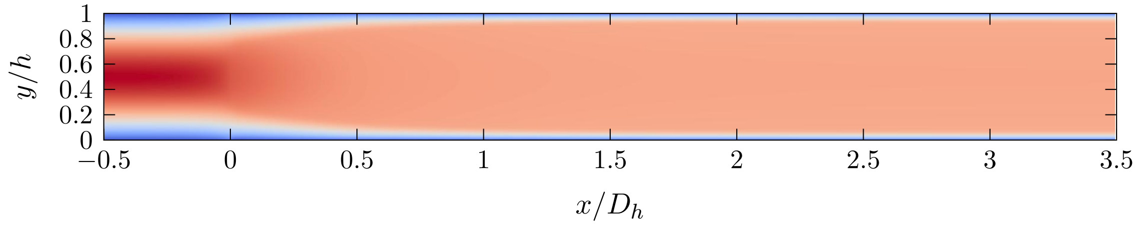

(d) $\mathrm{Re} = 2000,\ C_{\tau_y} = 0.2,\ \mathrm{He} = 4 \times 10^5$

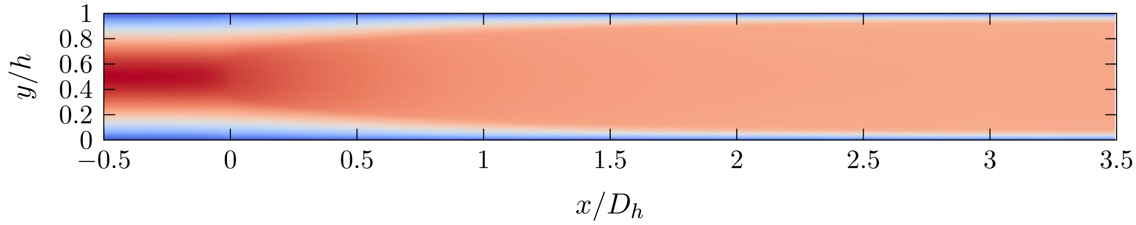

(e) $\mathrm{Re} = 4000,\ C_{\tau_y} = 0.1,\ \mathrm{He} = 8 \times 10^5$

Figure A.5: Normalized velocity at $\mathrm{Bi} = 100$. The active region starts at $x = 0$.

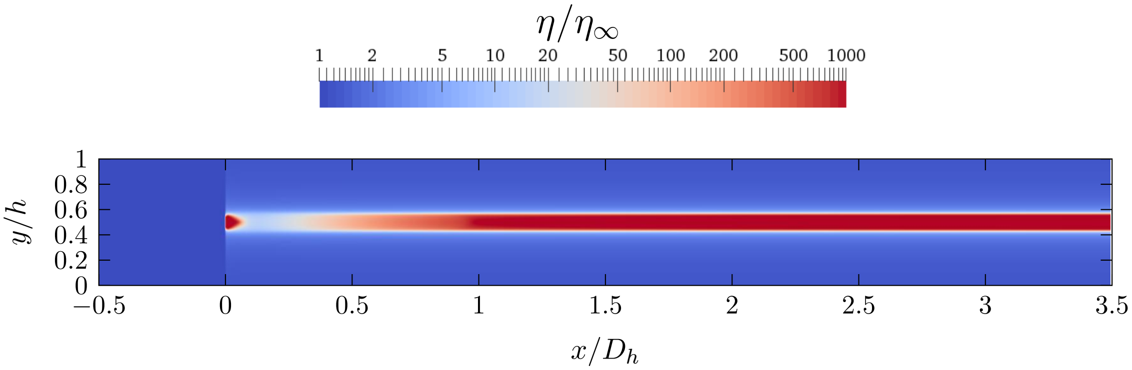

(a) $\mathrm{Re} = 0.1,\ C_{\tau_y} = 40,\ \mathrm{He} = 0.2$

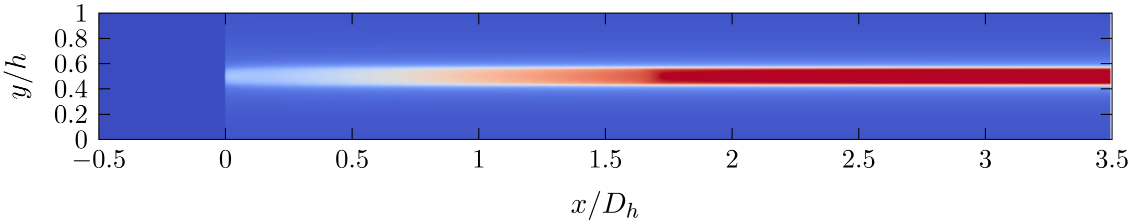

(b) $\mathrm{Re} = 100,\ C_{\tau_y} = 0.04,\ \mathrm{He} = 2 \times 10^2$

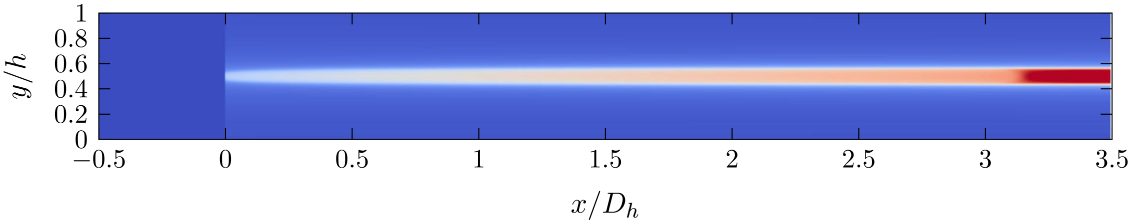

(c) $\mathrm{Re} = 500,\ C_{\tau_y} = 0.008,\ \mathrm{He} = 10^3$

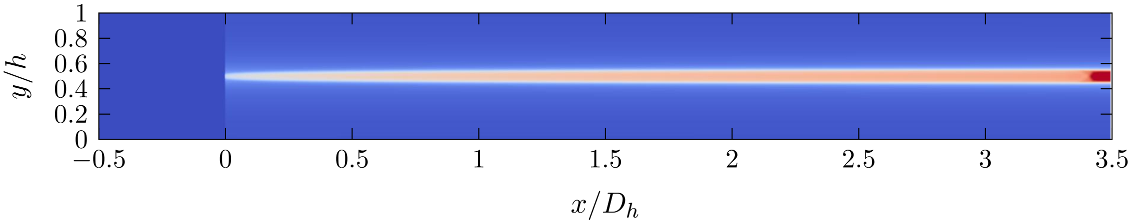

(d) $\mathrm{Re} = 2000,\ C_{\tau_y} = 0.002,\ \mathrm{He} = 4 \times 10^3$

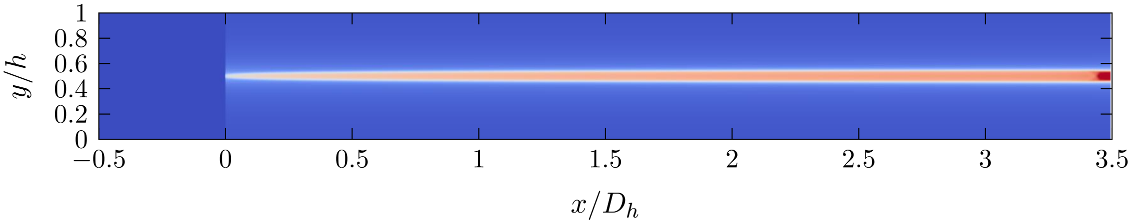

(e) $\mathrm{Re} = 4000,\ C_{\tau_y} = 0.001,\ \mathrm{He} = 8 \times 10^3$

Figure A.6: Normalized viscosity at $\mathrm{Bi} = 1$. The active region starts at $x = 0$.

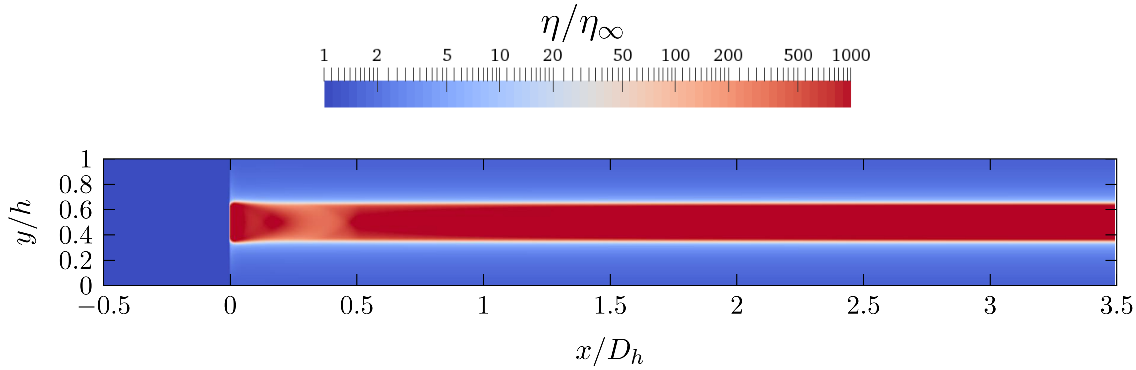

(a) $\mathrm{Re} = 0.1,\ C_{\tau_y} = 120,\ \mathrm{He} = 0.6$

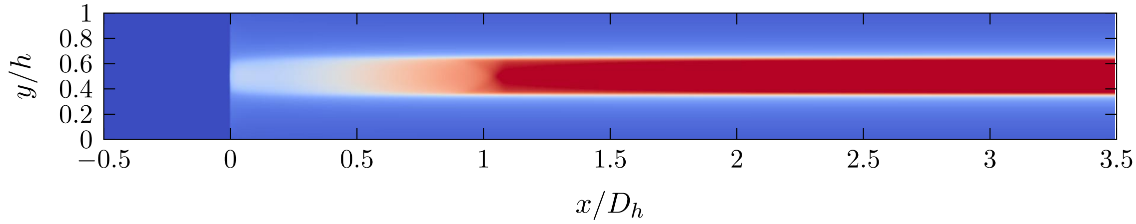

(b) $\mathrm{Re} = 100,\ C_{\tau_y} = 0.12,\ \mathrm{He} = 6 \times 10^2$

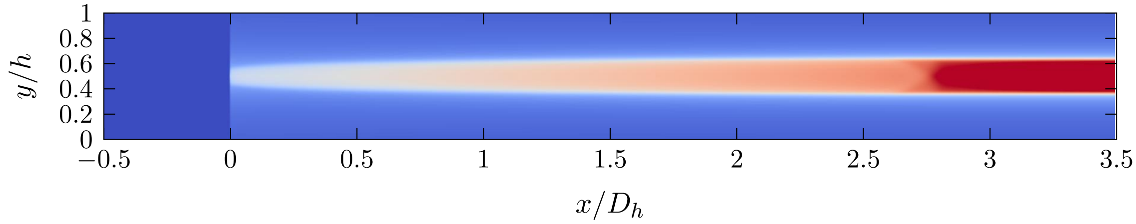

(c) $\mathrm{Re} = 500,\ C_{\tau_y} = 0.024,\ \mathrm{He} = 3 \times 10^3$

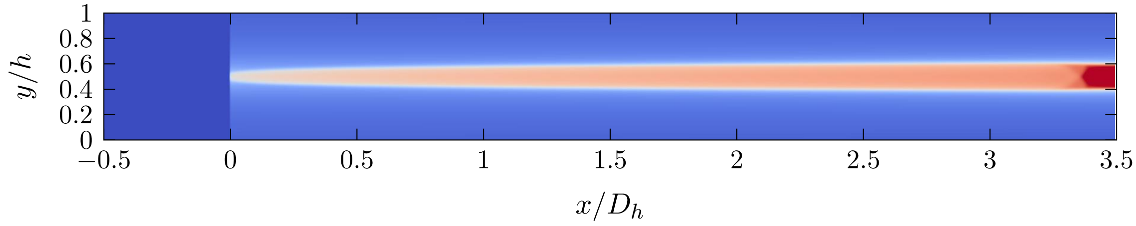

(d) $\mathrm{Re} = 2000,\ C_{\tau_y} = 0.006,\ \mathrm{He} = 1.2 \times 10^4$

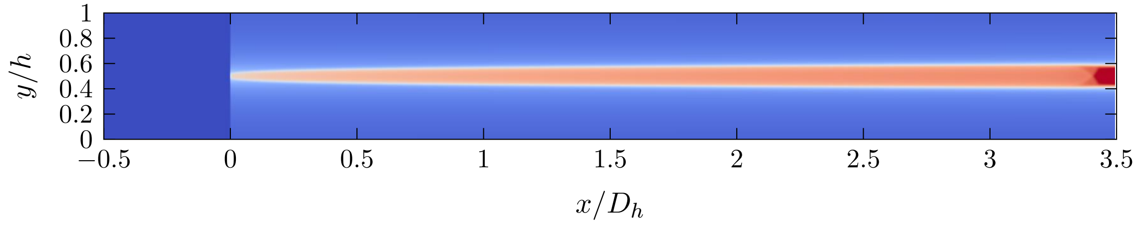

(e) $\mathrm{Re} = 4000,\ C_{\tau_y} = 0.003,\ \mathrm{He} = 2.4 \times 10^4$

Figure A.7: Normalized viscosity at $\mathrm{Bi} = 3$. The active region starts at $x = 0$.

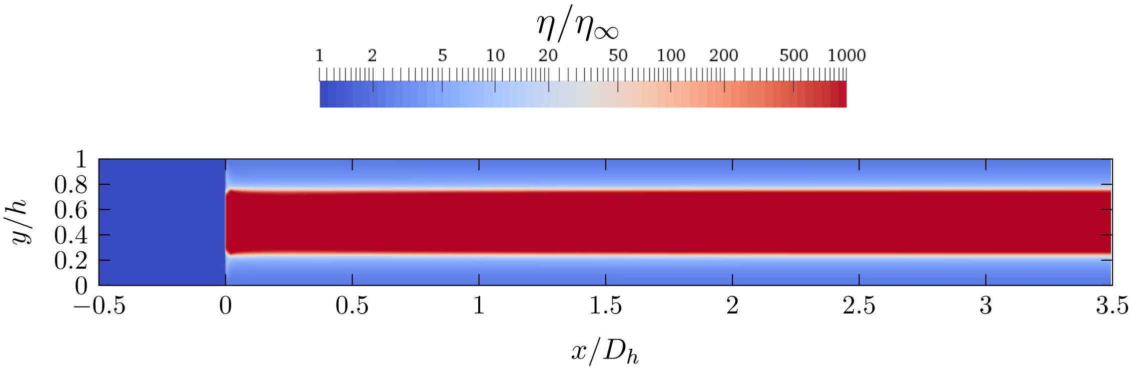

(a) $\mathrm{Re} = 0.1,\ C_{\tau_y} = 400,\ \mathrm{He} = 2$

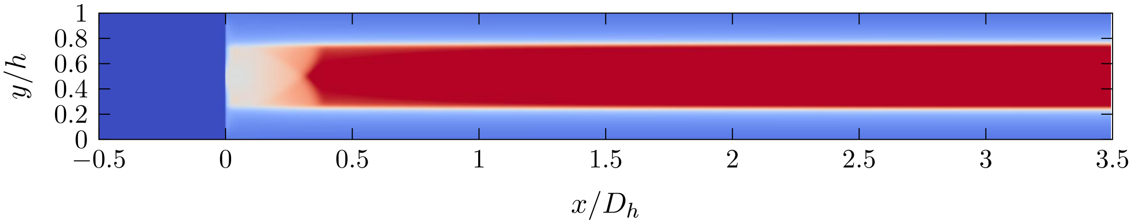

(b) $\mathrm{Re} = 100,\ C_{\tau_y} = 0.4,\ \mathrm{He} = 2 \times 10^3$

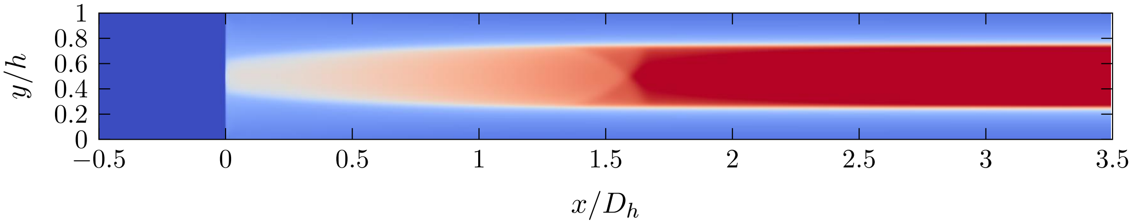

(c) $\mathrm{Re} = 500,\ C_{\tau_y} = 0.08,\ \mathrm{He} = 10^4$

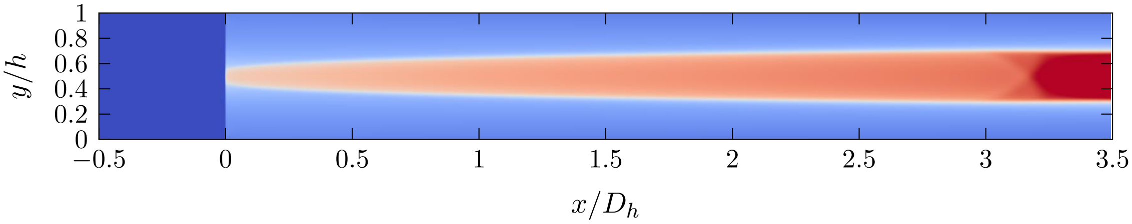

(d) $\mathrm{Re} = 2000,\ C_{\tau_y} = 0.02,\ \mathrm{He} = 4 \times 10^4$

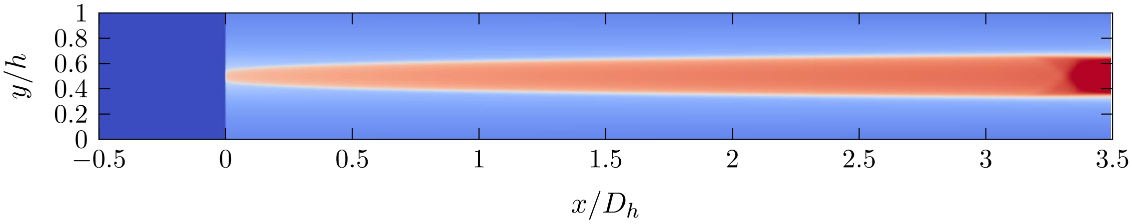

(e) $\mathrm{Re} = 4000,\ C_{\tau_y} = 0.01,\ \mathrm{He} = 8 \times 10^4$

Figure A.8: Normalized viscosity at $\mathrm{Bi} = 10$. The active region starts at $x = 0$.

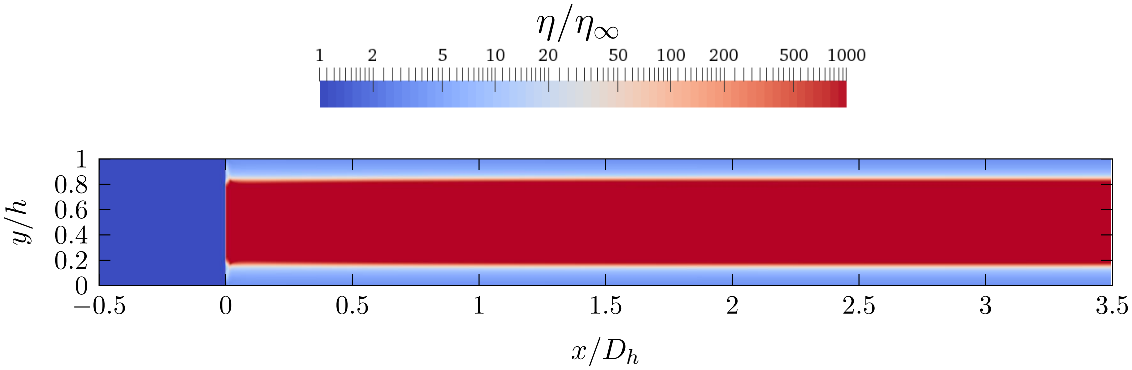

(a) $\mathrm{Re} = 0.1,\ C_{\tau_y} = 1200,\ \mathrm{He} = 6$

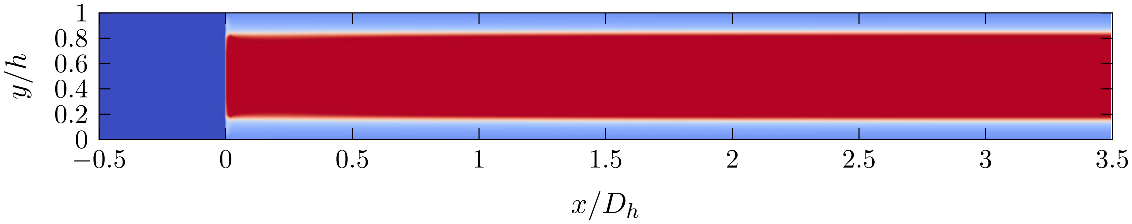

(b) $\mathrm{Re} = 100,\ C_{\tau_y} = 1.2,\ \mathrm{He} = 6 \times 10^3$

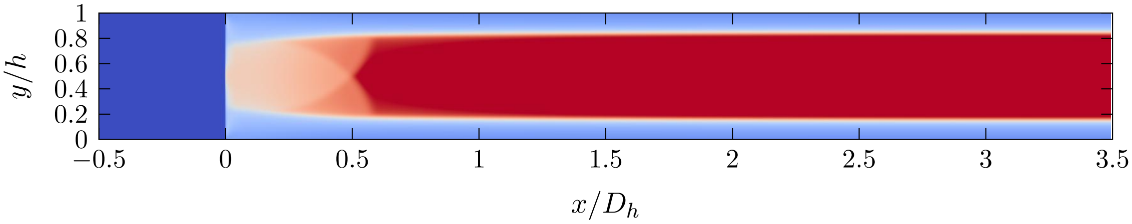

(c) $\mathrm{Re} = 500,\ C_{\tau_y} = 0.24,\ \mathrm{He} = 3 \times 10^4$

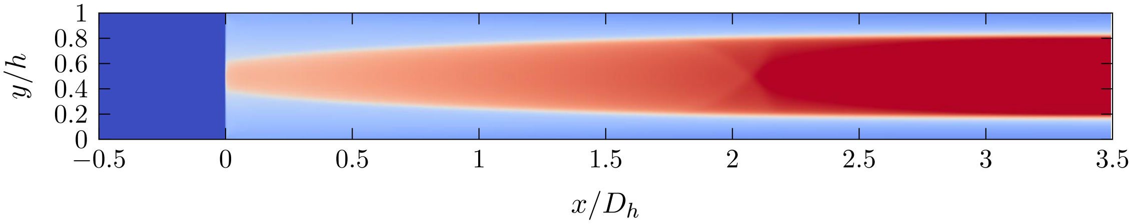

(d) $\mathrm{Re} = 2000,\ C_{\tau_y} = 0.06,\ \mathrm{He} = 1.2 \times 10^5$

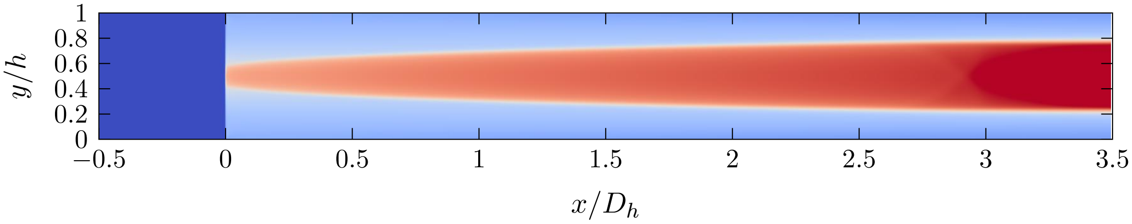

(e) $\mathrm{Re} = 4000,\ C_{\tau_y} = 0.03,\ \mathrm{He} = 2.4 \times 10^5$

Figure A.9: Normalized viscosity at $\mathrm{Bi} = 30$. The active region starts at $x = 0$.

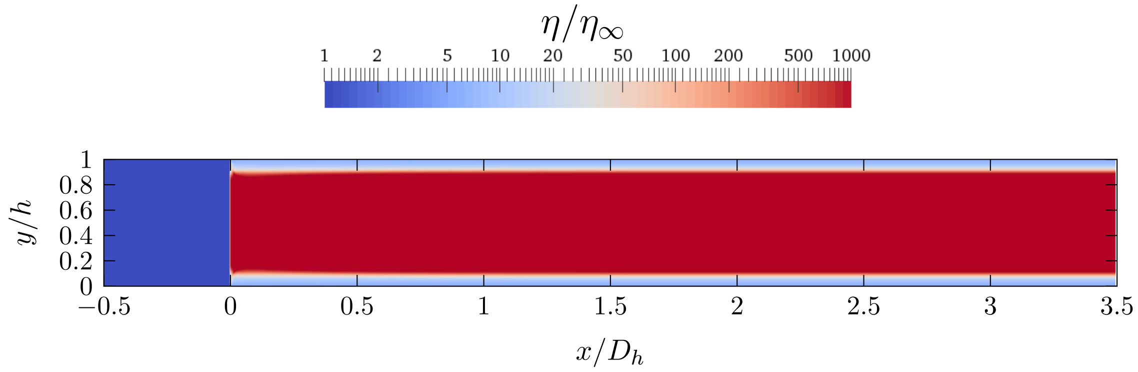

(a) $\mathrm{Re} = 0.1,\ C_{\tau_y} = 4000,\ \mathrm{He} = 20$

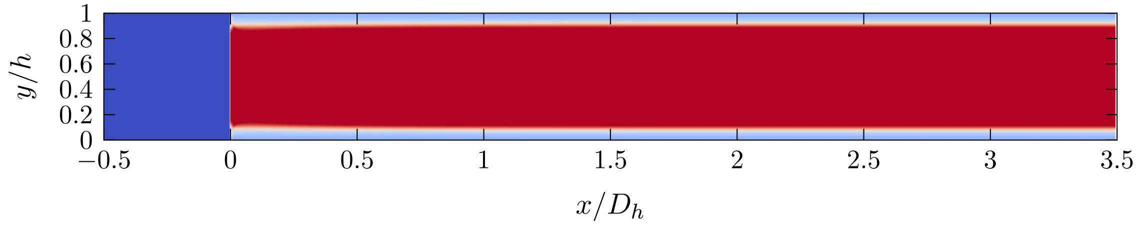

(b) $\mathrm{Re} = 100,\ C_{\tau_y} = 4,\ \mathrm{He} = 2 \times 10^4$

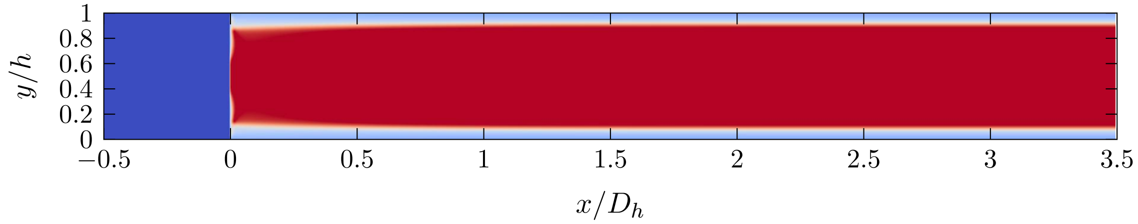

(c) $\mathrm{Re} = 500,\ C_{\tau_y} = 0.8,\ \mathrm{He} = 10^5$

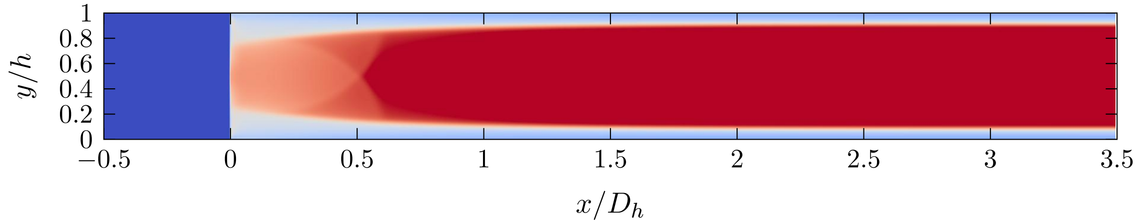

(d) $\mathrm{Re} = 2000,\ C_{\tau_y} = 0.2,\ \mathrm{He} = 4 \times 10^5$

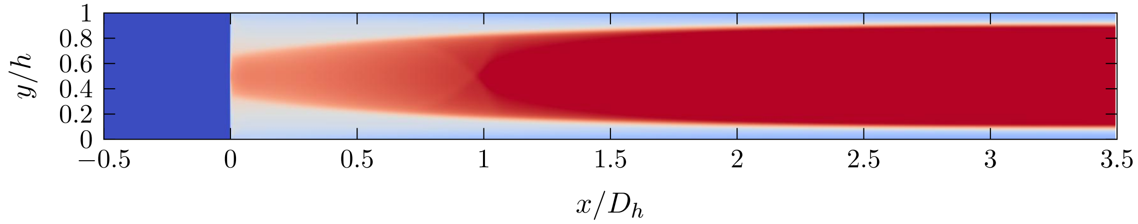

(e) $\mathrm{Re} = 4000,\ C_{\tau_y} = 0.1,\ \mathrm{He} = 8 \times 10^5$

Figure A.10: Normalized viscosity at $\mathrm{Bi} = 100$. The active region starts at $x = 0$.

Appendix B: Correction factors

Table B.1: n_p for $L_A/D_h = 13.97$

		Bi														
		0.1	0.2	0.5	1	2	3	5	7.5	10	15	20	30	50	100	200
	0.1	0.20	0.12	0.11	0.11	0.11	0.09	0.07	0.06	0.06	0.06	0.06	0.06	0.06	0.08	0.10
	1	0.19	0.12	0.11	0.10	0.11	0.09	0.07	0.06	0.06	0.05	0.05	0.06	0.06	0.08	0.10
	10	0.16	0.09	0.08	0.07	0.07	0.07	0.06	0.05	0.05	0.05	0.05	0.05	0.06	0.08	0.10
	100	−0.19	−0.24	−0.24	−0.22	−0.19	−0.16	−0.13	−0.10	−0.08	−0.05	−0.03	0.00	0.03	0.06	0.09
	200	−0.59	−0.61	−0.58	−0.55	−0.47	−0.41	−0.32	−0.26	−0.21	−0.15	−0.11	−0.06	−0.01	0.04	0.08
	500	−1.68	−1.65	−1.58	−1.49	−1.31	−1.16	−0.93	−0.74	−0.62	−0.46	−0.36	−0.25	−0.13	−0.03	0.05
	750	−2.52	−2.48	−2.38	−2.24	−1.98	−1.76	−1.43	−1.15	−0.96	−0.72	−0.57	−0.40	−0.23	−0.08	0.02
	1000	−3.32	−3.26	−3.14	−2.96	−2.63	−2.34	−1.91	−1.55	−1.30	−0.98	−0.78	−0.55	−0.33	−0.13	−0.01
	1250	−4.05	−3.98	−3.85	−3.64	−3.25	−2.91	−2.39	−1.95	−1.64	−1.23	−0.99	−0.71	−0.43	−0.19	−0.04
Re	1500	−4.70	−4.63	−4.49	−4.26	−3.83	−3.45	−2.86	−2.34	−1.97	−1.49	−1.20	−0.86	−0.53	−0.24	−0.07
	1750	−5.27	−5.20	−5.05	−4.82	−4.37	−3.96	−3.31	−2.72	−2.30	−1.75	−1.41	−1.01	−0.64	−0.30	−0.10
	2000	−5.78	−5.70	−5.55	−5.32	−4.86	−4.44	−3.74	−3.10	−2.63	−2.01	−1.62	−1.17	−0.74	−0.35	−0.13
	2200	−6.13	−6.06	−5.91	−5.67	−5.21	−4.79	−4.07	−3.39	−2.89	−2.22	−1.79	−1.29	−0.82	−0.40	−0.15
	2500	−6.60	−6.52	−6.38	−6.15	−5.69	−5.27	−4.53	−3.81	−3.27	−2.52	−2.04	−1.47	−0.94	−0.46	−0.18
	3000	−7.23	−7.15	−7.01	−6.79	−6.37	−5.96	−5.22	−4.47	−3.87	−3.02	−2.46	−1.78	−1.14	−0.58	−0.24
	3500	−7.72	−7.64	−7.50	−7.30	−6.91	−6.52	−5.81	−5.06	−4.43	−3.50	−2.87	−2.09	−1.34	−0.69	−0.30
	4000	−8.10	−8.02	−7.90	−7.71	−7.34	−6.99	−6.32	−5.57	−4.94	−3.97	−3.27	−2.40	−1.54	−0.79	−0.36
	4500	−8.41	−8.34	−8.21	−8.04	−7.70	−7.37	−6.74	−6.03	−5.41	−4.40	−3.66	−2.70	−1.75	−0.90	−0.42
	5000	−8.67	−8.59	−8.48	−8.31	−8.00	−7.69	−7.10	−6.43	−5.82	−4.81	−4.04	−3.00	−1.95	−1.01	−0.48

Table B.2: n_v for $L_A/D_h = 13.97$

		Bi														
		0.1	0.2	0.5	1	2	3	5	7.5	10	15	20	30	50	100	200
Re	0.1	0.20	0.12	0.11	0.11	0.11	0.09	0.07	0.06	0.06	0.06	0.06	0.06	0.06	0.08	0.10
	1	0.20	0.12	0.11	0.10	0.11	0.09	0.07	0.06	0.06	0.06	0.06	0.06	0.06	0.08	0.10
	10	0.18	0.11	0.10	0.09	0.09	0.08	0.07	0.06	0.05	0.05	0.05	0.06	0.06	0.08	0.10
	100	0.02	−0.03	−0.04	−0.03	−0.02	−0.01	0.00	0.01	0.01	0.03	0.03	0.04	0.06	0.08	0.10
	200	−0.16	−0.19	−0.18	−0.17	−0.14	−0.11	−0.07	−0.05	−0.03	−0.01	0.01	0.03	0.05	0.07	0.10
	500	−0.62	−0.61	−0.58	−0.55	−0.47	−0.40	−0.30	−0.22	−0.17	−0.11	−0.07	−0.02	0.02	0.06	0.09
	750	−0.96	−0.94	−0.90	−0.84	−0.73	−0.63	−0.49	−0.37	−0.28	−0.19	−0.13	−0.07	0.00	0.05	0.09
	1000	−1.27	−1.24	−1.19	−1.12	−0.98	−0.86	−0.67	−0.51	−0.40	−0.27	−0.19	−0.11	−0.03	0.04	0.09
	1250	−1.55	−1.51	−1.46	−1.38	−1.22	−1.07	−0.84	−0.65	−0.52	−0.35	−0.26	−0.15	−0.05	0.03	0.08
	1500	−1.80	−1.76	−1.70	−1.62	−1.44	−1.27	−1.01	−0.79	−0.63	−0.43	−0.32	−0.19	−0.08	0.02	0.08
	1750	−2.02	−1.98	−1.92	−1.83	−1.64	−1.46	−1.18	−0.92	−0.74	−0.52	−0.38	−0.24	−0.10	0.01	0.07
	2000	−2.21	−2.17	−2.11	−2.02	−1.83	−1.64	−1.33	−1.05	−0.85	−0.60	−0.45	−0.28	−0.13	0.00	0.07
	2200	−2.35	−2.31	−2.25	−2.16	−1.96	−1.77	−1.45	−1.15	−0.94	−0.67	−0.50	−0.31	−0.15	−0.01	0.06
	2500	−2.53	−2.49	−2.43	−2.34	−2.14	−1.95	−1.62	−1.30	−1.07	−0.76	−0.57	−0.36	−0.18	−0.03	0.06
	3000	−2.77	−2.74	−2.68	−2.59	−2.40	−2.21	−1.86	−1.53	−1.27	−0.92	−0.70	−0.45	−0.23	−0.05	0.05
	3500	−2.97	−2.93	−2.88	−2.79	−2.61	−2.42	−2.08	−1.73	−1.46	−1.07	−0.82	−0.53	−0.28	−0.07	0.04
	4000	−3.12	−3.09	−3.04	−2.96	−2.77	−2.59	−2.26	−1.91	−1.63	−1.22	−0.94	−0.62	−0.33	−0.10	0.03
	4500	−3.25	−3.21	−3.16	−3.09	−2.91	−2.74	−2.41	−2.06	−1.78	−1.35	−1.06	−0.70	−0.38	−0.12	0.02
	5000	−3.35	−3.32	−3.27	−3.20	−3.03	−2.86	−2.54	−2.20	−1.91	−1.48	−1.17	−0.79	−0.43	−0.14	0.01

Table B.3: n_p for $L_A/D_h = 7$

	Bi													
Re	0.1	0.2	0.5	1	2	5	7.5	10	15	20	30	50	100	200
1	0.02	0.02	0.04	0.05	0.06	0.04	0.03	0.03	0.03	0.03	0.03	0.03	0.04	0.05
10	−0.01	−0.01	0.01	0.02	0.03	0.02	0.02	0.02	0.02	0.02	0.03	0.03	0.04	0.05
100	−0.34	−0.32	−0.30	−0.27	−0.23	−0.16	−0.13	−0.10	−0.07	−0.05	−0.03	0.00	0.02	0.04
200	−0.70	−0.67	−0.63	−0.58	−0.51	−0.36	−0.29	−0.24	−0.17	−0.13	−0.09	−0.04	0.00	0.03
500	−1.68	−1.64	−1.57	−1.47	−1.30	−0.94	−0.76	−0.64	−0.48	−0.39	−0.27	−0.16	−0.06	0.00
750	−2.37	−2.32	−2.24	−2.12	−1.89	−1.41	−1.15	−0.97	−0.74	−0.60	−0.42	−0.26	−0.12	−0.03
1000	−2.91	−2.86	−2.77	−2.65	−2.41	−1.84	−1.53	−1.30	−1.00	−0.80	−0.58	−0.36	−0.17	−0.06
1250	−3.32	−3.27	−3.18	−3.06	−2.83	−2.23	−1.88	−1.61	−1.25	−1.01	−0.73	−0.46	−0.23	−0.09
1500	−3.63	−3.58	−3.50	−3.39	−3.16	−2.58	−2.20	−1.90	−1.49	−1.22	−0.88	−0.56	−0.28	−0.12
1750	−3.88	−3.83	−3.75	−3.64	−3.44	−2.88	−2.49	−2.18	−1.73	−1.42	−1.04	−0.67	−0.34	−0.15
2000	−4.07	−4.02	−3.95	−3.85	−3.66	−3.13	−2.75	−2.43	−1.95	−1.62	−1.19	−0.77	−0.39	−0.18
2200	−4.20	−4.15	−4.08	−3.99	−3.81	−3.30	−2.94	−2.62	−2.12	−1.77	−1.31	−0.85	−0.44	−0.20
2500	−4.35	−4.31	−4.24	−4.15	−3.99	−3.53	−3.18	−2.87	−2.37	−1.99	−1.49	−0.97	−0.50	−0.23
3000	−4.56	−4.51	−4.45	−4.37	−4.23	−3.82	−3.51	−3.22	−2.73	−2.33	−1.77	−1.17	−0.61	−0.29
3500	−4.71	−4.66	−4.60	−4.53	−4.40	−4.04	−3.76	−3.50	−3.03	−2.64	−2.05	−1.37	−0.72	−0.35
4000	−4.83	−4.78	−4.72	−4.66	−4.55	−4.22	−3.97	−3.73	−3.29	−2.90	−2.30	−1.56	−0.83	−0.41
4500	−4.93	−4.88	−4.82	−4.77	−4.66	−4.36	−4.13	−3.91	−3.50	−3.14	−2.54	−1.76	−0.94	−0.47
5000	−5.01	−4.96	−4.91	−4.85	−4.76	−4.48	−4.27	−4.07	−3.69	−3.34	−2.75	−1.94	−1.05	−0.52

Table B.4: n_v for $L_A/D_h = 7$

		Bi													
		0.1	0.2	0.5	1	2	5	7.5	10	15	20	30	50	100	200
	1	0.02	0.03	0.04	0.06	0.06	0.04	0.03	0.03	0.03	0.03	0.03	0.03	0.04	0.05
	10	0.01	0.01	0.03	0.04	0.05	0.03	0.03	0.03	0.03	0.03	0.03	0.03	0.04	0.05
	100	−0.13	−0.12	−0.10	−0.08	−0.06	−0.03	−0.02	−0.01	0.00	0.01	0.02	0.03	0.04	0.05
	200	−0.28	−0.26	−0.23	−0.21	−0.17	−0.11	−0.08	−0.06	−0.03	−0.02	0.00	0.02	0.03	0.05
	500	−0.66	−0.63	−0.60	−0.56	−0.48	−0.33	−0.25	−0.20	−0.13	−0.09	−0.05	−0.01	0.02	0.04
	750	−0.92	−0.89	−0.85	−0.80	−0.71	−0.50	−0.39	−0.31	−0.21	−0.16	−0.09	−0.03	0.01	0.04
	1000	−1.12	−1.09	−1.06	−1.01	−0.91	−0.66	−0.52	−0.42	−0.29	−0.22	−0.13	−0.06	0.00	0.04
	1250	−1.28	−1.25	−1.22	−1.17	−1.06	−0.80	−0.64	−0.52	−0.37	−0.28	−0.18	−0.08	−0.01	0.03
	1500	−1.40	−1.38	−1.34	−1.29	−1.19	−0.92	−0.75	−0.62	−0.45	−0.34	−0.22	−0.11	−0.02	0.03
Re	1750	−1.50	−1.47	−1.44	−1.40	−1.30	−1.03	−0.85	−0.71	−0.53	−0.40	−0.26	−0.13	−0.03	0.02
	2000	−1.58	−1.55	−1.52	−1.48	−1.38	−1.12	−0.94	−0.80	−0.60	−0.46	−0.30	−0.16	−0.04	0.02
	2200	−1.63	−1.60	−1.57	−1.53	−1.44	−1.18	−1.00	−0.86	−0.65	−0.51	−0.34	−0.18	−0.05	0.01
	2500	−1.69	−1.67	−1.64	−1.60	−1.51	−1.26	−1.09	−0.94	−0.72	−0.57	−0.39	−0.21	−0.07	0.01
	3000	−1.77	−1.75	−1.72	−1.68	−1.60	−1.36	−1.20	−1.06	−0.84	−0.67	−0.46	−0.26	−0.09	0.00
	3500	−1.83	−1.81	−1.78	−1.75	−1.67	−1.44	−1.28	−1.15	−0.93	−0.76	−0.54	−0.31	−0.11	−0.01
	4000	−1.88	−1.85	−1.83	−1.80	−1.72	−1.50	−1.35	−1.22	−1.00	−0.84	−0.61	−0.35	−0.13	−0.02
	4500	−1.91	−1.89	−1.87	−1.84	−1.76	−1.55	−1.40	−1.28	−1.07	−0.91	−0.67	−0.40	−0.16	−0.03
	5000	−1.95	−1.92	−1.90	−1.87	−1.80	−1.59	−1.45	−1.32	−1.12	−0.96	−0.73	−0.45	−0.18	−0.04

Table B.5: n_p for $L_A/D_h = 3.5$

	Bi															
Re	0.1	0.2	0.5	1	1.5	2	3	5	7.5	10	15	20	30	50	100	200
0.1	−0.02	−0.00	0.02	0.03	0.03	0.03	0.03	0.02	0.02	0.02	0.02	0.02	0.02	0.02	0.02	0.03
1	−0.03	−0.01	0.01	0.03	0.03	0.02	0.02	0.02	0.02	0.02	0.02	0.02	0.02	0.02	0.02	0.03
10	−0.06	−0.04	−0.02	−0.00	−0.00	−0.00	0.00	0.00	0.00	0.01	0.01	0.01	0.01	0.01	0.02	0.02
20	−0.09	−0.07	−0.05	−0.03	−0.03	−0.03	−0.02	−0.02	−0.01	−0.01	−0.00	0.00	0.01	0.01	0.02	0.02
50	−0.20	−0.17	−0.15	−0.13	−0.12	−0.11	−0.10	−0.08	−0.06	−0.05	−0.03	−0.02	−0.01	−0.00	0.01	0.02
100	−0.37	−0.34	−0.31	−0.29	−0.27	−0.25	−0.22	−0.17	−0.14	−0.11	−0.08	−0.06	−0.04	−0.02	0.00	0.01
200	−0.70	−0.67	−0.63	−0.59	−0.55	−0.51	−0.45	−0.37	−0.29	−0.25	−0.18	−0.15	−0.10	−0.06	−0.02	0.00
500	−1.47	−1.43	−1.38	−1.31	−1.24	−1.18	−1.07	−0.90	−0.74	−0.63	−0.49	−0.39	−0.28	−0.18	−0.08	−0.03
750	−1.83	−1.79	−1.74	−1.68	−1.62	−1.56	−1.45	−1.26	−1.07	−0.93	−0.73	−0.59	−0.43	−0.28	−0.14	−0.06
1000	−2.05	−2.01	−1.97	−1.91	−1.86	−1.81	−1.71	−1.53	−1.34	−1.19	−0.95	−0.79	−0.58	−0.38	−0.19	−0.09
1250	−2.19	−2.15	−2.11	−2.07	−2.02	−1.98	−1.89	−1.74	−1.56	−1.40	−1.15	−0.97	−0.73	−0.48	−0.25	−0.11
1500	−2.29	−2.25	−2.22	−2.17	−2.13	−2.10	−2.02	−1.89	−1.73	−1.58	−1.33	−1.13	−0.87	−0.58	−0.30	−0.14
1750	−2.36	−2.33	−2.29	−2.26	−2.22	−2.19	−2.12	−2.00	−1.85	−1.72	−1.48	−1.28	−1.00	−0.67	−0.36	−0.17
2000	−2.42	−2.39	−2.36	−2.32	−2.29	−2.26	−2.20	−2.09	−1.96	−1.84	−1.61	−1.42	−1.12	−0.77	−0.41	−0.20
2200	−2.46	−2.43	−2.40	−2.36	−2.33	−2.31	−2.25	−2.15	−2.03	−1.91	−1.70	−1.51	−1.21	−0.84	−0.46	−0.22
2500	−2.51	−2.48	−2.45	−2.42	−2.39	−2.37	−2.32	−2.22	−2.11	−2.01	−1.81	−1.64	−1.34	−0.95	−0.52	−0.26
3000	−2.58	−2.55	−2.52	−2.49	−2.47	−2.44	−2.40	−2.32	−2.22	−2.13	−1.96	−1.80	−1.52	−1.12	−0.63	−0.32
3500	−2.64	−2.60	−2.57	−2.54	−2.52	−2.50	−2.46	−2.39	−2.31	−2.23	−2.08	−1.93	−1.67	−1.27	−0.74	−0.37
4000	−2.68	−2.65	−2.61	−2.59	−2.57	−2.55	−2.52	−2.45	−2.38	−2.31	−2.17	−2.04	−1.80	−1.41	−0.84	−0.43
4500	−2.72	−2.68	−2.65	−2.63	−2.61	−2.59	−2.56	−2.50	−2.43	−2.37	−2.24	−2.13	−1.90	−1.53	−0.94	−0.49
5000	−2.75	−2.71	−2.68	−2.66	−2.64	−2.63	−2.60	−2.54	−2.48	−2.42	−2.31	−2.20	−1.99	−1.63	−1.04	−0.55

Table B.6: n_v for $L_A/D_h = 3.5$

	Bi															
Re	0.1	0.2	0.5	1	1.5	2	3	5	7.5	10	15	20	30	50	100	200
0.1	−0.02	−0.00	0.02	0.03	0.03	0.03	0.03	0.02	0.02	0.02	0.02	0.02	0.02	0.02	0.02	0.03
1	−0.02	−0.00	0.02	0.03	0.03	0.03	0.02	0.02	0.02	0.02	0.02	0.02	0.02	0.02	0.02	0.03
10	−0.04	−0.02	0.00	0.02	0.02	0.02	0.02	0.02	0.01	0.01	0.02	0.02	0.02	0.02	0.02	0.03
20	−0.05	−0.03	−0.01	0.00	0.01	0.01	0.01	0.01	0.01	0.01	0.01	0.01	0.01	0.02	0.02	0.02
50	−0.09	−0.07	−0.05	−0.04	−0.03	−0.03	−0.02	−0.01	−0.01	−0.00	0.00	0.01	0.01	0.01	0.02	0.02
100	−0.16	−0.14	−0.12	−0.10	−0.09	−0.08	−0.07	−0.05	−0.04	−0.02	−0.01	−0.00	0.00	0.01	0.02	0.02
200	−0.29	−0.26	−0.24	−0.22	−0.20	−0.19	−0.16	−0.12	−0.09	−0.07	−0.04	−0.03	−0.01	0.00	0.01	0.02
500	−0.58	−0.55	−0.53	−0.50	−0.47	−0.44	−0.40	−0.32	−0.25	−0.20	−0.14	−0.10	−0.06	−0.02	0.00	0.02
750	−0.72	−0.69	−0.67	−0.64	−0.62	−0.59	−0.54	−0.45	−0.36	−0.30	−0.22	−0.16	−0.10	−0.05	−0.01	0.02
1000	−0.80	−0.78	−0.76	−0.73	−0.71	−0.68	−0.64	−0.55	−0.46	−0.39	−0.29	−0.22	−0.14	−0.07	−0.02	0.01
1250	−0.86	−0.84	−0.82	−0.79	−0.77	−0.75	−0.70	−0.62	−0.53	−0.46	−0.35	−0.28	−0.18	−0.10	−0.03	0.01
1500	−0.90	−0.88	−0.86	−0.84	−0.82	−0.79	−0.75	−0.67	−0.59	−0.52	−0.40	−0.32	−0.22	−0.12	−0.04	0.00
1750	−0.93	−0.91	−0.89	−0.87	−0.85	−0.83	−0.79	−0.71	−0.63	−0.56	−0.45	−0.37	−0.26	−0.15	−0.05	−0.00
2000	−0.95	−0.93	−0.91	−0.89	−0.88	−0.86	−0.82	−0.74	−0.67	−0.60	−0.49	−0.41	−0.29	−0.17	−0.06	−0.01
2200	−0.96	−0.95	−0.93	−0.91	−0.89	−0.87	−0.84	−0.76	−0.69	−0.62	−0.52	−0.43	−0.32	−0.19	−0.07	−0.01
2500	−0.98	−0.97	−0.95	−0.93	−0.91	−0.89	−0.86	−0.79	−0.72	−0.65	−0.55	−0.47	−0.35	−0.21	−0.09	−0.02
3000	−1.01	−0.99	−0.97	−0.96	−0.94	−0.92	−0.89	−0.82	−0.75	−0.69	−0.59	−0.51	−0.40	−0.25	−0.11	−0.03
3500	−1.02	−1.01	−0.99	−0.98	−0.96	−0.94	−0.91	−0.84	−0.78	−0.72	−0.62	−0.55	−0.43	−0.29	−0.13	−0.04
4000	−1.04	−1.02	−1.01	−0.99	−0.97	−0.96	−0.92	−0.86	−0.80	−0.74	−0.65	−0.58	−0.46	−0.32	−0.15	−0.05
4500	−1.05	−1.03	−1.02	−1.00	−0.99	−0.97	−0.94	−0.88	−0.81	−0.76	−0.67	−0.60	−0.49	−0.35	−0.17	−0.06
5000	−1.06	−1.04	−1.03	−1.01	−1.00	−0.98	−0.95	−0.89	−0.82	−0.77	−0.68	−0.61	−0.51	−0.37	−0.19	−0.07

Table B.7: n_p for $L_A/D_h = 2$

	Bi												
Re	0.1	0.2	0.5	1	2	5	7.5	10	15	20	50	100	200
1	−0.05	−0.02	−0.01	−0.00	0.00	0.01	0.01	0.01	0.01	0.01	0.01	0.01	0.01
10	−0.08	−0.05	−0.04	−0.03	−0.02	−0.01	−0.01	−0.00	0.00	0.00	0.01	0.01	0.01
100	−0.37	−0.35	−0.32	−0.29	−0.25	−0.18	−0.14	−0.12	−0.09	−0.07	−0.03	−0.01	0.00
200	−0.67	−0.63	−0.60	−0.55	−0.49	−0.36	−0.29	−0.25	−0.19	−0.15	−0.06	−0.03	−0.01
500	−1.13	−1.10	−1.06	−1.02	−0.96	−0.78	−0.67	−0.59	−0.46	−0.38	−0.18	−0.09	−0.04
750	−1.28	−1.25	−1.22	−1.19	−1.14	−1.00	−0.90	−0.81	−0.66	−0.56	−0.28	−0.14	−0.07
1000	−1.36	−1.34	−1.31	−1.29	−1.24	−1.13	−1.04	−0.96	−0.82	−0.71	−0.37	−0.20	−0.10
1250	−1.42	−1.39	−1.37	−1.35	−1.31	−1.21	−1.14	−1.07	−0.95	−0.84	−0.47	−0.25	−0.12
1500	−1.46	−1.43	−1.41	−1.39	−1.36	−1.28	−1.21	−1.15	−1.04	−0.94	−0.55	−0.31	−0.15
1750	−1.49	−1.47	−1.44	−1.43	−1.40	−1.32	−1.27	−1.21	−1.11	−1.02	−0.63	−0.36	−0.18
2000	−1.52	−1.49	−1.47	−1.45	−1.43	−1.36	−1.31	−1.26	−1.17	−1.09	−0.71	−0.41	−0.21
2200	−1.54	−1.51	−1.49	−1.47	−1.45	−1.39	−1.34	−1.29	−1.21	−1.13	−0.76	−0.45	−0.23
2500	−1.56	−1.53	−1.51	−1.50	−1.47	−1.42	−1.37	−1.33	−1.26	−1.19	−0.84	−0.51	−0.27
3000	−1.60	−1.57	−1.54	−1.53	−1.51	−1.46	−1.42	−1.39	−1.32	−1.26	−0.94	−0.61	−0.33
3500	−1.62	−1.59	−1.57	−1.55	−1.54	−1.49	−1.46	−1.43	−1.37	−1.32	−1.03	−0.70	−0.38
4000	−1.64	−1.61	−1.59	−1.57	−1.56	−1.52	−1.49	−1.46	−1.41	−1.36	−1.10	−0.77	−0.44
4500	−1.66	−1.63	−1.61	−1.59	−1.58	−1.54	−1.51	−1.49	−1.44	−1.40	−1.16	−0.84	−0.50
5000	−1.68	−1.65	−1.62	−1.61	−1.59	−1.56	−1.53	−1.51	−1.47	−1.43	−1.21	−0.91	−0.55

Table B.8: n_v for $L_A/D_h = 2$

	Bi												
Re	0.1	0.2	0.5	1	2	5	7.5	10	15	20	50	100	200
1	−0.05	−0.02	−0.01	−0.00	0.00	0.01	0.01	0.01	0.01	0.01	0.01	0.01	0.01
10	−0.06	−0.03	−0.02	−0.01	−0.01	0.00	0.00	0.01	0.01	0.01	0.01	0.01	0.01
100	−0.17	−0.14	−0.13	−0.11	−0.10	−0.06	−0.04	−0.03	−0.02	−0.01	0.00	0.01	0.01
200	−0.28	−0.25	−0.23	−0.21	−0.18	−0.13	−0.10	−0.08	−0.05	−0.03	−0.00	0.01	0.01
500	−0.45	−0.43	−0.41	−0.39	−0.36	−0.28	−0.23	−0.19	−0.14	−0.10	−0.03	−0.00	0.01
750	−0.51	−0.49	−0.48	−0.46	−0.43	−0.36	−0.30	−0.26	−0.20	−0.16	−0.05	−0.01	0.00
1000	−0.54	−0.53	−0.51	−0.50	−0.47	−0.40	−0.35	−0.31	−0.25	−0.20	−0.08	−0.03	0.00
1250	−0.56	−0.55	−0.53	−0.52	−0.50	−0.43	−0.39	−0.35	−0.29	−0.24	−0.10	−0.04	−0.00
1500	−0.58	−0.56	−0.55	−0.54	−0.51	−0.45	−0.41	−0.37	−0.31	−0.27	−0.12	−0.05	−0.01
1750	−0.59	−0.57	−0.56	−0.55	−0.53	−0.47	−0.43	−0.39	−0.33	−0.29	−0.14	−0.06	−0.01
2000	−0.60	−0.58	−0.57	−0.56	−0.54	−0.48	−0.44	−0.41	−0.35	−0.31	−0.16	−0.07	−0.02
2200	−0.60	−0.59	−0.58	−0.56	−0.54	−0.49	−0.45	−0.42	−0.36	−0.32	−0.17	−0.08	−0.02
2500	−0.61	−0.59	−0.58	−0.57	−0.55	−0.50	−0.46	−0.43	−0.37	−0.33	−0.19	−0.09	−0.03
3000	−0.62	−0.60	−0.59	−0.58	−0.56	−0.51	−0.47	−0.44	−0.39	−0.35	−0.21	−0.11	−0.04
3500	−0.63	−0.61	−0.60	−0.59	−0.57	−0.52	−0.48	−0.45	−0.40	−0.36	−0.23	−0.12	−0.05
4000	−0.63	−0.62	−0.61	−0.60	−0.58	−0.53	−0.49	−0.46	−0.41	−0.37	−0.24	−0.14	−0.06
4500	−0.64	−0.62	−0.61	−0.60	−0.58	−0.53	−0.50	−0.47	−0.42	−0.38	−0.25	−0.15	−0.07
5000	−0.64	−0.62	−0.61	−0.60	−0.59	−0.54	−0.50	−0.47	−0.42	−0.39	−0.26	−0.16	−0.07

Appendix C: Temperature dependence of MR fluids

This is a reproduction of "Scaling temperature dependent rheology of magnetorheological fluids" by Stephen G Sherman, Louise A Powell, Andrew C Becnel and Norman M Wereley, published in Journal of Applied Physics [40].

C.1 Introduction

Magnetorheological (MR) fluids are suspensions of magnetic particles in oil, that upon the application of magnetic field, develop a field controllable yield stress, giving a suspension with a controllable apparent viscosity. This controllable viscosity enables a damper or other energy absorbing device to produce a rapidly controllable force output. These devices, due to their energy absorbing nature, operate over a wide range of temperatures (e.g. -40 to 150 °C), ideally with minimal change in performance with respect to temperature. However, in practice, MR devices see a significant reduction in force output with increase in temperature. Wilson *et al.* [124] characterized the temperature dependent performance of a flow mode damper using Lord MRF132DG fluid and finds substantial variation in device performance in the temperature range of 0 - 100 °C, with yield stress varying by up to 30% and post yield damping varying by up to 80%. Gordaninejad and Breese [125] tested a series of MR dampers, and observed a reduction in peak force of up to 50% over a temperature range of 20 - 70 °C. This dramatic drop-off in force is typically attributed to a reduction in yield stress and viscosity due to an increase in temperature.

Rheometer experiments by Weiss and Duclos [126] reported a 10% reduction in yield stress and 95% reduction in viscosity over the range of -40 to 150 °C, which in damper tests corresponded to a predicted 16% force loss vs. 18% measured. Later, Weiss *et al.* [127] patented a series of MR fluids with relatively independent temperature properties through the identification of carrier fluids that exhibit minimal temperature changes, an approach which we validate. Sahin *et al.* [128] characterized the yield stress of a custom grease-based MR fluid and shows that the temperature dependence can be expressed through an exponential relationship, and that the temperature change in viscosity is independent of shear rate. Finally, Lemaire *et al.* [129] examined the effects of Brownian motion by varying particle size and found that even when Brownian forces are relatively small, such forces can still affect the yield stress.

In this study, we investigate the effects of temperature on MR fluid off-state viscosity, as viscosity and its device-scale cousin, post yield damping, undergo the largest relative temperature changes. First, we analyze the field free state using the three fundamental forces acting on the particles (Brownian, shear, and magnetic) , through the relative role that they play in affecting fluid properties, using three non-dimensional numbers: the Mason number, Mn, the Peclet number, Pe and the ratio of magnetic to thermal energy, λ. Then, we validate our analysis through rheometer measurements on a simple fluid designed to conform to the assumptions present in the analysis, followed by measuring the temperature effects on a commercially available fluid. We also investigate the effects of remanent magnetization on fluid performance, whereas typical off-state experiments use previously unmagnetized fluid.

C.2 Background

MR fluids are typically modeled as Bingham plastics,

$$\tau = \tau_y + \eta_p \dot{\gamma}, \tag{C.1}$$

where under shear they resist movement up until a field dependent yield stress τ_y, after which they flow with a field independent viscosity η_p. When no field is applied, τ_y is small and apparent viscosity $\eta = \tau/\dot{\gamma} = \eta_p$ for large shear rates. Apparent viscosity of the MR fluid suspension can be broken down into three elements,

$$\eta = \eta_M + \eta_B + \eta_H \tag{C.2}$$

η_M is the component of viscosity from interparticle (magnetic) forces, η_B is the component of viscosity caused by Brownian motion, and η_H is the component of viscosity from the hydrodynamic drag of the particles.

The first factor affecting viscosity is the magnetic interactions of the particles. Typically, with no applied magnetic field, η_M is assumed to be negligible. However, even at zero field, remanent magnetization in the particles will cause the particles to cluster, potentially inducing a residual yield stress or increase in viscosity, giving some nonzero value to η_M. Since the particles for MR fluids are chosen to have minimal hysteretic effects, the magnetic interactions in the particles are extremely weak, so particle cluster formation will be opposed by Brownian motion. This can be characterized through the ratio of magnetic energy to thermal energy [39], known as the λ parameter, and is defined as

$$\lambda = \frac{\pi a^3 \mu_0 M^2}{18 k_B T}. \tag{C.3}$$

Typically λ is defined using H instead of M, but in this case using M is sensible as $H = 0$. This magnetic-thermal ratio characterizes the ability of the particle magnetic forces to overcome diffusive Brownian motion, and can be used to characterize temperature effects on particle structure. Typically, Brownian effects on the magnetic interactions are assumed to be negligible for $\lambda \gg 0$, however, from experiments on adjacent particle chains, values of $\lambda > 100$ can increase particle aggregation [130] through long-ranged fluctuations. From experiments on MR fluid particle size, effects on field-on stress attributed to Brownian motion have been reported up to $\lambda = 2000$ [129]. For typical field-on cases, with low representative values of $M = 100\,\mathrm{kA/m}$, T=400 K, and $a = 1\,\mu\mathrm{m}$, $\lambda > 10^6$, indicating that temperature, through Brownian motion, plays no role in the behavior of the particles. However, in the field-off case, where the $M_{rem} \approx 5\,\mathrm{kA/m}$, $\lambda \approx 10^3$, thermal effects are strong enough to disrupt particle structure. It is then possible that temperature could affect η_M, and thus overall suspension viscosity.

The magnitude of the contribution of η_m makes to the overall viscosity can be expressed by the Mason number,

$$\mathrm{Mn} = 144\frac{\eta_c\dot{\gamma}}{\mu_0 M^2}, \tag{C.4}$$

the ratio of hydrodynamic forces to magnetic forces. Using $\eta_c = 0.01\,\mathrm{Pa\,s}$ and $\dot{\gamma} = 100\,\mathrm{s}^{-1}$, $\mathrm{Mn} > 1$, indicatesthat hydrodynamic forces will be larger than the magnetic forces. Thus, it is reasonable to expect that η_M will be relatively small, so the expected temperature effects from the λ analysis should have minimal impact on the overall viscosity.

The relative contribution to fluid stress by Brownian motion, η_B, is characterized by the Peclet number [131],

$$\mathrm{Pe} = \frac{6\pi\eta_c\dot{\gamma}a^3}{k_B T}, \tag{C.5}$$

the ratio of advection by the flow to the rate of diffusion by Brownian motion. In this definition, $\mathrm{Pe} = 3/4\mathrm{Mn}\,\lambda$. From the theory of hard sphere suspensions, Brownian effects on viscosity are known to be negligible for $\mathrm{Pe} > 10^2$. Using the previous values for typical fluids, $\mathrm{Pe} > 10^3$ indicates that most MR fluids will see no contribution to viscosity from Brownian motion.

Finally, there is the hydrodynamic contribution to viscosity from the addition of the particles. In non-Brownian hard sphere theory, for a random suspension of spheres, the only parameter affecting viscosity is volume fraction, yielding predictions of the form $\eta = \eta_c f(\phi)$, typically given in the form of relative viscosity $\eta_r = \eta/\eta_c = f(\phi)$.

Relative viscosity can be described for these suspensions through the semi-empirical Quemada equation [131],

$$\eta_r = \left(1 - \frac{\phi}{\phi_{max}}\right)^{-2}. \tag{C.6}$$

Since temperature will have a negligible effect on volume fraction, relative viscosity will remain unchanged with temperature, and since the magnetic and Brownian components are also so small, relative viscosity of an MR fluid will remain fixed. Thus, we hypothesize that viscosity-temperature effects in an MR fluid are caused only by the changes in the viscosity of the carrier fluid. However, hard sphere theories operate under the assumption of a Newtonian carrier fluid, whereas practical MR fluids introduce additives or use carriers with non-Newtonian behavior to reduce particle settling[128], so extending these theories to practical fluids must be done with care.

In order to model temperature effects of the fluid, we choose the simple, well known Reynolds equation [132],

$$\eta(T) = \eta_{\text{ref}} \exp\left[-k\left(T - T_{\text{ref}}\right)\right]. \tag{C.7}$$

Then if we characterize the viscosity of multiple MR fluids and their carrier fluid, across a range of temperatures, and they all share a common value of k, then our hypothesis that carrier fluid effects are the only source of post yield viscosity changes will be confirmed.

C.3 Experiments

In order to characterize the temperature effects of viscosity in MR fluids and to demonstrate common scaling, we measure the off state viscosity of two MR fluids and their carrier fluid to show that all the fluids have the same scaling coefficient. Off-state viscosity was measured on an Anton Paar MCR300 rheometer, with an MRD180 measuring cell using parallel plate geometry with a 0.5mm gap and 150 µL samples. Temperature was controlled using a Julabo F25 refrigerating/heating circulator, with the sample left to rest for 3 minutes to achieve thermal equilibrium. To ensure uniformity, samples were mixed using a high shear mixer for 30 minutes before each test. Each test measured shear stress at shear rates from 10-1000 s^{-1} in an ascending log profile.

C.3.1 Simple MR Fluids

Two samples of simple MR fluid were prepared such that they closely matched non-Brownian particle theory (containing no stabilizers or additives) in order to avoid non-Newtonian behavior of the carrier fluid and to prevent any stabilizers from forming a coating of unknown thickness. To be representative of typical commercial fluids, we chose BASF CM grade spherical carbonyl iron powder ($> 99.5\%$ Fe, $a = 3.5 - 4.75\,\mu\text{m}$, $\rho = 7.78$ g/cm^3), having the standard large spherical particles and high saturation magnetism. The carrier fluid was Exxon Mobil SHF-41 polyalphaolephin hydrocarbon oil ($\rho = 0.82\,\text{g/cm}^3$). Two 15ml samples were mixed by weight, at 20 and 30 vol% (70.3 and 80.3 wt%), known as PlainFE20 and PlainFE30

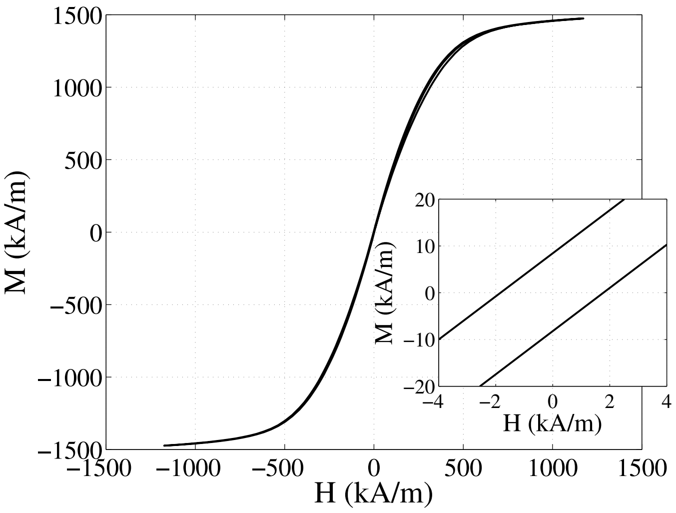

Figure C.1: Particle magnetization in the PlainFE30 fluid as a function of applied field.

respectively. Remanent particle magnetization was obtained through measurements of PlainFE30 fluid on a LakeShore 7400 series VSM. The results were scaled to individual particle magnetization, shown in Fig. C.1, yielding a measured remanence of $M = 8.4$ kA/m. Thus, at 300K, the measured value of η_c and $\dot{\gamma} = 100\ \mathrm{s}^{-1}$, $\mathrm{Pe} = 4.1 \times 10^5$, $\lambda = 2.4 \times 10^5$ and $\mathrm{Mn} = 2.2$. Therefore, the particles are expected to have minimal thermal effects on viscosity of the fluid for these model fluids.

Then, unmagnetized samples of the simple MR fluids and their carrier fluid were measured on the rheometer at temperatures from 5 to 55 °C, corresponding to the minimum chiller temperature and maximum rheometer temperature, in steps of 10 °C, with each fluid measured at least three times at each temperature. For each measurement, the flow curve was fit to (F.5) using the high shear rate values, $\dot{\gamma} > 150\,\mathrm{s}^{-1}$, with viscosities plotted against temperature in Fig. C.2. Then to confirm our hypothesis of common temperature scaling, we fit (C.7) to viscosity vs. temperature for PlainFE30, PlainFE20, and the carrier fluid SHF41, with the fit

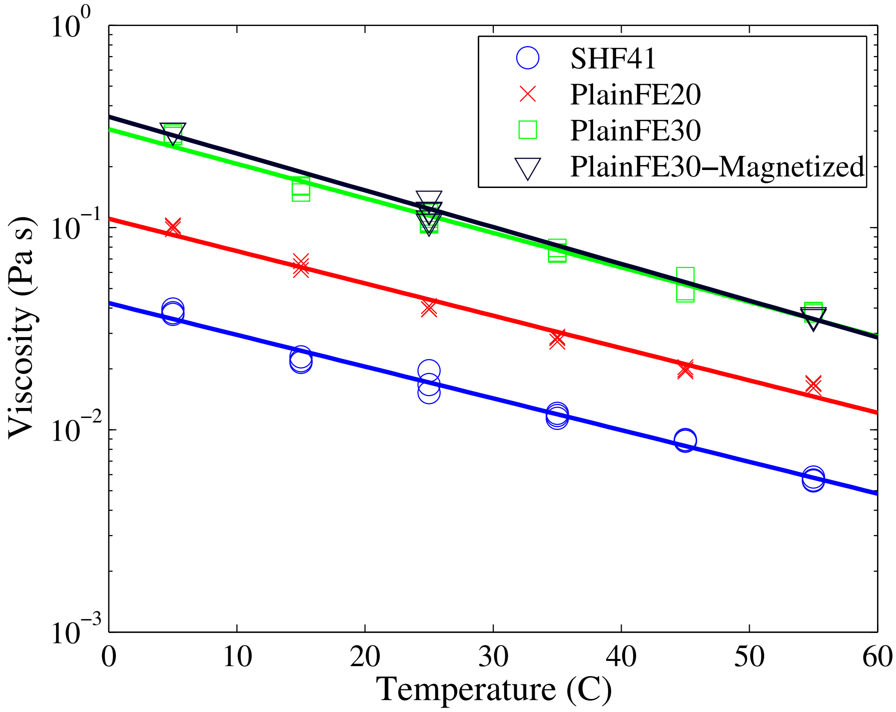

Figure C.2: Viscosity vs. temperature for the simple fluids, including the magnetized sample.

Table C.1: Custom Fluid Properties

Fluid Name	$\eta_{T=30C}$ (mPa s)	k	η_r
SHF41	14.3	0.0361	1
PlainFE20	36.6	0.0368	2.57
PlainFE30	94.1	0.0392	6.60
Magnetized FE30	100.5	0.0418	7.03

shown in Fig. C.2. A table of coefficients listed in Table C.1 shows that all three fluids have a value of k within 5% of the mean, which confirms our hypothesis that all the fluids scale similarly. We can also validate our results through the Quemada equation, which for a plausible value $\phi_{max} = 0.50$, gives results close to the values in Table C.1.

To examine the effects of magnetic hysteresis, two sets of measurements were conducted at T=25 °C. In the first, samples were magnetized by a 1 T neodymium

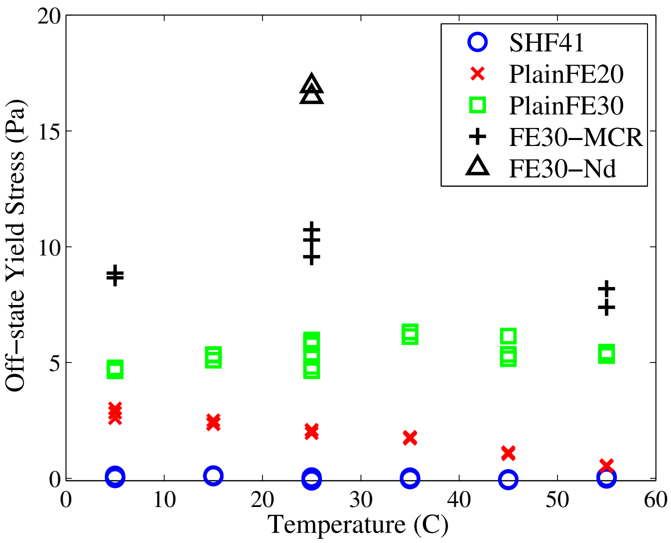

Figure C.3: Offstate yield stress for the simple fluids. FE30-MCR corresponds to samples magnetized by the rheometer and FE30-Nd for samples magnetized by a neodymium magnet.

magnet and then measured on the rheometer as before. In the second, the samples were placed in the rheometer with field applied at a nominal $B = 0.35\,\mathrm{T}$. Then the flux return of the rheometer was demagnetized with alternating fields with a period of two seconds, with the intention that the particles should reorient before they demagnetize significantly. When tested at room temperature, both methods produced viscosities indistinguishable from the unmagnetized samples, as shown in Fig. C.2. However, when looking at the off-state 'yield stress' from the high shear rate fit, shown in Fig. C.3, the magnetized samples clearly have a higher yield stress, with the more strongly magnetized sample having a higher yield stress, as expected. We also note that uniquely, the PlainFE20 sample shows a decrease in τ_y with temperature. However, the measured yield stresses are extremely small and can be effectively ignored for $\dot{\gamma} > 10\,\mathrm{s}^{-1}$.

C.3.2 Commercial MR Fluids

The previous fluids were designed to work with non-Brownian suspension theory, but practical MR fluids are synthesized using carrier fluids with multiple fluid additives, surfactants, and stabilizers, which can make the carrier fluid non-Newtonian, violating the assumptions of theory. To investigate temperature scaling in practical fluids, we tested commercially available MR fluids sold by Lord Corporation, which use a proprietary hydrocarbon oil and additive mixture, and large particles $a = 3 - 5\,\mu\text{m}$. To measure the rheology of the carrier fluid, the particles in a sample of fluid were allowed to settle, and the clear supernatant layer was decanted, allowing measurement of its viscosity in a rheometer. However, this procedure does not guarantee that the extracted fluid will be precisely representative of the carrier fluid, as the additives may not uniformly separate, introducing a possible source of error. Using the same experimental procedure as before, three commercially available fluids, Lord MRF132DG, LordMRF126CD and LordMRF122EG, and the carrier fluid from MRF132 and MRF126 are characterized. Particle remanent magnetization for MRF132 was found to be 5 kA/m. Assuming common composition for these fluids, $\mathrm{Pe} = 2.0 \times 10^5,\ \mathrm{Mn} = 3.2$, and $\lambda = 8.5 \times 10^4$, indicates that there should be no particle contribution to viscosity. Fig. C.4, and Table C.2 show that all three MR fluids scale nearlys identically, having values of k within 4% of the mean. However, the carrier fluids do not scale with a similar exponent, which we attribute to fluid additives that did not separate. This argument is bolstered by the fact that the relative viscosities in Table C.2 are much larger than those predicted by Eq. F.19,

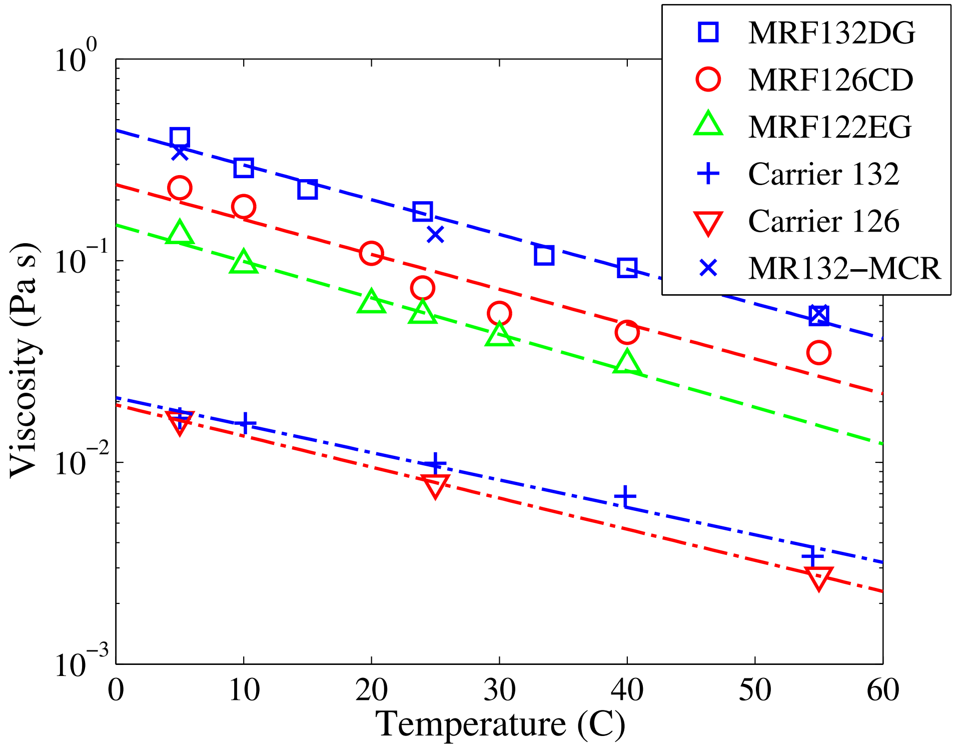

Figure C.4: Viscosity for temperature for a series of commercially available fluids and their extracted carrier fluid.

Table C.2: Lord Fluid Properties

Fluid Name	$\eta_{T=30C}$ (mPa s)	k	η_r
MRF132DG	135.0	0.0396	16.5
MRF126CD	72.2	0.0398	10.9
MRF122EG	43.1	0.0416	-
132C	8.2	0.0313	1
126C	6.6	0.0355	1

indicating the particle hydrodynamics are not the ones expected by hard sphere theory. Similarly, measurements of magnetized Lord fluids found, as previously mentioned, a minimal change of viscosity due to remanent magnetization.

C.4 Conclusion

Magnetorheological (MR) fluid viscosity is known to vary by over an order of magnitude throughout temperature operating range of MR fluids. In this paper, we perform a thorough analysis of the effect, and attribute it solely to changes in the viscosity of the carrier fluid. This means that if the carrier fluid viscosity-temperature relation is known, then the same relative change in viscosity will be present in an MR fluid made with that carrier liquid, an approach that has been used in patented temperature-stable MR fluids [127]. Theoretically, this claim is validated through a nondimensional analysis, finding that even in in the offstate, for typical MR fluids, $\mathrm{Pe} \gg 1, \lambda \gg 1$ and $\mathrm{Mn} > 1$, indicating that the magnetic and Brownian contributions to fluid viscosity will be zero. In order to obtain these numbers, the magnetic remanence of the particles in the fluid was measured, and this result was confirmed by performing measurements of viscosity before and after cycling the field, with no resulting change in viscosity. The effects of magnetic hysteresis on fluid properties were investigated, and we found a negligible increase in yield stress and no change in viscosity. Finally, we experimentally validated this claim by performing measurements of viscosity across temperature for a pair of custom MR fluids and corresponding carrier liquid, and we found that all of these fluids had an indistinguishable change in viscosity, a result we also found in measurements of related commercially available MR fluids. This development of a common scaling law allows for the temperature dependence of MR fluids to be characterized in fewer experiments, or possibly using only known carrier fluid properties.

Appendix D: Sheet formation at large scales

This work [19] originally appeared as "Parallel Simulation of Transient Magnetorheological Direct Shear Flows Using Millions of Particles" by Stephen G. Sherman, Derek A. Paley and Norman M. Wereley, published in IEEE Transactions on Magnetics .

D.1 Introduction

Magnetorheological (MR) fluids and electrorheological fluids are non-Newtonian fluids consisting of polarized particles suspended in a carrier fluid. Upon the application of magnetic/electric field, the particles form chains, causing the fluid to develop a field-dependent stress. The adjustable nature of these fluids makes them useful in a variety of applications, such as dampers and clutches, so developing an understanding of the particle structure dynamics is essential to understanding the behavior of these fluids.

The static equilibrium structure for ER/MR fluids is a thick column, but under shear these fluids develop into a lamellar sheet structure. These sheets have significant transient effects on the fluid [133], and their effects are not always agreed upon [134]. Similarly, the formation of these sheets has shown to be a complex

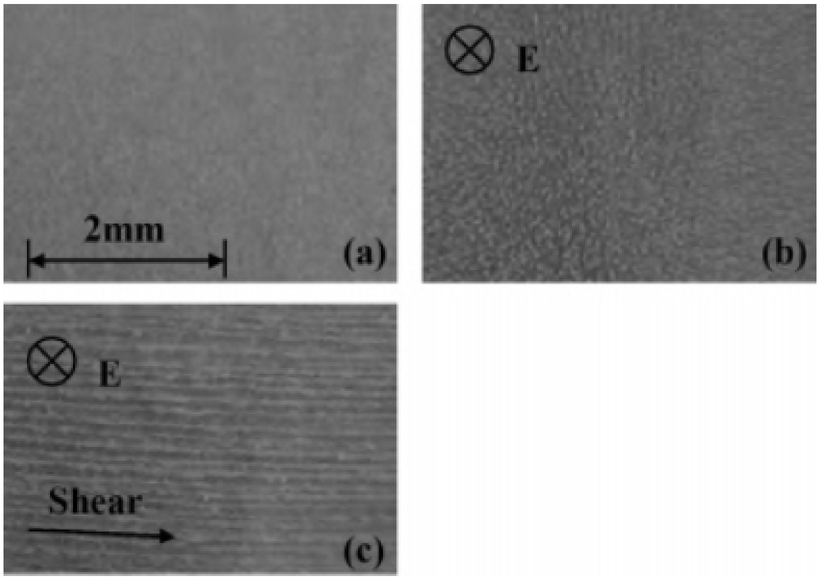

Figure D.1: Structural pattern of ER fluid under 3 conditions: (a) no electric field or shear, showing a random distribution of particles, (b) electric field is applied, causing chain formation and (c) with both electric field and shear flow, showing lamellar sheet formation.

function of time, shear rate, and field strength [135]. Figure D.1 reproduces a diagram from Cao *et al.* [136], showing the formation of chains and sheets in a $SrCO_3$-based ER fluid.

The primary method for gaining insight on the particle dynamics of these fluids is through simulations. However, boundary conditions are known to have significant effects on the particle behavior and rheological properties of the fluid, both experimentally [48] and numerically [137]. Therefore the simulation gap height could have a substantial effect on the results. MR fluid devices have gap heights on the order of 1 mm, which for a typical fluid would require simulating over 1 000 000 particles. Unfortunately, existing simulations [26] use at maximum 10 000 particles. In order to simulate at this scale, we use Nvidia's CUDA environment to run code on a commercial graphics card, allowing us to reach these length scales and simulate over one million particles [138].

We use our code to investigate the lamellar sheet formation at length scales on the order of 1 mm. At these large volume scales, direct visualization of sheet formation becomes difficult, so several nondimensional metrics are used to measure both chain and sheet formation independent of length scale. We then characterize the effects of simulation scale, shear rate, and magnetic field strength on lamellar sheet formation.

D.2 Model

We model the behavior of a magnetorheological fluid by simulating the trajectories of the particles in the fluid. Our model follows the work done by Klingenberg, [28], [34]. In these simulations, the particles are treated as induced point dipoles, with magnetization M, and the particle boundaries are represented by an exponential repulsion force. Since the carrier fluid is a viscous oil, particle accelerations can be neglected, simplifying the simulation to a kinematic model, offering a dramatic speedup. Brownian motion is also neglected without loss of generality. The fluid is treated as a continuum under uniform shear, and particle disturbances on the flow are neglected. Other simulation methods include finite element models and two-fluid models [139].

The simulations take place in the cubic volume shown in Fig D.2, with the external field $\mathbf{H}_0$ applied in the y direction. Fluid is sheared in the positive x direction. Lamellar sheet formation is expected to occur in the z direction. We

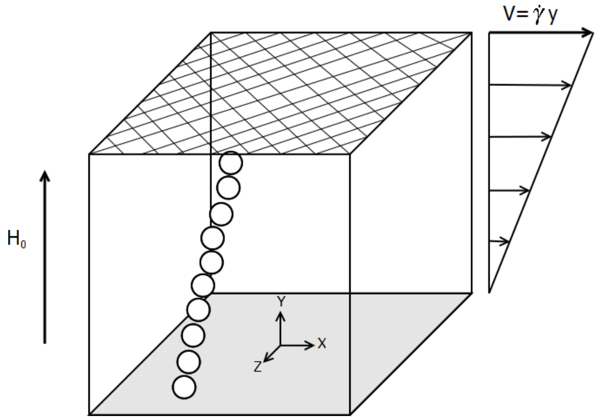

Figure D.2: Schematic of simulation volume.

enforce a no slip condition, which is required to generate a rheological response [137], at the upper and lower walls, pinning the particles to the surface of the wall. Periodic boundary conditions are used in the x and z directions.

In order to simulate at volume scales approaching 1mm, we use Nvidia's CUDA programming environment. CUDA runs highly parallel code on a commercial graphics cards, offering a speed up of 10–100x over single processor code [31]. The structure of the code is algorithmically quite similar to many molecular dynamics codes [140], allowing for straightforward implementation.

D.3 Results

Two sets of simulations were done, examining the effects of field strength and volume scale respectively. All the simulations were performed at shear rates of $\dot{\gamma}$ =250 s^{-1}, 500 s^{-1}, 1000 s^{-1} and 2000 s^{-1}, and run until a shear of $\gamma = 20$. The first set were done at M =300 kA/m and 600 kA/m at a simulation volume size of $h = 0.5$ mm, corresponding to $N = 208\,803$ particles and a volume fraction of $\phi = 0.3$.

To investigate the effects of volume size, simulations volumes of $h = 0.175\,\mathrm{mm}$, $0.5\,\mathrm{mm}$ and $0.875\,\mathrm{mm}$ were used, corresponding to $N = 8952$, $208\,803$ and $1\,119\,058$ particles, at a field strength of $M = 300\,\mathrm{kA/m}$. The particles had radius $a = 3.5\,\mu\mathrm{m}$, and the carrier fluid had viscosity $\eta_c = 0.1\,\mathrm{Pa\,s}$. Figure D.3 shows the graphical output of the simulation code. We nondimensionalize time by reporting it in units of shear.

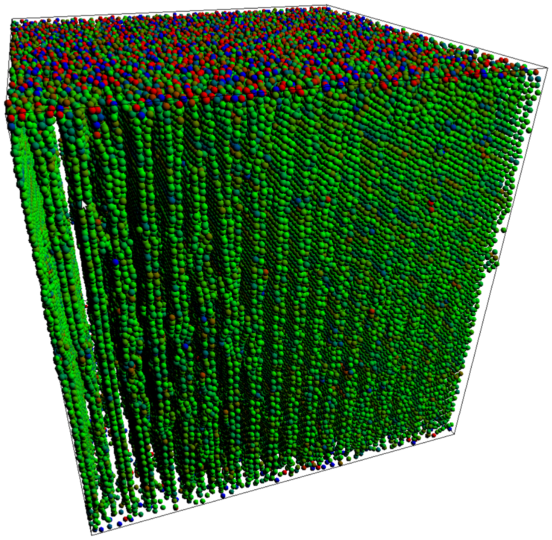

Figure D.3: Graphical output of the simulation code, at shear $\gamma = 8$ with $M = 300\,\mathrm{kA/m}$ and $\dot{\gamma} = 500\,\mathrm{s}^{-1}$, looking in the direction of shear.

The simulations were able to produce lamellar sheet formation, as shown in Figure D.3. At simulation start, the particles quickly form chains spanning top to bottom, and by $\gamma = 2$–3 the chains begin to form into wavy, interlinked sheet structures. By $\gamma = 6$–8, the structure has straightened out, and aggregated into sheets two particles thick, with strands of particles linking sheets. As time passes, these strands disappear and the two-particle-thick sheet mode dominates. Due to the random initial particle positions, occasionally a thicker structure will form.

The two-particle-thick sheets are thinner than those seen experimentally [136].

However our simulations cover at most 80 ms of time, and use uniformly sized particles in a uniform field. Experimental measurements are typically taken after several minutes of shearing, and time is known to have a significant effect on sheet formation [135]. Gradients in the magnetic field could cause large movements of the sheets, causing them to merge. Similarly, a distribution of particle sizes would promote a more irregular structure, increasing the adhesion between sheets. However, we note that the force cutoff of $8a$ means that this periodicity may be a numerical artifact.

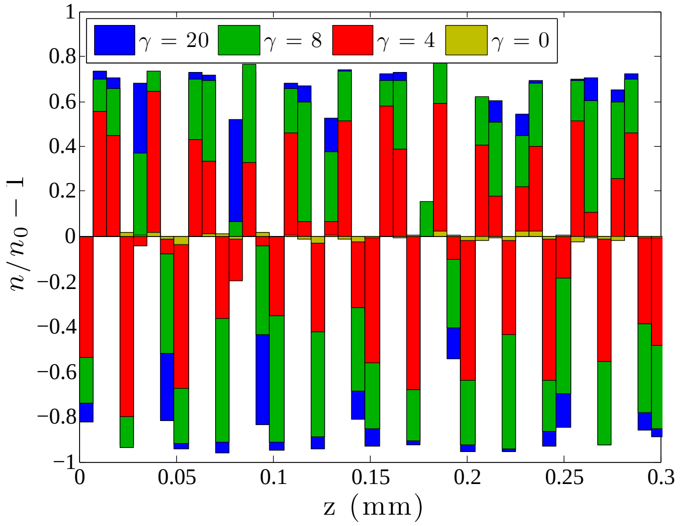

Figure D.4: Incremental number density of particles at $\mathbf{H}_0 = 100\,\mathrm{kA/m}$ and $\dot{\gamma} = 250\,\mathrm{s}^{-1}$ in a portion of a $h = 0.5\,\mathrm{mm}$ volume as γ increases.

At high particle counts, directly observing particle positions is difficult. Noting that there is a large variation in the particle distribution in the direction normal to both field and shear, Fig. D.4 shows particle density in the z direction for a portion of the volume when divided into bins one particle diameter thick. The number density n is nondimensionalized by the expected value for a uniform distribution of particles n_0. This plot shows that from a random initial condition at $\gamma = 0$, regions of high and low are accentuated until the trend of two-particle-thick sheets becomes clear at $\gamma = 8$, and achieves a steady state by $\gamma = 20$.

To allow for better analysis of the time history of sheet formation, we use the standard deviation of the number density in the z direction as a metric of sheet formation. A higher value indicates a larger variance of particle densities, and thus implies increased sheet formation. Figure D.5a plots the time histories for both $\mathbf{M}$ =300 kA/m and 600 kA/m. Increasing magnetization causes a decrease in the sheet formation time and an increase in magnitude of the sheet metric. Increasing shear rate increases the response and decreases the steady state value of the sheet metric. The results for $M = 600\,\mathrm{kA/m}, \dot{\gamma} = 1000\,\mathrm{s}^{-1}$ and $M = 300\,\mathrm{kA/m}, \dot{\gamma} = 250\,\mathrm{s}^{-1}$ overlap, as do $\mathbf{M} = 600\,\mathrm{kA/m}, \dot{\gamma} = 2000\,\mathrm{s}^{-1}$ and $\mathbf{M} = 300\,\mathrm{kA/m}, \dot{\gamma} = 1000\,\mathrm{s}^{-1}$ due to identical Mason numbers [35]. This metric of density variation effectively shows the sheet formation trend, although it is quite sensitive to initial conditions.

We can also use two metrics of chain formation: the connectivity, c, and chain length, L, to help measure the sheet formation. Connectivity is the number particle contact points, where two particles are in contact if the separation distance is small, or $r_{ij} - 2a < 0.1a$. Connectivity and chain length are nondimensionalized by comparing their values to the case of a single-width particle chain spanning the top and bottom plates. This yields an idealized value for connectivity, $c_0 = N(1 - 2a/h)$ and for chain length, $L_0 = h/2a$. Time histories for both c/c_0 and L/L_0 are plotted in Fig. D.5b and D.5c. Figure D.5b shows that, at high fields and low shear rates, the extended shearing associated with sheet formation causes a decrease in chain length, due to the separation of sheets, but connectivity increases monotonically (Fig. D.5c), indicating that the dense sheet structure allows for more particle interactions.

In Fig. D.6 examines the effects of volume size on the chain and sheet metrics. Figure D.6c shows that increasing volume size causes a slight increase in both the steady state connectivity and the time required to reach steady state, indicating increased aggregation in the larger volumes. Nondimensional chain length is plotted in Fig. D.6b, and shows a small drop in value with an increase in volume. All three metrics show a reduction in noise with an increase in volume size.

Figure D.6a shows that larger volume sizes decrease the both the rate of formation and the magnitude of the density variation in the fluid. Since connectivity, which measures particle packing, increases with volume, this result means that the straight, narrow sheets present at smaller volumes are instead being replaced by a dense but structure; and visual inspection of the simulation output agrees with this. These irregular structure are likely the early stages of thick structure formation.

This sheet formation effect can be explained by the larger volume size reducing the effects of boundary conditions. At small volume sizes, Pappas and Klingenberg [137] showed that the elimination of the pinned boundary condition causes rapid aggregation into thick structures, while a no-slip condition caused the formation of one-particle-thick sheets. It has also been shown that chain aggregation into columnar structures is dependent on chain length, with increasing chain length increasing the potential for aggregation [141]. Thus operating at the large length scales enabled by our high performance CUDA code is necessary to develop an accurate understanding of the chain and sheet formation dynamics of magnetorheological fluid.

D.4 Conclusion

We successfully simulated over a million particles, and demonstrated sheet formation at experimental volume scales. At high particle counts, direct visualization of the behavior of the fluid is difficult, so we computed the standard deviation of the particle density as a way to measure lamellar sheet formation of the fluid. We also used two metrics of chain formation, the chain length and connectivity, to aid in measuring and understanding the fluid structure.

Our simulations showed that simulation volume has a significant effect on the chain formation of the fluid, with larger volume sizes promoting the formation of thicker lamellar sheet structures, due to the decreased effects of boundary conditions. We also demonstrated that lamellar sheet formation is inhibited by increasing shear rates, and aided by increasing magnetic field strength.

For future work, we propose the use of a more direct metric of sheet formation, such as a directional connectivity [141], as well as examining the effects of particle volume fraction on the resulting structure.

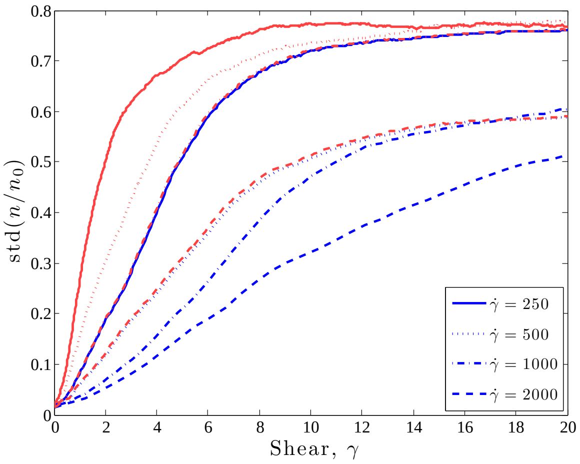

(a) Standard deviation of n/n_0

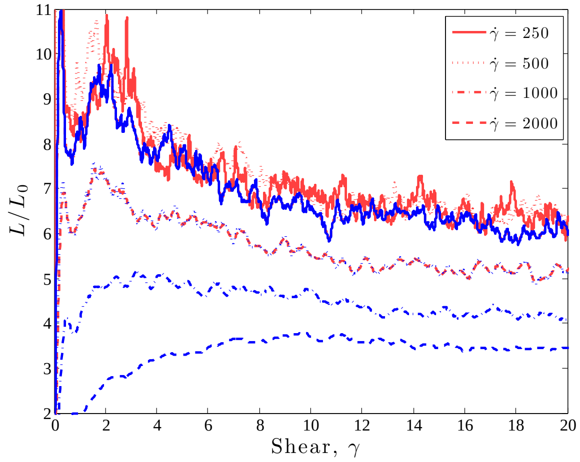

(b) Nondimensional chain length

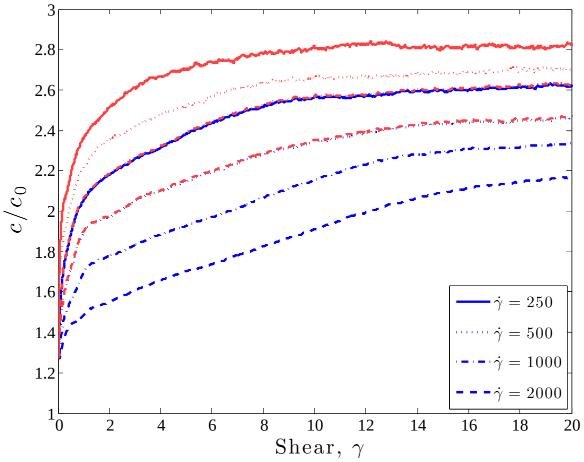

(c) Nondimensional connectivity

Figure D.5: Nondimensional chain parameters versus shear at $h = 0.5\,\mathrm{mm}$. Blue and red lines correspond to $\mathbf{M} = 300$ and $600\,\mathrm{kA/m}$ respectively.

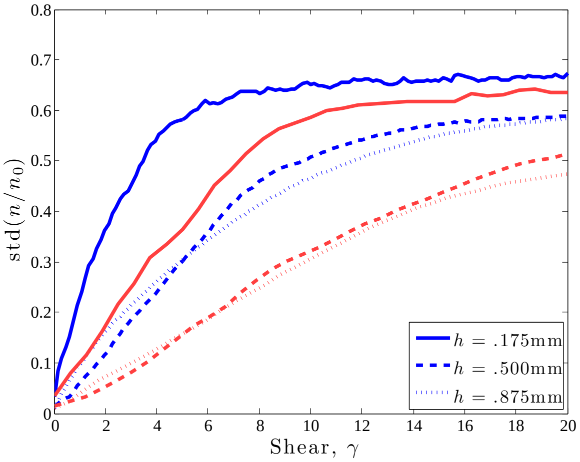

(a) Standard deviation of n/n_0.

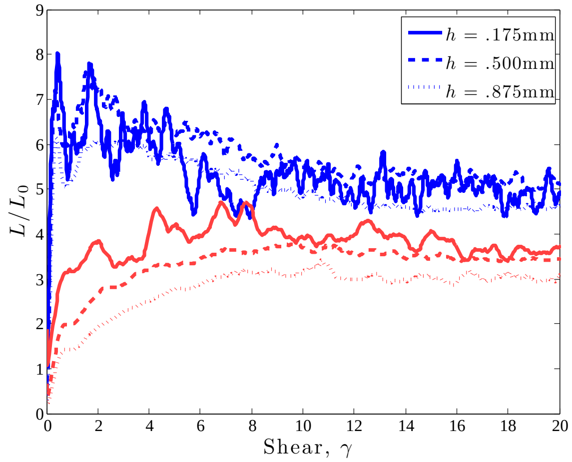

(b) Nondimensional chain length

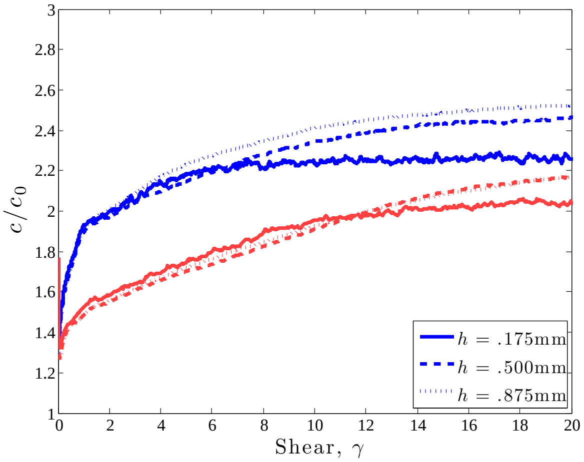

(c) Nondimensional connectivity

Figure D.6: Nondimensional chain parameters versus shear at $\mathbf{M} = 300\,\mathrm{kA/m}$. Blue and red lines correspond to $\dot{\gamma} = 500$ and $2000\,\mathrm{s}^{-1}$ respectively.

Appendix E: The effect of particle size distribution on chain structures in MR fluids

E.1 Summary

This work originally appeared as “Effect of particle size distribution on chain structures in magnetorheological fluid” by Stephen G. Sherman and Norman M. Wereley and published in IEEE Transactions on Magnetics [41].

E.2 Introduction

Magnetorheological fluids (MRFs) consist of micron scale carbonyl iron (CI) particles suspended in a carrier fluid. When external field is applied, interparticle magnetic forces cause the CI particles to align and form chain-like structures. These chain structures cause the MRF to develop a field controllable resistance to stress, in that these chains must break before the fluid will flow. Thus, if these chain structures are modified because of changes in particle composition, scale or morphology, then it follows that the field controllable resistance to stress will also change. Existing simulation and theoretical work has focused on *monodisperse* MRFs, or fluids where all the spherical particles have a uniform size. However, practical fluids are *polydisperse*, and such a distribution of particle sizes alters the chain structure that form in the presence of magnetic field. We simulate the effect of particle size distribution on fluid stress and on formation of particles into chain structures in shear flows of MRFs with a volume fraction of $\phi = 0.3$. Such a volume fraction is representative of practical MRFs used in vibration and shock isolation applications.

Particle size distribution plays a key role in bidisperse fluids, which have a bimodal particle distribution and have been shown to exhibit a synergistic increase in the yield stress of an MRF versus each particle suspended in a fluid alone [142]. This bidisperse effect is caused by the interactions of different size particles. Because the bidisperse effect is believed to be caused by the interactions of different particle sizes, modeling the size distribution is necessary for an accurate model of chain formation in MRFs.

For MRFs consisting of spherical particles suspended in a carrier fluid, experimental and theoretical work by Lemaire *et al.* [129] indicates that at small particle sizes and low volume fractions, particle size and size distribution strongly affects fluid properties, which the authors attribute to Brownian motion. To measure the role of Brownian motion in the fluid, Lemaire uses the ratio of magnetic forces to Brownian forces, $\lambda \propto a^3 M^2/T$, where a is the particle radius, M is the particle magnetic moment, and T is the temperature. At $\lambda = 10^3$ ($a < 0.5\,\mu\text{m}$, $M < 20\,\text{kA/m}$) and a low volume fraction $\phi = 0.05$, and a large particle size distribution, the smaller particles in the distribution are influenced by Brownian motion, reducing the fluid stress. However, for ferrofluids with silica particles, Brownian motion ceases to play a role at $\lambda = 10^9$ and large volume fractions $\phi = 0.2$.

There has been extensive research on simulating MRFs because simulations can offer unique insights into how particles form chain structures, and, in turn, how these chain structures affect MRF performance. While some simulation research has looked at bidisperse fluids, using a mixture of two uniform particle sizes [29], [143]. However, to our knowledge, no numerical investigations on the effects of the particle size distribution have been performed. Current simulations are also limited to extremely small numbers of particles, $N < 10^4$, so that there may be an in insufficient number of particles to accurately and effectively represent particle size distribution. However, we have developed a high performance CUDA-based simulation code capable of modeling up to 10^6 particles, allowing us to simulate chain formation in MRFs using a near experimental scale volume [19], [138]. In this study, we modify this simulation code to investigate the effects of log-normal particle size distribution on the performance of a typical MRF.

E.3 Background

To represent particle size range in MRF simulations, a log normal distribution is selected because it is the typical distribution observed in carbonyl iron (CI) powders, and is suitable for particle simulations [117]. The particle distribution function (see Fig. E.1) is given by

$$f(a) = \frac{1}{a\sigma_0\sqrt{2\pi}} \exp\left[-\frac{1}{2}\left(\frac{\ln a - \ln a_0}{\sigma_0}\right)^2\right], \tag{E.1}$$

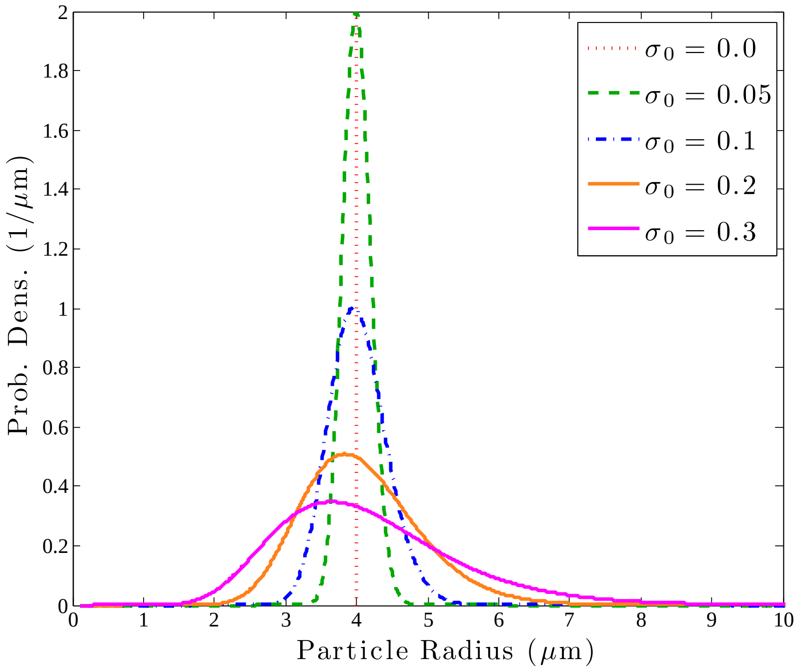

Figure E.1: Particle size distribution.

where a_0 is the median particle radius, and σ_0 is the distribution parameter. For $\sigma_0 \leq 0.1, \sigma_0 \approx \mathrm{std}(a/a_0)$. Typically, distributions with $\sigma_0 \leq 0.1$ are considered to be effectively *monodisperse*, and fluids with $\sigma_0 \geq 0.1$ are considered to be *polydisperse*. In a typical MRF, commercial CI powder are used, such as those made by BASF, where the particle size ranges is nominally $0.2 < \sigma_0 < 0.3$, and the smallest size distributions in Lemaire *et al.*[129] have $\sigma_0 \approx 0.1$. Note that this distribution is skewed, so for fixed a_0, the mean (and mass weighted mean) radius will increase with increasing σ_0. Thus, for a fluid with constant volume fraction, increasing σ_0 will reduce the number of total particles.

Prior work simulating MRFs has focused on monodisperse fluids. The simulation developed here follows the uniform particle size simulations of Klingenberg [28], [34], but particles of different size can interact. In this model, particles are magnetized solely by the external field, $\mathbf{H}_0 = H_0\mathbf{e}_y$, giving them a uniform magnetization

$\mathbf{M} = M\mathbf{e}_y$, and gives particle i with radius a_i the magnetic moment, $\mathbf{m}_i = 4/3\pi a_i^3\mathbf{M}$. From that, the force on dipole i from dipole j is given by:

$$\begin{aligned}\mathbf{F}_{ij}^m =& \frac{3\mu_0}{4\pi r_{ij}^4}[(\mathbf{m}_i \cdot \hat{\mathbf{r}}_{ij})\mathbf{m}_j + (\mathbf{m}_j \cdot \hat{\mathbf{r}}_{ij})\mathbf{m}_i + (\mathbf{m}_i \cdot \mathbf{m}_j)\hat{\mathbf{r}}_{ij} \\ & - 5(\mathbf{m}_i \cdot \hat{\mathbf{r}}_{ij})(\mathbf{m}_j \cdot \hat{\mathbf{r}}_{ij})\hat{\mathbf{r}}_{ij}],\end{aligned} \tag{E.2}$$

where r_{ij} is the position of particle i with respect to j. To avoid solving an n-body problem, we truncate forces at $4(a_i + a_j)$, which corresponds to a cut off when forces have fallen below 0.5% of their in-contact maximum. Observing that the attraction force has magnitude

$$F_0(a_i, a_j) = \frac{3\mu_0 m_i m_j}{4\pi(a_i + a_j)^4}, \tag{E.3}$$

with peak attraction force of $2F_0$ and a maximum repulsion force of $-F_0$.

Particle collisions are modeled using the repulsion force,

$$\mathbf{F}_{ij}^c = 2F_0(a_i, a_j)\exp\left[-k\left(\frac{r_{ij}}{a_i + a_j} - 1\right)\right]\hat{\mathbf{r}}_{ij}, \tag{E.4}$$

where the stiffness parameter, $k = 50$. This model has the disadvantage that force is applied outside of the particle sphere, but spring-based methods cause simulated particles to overlap. Note that this stiffness parameter is twice as large as used in [34]. This larger stiffness parameter is used to prevent overlap in the two-particle attractive case, although overlap may still occur due to long range forces. Minimizing overlap using the larger stiffness parameter enables more accurate measurements of particle structure.

Stress on the particles in volume V is computed via

$$\tau_{xy} = -\frac{1}{V}\sum_{i=1}^{N}(\mathbf{F}_i \cdot \mathbf{e}_x)(y_i - h/2) \tag{E.5}$$

where $\mathbf{e}_x$ is a unit vector in the x direction, y_i is distance from the bottom surface, and h is height of the simulation volume. A reference stress is computed

$$\tau^* == \frac{1}{16}\pi\mu_0 M^2, \tag{E.6}$$

which is independent of the particle radius, which implies that MRF performance should theoretically be unaffected by changes in particle size distribution.

Here, Couette flow of an MRF is simulated in the fluid volume in Fig. E.2. Despite the high particle volume fraction ($\phi = 0.3$) [117], the simplified model in [34] is used, where particles travel in an implicit carrier fluid where particles do not couple to the fluid. In steady state shear flow, the carrier fluid moves with velocity,

$$\mathbf{v}_\infty = \dot{\gamma} y \, \mathbf{e}_x. \tag{E.7}$$

Periodic boundary conditions are placed in the x and z directions, and the particles are given a slip boundary condition on the y border. We choose a slip condition for the sake of simplicity and ease of integration, though particle boundary conditions can have an effect on fluid stress and particle chain formation [48].

The drag force on a spherical particle moving with velocity $\mathbf{v}_i$ is modeled by

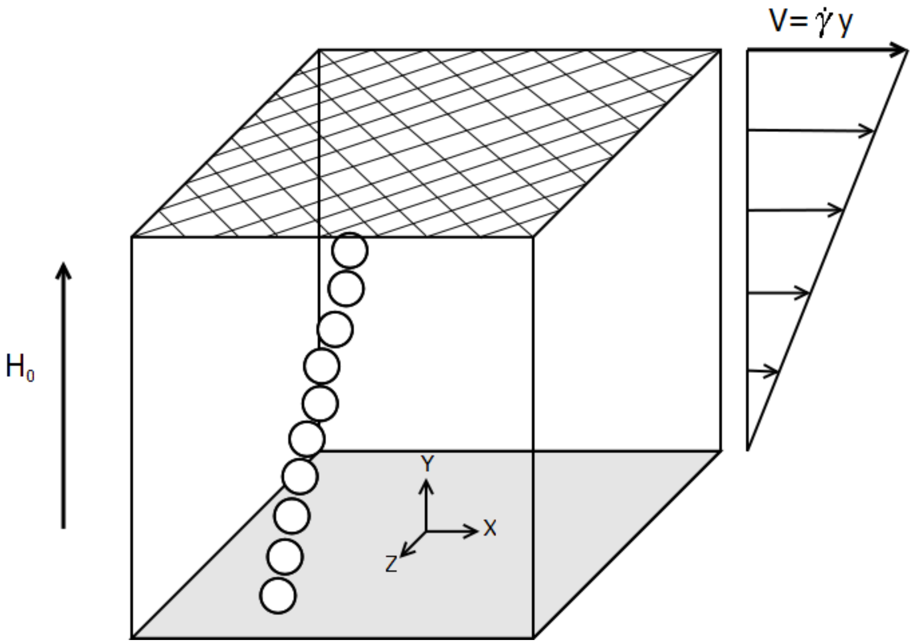

Figure E.2: Simulation volume.

Stokes drag,

$$\mathbf{F}_i^d = 6\pi a_i(\mathbf{v}_i - \mathbf{v}_\infty) \tag{E.8}$$

Stokes drag is valid here because of the Reynolds number, $\text{Re} < 10^{-2}$, due to the small particle size and viscous carrier fluid.

Drag force is used to compute the Mason number, Mn, that is, the ratio of hydrodynamic shear to magnetic shear forces:

$$\text{Mn} = \frac{6\pi\eta_c a_0^2\dot{\gamma}}{F_0} = \frac{9\eta_c\dot{\gamma}}{2\mu_0 M^2}, \tag{E.9}$$

where η_c is carrier fluid viscosity. Thus, Mn is independent of particle size. The viscous nature of the fluid can also be used to neglect particle acceleration, as the velocity response time is less than the duration of the forces [117], with response time $t_v = 2\rho_p a^2/9\eta_c = 40\,\text{ns}$, and ρ_p as particle density. Thus, if the particle is always at terminal velocity, then the particle dynamics can be represented by a first order model. Buoyancy forces are neglected because simulation time is much less (milliseconds) than settling times (days). Because simulated magnetizations are fairly large, $M = 300\,\mathrm{kA/m}$, $\lambda \approx 10^8$, Brownian forces are also neglected.

To measure the chain structures formed in the MRF, we use metrics quantifying chain formation from graph theory[19]. The particles are the vertices of the graph, and two particles are considered adjacent if $r_{ij} < 1.05(a_i + a_j)$. A value of 1.05 was chosen based on visual criteria. The first metric, *total particle connectivity*, c, is based on the total number of graph edges. By considering a fluid consisting solely of single width chains that span from top to bottom, the idealized total connectivity is $c_0 = N/(1 - 2a_0/h)$. A second metric is the *mean particle cluster size*, S, or the mean number of vertices in each connected component. Connected components are identified through a depth-first search [144]. A similar ideal value for S can be deduced based on the single-particle-width strand assumption, giving $S_0 = h/2a_0$.

E.4 Results

To analyze the effects of particle size distribution on fluid stress and chain formation, we investigated the effects of distribution parameter, σ_0, in a fluid with constant particle volume fraction, $\phi = 0.3$ and constant particle magnetization, $M = 300\,\mathrm{kA/m}$, at various shear rates. A range of discrete values of σ_0 were considered: 0 (uniformly sized particles), 1×10^{-3}, 2.5×10^{-3}, 5×10^{-3}, 0.01, 0.025, 0.05, 0.1, 0.2 and 0.3. The properties were measured under shear at $\dot{\gamma} = 30\,\mathrm{s}^{-1}$, $60\,\mathrm{s}^{-1}$,

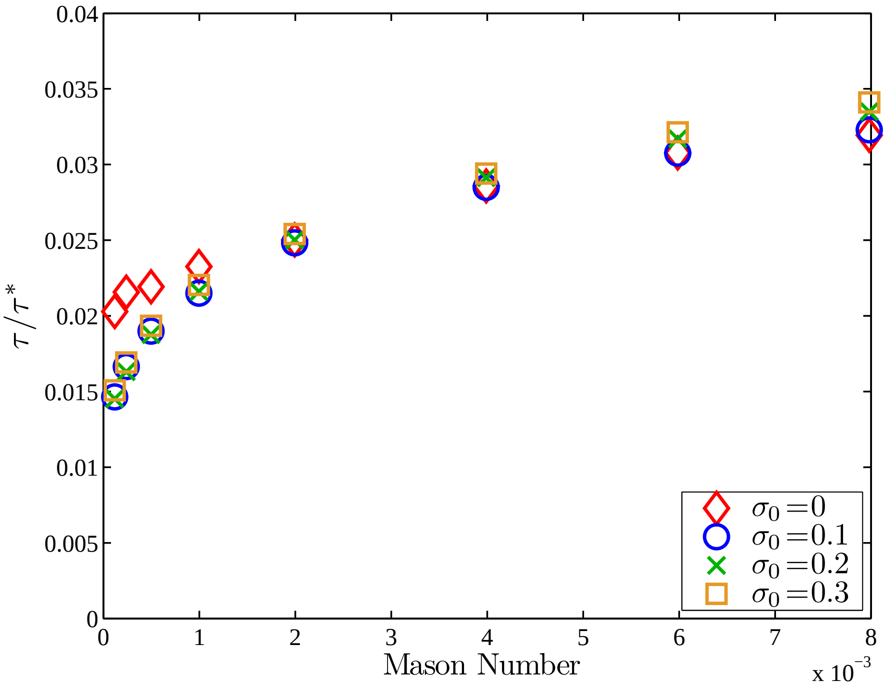

Figure E.3: Stress versus Mason number.

125 s^{-1}, 250 s^{-1}, 500 s^{-1}, 1000 s^{-1}, 1500 s^{-1} and 2000 s^{-1} until a nondimensional shear of $\gamma = 8$, corresponding to simulation times of 4 ms to 267 ms, and Mason numbers from 8×10^{-3} to 1.2×10^{-4} . Steady state quantities are computed from time averages during $\gamma = 4$ to $\gamma = 8$, and then results were averaged over 3 runs. All simulation runs occurred in a cubic volume with a constant median particle radius of $a_0 = 4\,\mu$m, a gap height of 0.5 mm, and with a carrier fluid viscosity of 0.1 Pa s. The integration method was a classic fourth-order Runge-Kutta scheme with a time step of 450 ns, with a limiter that recomputes the iteration at half the time step if the maximum particle displacement relative to the fluid is greater than $0.035a_0$.

Fig. E.3 depicts the flow curve, which shows that stress increases with Mn, and is broadly consistent for all fluids at high Mn. However at low Mason numbers, Mn $< 10^{-3}$, the uniform particle distribution has a significantly higher stress, and at

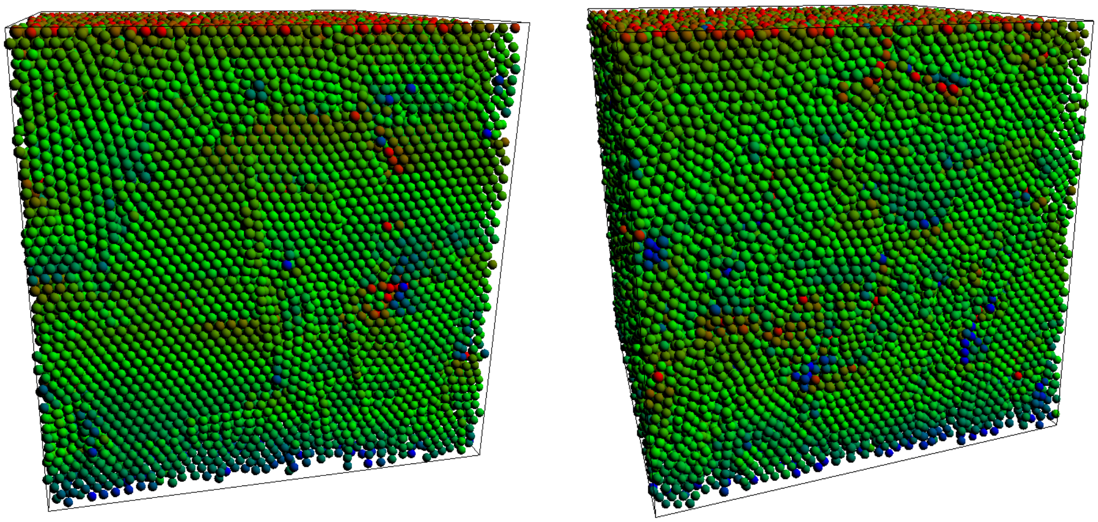

(a) $\sigma_0 = 0.0$ (b) $\sigma_0 = 0.05$

Figure E.4: Particle structure at $\gamma = 4$ and $\mathrm{Mn} = 2.4 \times 10^{-4}$ with a volume height of 0.35 mm. Colors correspond to force on the particles.

high Mn, Mn $> 5 \times 10^{-3}$, fluids with large particle size distribution exhibit a small increase in fluid stress, which indicates that particle size distribution effects MRF performance.

In order to identify over what range of distributions size parameter this occurs, Fig. E.5 τ/τ^* versus σ_0 for a variety of Mason numbers. At low Mason numbers, Mn $< 10^{-3}$, fluids with with a distribution of $\sigma_0 > 0.025$, exhibit a 25% decrease in stress over fluids with $\sigma_0 \leq 0.01$. At high Mason numbers, fluids with $\sigma_0 > 0.05$, increasing σ_0 causes a slight increase in stress. From these results, particles size distribution ceases to play a role when $\sigma_0 \leq 0.025$, which is significantly less than the value of $\sigma_0 = 0.1$ that is typically used in simulations. To explain why these changes occur, we hypothesize that the particle size distribution is altering the particle structure, and that the resulting new structure reduces the apparent viscosity.

One way to identify the change in particle structure caused by the size distribution is visually; Fig. E.4 compares a representative polydisperse fluid, $\sigma_0 = 0.05$, with a monodisperse MRF, $\sigma_0 = 0$, at Mn$= 2.4 \times 10^{-4}$. These images show that the chain structure in the monodisperse MRF forms a lattice-like sheet structure, while the polydisperse fluid develops a more irregular structure. As values of σ_0 and Mn increase, the chain structure irregularity also increases. These trends can be quantified using the following chain structure metrics.

The first metric of chain formation, mean cluster size, S/S_0, is plotted against distribution size parameter, σ_0, in Fig. E.6. Generally, increasing σ_0 and Mn causes a decrease in S. Increasing Mason number causes cluster size to decrease, because increasing shear force causes the particle clusters to break apart. The decrease in S/S_0 for $\sigma_0 > 0.025$ is due to the increasing distribution size parameter, which prevents particles from forming the lattice-like sheet structures of monodisperse MRFs. However, at low Mn, and for values of $0.025 \leq \sigma \leq 0.2$, the cluster size increases, so that the increase occurs over a similar range of distribution size parameter as the drop in stress observed in Fig. E.5. Here, the distribution size prevents particles from forming the regular lattice sheets observed in a monodisperse MRF, but the shear rate is low enough that the particles can form irregular structures with tenuous connections between different clusters, causing S/S_0 to rise significantly. The values of S/S_0 are so large that less than 10 clusters are in the simulated fluid volume. This further motivates the need for high particle count simulations.

The second metric is *particle connectivity*, c/c_0, which measures the number of particles with which each particle is in contact, or localized density. Figure E.7 plots particle connectivity, c/c_0, against σ_0. As Mn increases, connectivity drops. which

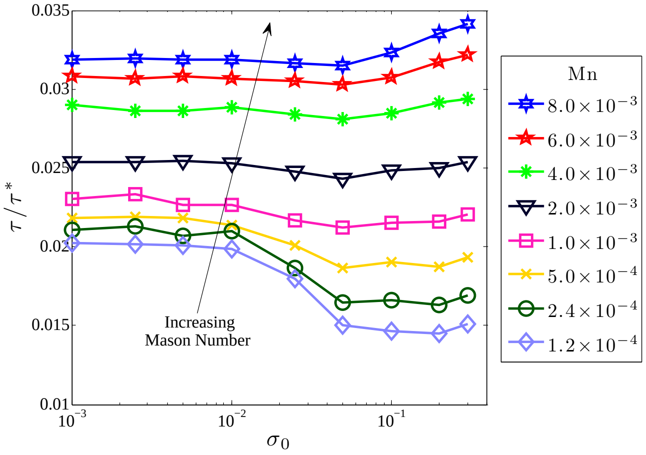

Figure E.5: Stress versus distribution size for various Mason numbers.

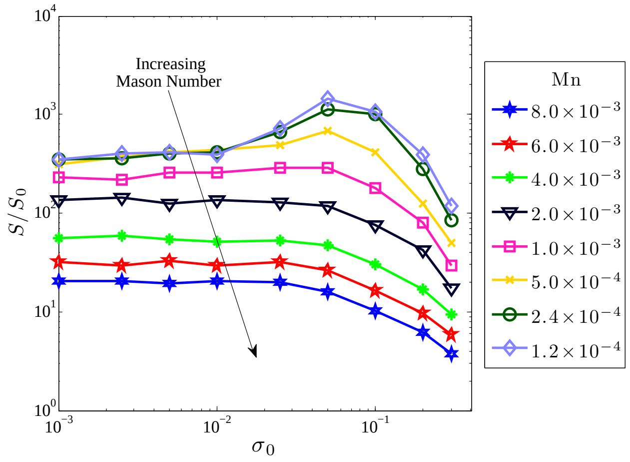

Figure E.6: Cluster size versus distribution size for various Mason numbers.

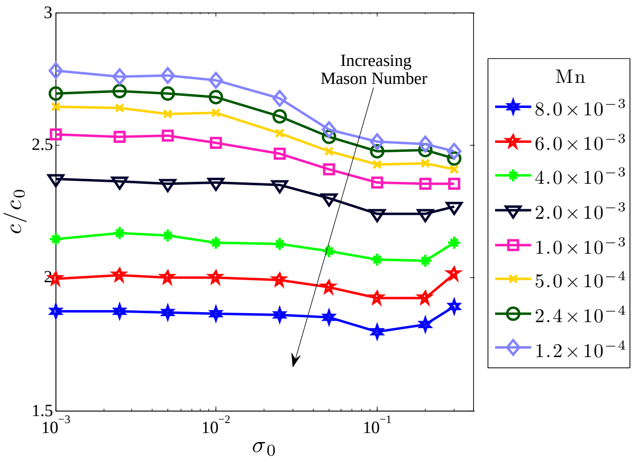

Figure E.7: Connectivity versus distribution size for various Mason numbers.

indicates that increased shearing is actually separating the majority of the particles. At low Mason numbers, for $\sigma > 0.025$, increasing distribution size parameter causes a drop in connectivity, because the distribution particle size promotes irregular structures over lattice-like structures. However, at high Mn and for $\sigma_0 \geq 0.2$, there is a slight rise in connectivity caused by shear forces pushing smaller particles into contact with larger ones.

However, all these results are over the range of $\gamma = 4$ to 8, the changes in particle structure may be coming from changes to the behaviors of the transients, rather than the steady-state properties.

E.5 Conclusions

Effects of log-normal particle size distribution on MRF behavior was investigated via high particle count (on the order of 10^6 particles) simulation based on CUDA. While simple theoretical models indicate that particle size distribution should have no effect on MRF performance, these large particle count simulations indicate that MRF behavior changes substantially as the size parameter, σ_0, increases. Simulations were done for median particle radius of $a_0 = 4\,\mu\text{m}$, carrier fluid viscosity of $0.1\,\text{Pa}\,\text{s}$, and particle volume fraction of $\phi = 0.30$. The significant findings are as follows.

1. MRFs behave as monodisperse fluids for narrow particle distributions having a size parameter, $\sigma_0 < 0.025$. This is well below practical size parameters in CI powders, typically $\sigma_0 \geq 0.1$, therefore, monodisperse MRFs would be difficult

to realize in practice.

2. Simulations show that particle sheets in monodisperse MRFs form lattice-like structures and, as the particle distribution size parameter increases, particles tend to form more irregular structures.
3. These increasingly irregular structures manifest as a 25% reduction in MRF shear stress at low Mn, and a slight increase in stress at high Mn.
4. Wide particle size distributions correspond to a reduction in particle cluster size, and a small increase in connectivity. The changes in cluster size also correspond well to the simulated stress values.

Based on these simulation results, we conclude that particle size distribution has a substantial effect on the structure and performance of magnetorheological fluids, so that accuracy of simulation codes may improve when realistic particle size distributions are utilized.

Appendix F: The Bingham and Mason numbers

F.1 Summary

This is a reproduction of the paper, ”Relating Mason number to Bingham number in magnetorheological fluids” published in the Journal of Magnetic Materials and Magnetism [53], and presented at the 10th Inertnaional Conference on the Scientific and Clinical Applications of Magnetic Carriers in Dresden, Germany.

F.2 Introduction

Magnetorheological (MR) fluids are a fluid composed of micron scale magnetizable particles suspended in a carrier fluid. Upon the application of field, the particles in the field align to form chain like structures, and these chains cause the fluid to develop a field dependent yield stress. The primary application of MR fluid has been in MR dampers and MR energy absorbers, where the controllable apparent viscosity allows for a controllable damping force or stroking load, which enables high performance vibration isolation [145] or shock mitigation that can adapt to payload weight and impact severity [146], [147].

Models of magnetorheological fluids have typically taken two perspectives:

either modeling the MR fluid as a collection of microscopic particles floating in a carrier fluid, or as a bulk fluid continuum. Microscopic modeling of MR fluids focuses on the behavior of the particles [26], [34], [141] by examining the formation and destruction of chain structures in the fluid with the goal of predicting yield stress. The primary forces on the particles that govern chain formation are viscous drag of the carrier fluid on the particle and the interparticle magnetic forces. The ratio of particle magnetic forces to viscous forces is known as the Mason number, Mn, [35], [148], [149], named after the work of S. G. Mason et. al. on the behavior of fluid droplets in the presence of electric field [150]. In the equations of motion, the Mason number is the governing parameter of the shear response of a particle in an MR fluid, and is an essential part of research on dynamic models of chain formation. The Mason number, Mn also has value in the analysis of experimental data, such as when apparent viscosity is plotted against Mason number, the apparent viscosity curves collapse to a single curve, thereby reducing the dimensionality of a dataset [35], [148].

At the bulk scale, one of the idealized descriptions of MR fluids is as a Bingham plastic [151], in which the applied magnetic field additively induces a field controllable yield stress to a Newtonian fluid. The Bingham number, Bi, which is the ratio of yield stress to viscous stress, describes the extent to which the controllable yield stress can exceed the viscous stress (typically $\mathrm{Bi} \gg 1$), and is an essential descriptor of Bingham plastic behavior. The Bingham number can be used to calculate flow rates, flow profiles, and pressure losses in devices using Bingham plastic fluids [80]. In particular, for shear mode MR devices, the Bingham number represents the controllable force ratio [152], and since MR fluids are used for the purpose of generating controllable forces, the Bingham number is an essential and fundamental parameter for the understanding and analysis of MR fluids at the bulk scale.

We seek to relate the Bingham number to the Mason number, two nondimensional numbers that represent fundamental descriptions of the behavior of MR fluid at macroscopic and microscopic scales, respectively. In particular, we focus on MR fluids typically used in energy absorbing devices. These MR fluids are typically suspensions of 1–10 µm diameter carbonyl iron particles with solids loading ranging from 20 to 50 volume percent, and well described by the Bingham plastic model. By mathematically relating Bingham number to Mason number, we enable microscopic Mason number based analyses to be directly extended to macroscopic or device scale Bingham number based problems. Alternatively, experimental Bingham number based results can be scaled down for comparison to Mason number based particle level analyses.

In this study, the Bingham number and the Mason number are developed, and it is shown that if microscopic forces map linearly to macroscopic forces, then the Bingham number and the Mason number are inversely related, or that the product of Bingham number and Mason number is a constant. This notion is confirmed through measurements of apparent viscosity. We experimentally validate the claim that microscopic and macroscopic forces are linearly related, and that this is akin to assuming that MR fluids are well described by the Bingham plastic model. Finally, the relationship between Mason number and Bingham number is used to examine the experimental relevance of a Mason number based result, as well as how such a

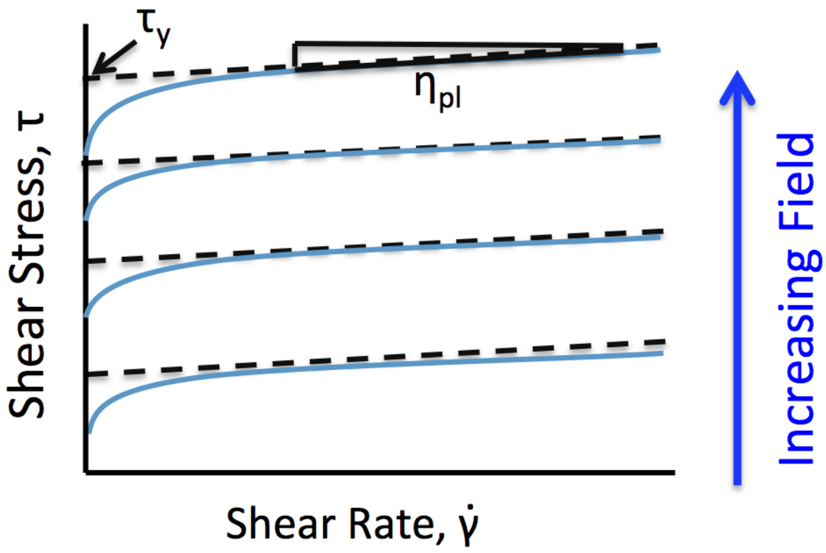

Figure F.1: Idealized rheogram or shear stress vs. shear rate diagram for an MR fluid

relationship would inform the MR fluid and/or device design process.

F.3 Background

To motivate the usage of these nondimensional numbers, both numbers are derived in the analytical context in which they arise.

F.3.1 The Bingham Number

For device scale analyses, the fluid is treated as a continuum with nonlinear rheological properties. A typical MR fluid shear stress vs. shear rate graph is shown in Fig. F.1. These shear stresses for each field strength are typically modeled by the Bingham plastic model,

$$\tau = \tau_y + \eta_{pl}\dot{\gamma}, \tag{F.1}$$

which has a plastic viscosity, η_{pl}, and a yield stress, τ_y. The yield stress is magnetic field dependent, and it is typical to assume that η_{pl} is independent of field strength, and equivalent to the off-state viscosity, η_{off}. In MR fluids, η_{pl} is chosen to be the slope of the high shear rate asymptote of the shear stress curve, and τ_y corresponds to the intersection of the high shear rate asymptote with the stress axis at $\dot{\gamma} = 0$.

A typical way in which MR fluid is used in damper design is the shear mode damper [152], where an upper plate moving with velocity, v, and area, A, moves over a stationary lower plate with a gap of d between the two plates. Here, the fluid velocity profile is linear, and the force on the upper plate is

$$F_d = (\tau_y + \eta_{pl}\frac{v}{d})A. \tag{F.2}$$

The force in conventional viscous dampers can be written in the form $F_d = c_0 v$, where c_0 is the damping, and for a Newtonian fluid in shear mode $c_0 = \eta A/d$. For the shear mode MR damper, rearranging into this form yields,

$$F_d = (\frac{\tau_y d}{\eta_{pl} v} + 1)\eta_{pl}\frac{A}{d}v = c_{eq}v, \tag{F.3}$$

where c_{eq} is the equivalent damping for a fluid with a yield stress. The ratio of equivalent damping to Newtonian damping yields the damping coefficient

$$\frac{c_{eq}}{c_0} = 1 + \frac{\tau_y d}{\eta_{pl} v} = 1 + \text{Bi} \tag{F.4}$$

which describes the effect that the addition of a yield stress has on damping force. For an MR fluid, where the yield stress is field controllable, this ratio is the controllable force ratio. The term that governs controllability is the Bingham number,

$$\mathrm{Bi} = \frac{\tau_y}{\eta_{pl}\dot{\gamma}_c}, \tag{F.5}$$

the ratio of magnetic forces (τ_y) to viscous forces ($\eta_{pl}\dot{\gamma}_c$) in the fluid, where $\dot{\gamma}_c$ is the characteristic shear rate of the system, which for a shear mode damper is $\dot{\gamma}_c = v/d$. Since the purpose of MR fluids is to generate a field controllable force, and the Bingham number represents the controllable force ratio of an MR device, it is clear that Bingham number is a fundamental representation of the behavior of MR fluids. In more complicated geometries, such as in pipe flow, the Bingham number becomes an essential intermediate quantity in the determination of the flow rate, flow profile, and controllable force output of an MR fluid device [80]. But at the fluid level, the Bingham number is a descriptive, empirical quantity, and doesn't tell us anything about what causes the MR effect, or how a fluid can be modified to improve its performance.

F.3.2 Mason Number

Modeling MR fluid at the particle level allows us to develop predictive models of fluid behavior, providing insight into the chain formation that underlies the MR effect. At the microscopic scale, MR fluids consist of magnetizable particles suspended in a carrier fluid under the influence of an applied magnetic field, H_0. Figure F.2 contains a diagram of two interacting particles under shear and applied magnetic field.

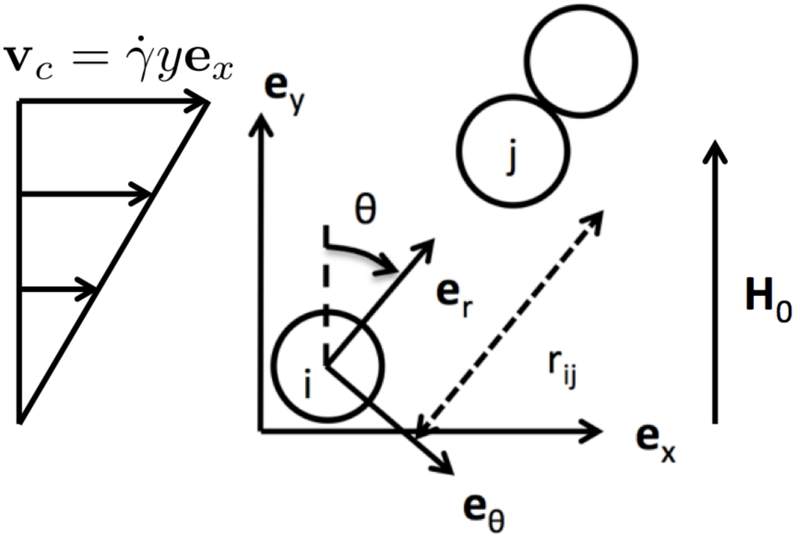

Figure F.2: Diagram of two particles in a shearing fluid.

Typically, these are spherical carbonyl iron particles with diameter $\sigma = 1 - 10\,\mu\text{m}$. The particles are usually modeled as perfect spheres with fixed point dipole moments m_i aligned with the applied field, $\mathbf{m}_i = \pi\sigma^3\mathbf{M}_p/6$, where magnetization, $\mathbf{M}_p = \chi_p\mathbf{H}_0$ is also aligned with the applied field. The force on particle i from particle j is

$$\mathbf{F}_{ij} = \frac{F_0}{(r_{ij}/\sigma)^4}\left[(3\cos^2\theta_{ij} - 1)\mathbf{e}_r + \sin 2\theta_{ij}\,\mathbf{e}_\theta\right] \tag{F.6}$$

with force magnitude

$$F_0 = \frac{3\mu_0 m^2}{4\pi\sigma^4} = \frac{\pi}{48}\mu_0 M_p^2\sigma^2. \tag{F.7}$$

This force magnitude can be turned into a reference stress, $\tau^* = F_0/\sigma^2$, which will be used to normalize shear stress.

The fluid interacts with particles via viscous drag, $F_i = -C_d(\dot{\mathbf{x}}_i - \mathbf{v}_c)$, where η_c is the carrier fluid viscosity, $\dot{\mathbf{x}}_i$ and $\mathbf{v}_c$ are the particle and carrier fluid velocity respectively, and C_d is the coefficient of drag, where for Stokes drag, $C_d = 3\pi\sigma\eta_c$.

In most microscopic models, the carrier fluid moves independently of the particles, allowing us to assume a carrier fluid velocity profile. In shear, the bulk fluid, and thus the carrier fluid moves with velocity $\mathbf{v}_c = \dot{\gamma} y \mathbf{e}_x$, where y is the distance from the stationary surface.

Solving for the trajectory of the particle, the equations of motions for the particle are

$$m_i \ddot{\mathbf{x}}_i + C_d \dot{\mathbf{x}}_i - \sum_{\substack{j=1 \\ j \neq i}}^{N} \mathbf{F}_{ij}(\mathbf{x}_i, \mathbf{x}_j) = C_d \dot{\gamma} y_i \, \mathbf{e}_x, \tag{F.8}$$

where $\mathbf{x}_i$ is the position of the ith particle, and for this equation only, m_i is the mass. The particle mass is small, so that the force contributions from particle acceleration are also small and occur at such a short time scale that $m_i \ddot{\mathbf{x}}_i$ can be set to zero [34]. This allows the full equations of motion to be placed into a kinematic form, which when placed in a dimensionless form yields

$$\frac{C_d}{F_0} \dot{\mathbf{x}}_i = \sum_{\substack{j=1 \\ j \neq i}}^{N} \frac{\mathbf{F}_{ij}(\mathbf{x}_i, \mathbf{x}_j)}{F_0} + \mathrm{Mn} \frac{y_i}{\sigma} \, \mathbf{e}_x, \tag{F.9}$$

where Mn is the Mason number, and is the sole term governing the shear response of the particles in the fluid. The Mason number is the ratio of microscopic shear forces to microscopic magnetic forces, defined as

$$\mathrm{Mn} = \frac{C_d \sigma \dot{\gamma}}{F_0} = \frac{3\pi \eta_c \dot{\gamma}}{\tau^*} = 144 \frac{\eta_c \dot{\gamma}}{\mu_0 M_p^2}. \tag{F.10}$$

Because Mason number governs shear behavior of the particle structures, it will govern the breaking and reforming of the chains in the fluid, and can be used to predict the shear response of the fluid.

When apparent viscosity, $\tau/\dot{\gamma}$, is plotted against Mason number for experimental data, the apparent viscosity curves collapse to a single master curve, so that apparent viscosity is solely a function of Mason number. Thus, the Mason number acts as a nondimensionalized input condition that yields one output condition, and it is through this result that we intend to relate the Bingham and Mason numbers. This nondimensionalization of experimental data allows low shear rate experimental data to be extrapolated to high shear rates, and will be used in our relationship between Bingham number and Mason number. In particular, this is useful as shear rates in practical MR devices can exceed $\dot{\gamma} > 10\,000\,\mathrm{s}^{-1}$, while rheometer experiments typically operate at $\dot{\gamma} < 1000\,\mathrm{s}^{-1}$.

The Mason number is often defined using the H field, where $M = 3\beta H$ with $\beta = (\mu_p - \mu_c)/(\mu_p + 2\mu_c)$ from the textbook problem of an isolated, linearly susceptible sphere in a uniform applied field, yielding

$$\mathrm{Mn}(H) = \frac{16\,\eta_c \dot{\gamma}}{\mu_0 \mu_c \beta^2 H^2}, \tag{F.11}$$

where μ_p and μ_c are the relative permeability of the particle and carrier fluid respectively. The H-based form has several benefits, among which are its amenability to theoretical analysis, applicability to inverse ferrofluids, and its ease of relation to the electric analogue used in electrorheological fluid analysis. While M is a derived quantity, experimentally, the magnetization curves of the fluid must always be known to determine the magnetic field within the testing device. The H-based analysis also requires measuring $\mu_p(H)$ for β, a process which involves measuring M. Using M or μ_p from a magnetometer invokes the assumption that the particle structure, and thus magnetization, is the same in both magnetometer and device, however in practice, this assumption appears successful [153]. Most importantly, Klingenberg showed that approaching saturation, the H based Mason number fails to deliver the desired coalescing of data onto a master curve [35]. In the context of device engineering, nonlinear magnetization must be accounted for, so that we choose to use a Mason number based on average particle magnetization. Also, because average particle magnetization is a measurable quantity, it can also be used to validate the assumed particle structure in models of MR fluids.

We also note that the Mason number definition sometimes varies in the literature. Here we define Mason number using a characteristic separation distance of a particle diameter, as it gives a useful definition of τ^*. This leads to a definition of Mn that is 32 times larger than that in [35].

F.4 Theory

We now seek to relate Mason number to Bingham number, so that microscopic results can be extended to macroscopic behavior, and vice versa. In order to relate Bingham number to Mason number, we observe that both are ratios of magnetic and viscous forces, at bulk and microscopic scales respectively. If we assume that the ratio of forces scales linearly from microscopic to bulk macroscopic properties, then

Bingham (magnetic/viscous) and Mason (viscous/magnetic) number are inversely related. Assuming that the characteristic shear rate is the same in both Bi and Mn, solving for $\dot{\gamma}$ in (F.10) gives

$$\dot{\gamma} = \frac{F_0}{\sigma^2}\frac{1}{3\pi\eta_c}\mathrm{Mn} = \frac{\tau^*}{3\pi\eta_c}\mathrm{Mn}.$$

This can then be substituted into (F.5),

$$\mathrm{Bi} = 3\pi\frac{\tau_y/\tau^*}{\eta_{pl}/\eta_c}\mathrm{Mn}^{-1}, \tag{F.12}$$

giving us a relationship between Bingham and Mason number, in terms of two ratios. The first ratio, the ratio of the yield stress of the bulk material to the magnetic forces between two particles,

$$\frac{\tau_y}{\tau^*} = \frac{\tau_y}{\pi\mu_0 M_p^2/48} \tag{F.13}$$

is defined as the *normalized yield stress.* The second is the ratio of suspension viscosity to carrier fluid viscosity,

$$\frac{\eta_{pl}}{\eta_c} = \frac{\text{Suspension Viscosity}}{\text{Carrier Viscosity}}, \tag{F.14}$$

the *normalized viscosity.* Normalized yield stress, τ_y/τ^* represents how effective the magnetic attraction between particles manifests as a yield stress, and η_{pl}/η_c represents how the addition of particles effects the suspension viscosity. Most importantly, we assert that these two ratios are constant fluid properties of fundamental interest, as will be shown below, and these are ratios that can be predicted from existing literature and theory.

Again, note that the Bingham number is the ratio of magnetically induced shear stress to viscous shear stress, and that the Mason number is the ratio of viscous shear stress to magnetically induced interparticle stress. Another useful perspective is that the product of Bingham number and Mason number is a constant, or

$$\mathrm{Bi}\ \mathrm{Mn} = 3\pi \frac{\tau_y/\tau^*}{\eta_{pl}/\eta_c} \tag{F.15}$$

thereby evincing our earlier hypothesis. The term on the right, a constant, acts as a figure of merit of the fluid-particle recipe, representing the effect the addition of particles has on yield stress divided by the corresponding increase in viscosity. This term will be expanded upon further in Section F.5.

F.4.1 Normalized Yield Stress

In order to argue that τ_y/τ^* is a fluid property, we need to show that yield stress scales roughly proportionally to average particle magnetization across field strength.For low volume fraction fluids, average particle magnetization as a yield stress scaling function has been shown to be a successful scaling law [36]. For the high volume fraction, high yield stress fluids of interest in controllable force applications, an estimate for τ_y/τ^* can be obtained using existing fits of B vs. H and τ_y vs. H for a range fluids, and then solving for τ_y/τ^*. Carlson [154] offers the empirical and widely used fits

$$\tau_y = 271.7C\phi^{1.524}\tanh(5.04\mu_0 H) \tag{F.16}$$

$$B = 1.91\phi^{1.133}\left[1-\exp(-10.97\mu_0 H)\right]+\mu_0 H \tag{F.17}$$

designed to cover iron-based fluids, including those sold by Lord Corporation. In these equations, τ_{MR} is in kPa, H is in A/m and the parameter C is 1.0, 1.16 or 0.95 depending on whether the carrier fluid is hydrocarbon oil, water, or silicon oil, respectively. Neglecting the effect of carrier fluid, we can substitute these equations into τ_y/τ^* and obtain

$$\frac{\tau_y}{\tau^*} = \frac{1.43\phi^{1.257}\tanh(5.04\mu_0 H)}{\left[1-\exp(-10.97\mu_0 H)\right]^2}. \tag{F.18}$$

For fields above H=100 kA/M, this equation is largely constant, depending solely on fluid volume fraction and carrier fluid, as initially required. However in the limit of H=0, (F.18) yields $\tau_y/\tau^* = \infty$, as M drops off faster than yield stress, but an examination of Carlson's data shows that his yield stress model overestimates the experimentally measured yield stress at low field strengths, so this issue can be neglected. Observing that for $0.2 \leq \phi \leq 0.5$, τ_y/τ^* is within 15% of ϕ, this allows the construction of the rule of thumb, $\tau_y/\tau^* \approx \phi$.

Beyond developing experimental rules of thumb for yield stress, normalized yield stress also appears in most particle level modeling work, however, typically in the form of τ_y/H^2. Pen and paper models work by assuming a particle structure, allowing the particles to magnetically interact, deforming the structure under shear, and then computing the interparticle forces to find the shear stress. Computational models follow a similar structure, but with a dynamic structural deformation[34], [41], [155]. In order to resolve some of the nonlinear magnetization in the particles, some models allow regions of the particle to saturate, obtaining $\tau_y \propto \phi\, H^{3/2} M_s^{1/2}$, but these models fail near M_s [156], [157]. The unsurprising solution is to work in terms of averaged particle magnetization, as it allows a model to work across the entire spectrum of applied field, as shown in [158]. The benefit of this nondimensional form for yield stress is that it takes τ_y, a field dependent term, and puts it in a form that is roughly independent of field, depends only on particle type and concentration, and can be predicted using various analytical methods.

F.4.2 Normalized Viscosity

The normalized viscosity ratio, η_{pl}/η_c, is the ratio of off-state viscosity to carrier viscosity. The typical assumptions about plastic viscosity are that it is independent of applied magnetic field, and can be determined by measurements of the fluid with no field applied. Since carrier fluid viscosity is independent of field, η_{pl}/η_c will be a function only of the addition of the particles, and thus a fundamental property of the fluid. Since the particles in an MR fluid are traditionally hard spheres, a prediction of this material property can be determined from the theoretical and empirical relations developed in the study of hard sphere dispersions [131], for example, the empirical

Quemada relation,

$$\frac{\eta}{\eta_c} = \left(1 - \frac{\phi}{\phi_{max}}\right)^{-2} \tag{F.19}$$

where ϕ_{max} is the maximum particle volume fraction. However, these hard sphere equations must be used with caution, as practical MR fluids use additives which significantly affect the plastic viscosity, and so generalized forms with more parameters may be required. Once an appropriate viscosity relationship has been found, Eq. (F.12) can be expressed as a function solely dependent on ϕ. The notion that normalized viscosity is constant can also be used to show that the highly temperature dependent post yield performance of MR fluids is caused only by changes in the carrier fluid [40].

However, while the assumption that η_{pl} is constant is effective in the practical analysis of MR devices, this assumption often breaks down when examining the rheogram of practical MR fluids. The plastic viscosity for a particular value of field is determined, in practice, from the high shear rate asymptote of rheogram or shear stress vs, shear rate data as shown Fig.F.1. These plastic viscosities for discrete values of magnetization, while reasonably similar in value, are not necessarily identical to the off-state viscosity, so that there exists varying levels of shear thinning. The theory of hard sphere dispersions tells us that viscosity is dependent on particle structure, so when field is applied and the particles form chains, the applicability of dispersion theory to determine η_{pl} is questionable. In an attempt to resolve this dilemma, Berli and de Vincente developed a structure based model for viscosity [159], and used it to model traditional MR fluids as well as inverse ferrofluids. Their analysis leads to low and high shear rate viscosity plateaus, which can be well represented for a typical MR fluid as a Casson plastic,

$$\tau^{1/2} = \tau_y^{1/2} + (\eta_\infty \dot{\gamma})^{1/2}. \tag{F.20}$$

This introduces a field dependent viscosity term that smooths the transition between pre- and post-yield behavior, improving the quality of the fit for some fluids, which typically tend be small particle (thermally influenceable) low yield stress fluids. However, for consistency with the device engineering literature and for ease of analysis, the widely accepted Bingham plastic constant (post-yield) viscosity approximation is sufficient for our purposes.

F.5 Experiment

The Bingham–Mason relationship can be measured directly by examining apparent viscosity. Apparent viscosity, $\eta_{\text{app}} = \tau/\dot{\gamma}$, is the viscosity of a Newtonian fluid that would give the measured stress at the current shear rate. For a Bingham plastic, where

$$\tau = \tau_y + \eta_{pl}\dot{\gamma} \tag{F.21}$$

the apparent viscosity is

$$\eta_{\text{app}} = \tau_y/\dot{\gamma} + \eta_{pl} \tag{F.22}$$

The high shear rate limit of apparent viscosity is denoted as η_∞, and for a Bingham plastic, $\eta_\infty = \eta_{pl}$. Apparent viscosity is often normalized by η_∞, which for a Bingham

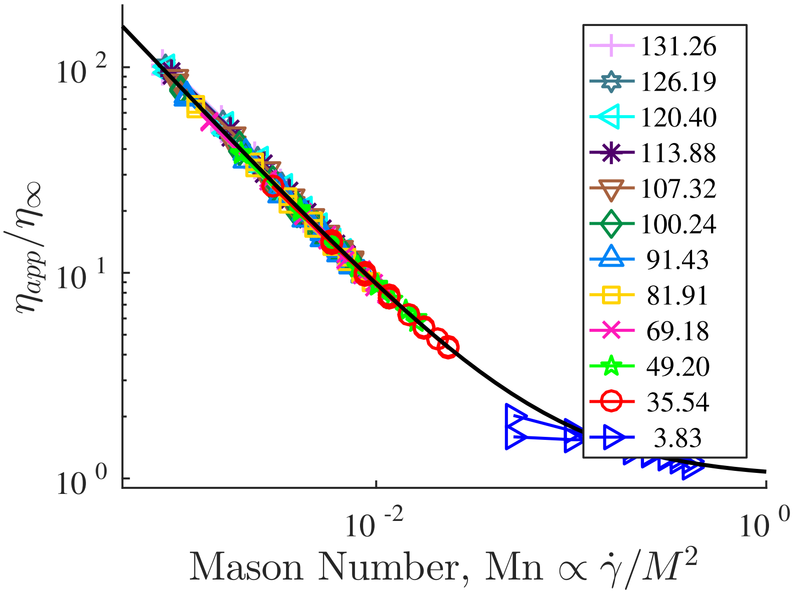

Figure F.3: Normalized apparent viscosity for Lord MRF-140CG

plastic yields,

$$\frac{\eta_{\text{app}}}{\eta_{\infty}} = \frac{\eta_{pl}}{\eta_{pl}} + \frac{\tau_y}{\eta_{pl}\dot{\gamma}} = 1 + \text{Bi}. \tag{F.23}$$

Thus a measurement of apparent viscosity leads directly to a measurement of Bingham number. For MR fluids, a well known result is that when apparent viscosity is plotted against Mason number, a set of curves of apparent viscosity coalesce to a single master curve [35], [159]. Therefore, by using normalized apparent viscosity plotted against Mason number, we obtain a single curve that allows us to directly relate Bingham number to Mason number for a particular MR fluid being measured.

Figure F.3 shows a measurement of apparent viscosity using the commercially available Lord MRF-140CG fluid, demonstrating the collapse of apparent viscosity curves across Mason number. This 20 °C temperature controlled data set was collected using a custom-built high shear rate ($\dot{\gamma} < 10\,000\,\text{s}^{-1}$) Searle cell magnetorheometer [37]. High shear rates are achieved by using a narrow ($d = 0.25\,\text{mm}$) active gap, and the concentric cylinder geometry ensures a uniform shear rate. Using $\dot{\gamma} \gg 0$ avoids nonlinearities associated with near yield flow, and ensures that the data is well modeled as a Bingham plastic. In this experimental procedure, a servomotor rotates the inner cylinder using an ascending staircase velocity profile, while the outer cylinder is connected to a fixed base by a $0.706\,\mathrm{N\,m}$ angular load cell. The applied magnetic field was simulated via a 2D axisymmetric FEM analysis and validated using sensing coil measurements of flux density, and the fluid magnetization was calculated using the characterized field and manufacturer supplied B-H data. Since the carrier fluid formulation for Lord fluids is proprietary, the carrier fluid was obtained by allowing a well mixed sample to separate, and then decanting the sediment-free upper layer. Carrier fluid viscosity was measured on an Anton Paar Phyisca MCR-300 rheometer, with the average of three runs to yield a viscosity value of $\eta_c = 9.9\,\mathrm{mPa\,s}$ at 25 °C.

For magnetorheological fluids, apparent viscosity is typically fitted to a curve of the form

$$\frac{\eta_{\mathrm{app}}}{\eta_\infty} = 1 + K\mathrm{Mn}^{-1}, \tag{F.24}$$

where K is a fitted parameter. In Fig. F.3, we show such a fit, with $K = 0.078$, and $\eta_\infty = 0.59\,\mathrm{Pa\,s}$. Since MR fluids are well described by the Bingham plastic model, from (F.23), $\eta_{\mathrm{app}}/\eta_\infty = 1 + \mathrm{Bi}$, and from our experiment $\eta_{\mathrm{app}}/\eta_\infty = 1 + K\mathrm{Mn}^{-1}$, then $\mathrm{Bi} \propto \mathrm{Mn}^{-1}$, validating (F.12).

The fitted parameter K is also known as the critical Mason number Mn^* [39], [148], [159], and corresponds to the Mason number where the low Mn asymptote of

$\eta_{\text{app}}/\eta_\infty$ intersects $\eta_{\text{app}}/\eta_\infty = 1$, or the Mason number where $\text{Bi} = 1$. From (F.12) the critical Mason number can be expressed as

$$\text{Mn}^* = 3\pi \frac{\tau_y/\tau^*}{\eta_{pl}/\eta_c}, \tag{F.25}$$

which is also the product of Mason and Bingham numbers (F.15). The critical Mason number serves two purposes: it acts as a conversion factor between Mason number and Bingham number, and also acts as a fluid figure of merit. Critical Mason number converts a nondimensionalized input condition (Mason number) to nondimensionalized output condition (Bingham number), so that these two numbers can be easily related. Critical Mason number acts as a controllable force figure of merit with respect to the addition of particles, and can be thought of the benefit the addition of particles has had on yield stress to the penalty paid as in increase in viscosity. Fluids with a large Mn^* possess a larger controllable force ratio, while Mn^* decreases with increased volume fraction. Finally, because τ_y/τ^* and η_{pl}/η_c are analytically accessible ratios, we now have a way to determine critical Mason number during the fluid design process.

However, note that Eq. F.24 is limited to fluids well described by the Bingham plastic model, a description not suited to all electrically and magnetically responsive fluids. In some of these fluids, the fluid scales between $\text{Mn}^{-2/3}$ and Mn^{-1}, where fluids with particles influenced by thermal motion depart from Mn^{-1} scaling [129], [160]–[162]. However these fluids are typically low yield stress fluids measured at low field strengths, and this is attributed to the effects of Brownian forces on the particle

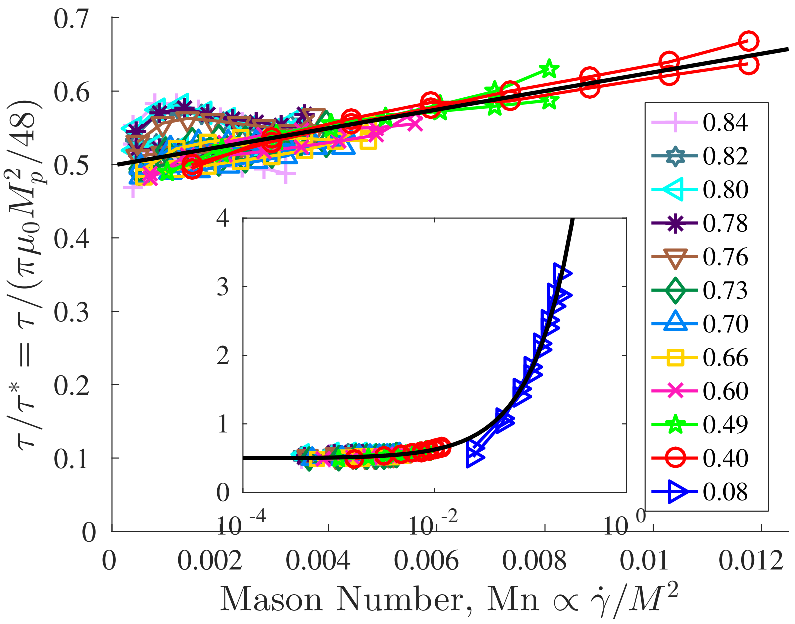

Figure F.4: Normalized stress vs Mason number, with high Mason number data as inset. The black line corresponds to a linear least squares fit, and shows how the low Mason based fit agrees with the inset high Mason number data.

[163]. However, in the context of controllable force applications, where high yield stress fluids are used, thermal effects on the particles are relatively small, and the Bingham plastic model and Mn^{-1} scaling are a proven success [35]. These effects manifest at high Mn, with experimental apparent viscosity data decreasing slower than (F.24) predicts. However for the purpose of relating Bi and Mn, typically at that point Bi is small ($\mathrm{Bi} < 2$), and thus negligible for controllable force applications. Such errors can potentially be resolved through the use of Casson plastic type models [159].

Finally, it should be noted that fitting a line to the apparent viscosity curve can be problematic, especially when high Mn data is unavailable, as there is no clear value for η_∞. An alternate approach is to plot normalized stress, τ/τ^* against Mason number, shown in Fig. F.4. The normalized stress plot demonstrates, like the apparent viscosity plot, that stress values can be collapsed across varying field strengths through Mason number based analysis, while retaining plastic viscosity information at low Mason numbers, unlike apparent viscosity, offering an alternate, improved master curve. This makes determining τ_y/τ^* and η_{pl}/η_c much easier, as for a Bingham plastic, normalized stress is given by

$$\frac{\tau}{\tau^*} = \frac{\tau_y}{\tau^*} + \frac{\eta_{pl}/\eta_c}{3\pi}\mathrm{Mn}. \tag{F.26}$$

Then a simple linear least-squares fit gives $\tau_y/\tau^* = 0.499$ and $\eta_{pl}/\eta_c = 59.9$, from which we generated the previously stated values for K and η_∞. This procedure has the benefit that it separates τ_y/τ^* and η_{pl}/η_c, allowing them to be fit separately, instead of confounding the two terms into K. This fitting procedure works even when there is no high Mason number data, as shown in Fig. F.4. The benefits of plotting in this form is that it clearly shows the successful normalization of yield stress, as well as that η_{pl}/η_c is independent of field, and separates them into discrete elements for easy linear fitting, and serves as a complement to typical stress-shear rate graphs and normalized apparent viscosity graphs. The downside of this plot is that since it is no longer log-log, it much more clearly shows errors and noise in experimental data, and can be quite sensitive to errors in characterization of the magnetic field.

F.6 Discussion

The primary purpose of our analysis is to develop a nondimensional scaling relationship to be used to relate the performance of different devices. In traditional device design, several output parameters (τ_y, η_{pl} and Bi) must be accounted for across a large input space (magnetic field strength, shear rate and temperature), requiring extensive experimental characterization. We want to avoid this, and here Mason number analysis shines – it allows the performance of MR fluid data to be reduced to one single master curve, dependent solely on Mason number. Then to obtain the desired output quantity of controllable force, Eq. F.12, yields the Bingham number. We also show that τ_y can be made independent of magnetization as τ_y/τ^*, and plastic viscosity can be temperature independent in the form of η_{pl}/η_c. This nondimensionalization allows us to take low shear rate, low field data measured on a small fluid sample, and extend it to a large scale energy absorbing device with high fields and high shear rates with a high level of confidence. This is demonstrated for a large scale energy absorbing device operating at $\dot{\gamma} > 25\,000\,\mathrm{s}^{-1}$ in [38].

For pen and paper analysis, there exists the notion of a Mason number above which no chains can form in the fluid, posing an upper limit on the existence of the MR effect. However, if this limiting Mason number occurs at a low Bingham number, the loss in yield stress will not be an issue for experimental devices. In [54], [55], the limiting Mason number was found to be $\mathrm{Mn} \approx 1$. Using (F.12), we can use our previously determined values of τ_y/τ^* and η_{pl}/η_c to find that at $\mathrm{Mn} = 1$, $\mathrm{Bi} = 0.08$, which indicates that this effect occurs at such low controllable force levels that it will have an insignificant effect on MR device performance.

The relation between Bingham and Mason number can also be used to inform the MR fluid design process. For example, let us assume we have a damper with a given device geometry, and we seek to design a fluid such that the damper has a high maximum damping force at maximum field (τ_y/τ^*), a large Bingham number (Mn^*), and a sufficient sedimentation time [52]. For maximizing τ_y/τ^*, we can seek to increase yield stress by increasing M or by raising τ_y/τ^* itself. To increase M, one option is to use particles made out of novel, highly magnetic materials, or alternatively to replace the carrier fluid with ferrofluids, with the intention of increasing the particle magnetization [164], [165]. To raise τ_y/τ^*, we can either increase volume fraction, or more interestingly, use novel particle formulations, such as fluids with nanowires, nonmagnetic particles or differently shaped particles [46], [166]–[169]. Once the particle geometry and type are chosen, choosing the volume fraction is a matter of managing the trade off between yield stress and viscosity, as raising volume fraction raises η_{pl}/η_c faster than τ_y/τ^*, reducing Mn^*. So if we seek to maximize controllable force, the only remaining free variable in (F.12) is η_c in Mason number. The final constraint, settling time, is expected to be dependent on the carrier fluid viscosity and density, and particle geometry, so for our case of fixed particle formulation, long settling times (large η_c) must be balanced against large controllable force ratios (small η_c).

F.7 Conclusion

We demonstrated that Bi $\propto$ Mn^{-1}, or Bi $\times$ Mn is a constant, in magnetorheological fluids, both theoretically and experimentally, resulting in Eq. F.12, a simple algebraic relation. Theoretically, we demonstrated that this behavior arises because microscopic forces and macroscopic forces are linearly related, and experimentally validated this relationship through measurements of apparent viscosity on a high shear rate Searle cell-type rheometer. It was shown that that the relationship between Bingham number and Mason number depends on two nondimensional quantities, τ_y/τ^* and η_{pl}/η_c, and we demonstrated that these ratios represent fundamental fluid properties that are experimentally and analytically accessible. These ratios also define the critical Mason number, Mn^*, through Eq. F.25. In order to identify these quantities, fluid stress measurements were placed in the form of τ/τ^* vs. Mn, allowing for easy identification of τ_y/τ^* and η_{pl}/η_c.

Finally, this relation was used to examine a Mason number corresponding to a theoretical upper limit on the performance of MR fluids, and showed that this Mason number corresponded to Bingham numbers outside the operational range for experimental results. Finally, the MR fluid design process was looked at through the lens of Bi $\propto$ Mn^{-1}, showing how current approaches for novel fluids fall within the recommendations made by the analytical methods in this paper.

F.8 Acknowledgements

S.G. Sherman was supported by a National Science Foundation Graduate Research Fellowship under Grant No. DGE1322106 during the course of this research. A.C. Becnel was supported by a National Defense Science and Engineering Fellowship.

Appendix G: The high shear rate chain limit

This is a reproduction of "Performance of magnetorheological fluids beyond the chain based shear limit" by Stephen G. Sherman and Norman M. Wereley, and published in the Journal of Applied Physics [54].

G.1 Introduction

Magnetorheological (MR) fluids consist of magnetizable particles suspended in a carrier fluid. Upon the application of the magnetic field, the fluid develops a field controllable resistance to stress, the MR effect. This rapidly alterable, field controllable resistance to stress has made MR fluids popular for use in semi-active damping applications. This 'MR' effect is typically attributed to the formation of particle chains in the fluid.

Martin and Anderson [55] observed that the length of stable chains is limited by the shear rate, so that above a critical shear rate, no stable chains exist in an MR fluid. Note that for a typical high volume-fraction MR fluid, the equilibrium state of the particles is sheets and not chains. But if we accept that chain formations are the appropriate model, and that particle chains generate resistance to stress in the fluid, then the MR effect would be mitigated, or even nonexistent, for regimes in which no stable chains can exist. Such a critical shear rate would provide an upper bound on the shear performance for an MR fluid. However, this critical shear rate, determined from a critical Mason number, is quite high and would correspond to a shear rate of $\dot{\gamma} = 200\,000\,\mathrm{s}^{-1}$ for a typical MR fluid at 20% of its saturation magnetization.

Measurements of fluid performance at high shear rates are quite difficult. Flow mode rheometers (e.g. a capillary rheometer or slit rheometer) can achieve shear rates in excess of $250{,}000\mathrm{s}^{-1}$, but these devices induce a varying shear rate across the gap, and at high flow velocities, the particles can exit the magnetized flow volume before the chains have had a chance to form, thereby masking the existence of chain restructuring [12]. Rotating parallel disk rheometers induce a varying shear rate in the MR fluid along the disk radius, and have the tendency to expel fluid from the device at high shear rates. Searle-cell magnetorheometer measurements have been limited to shear rates of $25\,000\,\mathrm{s}^{-1}$ [37].

In this study, we examine the behavior of MR fluids in this high shear rate region through a high performance simulation model [19], [41] based on the work of Klingenberg [34], allowing simple direct measurements of particle structure and fluid stress response. The critical Mason number for a finite-length chain of particles in shear flow is derived, with corrections for long-range forces and the use of the finite-stiffness collision model which is used in our simulations. Using direct simulations, observations are made on how the shear limit affects the static and dynamic yield stress for a range of low volume-fraction fluids.

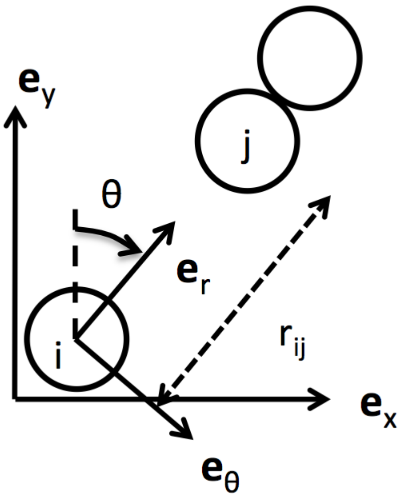

Figure G.1: Reference frames for the particle system.

G.2 Theory

The MR fluid model follows Martin and Anderson [55] and Klingenberg *et al.* [34], where uniformly sized spherical particles act as point dipoles aligned with the external field, H. Each particle is a sphere with a diameter σ, and corresponding moment $m = \frac{1}{6}\pi M\sigma^3$, with magnetization $M = 3\beta H$. The force on dipole i from j is

$$\mathbf{F}_{ij}^{m} = F_0 \frac{1}{(r_{ij}/\sigma)^4}[(3\cos^2\theta_{ij} - 1)\mathbf{e}_r + \sin(2\theta_{ij})\mathbf{e}_\theta], \tag{G.1}$$

where $F_0 = (3\mu_0 m_i m_j)/(4\pi\sigma^4)$, and the other quantities are shown in Fig. G.1. This force can be turned into a reference stress, $\tau^* = F_0/\sigma^2 = \pi\mu_0 M^2/48$.

The particles are assumed to be moving through an implicit carrier fluid with viscosity η_c. The fluid is moving with velocity $\mathbf{v}_c = \dot{\gamma}y\mathbf{e}_x$, where $\dot{\gamma}$ is the shear rate. Particles experience drag $\mathbf{F}^{\mathrm{d}} = 3\pi\sigma\eta_c(\mathbf{v}_c - \mathbf{v}_i)$. This drag can be used in the simulation code to neglect particle accelerations, such that $\mathbf{v}_i = \mathbf{F}_i/3\pi\eta_c\sigma + \mathbf{v}_\infty$. The particle component of stress on the fluid is

$$\tau_{xy} = -\frac{1}{V}\sum_{i=1}^{N}(\mathbf{F}_i \cdot \mathbf{e}_x)(y_i - y_{\mathrm{mid}}). \tag{G.2}$$

At this point it is useful to define the Mason number[35], the ratio of particle viscous forces to particle magnetic forces, here defined as

$$\mathrm{Mn} = \frac{3\pi\eta_c\sigma^2\dot{\gamma}}{F_0} = 144\frac{\eta_c\dot{\gamma}}{\mu_0 M^2}. \tag{G.3}$$

Chains rupture when shear forces exceed the magnetic forces holding the chain together. As in [55], it is assumed that (1) chains are linear, (2) particles are held separate by an infinitely stiff collision force, and (3) long range magnetic forces are negligible. For a finite chain of total length S, the interparticle forces reach their maximum value at the chain center. Solving for the force equilibrium yields

$$\begin{aligned} 2\tan\theta &= f\mathrm{Mn} && \text{(G.4)} \\ \frac{3\cos^2\theta - 1}{\sin\theta\cos\theta} &\geq f\mathrm{Mn}, && \text{(G.5)} \end{aligned}$$

where $f = S^2/8$ when S is even and $f = (S^2 - 1)/8$ when S is odd. This equation has a solution of a maximum angle of $\theta = \cos^{-1}(\sqrt{3/5}) = 39.23°$, and for each S a limiting Mason number above which no chains of that length can form. The $S = 2$ limiting Mason number, that is, the *critical Mason number*, above which no stable chain exists, is $\mathrm{Mn} = 3.266$.

However, in order to simulate these particles we need a repulsion force characterized by a finite stiffness to separate the particles. The standard repulsion force is

$$\mathbf{F}_{ij} = -2F_0 \exp\left[-k\left(\frac{r_{ij}}{\sigma} - 1\right)\right] \mathbf{e}_r. \tag{G.6}$$

Solving for the force equilibrium yields,

$$\begin{aligned} 2\tan\theta &= f\mathrm{Mn}\, r^5 && \text{(G.7)} \\ \cos\theta &= \sqrt{\frac{3}{5} + \frac{2}{5} r^4 \exp[-k(r-1)]}, && \text{(G.8)} \end{aligned}$$

which can be solved for the equilibrium positions of the particles. Two solutions exist to these equations, a close solution and a far solution, with the close solution representing the stable particle chain equilibrium point. For a value of $k = 50$, with the equilibrium point occurring at $\theta^c = 36.43°$ and $r^c = 1.046\sigma$, the critical Mason number for $S = 2$ is $\mathrm{Mn}^c = 2.364$, which is 72% of the infinitely stiff value.

For chains of length $S > 3$, the model must be corrected for long range forces on the particles. Accounting for the forces from the upper half of the chain on the lower half, we obtain the long range correction factor,

$$g(S) = \sum_{i=1}^{\mathtt{floor}(S/2)} \sum_{j=1}^{\mathtt{ceil}(S/2)} \frac{1}{(i+j-1)^4}. \tag{G.9}$$

Let ζ be the Reimann zeta function. In the limit of large S, g approaches $\zeta(3)$, as seen in [55]. Then, for longer chains, the limiting Mason number for a given chain length S is given by $\mathrm{Mn}^*(S) = g\mathrm{Mn}^c$. Another higher-order effect is that particle chains are not straight lines; the nonlinear shape increases the hydrodynamic force on the chain, reducing the critical Mason number. While Martin [55] developed a correction for this change in shape, simulation indicates that this correction is unnecessary for short chains.

G.3 Results

To evaluate what occurs as the stable particle chain size decreases, the conditions of the simulation framework developed in Klingenberg [34] are used. The simulation is conducted for $k = 50$, in a cubic volume of height $h = 62.5\sigma$. To ensure that chains form in the simulation, not sheets, low fluid volume fractions, ranging from $\phi = 0.005$ to 0.05, are used. Force interactions are neglected for particle seperations of $r \geq 4\sigma$. To capture the effects the high shear chain shortening, the static and dynamic yield stresses of the fluid are measured for Mason numbers ranging from 0.13 to 5.2, corresponding to a range of Mn numbers from the $S = 13$ limit to more than twice that of the $S = 2$ limit. Static stress τ_s is the smoothed peak value of stress, and dynamic stress τ_d is the steady state average.

The static yield stress is plotted versus Mason number in Fig. G.2. Vertical lines denote the critical Mason numbers for $S = 2$, 3 and 4. At each of these critical Mason numbers, discontinuities in stress can be observed, with the stress decreasing across the discontinuity as Mason number increases. These discontinuities also support the conclusion that chains in the fluid support the resistance to stress, as if the chains become shorter, and thus weaker, the ability of the MR fluid to resist

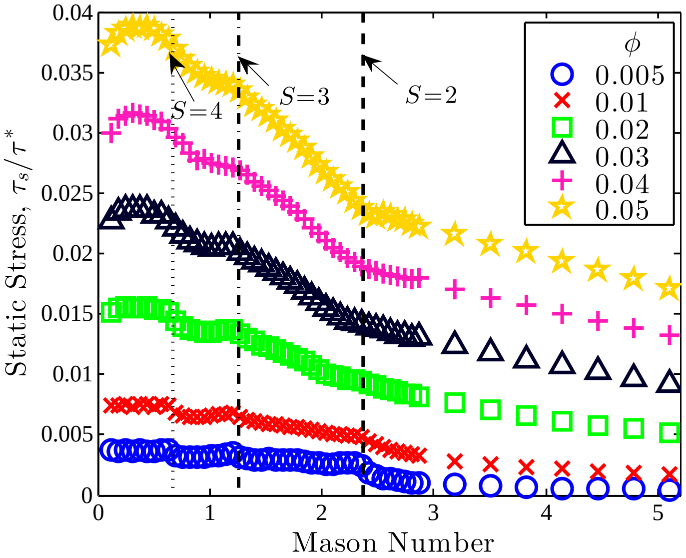

Figure G.2: Static stress with lines indicating the limiting Mason number for $S=2$, 3 and 4.

stress decreases. Changes in stress are not seen for $S > 4$, as the long-distance strengthening factor $g(4) \approx 0.95\zeta(3)$, so that any further strengthening will be small and hard to observe from the data.

Dynamic yield stress is plotted versus Mason number in Fig. G.3. The results are similar to those of the static stress for very low volume fractions, $\phi \leq 0.01$. Step reductions in dynamic stress can be observed at the limiting Mason numbers as Mason number increases. However, at higher volume fractions, the behavior is quite different, with stress increasing up to the $S = 3$ limit, and no distinct changes in the stress profile at the various limiting Mason numbers. It should also be noted that as the Mason number approaches the $S = 2$ value, the static yield stress is rapidly falling and approaching the value of the dynamic yield stress, until at $S = 2$, the dynamic and static yield stresses are nearly identical.

To gain insight into these behaviors, Fig. G.4 plots the mean particle cluster

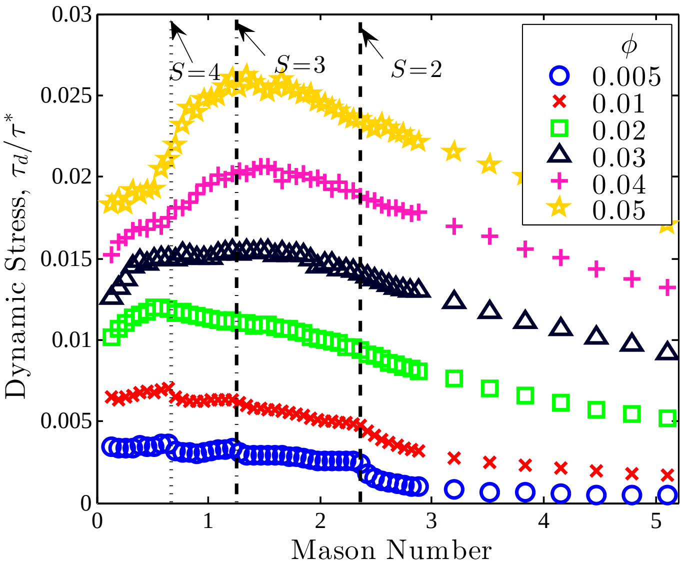

Figure G.3: Dynamic stress with lines indicating Mn* for $S=2$, 3 and 4.

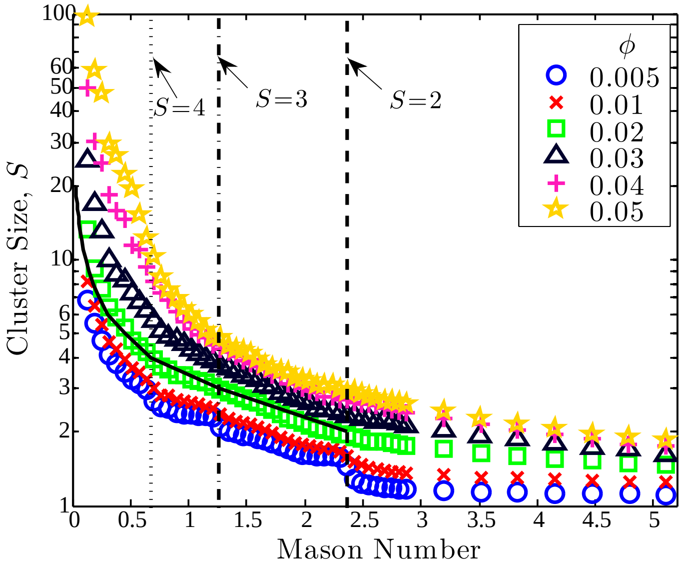

Figure G.4: Steady state chain length with dashed vertical lines indicating Mn* for $S=2$, 3 and 4. The solid line indicates the predicted value of cluster size.

size S versus Mason number. Particles i and j are considered to be in a cluster if $r_{ij} < 1.05\sigma$. For the very low volume fraction fluids, $\phi < 0.01$, there are clear steps in the cluster size at at each of the limiting Mason number values for S=2, 3, and 4, confirming that chains above the limiting size are breaking. The mean cluster size is below its predicted value because of a significant number of solitary particles in the simulation. There are also longer, unstable chains that form and break, with more of these unstable chains occurring as the volume fraction increases. At $\phi = 0.02$, the number of smaller and larger chains is roughly balanced, and the results closely match our prediction. For $\phi > 0.02$, the mean cluster size is larger than what the chain-based model predicts. Here, visual inspection reveals that instead of the particles forming chains in the fluid, they are forming small, sparsely filled sheets. These sheet formations allow a larger cluster size, and explain why, for particle volume fractions $\phi \geq 0.02$, both cluster size and stress measurements diverge from predictions based on particle-chain models.

G.4 Conclusions

Changes that occur in stress and particle cluster size when the Mason number exceeds the limit for stable chains were investigated. Above the critical Mason number and very low volume fractions $\phi \leq 0.01$, sudden or step reductions in the fluid stress and particle cluster size occurred at analytically predicted limiting Mason numbers. These results validated both theoretical predictions [55] and the simulation developed in this study. For volume fractions ranging from 1–5%, high shear-rate reductions of shear stress were observed, but no step changes occurred at the predicted intervals, which can be attributed to the formation of particle sheets, as opposed to particle chains, in the fluid. Reductions were observed in mean particle cluster size at the predicted limiting Mason numbers. However, it is cautioned that the step changes in shear stress at discrete limiting Mason numbers only occur for low-volume-fraction fluids in which the particles form chains. In higher particle volume fraction fluids, where the particles instead form sheets, insights from particle chain formation may be misleading.

Appendix H: Chain dynamics response time

H.1 Introduction

Magnetorheological fluid devices are used as controllable vibration and shock absorbers, and in these scenarios, rapid device response is needed. The time for an actuator to respond to a control input is the response time, and typical magnetorheological devices have response times of milliseconds, but this is a system level property, comprised of many elements. The precise response time of the fluid itself is not specifically known, but Laun and Gabriel [64] performs the best measurements available, and find response times of $t_r = 1 - 3\,\mathrm{ms}$.

Most response-time measurements are of devices and systems, and thus include many confounding factors. The largest component is the response time of the magnetic circuit, caused by its inductance. This response time can be significantly reduced through a power supply with feedback control [106]. There is also delay between the current applied to the magnetic circuit and the magnetic-field response, caused by eddy currents [64]. This delay can be estimated with a magnetics FEA program, and mitigated through material selection. Koo *et al.* [62] show the importance of device compliance in response time, and that increasing piston speeds will eliminate the effects of compliance. They also measure an increasing circuit response time with increasing applied current, but a decreasing force response time with applied current. Sahin *et al.* [63] conducts benchtop measurements of flow mode response time to a step current at a constant flow rate, and finds response times from 10 to 20 ms, with response time decreasing with increased applied current. This much larger than the values of Laun, but we show here that once the fluid dynamic response time is included, the response time falls into line with shear mode measurements.

Shear-mode response-time measurements offer a near direct measurement of the rheological response time. Kikuchi *et al.* [170] examine the response time to a step current, reporting results in terms of response shear, $\gamma_r = t_r\dot{\gamma}$, and Mason number, an approach we adopt. Despite opting to include magnetic circuit delays, they report a response shear of $\gamma_r = 1 - 5$. An alternative is to obtain response time from a sinusoidally varying field. Tests on fluids with nanoparticles [171] estimate $t_r < 5\,\mathrm{ms}$ at $\dot{\gamma} = 28\,\mathrm{s}^{-1}$ and $B = 0.05\,\mathrm{T}$, or $\mathrm{Mn} \approx 10^{-2}$, $\gamma_r = 0.14$. Highly refined parallel-plate measurements were conducted by Laun and Gabriel [64], considering both sinusoidal and step response times at $B = 1\,\mathrm{T}$, $\dot{\gamma} = 100\,\mathrm{s}^{-1}$, and found 63.2% response times of 3.2 ms under a sinusoidal current, 2.8 ms to an applied step current, and 1.8 ms when current is removed, corresponding to $\mathrm{Mn} \approx 3 \times 10^{-4}$ and $\gamma_r \approx 0.3$.

In this paper, we consider two elements of the response time: the rheological response time of the fluid, and the response time caused by the fluid dynamics. The rheological response time is straightforward: it is the time it takes for a stress to develop in response to an applied field. In flow mode, the change in rheology changes the velocity profile, causing a fluid dynamic response time. This fluid-dynamic response time is largely uninvestigated for controllable yield stress fluids, so we use the existing Bingham plastic literature [115] to develop estimates for various flow regimes. Switching focus to the rheological response time, we use a particle-dynamics simulation to show that the rheological response time is primarily dependent on the shear rate, and will have response shear $\gamma_r < 1$ for any Mason number. This fixed shear strain response allows us to neglect rheological time domain effects for most large displacement engineering problems, a useful result.

H.2 Background

Magnetorheological fluids are typically modeled as Bingham plastics. In the typical Bingham plastic model for MR fluids, $\tau = \tau_y + \eta_\infty \dot{\gamma}$, where τ_y is magnetic field dependent, and η_∞ is constant. The fundamental nondimensional number governing the bulk flow of Bingham plastics is the Bingham number,

$$\mathrm{Bi} = \frac{\tau_y}{\eta_\infty \dot{\gamma}_c} = \frac{\tau_y\, h}{\eta_\infty v_0}. \tag{H.1}$$

The characteristic shear rate, $\dot{\gamma}_c = v_0/h$, is an inverse characteristic time scale, where v_0 and h are the characteristic speed and length scale of the system.

To capture a rheological response time, we need a time dependent rheological model. The most basic time dependent rheological model is the Maxwell model [172], which when expressed in a fixed frame is

$$\tau + \lambda \frac{\partial \tau}{\partial t} = -\eta \dot{\gamma}$$

with a fixed relaxation time scale λ. However, correctly handling time dependence is complicated and we wish to avoid it. Our basic observation is that in steady shear experiments, the response time does not appear to be a constant fluid property nor does it scale with the particle dynamic time scale – instead the response time appears to scale with $\dot{\gamma}^{-1}$. This allows us to treat it as a response strain, a spatial effect.

But before we determine the fundamental rheological response time, we need to characterize the response time of the fluid system.

H.3 Fluid Dynamics

The key feature of fluid dynamic response times is that they are independent of velocity. For Newtonian fluids, Schlichting [114, p. 85] showed that fluid response time has a dimensionless time scale, T_r, where $T_r = \eta t_r/\rho h^2$, with t_r the physical time scale. From Schlichting, startup of Newtonian shear flow, the fluid will reach 90% convergence to steady state when $T_r \approx 0.15$. The Newtonian solution forms an upper bound for the controllable fluid response time, and here using typical values for MR fluid, $\eta_\infty = 0.1\,\mathrm{Pa\,s}, \rho = 3\,\mathrm{g/cm^3}, h = 1\,\mathrm{mm}$, indicates that $t_r < 5\,\mathrm{ms}$. For Bingham plastics, a reasonable estimate for response time is $T_r = 0.15/(1 + \mathrm{Bi})$, which is the Newtonian result using η instead of η_∞.

However, the relevant model problem for controllable fluid response time is not startup shear flow, but a fluid under steady shear which has a field suddenly applied. In this case, the steady state velocity profile is the same both with and without a yield stress, so there is no response time associated with a change in velocity profile.

Then, any measured response time will be the rheological response time, the subject of the next section.

In flow mode, there are two benchmark problems, a stationary flow which is suddenly accelerated, and the case of a flow that suddenly has magnetic field applied. For the impulsively accelerated flow, the response time can be approximated by classic startup flow, where a stationary Bingham plastic has a constant pressure applied. This has been worked extensively [115], and we take the analytical 1-D solutions and solve for a 90% midline velocity response time. Using their solutions, response time can be fit $T_r = 0.235/1 + 0.2\text{Bi}$. For a typical high speed MR fluid device, $\text{Bi} > 10$, $T_r < 0.1$, so $t_r < 3\,\text{ms}$.

We can also consider the response time of a steady pressure driven Newtonian flow that suddenly develops a yield stress. Here, the fluid dynamic response time is non-zero, as the steady state profile changes with the imposition of yield stress. To our knowledge, no correct analysis exists for this response time. However, Newtonian startup flow should be a conservative estimate for the flow mode step-field response time, and will be generally applicable.

For experimental validation of the startup-flow response time estimate, Sahin *et al.* [63] measure response times from 22 ms to 12 ms, when corrected for magnetic field effects, with fluid response time decreasing as field strength is increased. Using $T_r = 0.235/(1 + 0.2\,\text{Bi})$, $\text{Bi} \approx 30$ and $h = 3\,\text{mm}$, $t_r \approx 10\,\text{ms}$, around half the fluid response time. However, minimal fluid properties are reported, so this can only serve as a loose estimate. However, our claim is that once the fluid dynamic response time is accounted for, flow mode measurements begin to approach shear mode response times, which it does here.

H.4 Rheology

The basic idea of a controllable fluid rheological response time is that it takes some period of time for the yield stress inducing particle structure to form, and this microstructure response time causes the macroscopic stress response time. Here, we claim that the rheological response time does not scale with the particle dynamics response time, but with the shear rate.

In the classic acceleration free Klingenberg model [34], here modified for particles with non-uniform sizes, the dynamics are governed by:

$$\begin{aligned}
\frac{D_0\sigma}{F_0}\frac{D_i}{D_0}\frac{\dot{\mathbf{x}}_i}{\sigma} &= \sum_{\substack{j=1\\ j\neq i}}^{N}\left[\mathbf{F}_{ij}^{m}+\mathbf{F}_{ij}^{c}\right]+\mathrm{Mn}\frac{D_i}{D_0}\frac{y_i}{\sigma}\mathbf{e}_x \\
\mathbf{F}_{ij}^{m} &= \frac{F_m}{F_0}\frac{(3\cos^2\theta_{ij}-1)\mathbf{e}_r+\sin 2\theta_{ij}\mathbf{e}_\theta}{(r_{ij}/(a_i+a_j))^4} \\
\mathbf{F}_{ij}^{c} &= -2\frac{F_m}{F_0}\exp\left[-k\left(\frac{r_{ij}}{a_i+a_j}-1\right)\right]\mathbf{e}_r \\
F_m &= \frac{3\mu_0 m_i m_j}{4\pi(a_i+a_j)^4} \quad F_0=\frac{\pi}{48}\mu_0 M^2\sigma^2 \\
D_i &= 6\pi\eta_c a_i \qquad D_0 = 3\pi\eta_c\sigma \\
m_i &= 4/3\pi a_i^3 M \quad \tau_{yx}=\sum_{i=1}^{N}\frac{(\mathbf{F}_i\cdot\mathbf{e}_x)y_i}{V}.
\end{aligned}$$

Here, σ is the characteristic length scale, which is chosen to be the median particle diameter, k is the collision stiffness factor, η_c is the carrier fluid viscosity, individual particle radius a_i, $\mathbf{r}_{ij}$ the distance vector between particles i and j, and M the magnetization. In this formulation, the Mason number is $\mathrm{Mn} = D_0\sigma\dot{\gamma}/F_0 =$

$144\eta_c\dot{\gamma}/\mu_0 M^2$ and there is an associated particle dynamics time scale, $D_0\sigma/F_0 = 144\eta_c/\mu_0 M^2$. Then, if the microstructure causes the yield stress, and then rheological response time will scale with the particle dynamics time scale or $\propto 1/M^2$. A brief examination of the literature shows no direct investigations of the field dependence of response time,[63], [170], but the measurements we do have indicate only weak field dependence once fluid dynamic terms are corrected for. Again, for direct shear measurements, Laun and Gabriel [64] performs all measurements between 0 and 1 T for both sinusoidal and step currents, and demonstrate that the transient can be described very accurately by one fixed response time, indicating that the measured response time is field independent. This is expected, as the particle dynamics response time is very short, as $144\eta_c/\mu_0 M^2 \approx 0.5\,\mu\text{s}$ for a typical fluid with $\eta_c = 0.01\,\text{Pa s}$ and particles near saturation $M = 1500\,\text{kA/m}$. But if we consider that the response time is caused by the other time scale in the fluid, $\dot{\gamma}^{-1}$, the dimensionless time scale becomes a shear, $\gamma = t_r\dot{\gamma}$, and we observe that all high quality shear-mode response-time experiments have response shears with $\gamma < 1$.

This argument is made more powerful, as a response shear instead of time has been predicted by classic particle chain models. These models work by assuming the chains form instantaneously, and then are deformed under shear, with the shear deformation causing the shear stress response. The assumption of instantaneous chain formation can be justified from the Mason number, as typical experiments have $\text{Mn} < 10^{-2}$, so the particle dynamics response time is necessarily much shorter than the shear rate, and the instantaneous chain formation concept is thus reasonable. Typical analytical chain models will give shear stress as a function of chain angle, and where the angle is equivalent to a shear strain. The maximum in this relationship defines a response strain. Ginder and Davis [65] looks at partially magnetically saturated particle chains, and find $\gamma_r \approx .45$. Bossis *et al.* [163] reports $\gamma_r \approx 0.1$ using FEM models and experimental measurements of single width particle chains. Martin and Anderson [55] show maximum stress occurs at $\gamma \leq \sqrt{2/5}$ or $\gamma \leq 0.63$ for dipolar single width chains.

This response time as shear strain argument is bolstered by experiments showing the onset of yielding occurring at a fixed strain. Small amplitude oscillatory shear (SAOS) measurements can be used to formulate a Maxwell like fluid model with compliance at small strains [173], and such a model will contain a response time. An investigation into yielding process of MR fluids under SAOS through a variety of methods[174] concludes that flow and steady state shear stresses start at strains of $\gamma_r \approx 1$.

If we want to go beyond simple chain models, we can directly examine the rheological response time for complex structures by performing a particle dynamics simulation undergoing simultaneous structure formation and shearing. To do this, we use the previously described dynamics, with force interactions cut off at $4(a_i + a_j)$. The upper and lower walls are given hard wall boundary conditions, and the sides are given periodic boundary conditions. The only inputs to the system are the Mason number Mn, collision stiffness k, and the initial particle distribution. The particles are given a log-normal radius distribution, with all cases having a distribution parameter of $\sigma_{LN} = 0.2$. The use of a log normal distribution instead of a uniform particle distribution will affect the onset of yielding behavior, but is a more realistic choice

[41], [42]. These equations are integrated using an adaptive third order integration scheme [175], with integration error constrained to $10^{-3}\sigma$, which improves solver stability and accuracy at large time steps.

We start the particles in random positions, relax the configuration until all particles all well separated, and then instantly apply a magnetic field and shear rate. At this point the particles begin to form chains and, from here we record the stress and use the stress history to identify the response time. We define the response time as when shear stress, τ_{yx} reaches 90% of the maximum recorded stress value.

Figure H.1a plots simulated response time scaled by the particle dynamics time scale for volume fractions $\phi = 0.2$ to $\phi = 0.4$ in a cubic volume of $L = 50\sigma$ at $k = 100$, and shows a strongly decreasing response time with increasing Mason number. We also see a sudden drop in response time at $\mathrm{Mn} \approx 2$, near the critical Mason number where no chains can form, Mn=3.2 [54], [55]. Newtonian fluids should have a very fast response time, so this result confirms that once there are no chains, the fluid becomes Newtonian. However, at large Mason numbers, where magnetic forces are small, the isolated particle drag model means that the experimental relevance of these results is questionable.

Alternatively, Fig. H.1b plots the same data using the characteristic time scale of the fluid dynamics, the shear rate, $\dot{\gamma}^{-1}$, which gives us a response shear, $\gamma_r = t_r\dot{\gamma}$. This presentation allows validation against the previously discussed results [55], [64], [65], [163], [171], where reported values of γ_r have been scaled to a 90% response time. Then in this time scale perspective, we observe that $0.2 < \gamma_r < 1$ for five orders of magnitude in variation of Mason number, indicating that it holds roughly constant.

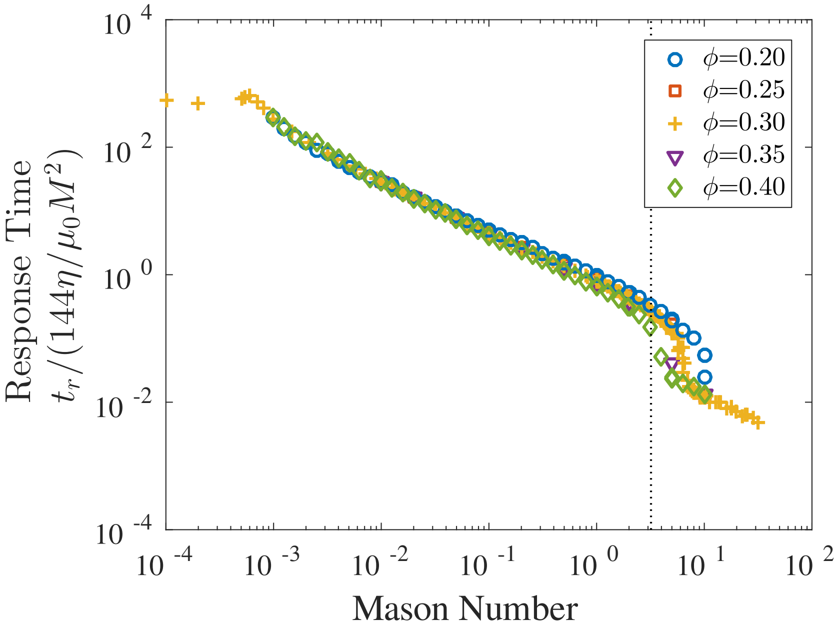

(a) T_r

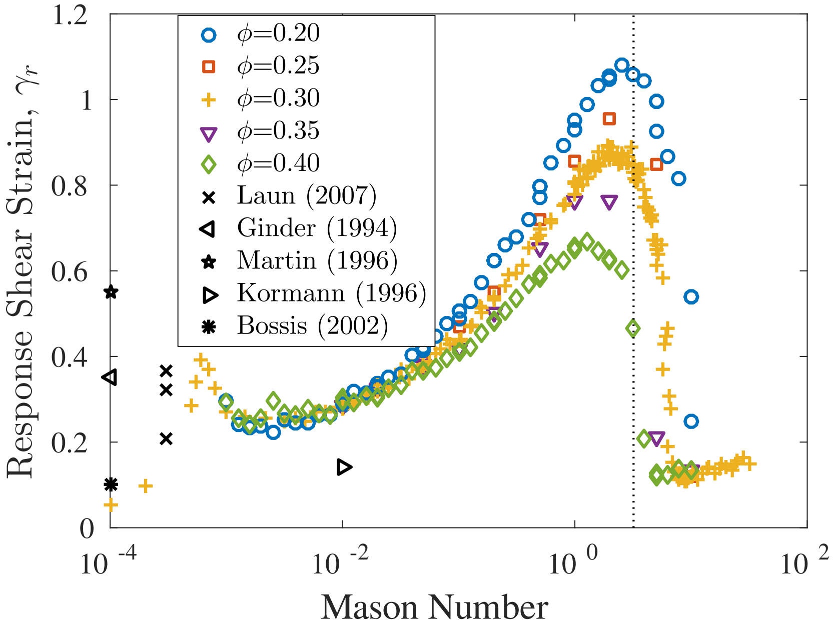

(b) γ_r

Figure H.1: Simulated dimensionless response time as a function of volume fraction.

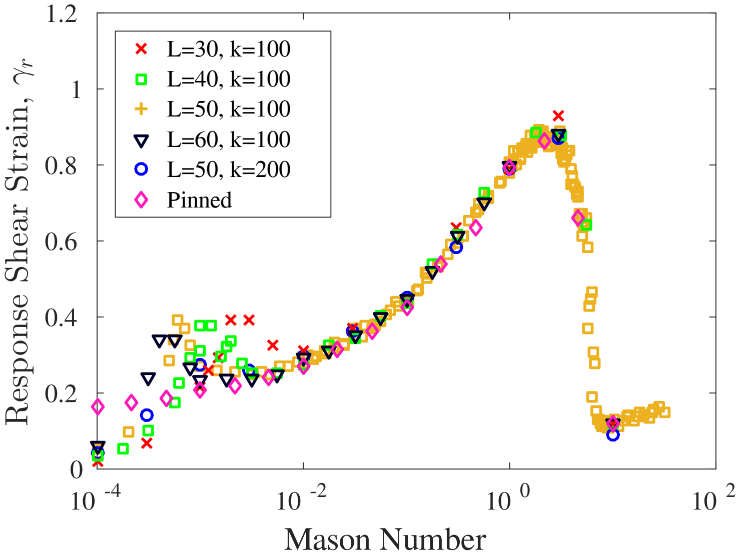

Figure H.2: Effects of simulation parameters on γ_r.

On this same graph, we can validate against the previously listed experimental and theoretical results, which have $0.1 < \gamma_r < 0.7$. While there is significant spread, measurements and models of response time are difficult to make, but critically, all results indicate that $\gamma_r < 1$.

We also note that at low Mason numbers, response time is significantly affected by choice of simulation parameters. Figure H.2 shows the effects of model parameters: collision stiffness k, total simulation length scale L, and boundary conditions. For stiffer values of k, response shear shows no change. However, wall slip boundary conditions and the size of the simulation volume has a substantial effect at low Mason numbers. The response strain has a peak at low Mason numbers, with the peak moving towards lower Mason numbers with increasing simulation size. At Mason numbers below the peak, the response strain rapidly falls off, as does shear stress. Martin and Anderson show a similar shear angle falloff for isolated chains with interacting with frictionless walls [55], caused by the walls limiting chain length, and thus shear stress. They show that by switching to boundary conditions with friction, they show that at low Mn, friction raises the maximum stable chain angle/shear. We simulate friction through pinned boundary conditions at $L = 50\sigma$ and $k = 100$, and we with pinned and unpinned results identical at Mn $> 10^{-2}$, but at low Mn, pinned simulations have a constant response strain. Since we use 10^5 particles versus the typical 10^3, this also indicates that pinning the particles is essential in small simulations for eliminating simulation size dependence. We also note that using pinned particles keep wall shear stresses constant from Mn $= 10^{-4}$ to 10^0. Overall, the parameter study confirms our basic result: response time scaling with shear rate, not the particle dynamics time scale.

Static chain models, dynamic particle models and experimental measurements all agree that maximum force will be reached by $\gamma < 1$. This implies that rising device speeds will cause a commensurate decrease in rheological response time, indicating that response time won't pose an issue for high speed devices. Instead, a fix response strain means an apparent shortening of the duct, as the fluid will require some displacement to develop a stress.

H.5 Conclusion

We claim that magnetorheological fluids have no response time, but instead a response shear. First we show that fluid flow has an associated fluid dynamic response time, and removing the fluid dynamic response time brings flow mode measurements into line with shear mode experiments. We then examined the rheological response time by simulating the particle dynamics under instantly applied shear and field, and showed that the simulated response time scales with $\dot{\gamma}^{-1}$, and showed that a response shear of $\gamma_r < 1$ agrees with both experimental measurements and basic chain models. This response shear means that devices can operate at short time scales, as long as the characteristic time scale of the fluid dynamics, $\dot{\gamma}_c^{-1}$, is less than the desired actuation time scale.

Bibliography

[1] A. Kareem, T. Kijewski, and Y. Tamura, "Mitigation of motions of tall buildings with specific examples of recent applications," *Wind and Structures*, vol. 2, no. 3, pp. 201–251, 1999.

[2] D. Hrovat, P. Barak, and M. Rabins, "SemiActive versus Passive or Active Tuned Mass Dampers for Structural Control," *Journal of Engineering Mechanics*, vol. 109, no. 3, pp. 691–705, 1983. DOI: `10.1061/(ASCE)0733-9399(1983)109:3(691)`.

[3] G. W. Housner, L. A. Bergman, T. K. Caughey, A. G. Chassiakos, R. O. Claus, S. F. Masri, R. E. Skelton, T. T. Soong, B. F. Spencer, and J. T. P. Yao, "Structural Control: Past, Present, and Future," *Journal of Engineering Mechanics*, vol. 123, no. 9, pp. 897–971, 1997. DOI: `10.1061/(ASCE)0733-9399(1997)123:9(897)`.

[4] B. Spencer and M. Sain, "Controlling buildings: a new frontier in feedback," *IEEE Control Systems Magazine*, vol. 17, no. 6, pp. 19–35, 1997. DOI: `10.1109/37.642972`.

[5] J. D. Carlson and M. R. Jolly, "MR fluid, foam and elastomer devices," *Mechatronics*, vol. 10, no. 4-5, pp. 555–569, 2000. DOI: `10.1016/S0957-4158(99)00064-1`.

[6] W. M. Winslow, "Induced fibration of suspensions," *Journal of Applied Physics*, vol. 20, no. 12, pp. 1137–1140, 1949. DOI: `10.1063/1.1698285`.

[7] J. Rabinow, "The Magnetic Fluid Clutch," *Transactions of the American Institute of Electrical Engineers*, vol. 67, no. 2, pp. 1308–1315, 1948. DOI: `10.1109/T-AIEE.1948.5059821`.

[8] J. D. Carlson, D. M. Catanzarite, and K. A. S. Clair, "Commercial Magnetorheological Fluid Devices," *International Journal of Modern Physics B*, vol. 10, no. 23-24, pp. 2857–2865, 1996. DOI: `10.1142/S0217979296001306`.

[9] A. L. Browne, J. D. McCleary, C. S. Namuduri, and S. R. Webb, "Impact Performance of Magnetorheological Fluids," *Journal of Intelligent Material Systems and Structures*, vol. 20, no. 6, pp. 723–728, 2008. DOI: `10.1177/1045389X08096358`.

[10] G. J. Hiemenz, Y.-T. Choi, and N. M. Wereley, "Semi-Active Control of Vertical Stroking Helicopter Crew Seat for Enhanced Crashworthiness," *Journal of Aircraft*, vol. 44, no. 3, pp. 90–90, 2007. DOI: `10.2514/1.26492`.

[11] F. D. Goncalves, "Characterizing the Behavior of Magnetorheological Fluids at High Velocities and High Shear Rates," PhD thesis, Viriginia Polytechnic Institute, 2005, p. 103.

[12] F. D. Goncalves, M. Ahmadian, and J. D. Carlson, "Investigating the magnetorheological effect at high flow velocities," *Smart Materials and Structures*, vol. 15, no. 1, pp. 75–85, 2006. DOI: `10.1088/0964-1726/15/1/036`.

[13] M. Mao, "Adaptive Magnetorheological Sliding Seat System for Ground Vehicles," PhD thesis, University of Maryland, 2011, p. 276.

[14] M. Mao, W. Hu, Y. T. Choi, N. M. Wereley, A. L. Browne, and J. C. Ulicny, "Experimental validation of a magnetorheological energy absorber design analysis," *Journal of Intelligent Material Systems and Structures*, vol. 25, no. 3, pp. 352–363, 2013. DOI: `10.1177/1045389X13494934`.

[15] H. Sodeyama, K. Suzuki, and K. Sunakoda, "Development of Large Capacity Semi-Active Seismic Damper Using Magneto-Rheological Fluid," *Journal of Pressure Vessel Technology*, vol. 126, no. 1, p. 105, 2004. DOI: `10.1115/1.1634587`.

[16] A. C. Becnel, S. G. Sherman, W. Hu, and N. M. Wereley, "Squeeze strengthening of magnetorheological fluids using mixed mode operation," *Journal of Applied Physics*, vol. 117, no. 17, 2015. DOI: `10.1063/1.4907603`.

[17] M. Ocalan and G. H. McKinley, "Rheology and microstructural evolution in pressure-driven flow of a magnetorheological fluid with strong particle-wall interactions," *Journal of Intelligent Material Systems and Structures*, vol. 23, no. 9, pp. 969–978, 2012. DOI: `10.1177/1045389X11429601`.

[18] D. J. Klingenberg and C. F. Zukoski, "Studies on the steady-shear behavior of electrorheological suspensions," *Langmuir*, vol. 6, no. 1, pp. 15–24, 1990. DOI: `10.1021/la00091a003`.

[19] S. G. Sherman, D. A. Paley, and N. M. Wereley, "Parallel Simulation of Transient Magnetorheological Direct Shear Flows Using Millions of Particles," *IEEE Transactions on Magnetics*, vol. 48, no. 11, pp. 3517–3520, 2012. DOI: `10.1109/TMAG.2012.2201214`.

[20] H. G. Lagger, C. Bierwisch, J. G. Korvink, and M. Moseler, "Discrete element study of viscous flow in magnetorheological fluids," *Rheologica Acta*, vol. 53, no. 5-6, pp. 417–443, 2014. DOI: `10.1007/s00397-014-0768-0`.

[21] H. G. R. Lagger, "Particle-based simulation of sheared magnetorheological fluids," PhD thesis, Albert Ludwigs University of Freiburg, 2014.

[22] H. G. Lagger, T. Breinlinger, J. G. Korvink, M. Moseler, A. Di Renzo, F. Di Maio, and C. Bierwisch, "Influence of hydrodynamic drag model on shear stress in the simulation of magnetorheological fluids," *Journal of Non-Newtonian Fluid Mechanics*, vol. 218, pp. 16–26, 2015. DOI: `10.1016/j.jnnfm.2015.01.010`.

[23] D. J. Klingenberg, F. van Swol, and C. F. Zukoski, “The small shear rate response of electrorheological suspensions. I. Simulation in the pointdipole limit,” *The Journal of Chemical Physics*, vol. 94, no. 9, p. 6160, 1991. DOI: `10.1063/1.460402`.

[24] D. J. Klingenberg, F. van Swol, and C. F. Zukoski, “The small shear rate response of electrorheological suspensions. II. Extension beyond the point dipole limit,” *The Journal of Chemical Physics*, vol. 94, no. 9, pp. 6170–6178, 1991. DOI: `10.1063/1.460403`.

[25] H. Ly, F Reitich, M. Jolly, H. Banks, and K Ito, “Simulations of Particle Dynamics in Magnetorheological Fluids,” *Journal of Computational Physics*, vol. 155, no. 1, pp. 160–177, 1999. DOI: `10.1006/jcph.1999.6335`.

[26] K Han, Y. T. Feng, and D. R. J. Owen, “Three-dimensional modelling and simulation of magnetorheological fluids,” *International Journal for Numerical Methods in Engineering*, vol. 84, no. 11, pp. 1273–1302, 2010. DOI: `10.1002/nme.2940`.

[27] R. T. Bonnecaze and J. F. Brady, “Dynamic simulation of an electrorheological fluid,” *The Journal of Chemical Physics*, vol. 96, no. 3, p. 2183, 1992. DOI: `10.1063/1.462070`.

[28] M Parthasarathy and D. J. Klingenberg, “Electrorheology: Mechanisms and models,” *Materials Science and Engineering: R: Reports*, vol. 17, no. 2, pp. 57–103, 1996. DOI: `10.1016/0927-796X(96)00191-X`.

[29] D. J. Klingenberg and J. C. Ulicny, “Enhancing magnetorheology,” *International Journal of Modern Physics B*, vol. 25, no. 07, p. 911, 2011. DOI: `10.1142/S021797921105847X`.

[30] J. C. Ulicny, K. S. Snavely, M. A. Golden, and D. J. Klingenberg, “Enhancing magnetorheology with nonmagnetizable particles,” *Applied Physics Letters*, vol. 96, no. 23, p. 231 903, 2010. DOI: `10.1063/1.3431608`.

[31] Nvidia, *NVIDIA CUDA C Programming Guide*, 2011.

[32] K. W. Yung, P. B. Landecker, and D. D. Villani, “An Analytic Solution for the Force Between Two Magnetic Dipoles,” *Magnetic and Electrical Separation*, vol. 9, no. 1, pp. 39–52, 1998. DOI: `10.1155/1998/79537`.

[33] M Parthasarathy and D. J. Klingenberg, “A microstructural investigation of the nonlinear response of electrorheological suspensions I. Start up of steady shear flow,” *Rheologica Acta*, vol. 34, no. 5, pp. 417–429, 1995. DOI: `10.1007/BF00396555`.

[34] D. J. Klingenberg, F. van Swol, and C. F. Zukoski, “Dynamic simulation of electrorheological suspensions,” *The Journal of Chemical Physics*, vol. 91, no. 12, p. 7888, 1989. DOI: `10.1063/1.457256`.

[35] D. J. Klingenberg, J. C. Ulicny, and M. A. Golden, “Mason numbers for magnetorheology,” *Journal of Rheology*, vol. 51, no. 5, p. 883, 2007. DOI: `10.1122/1.2764089`.

[36] F Vereda, J de Vicente, J. P. Segovia-Gutiérrez, and R Hidalgo-Alvarez, "Average particle magnetization as an experimental scaling parameter for the yield stress of dilute magnetorheological fluids," *Journal of Physics D: Applied Physics*, vol. 44, no. 42, p. 425 002, 2011. DOI: `10.1088/0022-3727/44/42/425002`.

[37] A. C. Becnel, W. Hu, and N. M. Wereley, "Measurement of magnetorheological fluid properties at shear rates of up to 25 000/s," *IEEE Transactions on Magnetics*, vol. 48, no. 11, pp. 3525–3528, 2012. DOI: `10.1109/TMAG.2012.2207707`.

[38] A. C. Becnel, S. Sherman, W. Hu, and N. M. Wereley, "Nondimensional scaling of magnetorheological rotary shear mode devices using the Mason number," *Journal of Magnetism and Magnetic Materials*, vol. 380, pp. 90–97, 2015. DOI: `10.1016/j.jmmm.2014.10.049`.

[39] J. de Vicente, D. J. Klingenberg, and R. Hidalgo-Alvarez, "Magnetorheological fluids: a review," *Soft Matter*, vol. 7, no. 8, p. 3701, 2011. DOI: `10.1039/c0sm01221a`.

[40] S. G. Sherman, L. A. Powell, A. C. Becnel, and N. M. Wereley, "Scaling temperature dependent rheology of magnetorheological fluids," *Journal of Applied Physics*, vol. 117, no. 17, p. 17C751, 2015. DOI: `10.1063/1.4918628`.

[41] S. G. Sherman and N. M. Wereley, "Effect of Particle Size Distribution on Chain Structures in Magnetorheological Fluids," *IEEE Transactions on Magnetics*, vol. 49, no. 7, pp. 3430–3433, 2013. DOI: `10.1109/TMAG.2013.2245409`.

[42] J. C. Fernández-Toledano, J. A. Ruiz-López, R. Hidalgo-Álvarez, and J. de Vicente, "Simulations of polydisperse magnetorheological fluids: A structural and kinetic investigation," *Journal of Rheology*, vol. 59, no. 2, pp. 475–498, 2015. DOI: `10.1122/1.4906544`.

[43] F Vereda, J. P. Segovia-Gutiérrez, J de Vicente, and R Hidalgo-Alvarez, "Particle roughness in magnetorheology: effect on the strength of the field-induced structures," *Journal of Physics D: Applied Physics*, vol. 48, 15309 (11p), 2015. DOI: `10.1088/0022-3727/48/1/015309`.

[44] M. T. Lopez-Lopez, P. Kuzhir, and G. Bossis, "Magnetorheology of fiber suspensions. I. Experimental," *Journal of Rheology*, vol. 53, no. 1, p. 115, 2009. DOI: `10.1122/1.3005402`.

[45] P. Kuzhir, M. T. Lopez-Lopez, and G. Bossis, "Magnetorheology of fiber suspensions. II. Theory," *Journal of Rheology*, vol. 53, no. 1, p. 127, 2009. DOI: `10.1122/1.3005405`.

[46] J de Vicente, J. P. Segovia-Gutiérrez, E Andablo-Reyes, F Vereda, and R Hidalgo-Alvarez, "Dynamic rheology of sphere- and rod-based magnetorheological fluids.," *The Journal of chemical physics*, vol. 131, no. 19, p. 194 902, 2009. DOI: `10.1063/1.3259358`.

[47] H. M. Laun, C. Gabriel, and C. Kieburg, "Wall material and roughness effects on transmittable shear stresses of magnetorheological fluids in plateplate magnetorheometry," *Rheologica Acta*, vol. 50, no. 2, pp. 141–157, 2011. DOI: `10.1007/s00397-011-0531-8`.

[48] B. Kavlicoglu, F. Gordaninejad, and X. Wang, "A Unified Approach for Flow Analysis of Magnetorheological Fluids," *Journal of Applied Mechanics*, vol. 78, no. 4, p. 041 008, 2011. DOI: `10.1115/1.4003346`.

[49] W. Li and X. Zhang, "The effect of friction on magnetorheological fluids," *Korea-Australia Rheology Journal*, vol. 20, no. 2, pp. 45–50, 2008.

[50] J. de Vicente and J. Ramírez, "Effect of friction between particles in the dynamic response of model magnetic structures.," *Journal of colloid and interface science*, vol. 316, no. 2, pp. 867–76, 2007. DOI: `10.1016/j.jcis.2007.08.022`.

[51] I. B. Jang, H. B. Kim, J. Y. Lee, J. L. You, H. J. Choi, and M. S. Jhon, "Role of organic coating on carbonyl iron suspended particles in magnetorheological fluids," *Journal of Applied Physics*, vol. 97, no. 10, pp. 10–13, 2005. DOI: `10.1063/1.1853835`.

[52] J. D. Carlson, "What Makes a Good MR Fluid?" *Journal of Intelligent Material Systems and Structures*, vol. 13, no. 7-8, pp. 431–435, 2002. DOI: `10.1106/104538902028221`.

[53] S. G. Sherman, A. C. Becnel, and N. M. Wereley, "Relating Mason number to Bingham number in magnetorheological fluids," *Journal of Magnetism and Magnetic Materials*, vol. 380, pp. 98–104, 2015. DOI: `10.1016/j.jmmm.2014.11.010`.

[54] S. G. Sherman and N. M. Wereley, "Performance of magnetorheological fluids beyond the chain based shear limit," *Journal of Applied Physics*, vol. 115, no. 17, 17B523, 2014. DOI: `10.1063/1.4867963`.

[55] J. E. Martin and R. A. Anderson, "Chain model of electrorheology," *The Journal of Chemical Physics*, vol. 104, no. 12, p. 4814, 1996. DOI: `10.1063/1.471176`.

[56] H. Sodeyama, K. Sunakoda, H. Fujitani, S. Soda, N. Iwata, and K. Hata, "Dynamic Tests and Simulation of Magneto-Rheological Dampers," *Computer-Aided Civil and Infrastructure Engineering*, vol. 18, no. 1, pp. 45–57, 2003. DOI: `10.1111/1467-8667.t01-1-00298`.

[57] H. M. Laun, C. Gabriel, and C. Kieburg, "Twin gap magnetorheometer using ferromagnetic steel plates: Performance and validation," *Journal of Rheology*, vol. 54, no. 2, p. 327, 2010. DOI: `10.1122/1.3302804`.

[58] D. Güth and J. Maas, "Characterization and modeling of the behavior of magnetorheological fluids at high shear rates in rotational systems," *Journal of Intelligent Material Systems and Structures*, p. 114, 2015. DOI: `10.1177/1045389X15577646`.

[59] D Güth, A Wiebe, and J Maas, "Design of shear gaps for high-speed and high-load MRF brakes and clutches," *Journal of Physics: Conference Series*, vol. 412, no. 1, p. 012 046, 2013. DOI: `10.1088/1742-6596/412/1/012046`.

[60] X. Wang and F. Gordaninejad, "Study of magnetorheological fluids at high shear rates," *Rheologica Acta*, vol. 45, no. 6, pp. 899–908, 2006. DOI: `10.1007/s00397-005-0058-y`.

[61] C. Gabriel and H. M. Laun, "Combined slit and plateplate magnetorheometry of a magnetorheological fluid (MRF) and parameterization using the Casson model," *Rheologica Acta*, vol. 48, no. 7, pp. 755–768, 2009. DOI: `10.1007/s00397-009-0369-5`.

[62] J.-H. Koo, F. D. Goncalves, and M. Ahmadian, "A comprehensive analysis of the response time of MR dampers," *Smart Materials and Structures*, vol. 15, no. 2, pp. 351–358, 2006. DOI: `10.1088/0964-1726/15/2/015`.

[63] H. Sahin, F. Gordaninejad, X. Wang, and Y. Liu, "Response time of magnetorheological fluids and magnetorheological valves under various flow conditions," *Journal of Intelligent Material Systems and Structures*, vol. 23, no. 9, pp. 949–957, 2012. DOI: `10.1177/1045389X12447984`.

[64] H. M. Laun and C. Gabriel, "Measurement modes of the response time of a magneto-rheological fluid (MRF) for changing magnetic flux density," *Rheologica Acta*, vol. 46, no. 5, pp. 665–676, 2007. DOI: `10.1007/s00397-006-0155-6`.

[65] J. M. Ginder and L. C. Davis, "Shear stresses in magnetorheological fluids: Role of magnetic saturation," *Applied Physics Letters*, vol. 65, no. 26, p. 3410, 1994. DOI: `10.1063/1.112408`.

[66] S. S. Abdali, E. Mitsoulis, and N. C. Markatos, "Entry and exit flows of Bingham fluids," *Journal of Rheology*, vol. 36, no. 2, p. 389, 1992. DOI: `10.1122/1.550350`.

[67] E. Mitsoulis, S. Marangoudakis, M. Spyratos, T. Zisis, and N. a. Malamataris, "Pressure-Driven Flows of Bingham Plastics Over a Square Cavity," *Journal of Fluids Engineering*, vol. 128, no. 5, p. 993, 2006. DOI: `10.1115/1.2236130`.

[68] A. J. Taylor, "Conduit flow of an incompressible, yield-stress fluid," *Journal of Rheology*, vol. 41, no. 1, p. 93, 1997. DOI: `10.1122/1.550802`.

[69] T. Min, H. G. Choi, J. Y. Yoo, and H. Choi, "Laminar convective heat transfer of a Bingham plastic in a circular pipeII. Numerical approach hydrodynamically developing flow and simultaneously developing flow," *International Journal of Heat and Mass Transfer*, vol. 40, no. 15, pp. 3689–3701, 1997. DOI: `10.1016/S0017-9310(97)00004-5`.

[70] G. C. Vradis, J. Dougher, and S. Kumar, "Entrance pipe flow and heat transfer for a Bingham plastic," *International Journal of Heat and Mass Transfer*, vol. 36, no. 3, pp. 543–552, 1993. DOI: `10.1016/0017-9310(93)80030-X`.

[71] E. J. Park, L. F. da Luz, and A. Suleman, "Multidisciplinary design optimization of an automotive magnetorheological brake design," *Computers & Structures*, vol. 86, no. 3-5, pp. 207–216, 2008. DOI: `10.1016/j.compstruc.2007.01.035`.

[72] D. a. Bompos and P. G. Nikolakopoulos, "CFD simulation of magnetorheological fluid journal bearings," *Simulation Modelling Practice and Theory*, vol. 19, no. 4, pp. 1035–1060, 2011. DOI: `10.1016/j.simpat.2011.01.001`.

[73] E. Gedik, H. Kurt, Z. Recebli, and C. Balan, "Two-dimensional CFD simulation of magnetorheological fluid between two fixed parallel plates applied external magnetic field," *Computers & Fluids*, vol. 63, pp. 128–134, 2012. DOI: `10.1016/j.compfluid.2012.04.011`.

[74] Z. Parlak and T. Engin, "Time-dependent CFD and quasi-static analysis of magnetorheological fluid dampers with experimental validation," *International Journal of Mechanical Sciences*, vol. 64, no. 1, pp. 22–31, 2012. DOI: `10.1016/j.ijmecsci.2012.08.006`.

[75] W. A. Bullough, R. J. Atkin, S. Urang, T. G. Kum, C. Musch, and T. Rober, "Two Dimensional Flow of an ESF: Experiment, CFD, Bingham Plastic Analysis," *International Journal of Modern Physics B*, vol. 15, no. 6-7, pp. 745–757, 2001. DOI: `10.1142/S0217979201005222`.

[76] J. Goldasz and B. Sapinski, "Nondimensional characterization of flow-mode magnetorheological/electrorheological fluid dampers," *Journal of Intelligent Material Systems and Structures*, vol. 23, no. 14, pp. 1545–1562, 2012. DOI: `10.1177/1045389X12447293`.

[77] J. Gołdasz and B. Sapiński, "CFD Study of the flow of MR fluids," in *Insight into Magnetorheological Shock Absorbers*, Cham: Springer International Publishing, 2015, pp. 117–130, ISBN: 978-3-319-13232-7. DOI: `10.1007/978-3-319-13233-4`.

[78] E. Mitsoulis, "Flows of viscoplastic materials: Models and computations," *Rheology Reviews*, vol. 2007, pp. 135 –178, 2007. DOI: `10.1016/S0045-7949(96)00167-8`.

[79] T. C. Papanastasiou, "Flows of Materials with Yield," *Journal of Rheology*, vol. 31, no. 5, p. 385, 1987. DOI: `10.1122/1.549926`.

[80] N. M. Wereley and L. Pang, "Nondimensional analysis of semi-active electrorheological and magnetorheological dampers using approximate parallel plate models," *Smart Materials and Structures*, vol. 7, no. 5, pp. 732–743, 1998. DOI: `10.1088/0964-1726/7/5/015`.

[81] B. O. A. Hedström, "Flow of Plastic Materials in Pipes," *Industrial & Engineering Chemistry*, vol. 44, no. 3, pp. 651–656, 1952. DOI: `10.1021/ie50507a056`.

[82] G. W. Govier and K Aziz, *The Flow of Complex Mixtures in Pipes.* New York: Van Nostrand Reinhold, 1972.

[83] D. J. Peel, R Stanway, and W. A. Bullough, “Dynamic modelling of an ER vibration damper for vehicle suspension applications,” *Smart Materials and Structures*, vol. 5, no. 5, pp. 591–606, 1996. DOI: `10.1088/0964-1726/5/5/008`.

[84] A. N. Alexandrou, E. Duc, and V. Entov, “Inertial, viscous and yield stress effects in Bingham fluid filling of a 2-D cavity,” *Journal of Non-Newtonian Fluid Mechanics*, vol. 96, no. 3, pp. 383–403, 2001. DOI: `10.1016/S0377-0257(00)00199-3`.

[85] D Bresch, E. D. Fernández-Nieto, I. R. Ionescu, and P Vigneaux, “Augmented Lagrangian Method and Compressible Visco-plastic Flows: Applications to Shallow Dense Avalanches,” in *New Directions in Mathematical Fluid Mechanics*, Basel: Birkhäuser Basel, 2009, pp. 57–89. DOI: `10.1007/978-3-0346-0152-8_4`.

[86] R. W. Phillips, “Engineering applications of fluids with a variable yield stress,” PhD thesis, University of California, Berkeley, 1969, p. 205.

[87] N. M. Wereley, J. Lindler, N. Rosenfeld, and Y.-T. Choi, “Biviscous damping behavior in electrorheological shock absorbers,” *Smart Materials and Structures*, vol. 13, no. 4, pp. 743–752, 2004. DOI: `10.1088/0964-1726/13/4/012`.

[88] S. S. Chen, L. T. Fan, and C. L. Hwang, “Entrance region flow of the Bingham fluid in a circular pipe,” *AIChE Journal*, vol. 16, no. 2, pp. 293–299, 1970. DOI: `10.1002/aic.690160224`.

[89] V. L. Shah and R. J. Soto, “Entrance flow of a bingham fluid in a tube,” *Applied Scientific Research*, vol. 30, no. 4, pp. 271–278, 1975. DOI: `10.1007/BF00386695`.

[90] E. B. Bagley, “End Corrections in the Capillary Flow of Polyethylene,” *Journal of Applied Physics*, vol. 28, no. 5, p. 624, 1957. DOI: `10.1063/1.1722814`.

[91] H. G. Weller, G Tabor, H Jasak, and C Fureby, “A tensorial approach to computational continuum mechanics using object-oriented techniques,” *Computers in Physics*, vol. 12, no. 6, pp. 620–631, 1998. DOI: `10.1063/1.168744`.

[92] S. Patankar, *Numerical heat transfer and fluid flow*. CRC Press, 1980.

[93] P. Kuzhir, G. Bossis, V. Bashtovoi, and O. Volkova, “Effect of the orientation of the magnetic field on the flow of magnetorheological fluid. II. Cylindrical channel,” *Journal of Rheology*, vol. 47, no. 6, p. 1385, 2003. DOI: `10.1122/1.1619378`.

[94] R. G. Owens and T. N. Phillips, *Computational Rheology*. London: Imperial College Press, 2002, p. 417, ISBN: 1-86094-186-9.

[95] F. M. White, *Viscous Fluid Flow*, Second. Boston: McGraw-Hill, 1991.

[96] W. Hanks and D. R. Pratt, “On the Flow of Bingham Plastic Slurries in Pipes and Between Parallel Plates,” *Society of Petroleum Engineering Journal*, vol. 7, no. 04, pp. 342–346, 1967. DOI: `10.2118/1682-PA`.

[97] U. Lange, L. Richter, and L. Zipser, "Flow of Magnetorheological Fluids," *Journal of Intelligent Material Systems and Structures*, vol. 12, no. 3, pp. 161–164, 2001. DOI: `10.1106/PF05-DTU2-2QTD-28B6`.

[98] H. Fujitani, H. Sodeyama, T. Tomura, T. Hiwatashi, Y. Shiozaki, K. Hata, K. Sunakoda, S. Morishita, and S. Soda, "Development of a 400kN magnetorheological damper for a real base-isolated building," in *Smart Structures and Materials 2003: Damping and Isolation*, G. S. Agnes and K.-W. Wang, Eds., vol. 5052, 2003, pp. 265–276, ISBN: 1111111111. DOI: `10.1117/12.483810`.

[99] S.-B. Choi, M.-H. Nam, and B.-K. Lee, "Vibration Control of a MR Seat Damper for Commercial Vehicles," *Journal of Intelligent Material Systems and Structures*, vol. 11, no. December 2000, pp. 936–944, 2001. DOI: `10.1106/AERG-3QKV-31V8-F250`.

[100] S.-B. Choi, M.-S. Seong, and S.-H. Ha, "Vibration control of an MR vehicle suspension system considering both hysteretic behavior and parameter variation," *Smart Materials and Structures*, vol. 18, no. 12, p. 125 010, 2009. DOI: `10.1088/0964-1726/18/12/125010`.

[101] F Gordaninejad, X Wang, G Hitchcock, K Bangrakulur, S Ruan, and M Siino, "Modular High-Force Seismic Magneto-Rheological Fluid Damper," *Journal of Structural Engineering*, vol. 136, no. 2, pp. 135–143, 2010. DOI: `10.1061/(ASCE)0733-9445(2010)136:2(135)`.

[102] Z. C. Li and J Wang, "A Gun Recoil System Employing A Magnetorheological Fluid Damper," *Smart Materials and Structures*, vol. 21, no. 10, p. 105 003, 2012. DOI: `10.1088/0964-1726/21/10/105003`.

[103] Z.-X. Li and L.-H. Xu, "Performance Tests and Hysteresis Model of MRF-04K Damper," *Journal of Structural Engineering*, vol. 131, no. 8, pp. 1303–1306, 2005. DOI: `10.1061/(ASCE)0733-9445(2005)131:8(1303)`.

[104] A. Rodriguez, N. Iwata, F. Ikhouane, and J. Rodellar, "Modeling and Identification of a Large-Scale Magnetorheological Fluid Damper," *Advances in Science and Technology*, vol. 56, pp. 374–379, 2008. DOI: `10.4028/www.scientific.net/AST.56.374`.

[105] J. W. Tu, J. Liu, W. L. Qu, Q. Zhou, H. B. Cheng, and X. D. Cheng, "Design and Fabrication of 500-kN Large-scale MR Damper," *Journal of Intelligent Material Systems and Structures*, vol. 22, no. 5, pp. 475–487, 2011. DOI: `10.1177/1045389X11399942`.

[106] G. Yang, "Large-Scale Magnetorheological Fluid Damper for Vibration Mitigation," PhD thesis, University of Notre Dame, 2001, p. 480.

[107] Y.-T. Choi, R. Robinson, W. Hu, N. M. Wereley, T. S. Birchette, A. O. Bolukbasi, and J. Woodhouse, "Analysis and Control of a Magnetorheological Landing Gear System for a Helicopter," *Journal of the American Helicopter Society*, vol. 61, no. 3, pp. 1–8, 2016. DOI: `10.4050/JAHS.61.032006`.

[108] M. Mao, W. Hu, Y.-T. Choi, N. M. Wereley, A. L. Browne, J. Ulicny, and N. Johnson, "Nonlinear modeling of magnetorheological energy absorbers under impact conditions," *Smart Materials and Structures*, vol. 22, no. 11, p. 115 015, 2013. DOI: `10.1088/0964-1726/22/11/115015`.

[109] H. J. Singh, W. Hu, N. M. Wereley, and W. Glass, "Experimental validation of a magnetorheological energy absorber design optimized for shock and impact loads," *Smart Materials and Structures*, vol. 23, no. 12, p. 125 033, 2014. DOI: `10.1088/0964-1726/23/12/125033`.

[110] H. E. Merritt, *Hydraulic Control Systems.* New York: John Wiley and Sons, 1967.

[111] R. M. Sadri and J. M. Floryan, "Accurate Evaluation of the Loss Coefficient and the Entrance Length of the Inlet Region of a Channel," *Journal of Fluids Engineering*, vol. 124, no. 3, p. 685, 2002. DOI: `10.1115/1.1493813`.

[112] K. Wilson, "Transitional and Turbulent Flows of Bingham Plastics," *Mineral Processing and Extractive Metallurgy Review*, vol. 20, no. 1, pp. 225–237, 2000. DOI: `10.1080/08827509908962474`.

[113] M. Malin, "The Turbulent Flow of Bingham Plastic Fluids in Smooth Circular Tubes," *International Communications in Heat and Mass Transfer*, vol. 24, no. 6, pp. 793–804, 1997. DOI: `10.1016/S0735-1933(97)00066-3`.

[114] H. Schlichting, *Boundary-Layer Theory*, 6th ed. McGraw-Hill, 1968.

[115] I. Daprà and G. Scarpi, "Start-up of channel-flow of a Bingham fluid initially at rest," *Rendiconti Lincei Matematica e Applicazioni*, vol. 15, no. 2, pp. 125–134, 2004.

[116] Y.-T. Choi and N. M. Wereley, "Comparative Analysis of the Time Response of Electrorheological and Magnetorheological Dampers Using Nondimensional Parameters," *Journal of Intelligent Material Systems and Structures*, vol. 13, no. 7-8, pp. 443–451, 2002. DOI: `10.1106/104538902028557`.

[117] C. T. Crowe, J. D. Schwarzkopf, M. Sommerfeld, and Y. Tsuji, *Multiphase Flow with Droplets and Particles*, 2nd. Boca Raton: CRC Press, 2012, ISBN: 978-1-4398-4050-4.

[118] ASTM D341-09, "Standard Practice for Viscosity-Temperature Charts for Liquid Petroleum Products," ASTM International, West Conshohocken, PA, Tech. Rep., 2015. DOI: `10.1520/D0341-09R15`.

[119] S. R. Hong, N. M. Wereley, Y. T. Choi, and S. B. Choi, "Analytical and experimental validation of a nondimensional Bingham model for mixed-mode magnetorheological dampers," *Journal of Sound and Vibration*, vol. 312, no. 3, pp. 399–417, 2008. DOI: `10.1016/j.jsv.2007.07.087`.

[120] G. Yang, B. F. Spencer, H.-J. Jung, and J. D. Carlson, "Dynamic Modeling of Large-Scale Magnetorheological Damper Systems for Civil Engineering Applications," *Journal of Engineering Mechanics*, vol. 130, no. 9, pp. 1107–1114, 2004. DOI: `10.1061/(ASCE)0733-9399(2004)130:9(1107)`.

[121] H. Fujitani, H. Sodeyama, K. Hata, Y. Komatsu, N. Iwata, K. Sunakoda, and S. Soda, "Dynamic performance evaluation of a 200kN magneto-rheological damper," *Technical Note of National Institute for Land and Infrastructure Management*, vol. 41, pp. 349–356, 2002.

[122] M. J. Crochet and K Walters, "Numerical Methods in Non-Newtonian Fluid Mechanics," *Annual Review of Fluid Mechanics*, vol. 15, no. 1, pp. 241–260, 1983. DOI: `10.1146/annurev.fl.15.010183.001325`.

[123] M. Mao, W. Hu, Y.-T. Choi, and N. M. Wereley, "A Magnetorheological Damper with Bifold Valves for Shock and Vibration Mitigation," *Journal of Intelligent Material Systems and Structures*, vol. 18, no. December, 2007. DOI: `10.1177/1045389X07083131`.

[124] N. L. Wilson, N. M. Wereley, W. Hu, and G. J. Hiemenz, "Analysis of a magnetorheological damper incorporating temperature dependence," *International Journal of Vehicle Design*, vol. 63, no. 2/3, p. 137, 2013. DOI: `10.1504/IJVD.2013.056102`.

[125] F. Gordaninejad and D. G. Breese, "Heating of Magnetorheological Fluid Dampers," *Journal of Intelligent Material Systems and Structures*, vol. 10, no. 8, pp. 634–645, 1999. DOI: `10.1106/55D1-XAXP-YFH6-B2FB`.

[126] K. D. Weiss and T. G. Duclos, "Controllable fluids: the temperature dependence of post-yield properties," *International Journal of Modern Physics B*, vol. 08, no. 20-21, pp. 3015–3032, 1994. DOI: `10.1142/S0217979294001275`.

[127] K. D. Weiss, J. D. Carlson, T. G. Duclos, and K. J. Abbey, *Temperature independent magnetorheological materials*, U.S. Patent, 1997.

[128] H. Sahin, X. Wang, and F. Gordaninejad, "Temperature Dependence of Magneto-rheological Materials," *Journal of Intelligent Material Systems and Structures*, vol. 20, no. 18, pp. 2215–2222, 2009. DOI: `10.1177/1045389X09351608`.

[129] E Lemaire, A. Meunier, G. Bossis, J. Liu, D. Felt, P. Bashtovoi, and N. Matoussevitch, "Influence of the particle size on the rheology of magnetorheological fluids," *Journal of Rheology*, vol. 39, no. 5, p. 1011, 1995. DOI: `10.1122/1.550614`.

[130] E. Furst and A. Gast, "Dynamics and lateral interactions of dipolar chains," *Physical Review E*, vol. 62, no. 5, pp. 6916–6925, 2000. DOI: `10.1103/PhysRevE.62.6916`.

[131] J. Mewis and N. J. Wagner, *Colloidal Suspension Rheology*. Cambridge: Cambridge University Press, 2012, p. 393, ISBN: 9780521515993.

[132] D. Kneževi and V. Savi, "Mathematical modeling of changing of dynamic viscosity, as a function of temperature and pressure, of mineral oils for hydraulic systems," *Facta Universitatis: Mechanical Engineering*, vol. 4, pp. 27–34, 2006.

[133] S. L. Vieira, L. B. Pompeo Neto, and A. C. F. Arruda, "Transient behavior of an electrorheological fluid in shear flow mode," *Journal of Rheology*, vol. 44, no. 5, p. 1139, 2000. DOI: `10.1122/1.1289282`.

[134] S Henley and F. E. Filisko, "Flow profiles of electrorheological suspensions: An alternative model for ER activity," *Journal of Rheology*, vol. 43, no. 5, p. 1323, 1999. DOI: `10.1122/1.551024`.

[135] S. Viera, M. Nakano, S. Henley, F. E. Filisko, L. Pompeo Neto, and A. Arruda, "Transient behavior of the microstructure of electrorheological fluids in shear flow mode," *International Journal of Modern Physics B*, vol. 15, no. 6-7, pp. 695–703, 2001. DOI: `10.1142/S0217979201005179`.

[136] J. G. Cao, J. P. Huang, and L. W. Zhou, "Structure of electrorheological fluids under an electric field and a shear flow: experiment and computer simulation.," *Journal of Physical Chemistry. B*, vol. 110, no. 24, pp. 11 635–9, 2006. DOI: `10.1021/jp0611774`.

[137] Y. Pappas and D. J. Klingenberg, "Simulations of magnetorheological suspensions in Poiseuille flow," *Rheologica Acta*, vol. 45, no. 5, pp. 621–629, 2005. DOI: `10.1007/s00397-005-0016-8`.

[138] S. G. Sherman, D. A. Paley, and N. M. Wereley, "Massively Parallel Simulations of Chain Formation and Restructuring Dynamics in a Magnetorheological Fluid," *ASME Conference Proceedings*, vol. 2011, no. 54716, pp. 651–658, 2011. DOI: `10.1115/SMASIS2011-5188`.

[139] K. von Pfeil, M. D. Graham, D. J. Klingenberg, and J. F. Morris, "Structure evolution in electrorheological and magnetorheological suspensions from a continuum perspective," *Journal of Applied Physics*, vol. 93, no. 9, p. 5769, 2003. DOI: `10.1063/1.1563037`.

[140] J Anderson, C Lorenz, and A Travesset, "General purpose molecular dynamics simulations fully implemented on graphics processing units," *Journal of Computational Physics*, vol. 227, no. 10, pp. 5342–5359, 2008. DOI: `10.1016/j.jcp.2008.01.047`.

[141] M Mohebi, N Jamasbi, and J. Liu, "Simulation of the formation of nonequilibrium structures in magnetorheological fluids subject to an external magnetic field," *Physical Review E*, vol. 54, no. 5, pp. 5407–5413, 1996. DOI: `10.1103/PhysRevE.54.5407`.

[142] R. T. Foister, *Magnetorheological Fluids*, U.S. Patent, 1997.

[143] Y Ido, T Inagaki, and T Yamaguchi, "Numerical simulation of microstructure formation of suspended particles in magnetorheological fluids.," *Journal of Physics Condensed Matter*, vol. 22, no. 32, p. 324 103, 2010. DOI: `10.1088/0953-8984/22/32/324103`.

[144] R. Tarjan, "Depth-first search and linear graph algorithms," *SIAM Journal on Computing*, vol. 1, no. 2, pp. 146–160, 1972.

[145] Y.-T. Choi and N. M. Wereley, "Biodynamic Response Mitigation to Shock Loads Using Magnetorheological Helicopter Crew Seat Suspensions," *Journal of Aircraft*, vol. 42, no. 5, pp. 1288–1295, 2005. DOI: `10.2514/1.6839`.

[146] N. M. Wereley, Y.-T. Choi, and H. J. Singh, "Adaptive Energy Absorbers for Drop-induced Shock Mitigation," *Journal of Intelligent Material Systems and Structures*, vol. 22, no. 6, pp. 515–519, 2011. DOI: `10.1177/1045389X10393767`.

[147] H. J. Singh and N. M. Wereley, "Adaptive magnetorheological shock isolation mounts for drop-induced impacts," *Smart Materials and Structures*, vol. 22, no. 12, p. 122 001, 2013. DOI: `10.1088/0964-1726/22/12/122001`.

[148] L. Marshall, C. F. Zukoski, and J. W. Goodwin, "Effects of electric fields on the rheology of non-aqueous concentrated suspensions," *Journal of the Chemical Society, Faraday Transactions 1*, vol. 85, no. 9, p. 2785, 1989. DOI: `10.1039/f19898502785`.

[149] S. Melle, O. Calderón, M. Rubio, and G. Fuller, "Microstructure evolution in magnetorheological suspensions governed by Mason number," *Physical Review E*, vol. 68, no. 4, p. 041 503, 2003. DOI: `10.1103/PhysRevE.68.041503`.

[150] R. S. Allan and S. G. Mason, "Particle Behaviour in Shear and Electric Fields. I. Deformation and Burst of Fluid Drops," *Proceedings of the Royal Society A: Mathematical, Physical and Engineering Sciences*, vol. 267, no. 1328, pp. 45–61, 1962. DOI: `10.1098/rspa.1962.0082`.

[151] G. M. Kamath, M. K. Hurt, and N. M. Wereley, "Analysis and testing of Bingham plastic behavior in semi-active electrorheological fluid dampers," *Smart Materials and Structures*, vol. 5, no. 5, pp. 576–590, 1996. DOI: `10.1088/0964-1726/5/5/007`.

[152] N. M. Wereley, J. U. Cho, Y. T. Choi, and S. B. Choi, "Magnetorheological dampers in shear mode," *Smart Materials and Structures*, vol. 17, no. 1, p. 015 022, 2008. DOI: `10.1088/0964-1726/17/01/015022`.

[153] J de Vicente, G Bossis, S Lacis, and M Guyot, "Permeability measurements in cobalt ferrite and carbonyl iron powders and suspensions," *Journal of Magnetism and Magnetic Materials*, vol. 251, no. 1, pp. 100–108, 2002. DOI: `10.1016/S0304-8853(02)00484-5`.

[154] J. D. Carlson, "MR fluids and devices in the real world," *International Journal of Modern Physics B*, vol. 19, no. 7-9, pp. 1463–1470, 2005. DOI: `10.1142/S0217979205030451`.

[155] D. J. Klingenberg, C. H. Olk, M. A. Golden, and J. C. Ulicny, "Effects of nonmagnetic interparticle forces on magnetorheological fluids.," *Journal of Physics Condensed Matter*, vol. 22, no. 32, pp. 324 101–324 105, 2010. DOI: `10.1088/0953-8984/22/32/324101`.

[156] J. Ginder, L. Davis, and L. Elie, "Rheology of magnetorheological fluids: models and measurements," *International Journal of Modern Physics B*, vol. 10, no. 23n24, pp. 3293–3303, 1996. DOI: `10.1142/S0217979296001744`.

[157] G Bossis, S Lacis, A Meunier, and O Volkova, "Magnetorheological fluids," *Journal of Magnetism and Magnetic Materials*, vol. 252, pp. 224–228, 2002. DOI: `10.1016/S0304-8853(02)00680-7`.

[158] M. R. Jolly, J. D. Carlson, and B. C. Muñoz, "A model of the behaviour of magnetorheological materials," *Smart Materials and Structures*, vol. 5, no. 5, pp. 607–614, 1996. DOI: `10.1088/0964-1726/5/5/009`.

[159] C. L. A. Berli and J. de Vicente, "A structural viscosity model for magnetorheology," *Applied Physics Letters*, vol. 101, no. 2, p. 021 903, 2012. DOI: `10.1063/1.4734504`.

[160] T. Halsey, J. Martin, and D. Adolf, "Rheology of electrorheological fluids," *Physical Review Letters*, vol. 68, no. 10, pp. 1519–1522, 1992. DOI: `10.1103/PhysRevLett.68.1519`.

[161] B. J. de Gans, N. J. Duin, D. van den Ende, and J. Mellema, "The influence of particle size on the magnetorheological properties of an inverse ferrofluid," *The Journal of Chemical Physics*, vol. 113, no. 5, p. 2032, 2000. DOI: `10.1063/1.482011`.

[162] O. Volkova, G. Bossis, M. Guyot, V. Bashtovoi, and A. Reks, "Magnetorheology of magnetic holes compared to magnetic particles," *Journal of Rheology*, vol. 44, no. 1, p. 91, 2000. DOI: `10.1122/1.551075`.

[163] G Bossis, O Volkova, S Lacis, and A Meunier, "Ferrofluids," in *Ferrofluids*, ser. Lecture Notes in Physics, S. Odenbach, Ed., vol. 594, Berlin, Heidelberg: Springer Berlin Heidelberg, 2002, pp. 202–230, ISBN: 978-3-540-43978-3. DOI: `10.1007/3-540-45646-5`.

[164] J. D. Carlson and K. D. Weiss, *Magnetorheological materials based on alloy particles*, U.S. Patent, 1995.

[165] J. M. Ginder, L. D. Elie, and L. C. Davis, *Magnetic Fluid-Based Magnetorheological Fluids*, U.S. Patent, 1996.

[166] D. T. Zimmerman, R. C. Bell, J. A. Filer, J. O. Karli, and N. M. Wereley, "Elastic percolation transition in nanowire-based magnetorheological fluids," *Applied Physics Letters*, vol. 95, no. 1, p. 014 102, 2009. DOI: `10.1063/1.3167815`.

[167] G. T. Ngatu, N. M. Wereley, J. O. Karli, and R. C. Bell, "Dimorphic magnetorheological fluids: exploiting partial substitution of microspheres by nanowires," *Smart Materials and Structures*, vol. 17, no. 4, p. 045 022, 2008. DOI: `10.1088/0964-1726/17/4/045022`.

[168] L. A. Powell, N. M. Wereley, and J. Ulicny, “Magnetorheological Fluids Employing Substitution of Nonmagnetic for Magnetic Particles to Increase Yield Stress,” *IEEE Transactions on Magnetics*, vol. 48, no. 11, pp. 3764–3767, 2012. DOI: `10.1109/TMAG.2012.2202885`.

[169] K. Shah, D. Xuan Phu, and S.-B. Choi, “Rheological properties of bi-dispersed magnetorheological fluids based on plate-like iron particles with application to a small-sized damper,” *Journal of Applied Physics*, vol. 115, no. 20, p. 203 907, 2014. DOI: `10.1063/1.4879681`.

[170] T. Kikuchi, J. Noma, S. Akaiwa, and Y. Ueshima, “Response time of magnetorheological fluid-based haptic device,” *Journal of Intelligent Material Systems and Structures*, vol. 27, no. 7, pp. 3–4, 2015. DOI: `10.1177/1045389X15596621`.

[171] C. Kormann, H. Laun, and H. Richter, “MR Fluids with Nano-Sized Magnetic Particles,” *International Journal of Modern Physics B*, vol. 10, no. 23n24, pp. 3167–3172, 1996. DOI: `10.1142/S0217979296001604`.

[172] F. A. Morrison, *Understanding Rheology.* New York: Oxford University Press, 2001, pp. 188–190.

[173] H. M. Laun, C. Gabriel, and C. Kieburg, “Magnetorheological Fluid in Oscillatory Shear and Parameterization with Regard to MR Device Properties,” *Journal of Intelligent Material Systems and Structures*, vol. 21, no. 15, pp. 1479–1489, 2009. DOI: `10.1177/1045389X09351759`.

[174] J. C. Fernández-Toledano, J. Rodríguez-López, K. Shahrivar, R. Hidalgo-Álvarez, L. Elvira, F. Montero de Espinosa, and J. de Vicente, “Two-step yielding in magnetorheology,” *Journal of Rheology*, vol. 58, no. 5, pp. 1507–1534, 2014. DOI: `10.1122/1.4880675`.

[175] P. Bogacki and L. F. Shampine, “A 3(2) pair of Runge - Kutta formulas,” *Applied Mathematics Letters*, vol. 2, no. 4, pp. 321–325, 1989. DOI: `10.1016/0893-9659(89)90079-7`.